In-situ Studies Following the Formation of Nanostructured Materials

Glen J Smales

A dissertation submitted in partial fulfilment
of the requirements for the degree of
Doctor of Engineering
of
University College London.

Department of Chemistry
University College London

2019

I, Glen J Smales, confirm that the work presented in this thesis is my own. Where information has been derived from other sources, I confirm that this has been indicated in the work.

Abstract

The work described within this thesis, primarily focuses on furthering the understanding of the formation of nanostructured materials, predominantly through the use of *in-situ* small-angle X-ray scattering (SAXS) experiments. The main aim of the work is to expand the knowledge of the mechanistic aspects of the formation and growth of nanostructured porous solids.

In-situ SAXS and complimentary *ex-situ* microscopy studies have been utilised to probe the formation of silicalite-1 from three different silica precursors (Tetraethyl Orthosilicate, Ludox AS-40 and Fumed silica), yielding new insights into the mechanistic growth of zeolites. Each system was probed individually, using the same synthesis ratios and conditions to make direct comparisons of the three systems possible. With this study, the presence of multiple, distinct paths for the formation of silicalite-1 were observed, showing that the route of formation is dependent, greatly upon the choice of silica source.

The formation of hierarchical silicalite-1 from self-templating silica precursors was probed using *in-situ* SAXS and *ex-situ* microscopy studies to provide insights on the formation of this novel material.

In-situ SAXS/WAXS studies were performed to probe the mechanism of formation of ZIF-8 at different temperatures. *In-situ* SAXS measurement were utilised to monitor the shape and size evolution of particles as they grow in solution, whilst *in-situ* WAXS measurements allowed for the crystallisation simultaneous. The use of both techniques proved to be ideal for determining morphological changes within these solution phase reactions, whilst making it possible to follow the formation at a high temporal resolution.

Finally, a new *in-situ* hydrothermal cell was developed for the prevention of

sample sedimentation. The cell was designed predominantly for use at scattering beamlines, and is capable of preventing the sedimentation of particles held within a solutions through the use of rotation.

Impact Statement

Studying the formation of materials inherently has academic benefits, however with a greater understanding of the processes involved during the synthesis of materials, these academic benefits can become commercially relevant. This is very true when it comes to understanding the formation and growth mechanisms that are active during the synthesis of nanostructured materials such as zeolites and metal-organic frameworks (MOFs). With a better understanding of the underlying processes occurring during the formation of nanostructured materials, comes the potential to improve their effectiveness within specific applications. For example, zeolites play a critical role in industrial applications such as catalysis, and with a greater understanding of their formation comes the potential to better control the final morphology and the overall properties of the materials obtained. This has the potential to make nanostructured products more efficient and effective in specific applications, hence, obtaining a greater understanding of the formation of these materials can have great benefits on their industrial success.

Studying the formation of Macroporous zeolites again has similar advantages to studying the formation of conventional materials. However, the development of simple synthetic procedures to create hierarchical zeolite structures, without the use of long, multi-step processes is also advantageous, as it means that the synthesis of hierarchical zeolite structures is more accessible, which could increase academic research in the field, especially in exploring ways to extend the synthesis procedures, within this thesis, to different zeolite structures.

The development of a new in-situ hydrothermal cell predominantly for use at scattering beamlines, allows for the collection of good quality data that is representative of the sample as a whole, and not just of what can be suspended in the beam. It does this by preventing the sedimentation of particles through rotation, making it is easier to follow the nucleation and growth of particles within heterogeneous systems. The rotating in-situ cell presented within this thesis will be actively utilized at Diamond Light Source, predominantly on beamline I22 for high temperature, high pressure experiments utilizing a variety of different window materials that can be tailored to experimental needs. This cell will facilitate a wide variety of experiments and will benefit a broad range of science at a facility utilized by a large community of national and international scientists working in both academia and industry.

Acknowledgements

Firstly, I would like to thank my supervisors, Professor Gopinathan Sankar and Dr Andy Smith, for their help and encouragement over the past few years. Without their vast knowledge and hard work I would not be where I am today. A special thank you goes to I22 staff Dr Nick Terrill, Dr Tim Snow and Dr Olga Shebanova for being so welcoming at Diamond, and thanks also goes to Mike, Steve and Lee in the workshop who have been very helpful throughout the past few years.

I would like to thank UCL staff, particularly Martin Vickers, Dr Jeremy Cockcroft, and Dr Steve Firth for their help and valuable advice whilst at UCL. I would also like to thank members of the Sankar group and my friends at UCL; Ian, Adam, Husn, Anastasia, Tom, Huw, Ines, Simon, Anna, Jenny, Jacob and Qam, whom without my time at UCL would not have been then same.I would also like to thank the staff at the various beamlines I have had the pleasure of visiting over the past few year, in particular to Dr Paul Thompson and Dr Daniel Hermida Merino, and special thanks goes to my collaborators Dr Ian Johnson, Dr Tom Bennett and Prof Richard Walton.

Finally, I would like to thank my family and friends for all their support over the past few years, in particular Holly, Bryn, Tom and my Mother for their unconditional love and support.

Contents

List of Figures

List of Tables

Chapter 1

Introductory Material

1.1 Nucleation and Growth

1.1.1 Introduction

In the modern world there is a constant push toward the use of greener and more efficient processes. This is also true in the world of solid-state materials chemistry, where more efficient and greener processes for the production of crystals are becoming more and more important. For example, both cost and material efficiency has always been a vital requirement for the production of catalysts, gas-storage materials, semiconductors, pharmaceuticals, and radioactive waste storage. To be able to produce materials with specific functionalities, it becomes essential to possess an understanding of how the materials are formed, so that an element of control can be employed in the materials production. This means that desirable properties can be utilised in applications more effectively, as with an understanding of a materials formation comes the potential to control crystal perfection, size, intergrowths and chirality to name only a few. This again has the potential to cut final production costs, which is essential when manufacturing materials with real world applications.[1] The issues that can arise from controlling crystal growth are also synonymous to those observed in nanoporous materials, and by understanding the growth mechanics of these materials, it may become possible to identify and control their overall properties. With this knowledge and through consideration of energetics it may be possible to predict the effects that modifications to growth conditions can have, eventually leading to the production of highly specialised materials with specific properties and morphologies.[2, 3]

1.1.2 History of Nucleation and Growth

At first, the growth of crystals was performed empirically, but with a greater understanding, aspects of control were obtained. It was discovered that crystal growth rates, crystal perfection and overall crystal size could be greatly influenced through fundamental understanding. The study of crystal growth has been ongoing for many years, by a vast number of people from different fields, which has provided strong foundations upon which newer ideas could be built. However, even with the remarkable progress that has been made over the years, the development of newer materials has provided a constant source of new challenges relevant to the understanding of crystallization.

Most scientists understand that the tools, syntheses and ideas they use everyday are part of a bigger picture that has been added to over decades, if not centuries. The incremental advances in thoughts and ideas that science undergoes everyday adds up, resulting in refinements in future work and eventually leading to new innovative works. One of the first documented accounts regarding nucleation and growth of crystalline solids dates back nearly 2000 years (77 - 79 AD).[4] It is in this encyclopaedia of natural history where works on the crystallisation of iron, copper and zinc sulfate were first summarised, taking note of the great deal of knowledge and understandings gained from ancient times on these substances. This early documentation of crystal growth would go on to be referenced a great deal over time. For example, Biringuccio and Agricola, in medieval times (nearly 1500 years later) noted this work when synthesising crystals for use in medicines, dyes and many other applications.[5, 6] This shows how important the subject of crystal growth is, but it also shows how previous knowledge can be iterated on to progress the future of science. There is little available documentation that can be found from the Dark Ages, or the time between Pliny the Elder's "Natural History" and Biringuccio and Agricola's "Concerning Pyrotechnics" in the 1540s, however, science was still slowly progressing.

Early studies focused on crystal morphology of naturally occurring minerals.

In 1564, Gessner, looked at how crystals differed physically, through the study of the angles present within a crystal and comparing the angles found in a multitude of different crystal structures.[7] Next came the famous ”De Metallicis” paper by Cæsalpinus.[8] The author, a celebrated botanist in his time, noted that the shape of crystals grown from aqueous solutions (such as sugar, salt) were characteristic of that material, i.e. each different salt crystal would have its own specific shape. In 1669, Steno, a Danish scientist, discovered that the angles between corresponding faces of quartz crystals remained that same, even though the appearance of the crystals may seem different, something that would be later known as the ”the law of constant interfacial angles”.[9, 10] Then, Romé de l'Isle, in 1772 concluded that each crystalline substance with a specific composition possessed a similar, but particular crystal shape.[11] From this work, Romé de l'Isle, would also find the six fundamental crystal forms that all others can be derived.

After these initial discoveries, people began to turn their attention to crystal growth and the underlying mechanisms involved. In 1848, Bravais, added eight more structures to those proposed by Romé de l'Isle, creating the 14 ”Bravais” lattices of three-dimensional crystals we know today.[12] This discovery provided a basis for understanding symmetry, morphology and anisotropy of crystal structures. Early studies showed how morphology could be affected by external forces (e.g. nutrient supply) and internal features (e.g. dimensions, atomic sizes, bond energies). This triggered Gibbs' quantitative studies of the thermodynamics of crystal growth. He began by studying how different phases behaved in heterogeneous systems under different temperature and pressure conditions.[13, 14] This seminal work on crystal growth would also include the first and second laws of thermodynamics. Gibbs proposed that for crystallisation to be viable there must be a nutrient phase present in a metastable state. The free energy at constant volume, or the Gibbs free energy at constant pressure, must exceed that of the crystals and the excess energy can be considered the driving force for crystallisation. It was also discovered that metastability can be achieved in one of two ways; through supercooling a melt, or by supersaturating a solution/vapour, and that during the process of crystallization, latent heat is evolved. Gibbs also contributed that nucleation can occur due to fluctuations between heterogeneous phases within a metastable homogeneous phases, hence nucleation can be either homogeneous or heterogeneous. Gibbs also showed how the maximum amount of supercooling or supersaturation is dependent upon thermodynamic properties of the material as well as various external forces, such as mechanical vibration and the nature of the crystal surface.

Next, at the start of the 20th century, Wilson began to probe the velocity of solidification and viscosity of supercooled liquids, whilst Knudsen started to look at kinetic molecular theory.[15, 16] Later, Volmer and Estermann introduced the idea of layer-by-layer growth or the adsorption-layer theory.[17] Volmer and Estermann came upon this idea when measuring the tangential growth rate of mercury crystals from a vapour state at low temperatures. They proposed that there was an adsorption-layer between the crystal and nutrient phase, where the crystallizing species loses some latent heat, whilst some surface mobility is maintained in the layer parallel to that of the crystal surface. The species are then incorporated into the crystal lattice at the edges of incomplete layers.

In 1928, Kossel proposed the kinetic theory (atomistic view on crystal growth) as opposed to the continuum thermodynamic interpretation, similar to that proposed by Stranski in the same year.[18, 19] These theories were based on mass transport of the crystallizing species to the growth interface, and that the processes occurring at the interfaces were not negligible, something that is now known as the Kossel-Stranski model. This work was based on observations made when looking at rock salt structures, and observing that no other faces except those of the cubic structure were in fact possible. Other faces are not present on the surface as complete planes, but instead made up of alternating faces several atoms thick (kinetic roughening). This work contributed to the the terrace-ledge-kink (TLK) theory where it is suggested that the incorporation of an atom requires a lateral spreading of the steps across a surface.[20]

Taylor, next proposed that the *plastic* deformation of ductile materials could be explained by the presence of dislocations, a theory initially developed by Volterra in

1905.[21, 22] Fifteen years later, Frank and Reed contributed to the fundamentals of crystal growth with laws governing dislocation branching.[23] The Frank-Reed mechanism for the generation of dislocations (a mechanism conceived independently by both scientists), showed how two-dimensional nucleation theory could not explain high crystal growth rates at low supersaturation, however, it could be accounted for in the presence of a screw dislocation on the growth face. This would lead to the continuous step generation or, as it is better known, ”spiral growth”.[24] In 1937, Donnay and Harker began work on classifying different crystal faces, with only one type forming crystal facets. In ionic crystals, the energy released during growth was defined as E(*hkl*) and by assuming a proportionality with the growth rate, it was possible to generate growth forms, something that was later confirmed by Hartman and Perdok.[25, 26] The calculated forms were similar to those seen in both natural and synthetic crystals, and the differences could be accounted for by the presence of impurities. This led to studies on the incorporation of impurities into fast growing crystals. These studies showed how it is possible to alter the final shape of the crystals obtained.[10, 26] This trend of purposeful doping of crystal structures continued through the 1950s, so that better control of crystal purity and the uniform introduction of dopants could be utilised in electronic devices.

Next, Burton, Prim and Slichter described how dopants and impurities are distributed (the BPS equation).[27] By observing solute concentrations, diffusion, and both the solute and solid-liquid distribution coefficients in crystals, BPS were able to describe what the concentration of dopants/impurities would be within the final crystal structure as a function of the initial melt concentration and a growth rate:

$$K_{eff} = \frac{K_0}{K_0 + (1 - K_0)e^{\frac{-R\delta_D}{D}}} \tag{1.1}$$

Where K_{eff} is the effective segregation coefficient, K_0 is the interface/equilibrium segregation coefficient, R is the growth rate, δ_D is the diffusion boundary layer thickness, and D is the solute diffusion coefficient. The BPS theory has been utilised for well-behaved systems, however, is has its limitations in its original form. However, multiple modifications to this theory have been added to improve its validity to a variety of different systems.[10, 27] The influence of surface structure on growth rate of perfect crystals was also first looked at by Burton.[28] This work focused on how growth can be affected by the surface through considering two different surfaces; the first which is atomically flat, and the second that is a disordered surface containing ledges, steps, kinks and terraces. This work confirmed the earlier suggestion that disordered surfaces with kinks should grow much faster than step-free terraces. This increase in growth rate occurs as atoms can only join the crystal lattice at kinks, reducing the Gibbs potential of the bulk atoms in the crystal. For example, only the (110) and (111) faces of a cubic system will be flat, and all others will be stepped, hence growth occurs through the attachment of atoms at Kossel-Stranski kinks on step ledges, and hence for an atomically flat surface no growth occurs through atomic addition but instead *via* the nucleation of islands and clusters of atoms on the surface itself. The stability of these clusters is given by the Gibbs-Thomson relationship that describes their solubility. The cluster also needs to reach a critical size so that it can grow into a new lattice layer, hence, the frequency of nucleation determines the rate at which propagation can occur.

In 1951, Burton and Cabrera extended on Frank's 1949 theory that considered the existence of spiral dislocation acting as growth steps on flat surfaces. This extension took into account the diffusion of adsorbed atoms across a crystal surface in terraces where secondary nucleation is required. This resulted in the BCF theory, where the boundary between crystalline and nutrient phases are considered to be sharp, i.e. the interface has no thickness, something that was originally proposed by Kossel-Stranski, opposing the model proposed by Gibbs' finite thickness model.[29] The BCF theory states that the atoms/molecules can only be part of the crystalline material or the nutrient. This is known as layer-by-layer growth.

In 1958, the concept of roughening was used to try and shed light on the solid-liquid interface structure by trying to answer why many non-metal, melt-grown crystals formed certain faceted euhedral shapes not observed in metal crystals.[30] Through the use of Bragg-Williams model and taking into account nearest neighbour bonds in the solid, and lateral bonds within the melt interface, it was possible to gain information on the solid-liquid interface structure. The free energy needed for the singular addition of atoms to an atomically smooth surface could be calculated for the formation of a single monolayer. If the difference in free energy, associated with the of the random addition of atoms to the surface, is known, the $\alpha - factor$ for the solid-liquid transition can be obtained:

$$\alpha = (\frac{\Delta H}{KT_{eq}})(\frac{\eta}{\nu}) \tag{1.2}$$

where ΔH is the enthalpy of crystallisation, or the change in internal energy associated with the transfer of a single atom from the bulk liquid to that of the solid, K is the Boltzmann constant, η is the number of nearest neighbours of an atom on the surface, ν is the number of nearest neighbours of an atom in the crystal, and T_eq is the equilibrium temperature at which the phase change occurs. The $\alpha - factor$ is made up of two terms; the first consisting of the entropy of melting, divided by a gas constant, and the second, a structure dependent term that takes crystal structure and specific surface area into account. Materials with an $\alpha - factor < 2$ are said to grow with non-singular interfaces, and materials with an $\alpha - factor > 2$ contain facets on the growing interfaces. This equation has been used to explain the difference observed between simple centro-symmetric crystal structures and those of more complex crystal structures.[31, 32]

The introduction of the BCF and its further development to incorporate more realistic, disordered interfaces several atomic layers thick, laid the foundations for a more stable theoretical foundation for understanding experimental results. In 1953, work on understanding interface instabilities through crystal growth was conducted by Rutter, where it was postulated that the observation of honeycomb-like structures, formed when solidifying metals containing small amounts of impurities, could be due to instability within the growth interface.[33] These observations led to the idea that the impurities were contained within a boundary layer at the solid-liquid interface, reducing the melting point of the liquid at this point, and in turn, causing supercooling within this region (constitutional supercooling).[34] This effect can be expressed as:

$$\frac{G}{R} > mC_0 \frac{(\frac{1}{K_0} - 1)}{D} \tag{1.3}$$

which shows how the ratio between the temperature gradient within the liquid, G, and growth velocity, R, needs to be above a critical value for stable growth to become viable, whilst avoiding constitutional supercooling. The value is dependent upon the properties of the materials within the system, for example the melt concentration, C_0, the slope of the liquidus curve, m, the segregation coefficient, k_0, and the diffusion coefficient, D. Essentially, to produce single phase crystals either the growth rate at a given temperature gradient must be decreased, or the temperature gradient itself must be increased. As faster growth rates are generally more desirable large efforts were placed on building specialised equipment to achieve steep thermal gradients.

It has been shown that variations in growth conditions, such as the addition of mechanical stirring and temperature changes, can have significant effects on crystal growth, due to the introduction of interface instabilities. This is a well known phenomena noted in a great deal of early studies, however it wasn't until 1963, that Millins and Sekerka were able to explain why these changes occurred.[35] Millins and Sekerka first described the mathematical theory of linear morphological interface stability, through modelling the effects of sinusoidal ripples (small perturbations) on a growth plane within a unstirred melt that can either grow or decay over time. This research led to further develop the understanding of the relationship between the destabilizing effects of the diffusion field and the influence of surface free energy on boundary conditions. This research led to more realistic interpenetration of interfaces where each interfacial atom is not ascribed to one or the other phase, but to a disordered interface layer several atoms thick. In this layer atoms can move randomly and over time begin to transition between the fully ordered crystal bulk and the disordered melt. This allowed for the prediction of kinetic coefficients for linearly connecting supercooling, ΔT, at the crystal-melt interface to the rate of growth, V, for liquids and metals:

$$V = A\sqrt{\frac{kT}{\frac{m\Delta T}{T_e}}} \tag{1.4}$$

Where m is the mass of the atoms, and A is a numerical coefficient determined by the structure of the liquid. The constitutional supercooling criteria was extended to include more terms affecting interface stability.[36] This showed that the temperature gradient normal to the growing interface, the slope of the liquidus, the growth velocity, the mass, the latent heat, the interfacial energy density and the thermal conductivities of both the liquid and the solid, all have significant effects on the stability of the interface.[37, 38, 39]

Generally, early work on understanding crystal morphology and growth has come from observation on naturally occurring crystals, or crystals produced from solution or vapour lab based methods. However, interest in more complex morphologies, such as dendrites or multiphase eutectics, has led to research on understanding the underlying mechanisms involved in crystal growth. For example snowflakes, which are probably the best known example of dendritic growth, grow when microscopic supercooled water droplets held within clouds freeze. However, the ambient conditions when this process occurs can also have a great influence upon their morphology. Dendritic growth is said to occur through a steady-state propagation of the tip, through time-dependent crystallisation of secondary side branches.[40, 41] Ivantsov, was the first to identify the formation of these repeating patterns in 1947.[42] It was also postulated that when considering pure materials, growth is thought to be controlled by the diffusion of latent heat away from the advancing growth interface. However, for non-pure systems (e.g. alloys), growth is said to be driven by the build-up of solute at interface boundaries, and where chemical diffusion can dominate over thermal transport.[43]

The transport of heat and mass throughout crystal growth is also of great importance for the control of crystal growth processes. Melt growth is said to be dominated by the transport of heat, whilst solution and vapour growth is generally dominated by mass transport. As crystals grow, latent heat is evolved, in turn altering the speed of growth. Hence, the geometry of the system, its thermal properties, ambient conditions, and growth rates are all important factors to consider. It is also important to consider if there are sufficient sources of nutrients to sustain growth, though the rate at which these nutrients reach the boundary interface can also have profound effects on the growth rate, as well as the overall crystal perfection. The concentration of dopants and impurities within the boundary interface is often variable in comparison to that of concentrations seen in the bulk. This also has effects upon mass transport within the system, whilst instabilities in the heat of mass flow can result in the formation of defects.

The early work preformed to better understand crystal growth gave modern scientists the building blocks to continually further our understanding. Previous studies on crystal growth have been successful in inspiring modern studies. With a constant thirst for knowledge and improving analytical techniques comes a greater understanding of crystal nucleation and growth, and with this greater understanding comes greater control when synthesising materials. The ability to tune syntheses to control the final crystal size and morphology of materials, the formation of defects and the overall properties of a material all stem from gaining a greater understanding of crystal nucleation and growth processes.

1.1.3 Principles of Nucleation and Growth

Crystal formation from solutions begins with nucleation. The term, nucleation, encompasses a series of atomic and molecular processes where atoms and molecules of a reactant phase come together forming clusters of a new product phase large enough to continue growing irreversibly, and hence, can then be considered as critical nuclei.[44] This is known as primary nucleation, which can occur homo- or heterogeneously, either spontaneously in the absence of a secondary phase, or, in the presence of a secondary phase (e.g. foreign particles) within a solution, respectively. For nucleation to occur a state of supersaturation needs to be reached. Supersaturation is the driving force needed for nucleation and growth of crystals to occur. It is defined as the difference between the chemical potential ($\Delta\mu$) a molecule in a solution (μ_s) and that within the bulk of a crystal (μc):

$$\Delta\mu = \mu_s - \mu_c \tag{1.5}$$

Thermodynamically this can be expressed as:

$$\Delta\mu = KTlnS \tag{1.6}$$

where k is the Boltzmann constant, T is the absolute temperature and S is the supersaturation ratio. When $\Delta\mu > 0$ the solution is said to be supersaturated and nucleation/growth can occur, and when $\Delta\mu < 0$ the solution is said to be undersaturated, meaning, dissolution transpires.[44]

Energetically, the work needed for a cluster to form of n molecules is the difference between the free energy of the system in its final and initial states but terms relating to the interface that arises between the nuclei and the solution are also required. Assuming the nucleus is spherical this can be expressed as:

$$\Delta G_r = -n\Delta\mu + 4\pi(r^2\mu\sigma) \tag{1.7}$$

where r is the radius of the nucleus, σ is the free energy of the surface. For nucleation to be favourable an energetic barrier (ΔG^*) must be overcome, where the nucleus radius is known as the critical radius or is also referred to as the critical nuclei size and can be defined as:

$$r^* = \frac{2\sigma(V)}{kTlnS} \tag{1.8}$$

where V is the volume of the molecules within the crystal.[44, 45] The rate of nucleation can be defined as the number of nuclei formed per unit volume per unit of time and can be expressed as an Arrhenius-type equation:

$$J = Aexp(\frac{-\Delta G^*}{kT}) \tag{1.9}$$

Where A is dependent upon the supersaturation of the system, and the rate of nucleation is zero until a point of critical supersaturation ($\Delta\mu_c$) has been reached where the rate of nucleation increases exponentially.[45]

From the above equations it can be seen that ΔG^* and r^* depend a great deal on the free energy of the surface, σ, meaning that anything affecting this will have an effect upon nucleation. For example the addition of foreign bodies into a system decreases σ which in turn means that the values for ΔG^* and r^* are reduced, making nucleation more favourable at a constant supersaturation. However, the critical supersaturation also decreases with σ, which means heterogeneous nucleation is more favourable than that of homogeneous nucleation.[46] The surface free energy is reduced most significantly when the substrate and the nucleating materials are identical, making secondary nucleation (nucleation induced by the presence of crystals of the same substance) more favourable than hetero- and homogeneous nucleation processes, whilst also causing supersaturation to lower.

The time taken for a system to reach supersaturation and begin to form crystals is known as the induction time of a system, which is dependent upon the setting of a $t = 0$ and the technique being used to measure crystal formation. The induction time, t_i, is effected by a great deal of factors including the presence of impurities, supersaturation and viscosity to name only a few. The induction time can be defined as:

$$t_i = t_r + t_n + t_g \tag{1.10}$$

where t_r is the time of relaxation (how long the system needs to achieve a quasi-steady-state distribution of molecular clusters), t_n is the time needed for nuclei to form and t_g is the time required for nuclei to grow to a detectable size.[45]

After nucleation has occurred secondary growth processes can start. Crystal growth can be described as the process where atoms/molecules being to be incorporated into the surface of a crystalline material, resulting in an incremental increase in overall crystal size of the material. This secondary growth process, in general, can be broken down into four steps:

1. The transport of atoms/molecules to a surface;

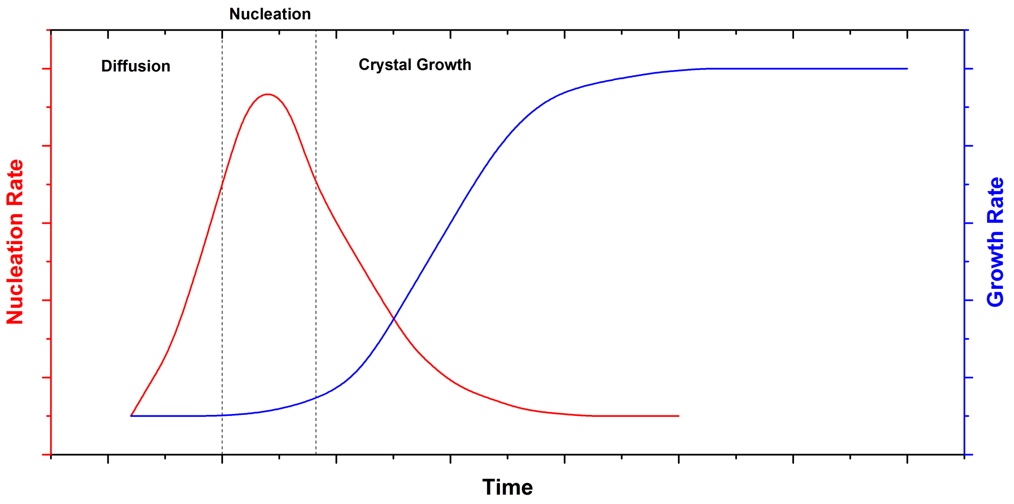

Figure 1.1: Schematic representation of both the rate of nucleation and rate of crystal growth described with a typical S-shaped curve, as seen for a multitude of inorganic systems such as zeolites.

2. Attachment of atoms to the surface;

3. The movement of atoms across the surface;

4. Attachment of atoms to the surface edges/kinks.

These steps can be thought of as either transport and surface processes, hence growth can be said to be either transport or surface controlled depending upon which step is the slowest.[47, 3]

1.2 Scope of the Thesis

The main objective of this project is to explore the formation of nanostructured materials through the use of *in-situ* scattering studies. It is thought that through obtaining a greater understanding of the processes involved in the formation of a material that its properties can eventually be tailored and tuned to preform specific tasks more efficiently than before. Many studies have been conducted on the phenomenon of zeolite crystallisation, though very few studies have been preformed *in-situ* under conventional synthesis conditions to obtain time-resolved data. Chapter 2 of this thesis describes the theory and practice of techniques used within this body of work. Chapter 3 introduces zeolites, their history and historical studies on zeolite nucleation. The main body of work in this chapter focuses on following the formation of silicalite-1 from three different silica precursors. So that the full picture of the formation process can be probed, complimentary techniques are utilised to make it possible to obtain information that is representative of the system as a whole. *Ex-situ* TEM microscopy is uesd to provide information on the finer details of the system, whilst *in-situ* small-angle x-ray scattering (SAXS) methods provide information that is representative of the overall system as a whole, making it possible to propose a formation mechanism that isn't restricted to observation made from a single methodology. Chapter 4 introduces strategies for synthesising hierarchical zeolites. The main body of work within this chapter then explores the formation of hierarchical silicalite-1 using *ex-situ* microscopy and *in-situ* SAXS. The direct hierarchical of macroporous silicalite-1 under conventional synthesis conditions is probed to obtain valuable information on the mechanism behind the formation of macropores within the zeolite structure. Chapter 5 introduces metal-organic frameworks (MOFs) and the theory behind their nucleation in literature. The main focus of this chapter looks at the formation of Zeolitic imidazolate framework-8 (ZIF-8) using *in-situ* SAXS and wide-angle x-ray scattering techniques. The use of both techniques is ideal for determining the morphological changes occurring during the formation of crystalline ZIF-8 within a solution phase reactions. Chapter 6 focuses on the design and commissioning of a new *in-situ* hydrothermal cell capable of preventing the sedimentation of particles within solution through rotation of the sample chamber. The body of work surrounding the development and commisioning of this *in-situ* cell is proceeded by a history of hydrothermal synthesis and the history development of equipment utilised within hydrothermal synthesis. General conclusions and further work are then discussed in Chapter 7.

Bibliography

[1] B Subotič, J Bronic, and T A Jelic. Theoretical and Practical Aspects of Zeolite Nucleation. In *Ordered Porous Solids*, pages 127–185. 2009.

[2] M W Anderson, O Terasaki, T Ohsuna, A Philippou, S P MacKay, A Ferreira, J Rocha, and S Lidin. Structure of the microporous titanosilicate ETS-10. *Studies in Surface Science and Catalysis*, 98(C):258–259, 1995.

[3] J Čejka, A Corma, and S Zones. *Zeolites and Catalysis: Synthesis, Reactions and Applications*, volume 1-2. 2010.

[4] G P Secundus (Pliny the Elder) and H Rackham. *Natural History, Volume IX: Books 33-35*. Loeb Classical Library, Harvard University Press, 1940.

[5] G Agricola. *On the Nature of Metals (De Re Metallica)*. Dover Publications, New York, 1950.

[6] V Biringuccio. *The Classic Sizteenth-Century Treatise on Metals and Metallurgy (Concerning Pyrotechnics, The Pirotechinca)*. Dover Publications, new editio edition, 2013.

[7] C Gessner. *On the fossils (De rerum fossilium)*. Excudebat Lacobus Gesnerus, Tiguri, 1565.

[8] A Cesalpino. *Of the Three Books of Metals (De metallicis libri tres.)*. Romae, Ex typographia Aloysii Zannetti, Rome, 1596.

[9] N Steensen. *Solids naturally contained within a solid dissertation (De solido intra solidum naturaliter contento dissertationis prodromus)*. Florentiæ, 1669.

[10] R Feigelson. *50 Years Progress in Crystal Growth*. Elsevier Science Inc., 1st editio edition, 2004.

[11] J B L Romé de L'Isle. *Essay of crystallography or description of geometric figures (Essai De Cristallographie, Ou Description Des Figures Géométriques)*. L'Academie Electorale des Sciences Utiles de Mayence, Paris, 1772.

[12] A Bravais. *Memoire sur les systemes formes par des points distribues regulierement sur un plan ou dans l'espace*. Gauthier-Villars, Imprimeur-Libraire, Paris, 1850.

[13] J W Gibbs. A Method of Geometrical Representation of the Thermodynamic Properties of Substances by Means of Surfaces. *Transactions of the Connecticut Academy of Arts and Sciences*, pages 382–404, 1873.

[14] D H Andrews. The Collected Works of J. Willard Gibbs. Two volumes. *Journal of Chemical Education*, 6(3):591, mar 1929.

[15] H Wilson. Reviews-On the velocity of solidification and viscosity of supercooled liquids. *The Journal of Physical Chemistry*, 5(2):151–151, jan 1900.

[16] M Knudsen. The laws of molecular flow and internal friction flow of gases through tubes (Die Gesetze der Molekularströmung und der inneren Reibungsströmung der Gase durch Röhren). *Annalen der Physik*, 333(1):75–130, 1909.

[17] G W Sears. A growth mechanism for mercury whiskers. *Acta Metallurgica*, 3(4):361–366, jul 1955.

[18] W Kossel. Zur Begrenzung des Systems der Elemente. *Die Naturwissenschaften*, 16(17):298–299, apr 1928.

[19] I N Stranski. On the theory of crystal accretion. *Zeitschrift Fur Physikalische Chemie - Stochiometrie Und Verwandtschaftslehre*, 136(3):259, 1928.

[20] W Kossel. *Quantum theory and chemistry (Quantentheorie und Chemie)*. Leipzig: S. Hirzel, Leipzig, 1928.

[21] G I Taylor. The Mechanism of Plastic Deformation of Crystals. Part I. Theoretical. *Proceedings of the Royal Society A: Mathematical, Physical and Engineering Sciences*, 145(855):362–387, jul 1934.

[22] V Volterra. Note on the Application of the Method of Images to Problems of Vibrations. *Proceedings of the London Mathematical Society*, s2-2(1):327–331, 1905.

[23] F C Frank. The Influence of Dislocations on Crystal Growth. *Discussions of the Faraday Society*, (48):48–54, 1949.

[24] C M Heck. American Physical Society. 5:686, 1937.

[25] J. D. H. Donnay and D. Harker. A New Law of Crystal Morphology Extending the Law of Bravais. *Am. Mineral.*, 22:446, 1937.

[26] P Hartman and W G Perdok. On the relations between structure and morphology of crystals. III. *Acta Crystallographica*, 8(9):525–529, 1955.

[27] J A Burton, R C Prim, W P Slichter, and J D Strutchers. The distribution of solute in crystals growth from the melt. Part II. Experimental. *The Journal of chemical physics*, 21(1953), 1953.

[28] N Cabrera and W K Burton. Crystal growth and surface structure. Part II. *Discussions of the Faraday Society*, 5:40, 1949.

[29] W K Burton, N Cabrera, and F C Frank. The Growth of Crystals and the Equilibrium Structure of their Surfaces. *Philosophical Transactions of the Royal Society A: Mathematical, Physical and Engineering Sciences*, 243(866):299–358, 1951.

[30] R H Doremus, B W Roberts, and D Turnbull. *Growth and Perfection of Crystals*. New York, jul 1958.

[31] A A Chernov. Notes on interface growth kinetics 50 years after Burton, Cabrera and Frank. *Journal of Crystal Growth*, 264(4):499–518, 2004.

[32] K A Jackson and J D Hunt. Transparent compounds that freeze like metals. *Acta Metallurgica*, 13(11):1212–1215, 1965.

[33] J W Rutter and B Chalmers. A Prismatic Substructure Formed During Solidification of Metals. *Canadian Journal of Physics*, 31(1):15–39, jan 1953.

[34] W A Tiller, K A Jackson, J W Rutter, and B Chalmers. The redistribution of solute atoms during the solidification of metals. *Acta Metallurgica*, 1:428, 1953.

[35] W W Mullins and R F Sekerka. Morphological Stability of a Particle Growing by Diffusion or Heat Flow. *Journal of Applied Physics*, 34(2):323–329, feb 1963.

[36] W A Tiller, K A Jackson, J W Rutter, and B Chalmers. The redistribution of solute atoms during the solidification of metals. *Acta Metallurgica*, 1(4):428–437, jul 1953.

[37] D T J Hurle. Interface stability during the solidification of a stirred binary-alloy melt. *Journal of Crystal Growth*, 5(3):162–166, jun 1969.

[38] A A Chernov. Stability of faceted shapes. *Journal of Crystal Growth*, 24-25:11–31, oct 1974.

[39] S R Coriell and R F Sekerka. The effect of the anisotropy of surface tension and interface kinetics on morphological stability. *Journal of Crystal Growth*, 34(2):157–163, 1976.

[40] G F Bolling and W A Tiller. Growth from the melt. III. dendritic growth. *Journal of Applied Physics*, 32(12):2587–2605, 1961.

[41] Z K Liu and Y A Chang. On the applicability of the Ivantsov growth equation. *Journal of Applied Physics*, 82(10):4838–4841, nov 1997.

[42] G P Ivantsov. Crystal Growth. *Dokl. Akad Nauk SSSR*, 58:567, 1947.

[43] D R Hamilton and R G Seidensticker. Propagation Mechanism of Germanium Dendrites. *Journal of Applied Physics*, 31(7):1165–1168, jul 1960.

[44] D Kashchiev. Driving force for nucleation. pages 9–16. 2000.

[45] J W Mullin. Nucleation. In *Crystallization*, pages 181–215. 2001.

[46] D Kashchiev and G M van Rosmalen. Review: Nucleation in solutions revisited. *Crystal Research and Technology*, 38(78):555–574, 2003.

[47] R Nitsche, D Elwell, and H J Scheel. Crystal Growth from High-Temperature Solutions. Academic Press 1975. *Kristall und Technik*, 11(3):K28–K29, 1976.

Chapter 2

Experimental Methods

2.1 Light Scattering Theory

2.1.1 Introduction

Light scattering techniques were first developed in the 19th century when Augustin-Jean Fresnel and Thomas Young observed the scattering maxima and minima in the shadow space of a single strand of hair.[1] They hypothesised that the pattern was present due to the interference of waves from both side of the hair strand, a deduction that would become the basis of Robert Maxwells fundamental laws of electromagnetism.[2] X-rays were initially discovered in 1895, however, it wasnt until 1913 when William Bragg published a paper on the X-ray diffraction (XRD) of crystals that their significance to science was first realized.[3] In this paper, Bragg, showed how a diffraction pattern could be used to determine inter-atomic distances in reciprocal space.

Bragg utilized his knowledge of wide-angle scattering of X-rays, and the law that bears his name to win the Nobel prize, and in turn making it apparent how light scattering techniques would have a huge role to play in science. Bragg's law shows how at wide-angles atomic distances could be measured, but also showed how at small angles, X-rays could be utilised to measure features much larger than those of the spacings between lattice planes. In 1930, the first small-angle X-ray scattering (SAXS) experiment was recorded by André Guinier and Günther Porod, however, it wasnt until the late 1930s that SAXS would gain any real attention when it was discovered that the scattering of X-rays at small-angles is dependent upon the curvature of the scatterer, and the smaller the surface curvature, the smaller the observed scattering angle.[4]

2.1.2 X-ray Interactions with Matter

X-rays are electro-magnetic radiation of a wavelength shorter than that of visible light. The waves propagate as an alternating electric field ($\vec{E}$) creating an alternating magnetic field ($\vec{H}$) and vice versa.[5] These fields and their direction of propagation are always perpendicular to each other. When X-rays interact with matter generally three things occur. Part of the incident X-rays will be scattered, part will pass through the material and part will be absorbed and converted into other forms of energy (e.g. heat, fluorescence radiation).

The irradiation of an atom with X-rays can result in the expulsion of an electron. In this process the energy of the X-ray radiation is used up, as the photon is absorbed, and an electron hole is left behind, leaving the atom in an unstable form. To rectify this state of disorder, the electrons within the atom rearrange to fill the hole, however as a result of this rearrangement, fluorescence radiation is emitted (radiation of a different wavelength to that of the incident X-ray). The phenomena of X-ray absorption is most efficient at absorption edges or where the electrons have the greatest possibility to be expelled from a specific atom.[6] These values are generally presented as mass-absorption coefficients, ($\frac{\mu}{\rho}$), where μ is the linear absorption coefficient and ρ is the density of the material. However, to obtain the best quality X-ray scattering data, the absorption of X-rays by the sample must be kept to a minimum. This can be achieved either by using a monochromatic beam, and/or by optimising the sample thickness, d_{opt}, due to its dependency on the linear absorption coefficient of a material:

$$d_{opt} = \frac{1}{\mu} \tag{2.1}$$

The scattering of X-rays can occur either elastically or inelastically. This means that scattered radiation can be of a different wavelength to that of the incident radiation, e.g. Compton scattering (inelastic scattering), or it can be of the same wavelength as that of the incident radiation, e.g. Rayleigh or Thomson scattering (elastic scattering).[7] Compton scattering occurs when a photon hits an electron and is bounced away, losing some of its energy in the process. This means that the scattered radiation is of a different wavelength than that of the incident radiation and has no phase relationship with that of the incident radiation (incoherent scattering). Hence, no interference phenomena occurs, and no structural information can be obtained from this radiation.

On the other hand, Rayleigh and Thomson scattering occurs when photons collide with strongly bound electrons where there is no energy transfer. When this occurs, the electron begins to oscillate at the same frequency as that of the incoming radiation, causing the electrons to emit radiation at the same frequency. As these waves radiate from the electrons they can interact coherently, resulting in an interference pattern that can be detected and contains structural information on the scatterer.

2.1.3 X-ray Scattering Theory

When an X-ray is scattered by an atom, a spherical wave is emitted (Thompson-scattering). These outgoing waves are synchronised with those of the incoming plane wave, producing interference patterns that can be collected by a detector. The interference can be either in phase (constructive), out of phase (destructive) or somewhere in the middle of both.[5] This mix of constructive and destructive phases can be caused due to the observation angle, 2θ, the sample orientation, and the distance between scattering atoms, r. Constructive and destructive interference creates brighter and darker spots at the detector respectively, with the resulting 2D interference pattern being characteristic of the internal structures within the probed material, i.e. the detected pattern contains information on the orientation and distances between atoms, relative to each other, within the material. The distances measured are relative to that of the incident radiation wavelength, λ, whilst the angle can be measured in terms of scattering angle, 2θ. However, scattering patterns are generally presented as a function of the scattering vector, q, to decouple them from the incident wavelength used for data collection:

$$q = \frac{4\pi}{\lambda} sin\theta \tag{2.2}$$

q is termed the momentum transfer, which is the modulus of the scattering vector with units of length^{-1}.

Absorption process are utilised for the detection of X-rays. This is because when X-ray photons are impacted onto the surface of a suitable detector material, free electrons are produced as a result of the photons being absorbed.[8] Acceleration, multiplication and amplification processes are then utilised to produce electrical pulses that can be counted and then outputted as numbers correlating to either intensity or count rate. Image plates also accumulate the energy of absorbed X-rays, which can then be utilised to obtain information on the number of photons that hit the detector. From scattering experiments only the squared amplitude of the wave, $I_s = |\vec{E_s}|^2$ (intensity) and not solely the amplitude on its own, meaning information on the phase of the electric field is lost, hence holographic reconstructions of a three-dimensional structure are essentially unobtainable. This means that the structural analysis of scattering data will always have ambiguities that need to be overcome through other knowledge of the systems being probed.

The scattering of X-rays by a particle can be thought of as an interference pattern. This interference pattern is produced from all the scattering particles within it (electrons/atoms), and when the amplitudes of the individual scattering waves are summed and squared at the detector, the resultant interference pattern can be said to be characteristic of the form (or shape) of the particle itself.[5] This phenomena is referred to as the form factor. It is a ”factor” as it must be scaled by a constant in order to match the experimental intensity units, however, for structural determination this is not necessary. When considering real samples and real scattering experiments, multiple particles are illuminated at the same time by the incident beam, this means that in practice the form factor can only be considered to be from a single particle, if all illuminated particles are identical in both shape and size (e.g. monodisperse sample). This is also only true if the sample is dilute enough, so as to

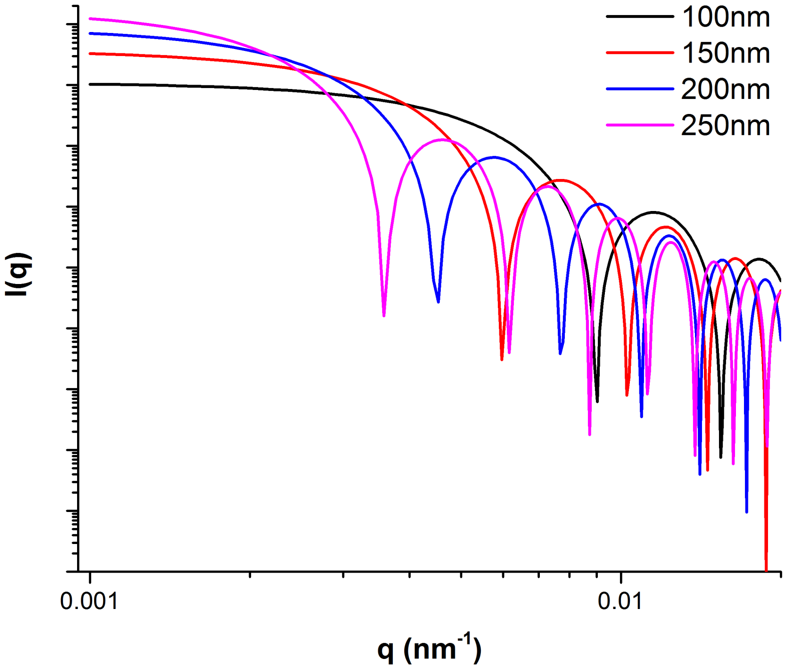

Figure 2.1: Simulated scattering curves from spherical particles of increasing size.

negate inter-particle scattering. Otherwise, the resultant from factor should actually be considered as a summed average of form factors produced from all illuminated particles within the probed system.

When probed systems are concentrated or densely packed, making the inter-particle distance within the sample the same magnitude as that of the particles themselves, the interference pattern begins to contain contributions from neighbouring interactions. This additional interference multiplies with the form factor of the single particle and is know as the structure factor. This is because it contains information on particle positions with respect to one another, or the structure of the material. Concentration effects become visible at small scattering angles with the formation of additional waves, and either a descent or rise in intensity at low q, due to repulsive and attractive particle interaction respectively.[9] The presence of structural waves can develop into pronounced peaks when particles are aligned into highly ordered/periodic arrangements. These peaks are known as Bragg peaks and their maxima position, q_{peak} is related to the distance between aligned particles, d_{Bragg}:

$$d_{Bragg} = \frac{2\pi}{q_{Peak}} \tag{2.3}$$

With concentrated or densely packed systems there is also the possibility that the particles can align themselves with respect to each other. This ordering means that there is an increased probability that there will be a next-neighbour at a set distance. However, there is less probability that this order spreads to further next-neighbours at longer distances, and due to this their relative positions can be considered to be more random. The presence of this short-range order can create a build up of structure factor within the scattering data, hence, peaks within the structure factor become much more prominent with a greater order of particles.[5] When the domain size of ordered particles increases (more long-range order) the system can then be considered crystalline, and the structure factor is in fact the more commonly known lattice factor. This presence of long range order is generally observed as a set of narrow, intense peaks, positioned at well-defined angles indicative of the crystalline symmetry .

Particles can also show preferential orientation effects with respect to each other. This is especially true when the probed particles are non-spherical. This can be observed in a 2D scattering pattern as a modulation of scattering intensity. When a sample is randomly orientated (isotropic) the scattering pattern will show equal intensity along concentric circles around the incident beam, however, if there are orientation effects within the sample this concentric homogeneity will no longer present, and there will be parts with greater and less intensity, providing information on the orientation of particles within the probed sample.

For the comparison of theoretical and experimental scattering data, theoretical data can be scaled using an arbitrary constant. This has no effect on the structural data held within the scattering curve and therefore has no effect on the particle shape or size. However, when trying to obtain information on particle number density or the molecular weights of particles the scaling of the scattering intensity becomes important, as it is proportional to that of the squared particle volume.[10] The scattering cross-section of an electron, σ, is the scattered energy produced by an incident beam of unit energy cm^{-2}. If a particle is illuminated by an X-ray beam with an energy density, i_0, the resultant scattered intensity can be denoted as $i_0\sigma$, where the units would be arbitrary units (e.g. counts per second, Watts, Joules). The incident beams intensity is generally altered by the sample before it reaches the detector, hence the scattered intensity needs to take into account the sample transmittance, T, the sample to detector, R, the detector pixel size, A, and the polarization angle of the incident beam, φ, relative to that of the plane of observation.

$$I_0 = i_0 \cdot \sigma \cdot \frac{A}{R^2} \cdot T \cdot [(sin\varphi)^2 + (cos\varphi)^2 cos(2\theta)^2] \tag{2.4}$$

With SAXS experiments the polarization term can generally be ignored, though this does not hold true for diffraction experiments.[5] From lab sources polarization tends to be random amounting to $\varphi = 45°$, and at synchrotron sources polarization can vary from $\varphi = 0° - 90°$ (horizontal and vertical polarization). Samples with greater electron density have the potential to scatter more, and if a sample was made up of a sole particle of volume, V_1, and electron density, ρ_1, then the number of wave amplitudes scattered is equal to $V_1\rho_1$. The intensity will be the square of all wave amplitudes produced by this volume, and the total scattering intensity for the particle, $I_1(q)$, can be written as:

$$I_1(q) = I_0 \cdot \rho_1^2 \cdot V_1^2 \cdot P(q) \tag{2.5}$$

where $P(q)$ is the particle form factor. For many experiments, samples must be embedded within a matrix material so that data can be collected. This become a problem when considering that every scattered photon carries structural information about the materials that scatter it. Hence, it is important to be able to distinguish the scatter from both the sample and the matrix material that supports it, hence in general, subtraction of the scattering patterns obtained from the matrix material and the sample holder are performed. For this subtraction to work there must be a electron density difference, or contrast, between the sample and the matrix material.

The greater the contrast the easier it is to observe the sample, as if both the sample and matrix had similar electron densities they would be indistinguishable. Through varying the contrast between sample and support matrix components can be almost removed from the scattering data, however this is not always possible without altering the samples structure or the processes that are wanting to be probed. This is where other scattering techniques such as SANS where neutron scattering cross sections are greatly different to those of X-rays scattering cross section, and also techniques such as anomalous small-angle X-ray scattering (ASAXS) can be utilised where the system is probed using different wavelengths of X-rays.[11] One of the wavelengths used to probe the system needs to be close to the adsorption edge of a particular element within the sample, which alters the contrast dramatically. When a sample with an electron density, ρ_1, is held within a matrix with electron density, ρ_2, the scattering intensity sample can be expressed as:

$$\Delta I_1(q) = I_0 \cdot (\Delta\rho)^2 \cdot V_1^2 \cdot P(q) \tag{2.6}$$

Where $\Delta\rho = \rho_1 - \rho_2$. For a sample containing N particles that are all identical the scattering intensity can be simplified to:

$$\Delta I_1(q) = N \cdot \Delta I_1(q) \cdot S(q) \tag{2.7}$$

$S(q)$ is the structure factor, which considers the particles positions with respect to each other. Hence, for dilute systems, $S(q) = 1$ and the structure factor can be ignored.

It can be seen from equation 2.6 that the scattering intensity increases with particle volume. For example, the volume of a sphere increases by the third power of its radius, hence, the scattering intensity increases by the sixth power. To put this in perspective if you had a sample with one million particles within it that are 1 nm in size, but there is a 1 ppm impurity of 10 nm particles, the scattering intensity of the 10 nm particle and the all the 1 nm particles would be equal. An impurity such as this would be almost impossible to detect using microscopy. Another observation from equation 2.6 is that the scattering intensity is also reliant on contrast squared.[5] This means that both voids and particles can give the same intensity as both positive and negative values of contrast will result in the same answer. Hence, what is actually being observed in the scattering data can be quite ambiguous and requires further knowledge of the systems being probed.

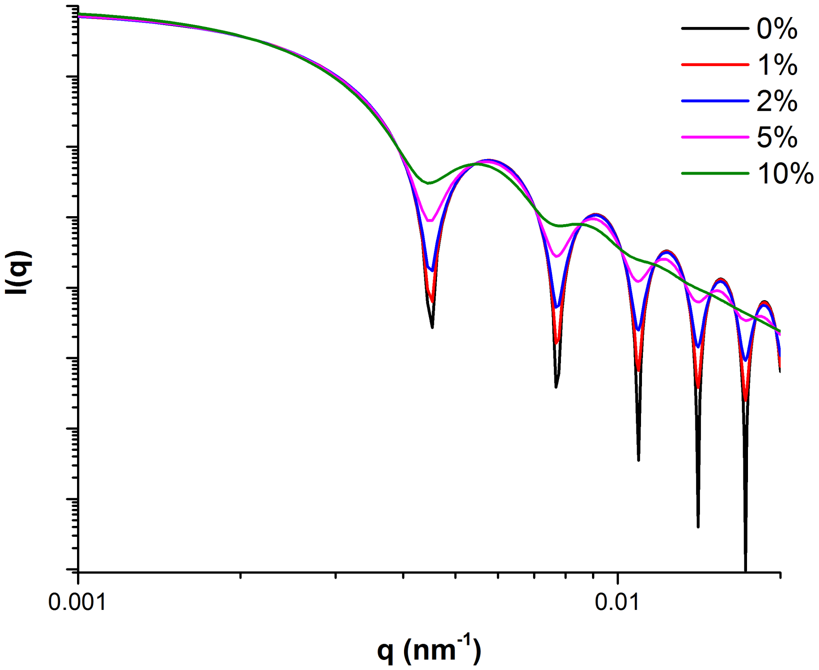

Figure 2.2: Simulated scattering curves from a system containing spherical particles with increasing polydispersity.

The assumption that all particles in a sample are identical is very rarely true (unless considering proteins). Generally samples will contain a range of particle sizes, meaning they can be considered polydispersed, or they contain particles of different shapes making them polymorphous. Scattering data obtained from polymorphous or polydispersed samples can be considered as the sum of N form factors present within the sample, weighted with respect to each particles contrast, $\Delta\rho_i$, and volume, V:

$$\Delta I(q) = I_0 \cdot \sum_{i=1}^{N} (\Delta\rho)_i^2 \cdot V_i^2 \cdot P_i(q) \tag{2.8}$$

Assuming the probed system is dilute ($S(q) = 1$).[12] Due to this summation an average form factor for the system is obtained which no longer exhibit sharp minima (figure 2.2). Conversely, scattering data from monodisperse samples will possess well-developed minima.

2.2 Powder X-ray Diffraction (PXRD)

In 1913, William Braggs paper on the X-ray diffraction of crystals showed how diffraction patterns can be utilised to determine inter-atomic distances in reciprocal space.[3] This explained how diffraction peaks can be treated as reflection from lattice planes within the probed crystals. The scattering of X-rays, by these planes, produces a diffraction pattern containing a great deal of information related to atomic arrangements within the probed crystalline structure. As powder X-ray diffraction (PXRD) is not solely affected by the kind of atoms within a sample, but by how they are arranged within it, it is possible to distinguish between chemically identical materials, as long as they have distinctive crystal structure (e.g. silicalite-1, quartz and SiO_2 glass). For a diffraction pattern to be produced crystals or crystallites in the sample must be correctly orientated with respect to the X-ray beam. For example, in a powdered sample there are hundreds/thousands of crystals in any number of different orientations, which, statistically means there will be at least some crystals in the correct orientation for an apt diffraction event to occur. The Bragg equation must be satisfied for a crystal to diffract light:

$$n\lambda = 2sin\theta \tag{2.9}$$

Where λ is the wavelength of radiation used, d is the spacing between Miller planes, θ is the angle between the incident beam and the crystal plane, and n is the order of diffraction represented by an integer value. The Bragg equation is fulfilled when X-rays are scattered from successive Miller planes (figure 2.3). The Bragg equation expresses how the diffracted X-rays travel different distances to the detector, and when the difference is of an integer value of wavelengths the beams interfere constructively at the detector.

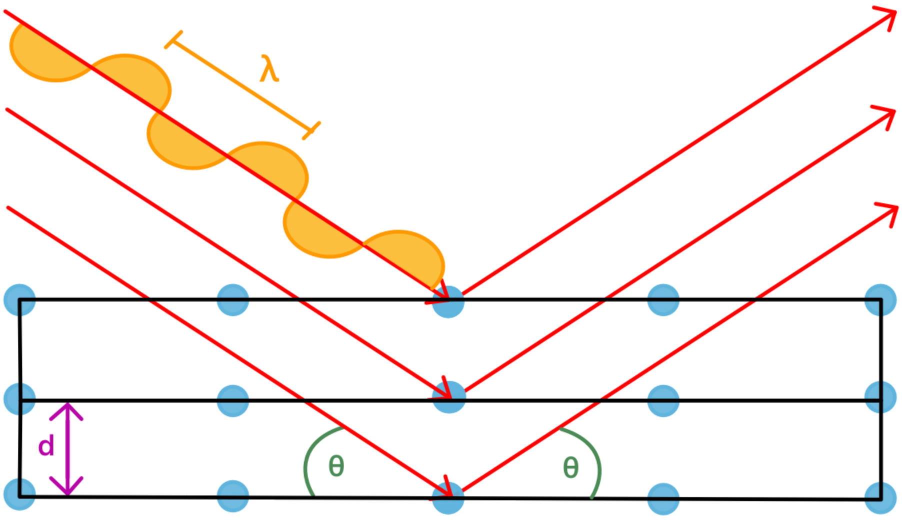

Figure 2.3: Schematic diagram of X-ray diffraction from part of a single crystal.

Information of the unit cell parameters is given by the position of these peaks in the diffraction pattern whilst the intensity of the peaks provides information on atomic positions. However, in certain situations, preferred crystal orientation can distort these intensities, and can be used to interpret orientation effects in some samples.

2.2.1 Williamson-Hall Analysis

From XRD data it is possible to estimate both the size and strain of a material through evaluating the broadening of powder diffraction peaks.[13] The Williamson-Hall method does this by relying on the approximation that size broadening, β_L, and strain broadening, β_e, vary with respect to that of the Bragg angle, θ:

$$\beta_L = \frac{K\lambda}{L \cdot cos\theta} \tag{2.10}$$

$$\beta_e = C_\varepsilon \cdot tan\theta \tag{2.11}$$

As the size broadening varies with $\frac{1}{cos\theta}$ and strain varies with $tan\theta$ their individual contribution can be determined by convolution. The Williamson-Hall method for overcoming this convolution is to assume is is a simple sum:

$$\beta_{total} = \beta_e + \beta_L = C_\varepsilon \cdot tan\theta + \frac{K\lambda}{L \cdot cos\theta} \tag{2.12}$$

And by multiplying by $cos\theta$:

$$\beta_{total} cos\theta = C_\varepsilon \cdot sin\theta + \frac{K\lambda}{L} \tag{2.13}$$

Which is of the standard equation form for a straight line, $y = mx + C$ where m is the gradient and c is the intercept. Hence, by plotting $\beta_{total} cos\theta$ versus $sin\theta$ it is possible to obtain the strain component from the slope C_ε and the size component from the intercept, $\frac{K\lambda}{L}$.[14, 15]

2.3 Small-angle X-ray Scattering

Small-angle scattering (SAS) is a naturally occurring phenomenon that can be observed everyday in nature. When the sun passes behind a thin covering of high altitude cloud a halo of light can be seen, this ring of light appears due to the small-angle scattering of light by ice and water particles within the atmosphere. If the angular distance or the intensity gradient of the rings were measured, the size and shape of the scattering particles could be resolved and if these particles were spaced close together it would also be possible to obtain information on the interaction of particles, as well as their inter-particle distances.

SAS as an analytical technique is used to determine the shape and size of objects much smaller than can be seen by the naked eye, through observing how radiation scatters off of these objects. SAS takes a multitude of forms related to the radiation used e.g. Small-Angle Light, X-ray, and Neutron Scattering (SALS, SAXS and SANS respectively) and these techniques can be used to measure particles in a range from 1 μm to several $\AA$ in size.

Scattering techniques take advantage of how light waves interact with a sample that has contrasting features. These interactions are elastic in most cases, hence, it is assumed that no photon energy is lost and the scattering effects can be treated purely as wave interference effects. In SAXS, X-rays are exposed to a sample and a small fraction of the X-rays deviate from their original path as they hit contrasting features within the sample, and the degree of scattering is recorded using a position-sensitive detector. The requirement of contrast in a sample limits the types of samples that can be measured to, for example, proteins in solution, colloidal solutions, polydispersed particles, pore structures and single-phase samples with density differences. In SAXS the contrast is the difference in electron density seen within the sample, in SANS it is the neutron scattering cross-section and in SALS it is the transmittance contrast and as these techniques utilize three different properties for distinguishing contrast opening up scattering to a multitude of systems where if one technique does not work another could be used instead.

2.3.1 Basic Theory

X-ray diffraction occurs due to the interference of scattered waves from electrons. The energy of the X-rays used in SAXS experiment are greater than that of the atomic binding energies of the electrons within the sample, hence, the electrons can be considered free. At small angles the scattered waves can be considered elastic in nature at small angles, meaning that inelastic/Compton scattering can be disregarded.[5] The wavelength of an X-ray is in the region of a single Angstrom meaning that they will scatter at small angles in the presence of nano-sized structures, making SAXS ideal for the exploration of nanoparticles. The scattering intensity of a simple system of nano-structural, mono-dispersed colloidal spheres, of radius, r, within a medium that is of a different electron density to that of the nano-structural particles can be written mathematically as:

$$I(q) = Nr_e^2 \cdot \Delta\rho^2 \cdot V^2 \mid F(q) \mid^2 S(q) \tag{2.14}$$

Where N is the particle number density, r_e is the radius of an electron, ρ is the electron density, V is the average particle volume, $F(q)$ is the particle form factor, which provides information on the size and shape of the particles, $S(q)$ is the structure factor contains information on the interactions and distances between particles, and q is the momentum transfer, which is the modulus of the scattering vector with units of length^{-1} (see 2.2).[16] In SAXS there are a great deal of advantages for using q instead of θ (the scattering angle) as q is independent of the X-ray wavelength consequently making a direct comparison of results much easier.

The measured scattering after background subtractions have been accounted for can be expressed as:

$$\Delta I(q) = K \cdot F(q) \cdot S(q) \tag{2.15}$$

Where ΔI is the background-subtracted intensity and K is a factor accounting for the electron density contrast between scatterers and the surrounding matrix. When considering simple colloidal spheres separated by a distance much greater than that of the particles themselves, the structure factor, $S(q)$, can be neglected, and the scattering intensity becomes solely dependent upon the particle shape, while the form factor, $F(q)$, is a result of coherent scattering from particles within the system, with the interference pattern being characteristic of the scattering particles shape.[5] However, in real systems, multiple particles are observed simultaneously causing discrepancies in the form factor if the sample is not dilute enough to allow for inter-particle distances that are much larger than that of the probed particles and the wavelength of the incident X-rays, if the particles are not monodisperse. However, if the probed particles are polydispersed, the resulting scattering pattern will be made up of the form factors for each particle morphology present within the system, resulting in a smearing of form factors.

The form factor is dependent upon the specific shape of the scatterers, however, Guinier showed how this can be approximated to a Gaussian function at low angle:[17]

$$F(q) \cong a_0 \cdot e^{(\frac{-R_G^2 q^2}{3})} \tag{2.16}$$

Where a_0 is taken as the scattering intensity when extrapolated to zero scattering angle and R_G is the radius of gyration which is related to particle size, where for example in the case of monodisperse spheres, particle size can be calculated as:

$$R = \sqrt{\frac{5}{3}R_g} \tag{2.17}$$

To determine the parameters from a real data set, a so-called Guinier plot is required where the logarithm of the intensity is plotted against q^2.

$$ln(\Delta I_{(q)}) = ln(a_0)^{-\frac{R_G^2 q^2}{3}} \tag{2.18}$$

With this R_G and a_0 can be determined by straight-line fitting of the graph, from the slope $-(\frac{R_G^2}{3})$ and $ln(a_0)$ is determined from the y-intercept.

2.3.2 SAXS Data Correction

After data collection, corrections need to be performed. These corrections are very important when dealing with SAXS data, as it is very easy to insufficiently correct and then either over- or under-fit possibly featureless data sets. There is now a widely accepted, standardised sequence of steps for the correction of SAXS data to obtain data on an absolute scale.[10]

1. Read-in:

   First, the data needs to be read-in to the data reduction software such as the free software package DAWN provided by Diamond Light Source. The read-in procedure does not just mean reading in the raw SAXS data collected from an experiments but also the parameters associated with how the data was collected (e.g. sample-to-detector distance, beam center, X-ray source energy etc).

2. Masking:

   The data then undergoes a masking procedure. This is so that any ”invalid” data points are excluded . An example of ”invalid” data points include hot pixels, pixels hidden behind the beamstop/beamstop arms and data collected from between detector modules.

3. Estimation of uncertanties:

Some uncertainties need to be estimated, in particularly those associated with counting or the Poisson uncertainty, which are calculated on the number of photons that are counted by the detector.

4. Deadtime Correction:

   The deadtime is then taken into account, this returns an estimate of the number of photons that arrived at each pixel of the detector. This is calculated using the detected count rate.

5. Dark current correction:

   The removal of dark current needs to be performed. This is essentially the removal of background radiation collected by the detector (including cosmic rays).

6. Time normalization:

   The normalization of time comes next. This is done so that the measurement is independent of the duration of the taken measurement.

7. Flux normalization:

   Again, similar to the above time normalization step, this is to make sure the measurements are independent of the flux of the incident beam.

8. Transmission correction:

   The data should be corrected for sample transmission, or the probability of absorption within the sample. This is a scaling correction that should be obtained by dividing the flux of all scattered, diffracted and transmitted light, by that of the incident flux.

9. Sample self-absorption:

   Sample self-absorption should also be accounted for, with the increased likely hood that scattered light is absorbed as it travels through the sample. This is a direction dependent modification for the transmission correction.

10. Frame averaging:

    The averaging of frames is recommended for when photon-counting direct-detection systems are used for measurements, where in general, multiple short frames/exposures are taken for each measurement to avoid pixel saturation. The averaging of frames allows for temporal variations, arising from sample instabilities and or instrument changes occurring within the measurements to be perceived.

11. Background subtraction:

    The removal of a background can then be preformed. The background data should have also been subjected to the above corrections prior to subtraction from the experimental data.

12. Flat field correction:

    A flat field correction should then be applied to the data. Here, a multiplication matrix (normalized to 1) is used to correct for inter-pixel differences in sensitivity.

13. Angular efficiency correction:

    An angular efficiency correction can be utilised to compensate for variations in detector efficiencies, which is dependent upon the angle of incidence for photons hitting the detector surface. This step also aids in correcting for detector imperfections.

14. Solid angle correction:

    A correction for solid angle should next be preformed for each pixel. This is calculated using the instrument geometry.

15. Polarization:

    A correction for polarization, compensating for differences in scattering event probabilities, for the polarized and unpolarized beam. For the unpolarized beam this is an isotropic (azimuthally uniform) correction, and this should be preformed prior to the subtraction of a second background to ensure that older dispersant measurements can still be utilized for corrections on future samples.

16. Sample thickness correction:
    The sample thickness should also be accounted for, so as to normalize the data into units of reciprocal length.

17. Absolute unit conversion:
    The data is then ready to be converted into absolute units. This is done by scaling the data to units of scattering cross section or by the fraction of radiation that is scattered per length of material per solid angle.

18. Displaced volume correction:
    This applies to samples that are dispersions, with high volume fractions of analyte. These samples should be corrected for their displaced volume, however, this should only be preformed on the solvent scattering signal.

19. Remapping:
    The data can then be remapped into q or 2θ.

20. Averaging:
    By averaging the data at this stage, you can reduce the dimensionality and size of the dataset (generally from 2D to 1D). For isotropic data this can be done azimuthally, and for anisotropic data this can be done radially. When dealing with anisotropic data, radial averaging over a limited data range can be utilised to extract information on orientation effects.

Once all of these steps have been completed, the resulting data will be on an absolute intensity scale and ready for fitting.

2.3.3 SAXS Data Analysis

Monte Carlo regression fitting of small-angle scattering data has become a popular method of fitting SAXS data over the past few years.[18, 19] This methods utilises random populations of particles, in a trial-and-error, brute-force process to retrieve form-free particle size distributions from small-angle scattering data. Monte Carlo rejection sampling is used to uncover model parameter distributions. For example, through the use of these methods it is possible to obtain size distributions of scatterers from small-angle scattering data.

To perform these fits, the Monte Carlo simulation is provided with a set of independent, non-interacting contributions from a chosen scattering model. The model can be chosen from a catalogue of theoretical models to describe a specific particle shape. This model choice determines the parameters that can be altered during the fitting process, for example, if a spherical model is chosen then the only parameter that is considered is that of the particle radius, however with more complex shapes more parameters are considered. Monte Carlo simulations also take into account the difference in scattering length densities between the probed sample and the dispersant/matrix it is held within. Hence, only when all this information is fed into the simulation, optimization procedures can proceed.

This process essentially progresses through random iterations of potential fit parameters, by randomly simulating contributions to the theoretical model until a convergence criterion is met. The optimization of this process begins with a non-interacting distribution of scatterers of a user defined shape. The size of these particles in this initial distribution are chosen randomly, and the sum of the total model scattering pattern is given as the weighted sum of all the scatters present in the distribution. From this, a χ^2 value is calculated between the model and that of the measured scattering data once it has been weighted by measured uncertainty estimates. Through the use of a least squares minimization procedure, the model data is then scaled to that of the experimental data to within these experimental uncertainties. After this, the Monte Carlo simulation can then take place, where with each iteration, a single random scatterer is altered. After this alteration, the new total scattering pattern of the model is calculated, and if χ^2 is reduced, the change to the model is accepted. This process of randomly altering the model parameters continues iteratively, until a convergence criterion is met (generally when $\chi^2 \leq 1$). Throughout this process, the minimum observability limit for each particle distribution is also calculated. This calculates the minimum volume fraction of scatterers that is required for a population of that specific shape and size, to be measurable within a scattering pattern.

This method of fitting small-angle scattering data have its drawback. It can be a very slow process due to its brute-force iterative approach to data fitting. This also means that it is quite computationally intensive

2.4 Intense Radiation Sources

2.4.1 Synchrotron Radiation

Synchrotron radiation is the electromagnetic radiation emitted by electron near relativistic velocities. As an electron approaches the speed of light in a curved trajectory, the particles accelerate in a radial direction, but decelerate in the direct path. This results in the release of a polychromatic fan of radiation tangential to that of the beam path. This polychromatic fan of radiation is comprised of a broad range of photon energies from microwaves to hard X-rays, and is highly directional. The fan, however can be harnessed through the utilisation of highly specialised X-ray optics, making it possible to preform unique experiments not possible in a lab environment. There are a great deal of synchrotron sources around the world, however the three largest and possibly well known in the world are; The European Synchrotron Radiation Facility (ESRF), with a 6 GeV storage ring in Grenoble, France; The Advanced Photon Source (APS), with a 7 GeV ring in Chicago, USA; and SPring-8, which is the worlds largest synchrotron with the highest energy storage ring at 8 GeV, in Hyogo Prefecture, Japan.

All modern synchrotron are made up of the same five major components:

1. Electron Gun:
   Electrons are initially produced from a cathode ray tube. A high voltage cathode is heated under vacuum, which in-turn gives the electrons within the cathode sufficient energy to escape from its surface. This process is known as thermionic emission, and the electrons produced from the electron gun are then accelerated towards the next a linear accelerator using earthed anodes.

2. Linear Accelerator (LINAC):
   The LINAC takes the constant steam of electrons coming from the electron

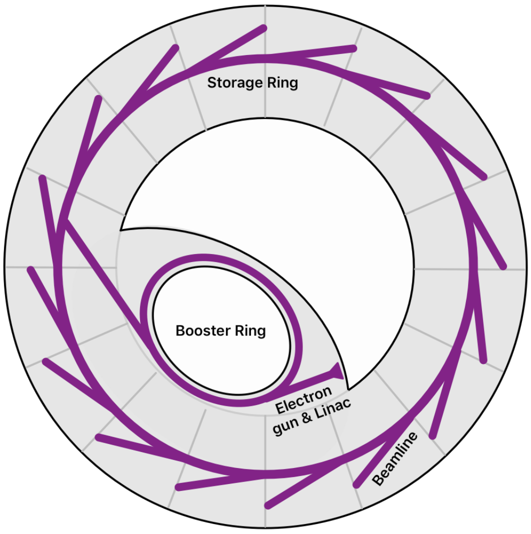

Figure 2.4: Diagram of a synchrotron showing the major components found within a synchrotron radiation facilities.

gun and accelerates them. It does this through the use of a series of radio frequency (RF) cavities. In this process the electrons are accelerated to approximately 100 MeV and the electrons are grouped together into bunches.

3. Booster Ring:

   The booster ring accepts the accelerated electrons from the LINAC. Here the electrons energy is increased to match that of the electrons held within the synchrotron storage ring. The booster ring is made up of a series of RF cavities and dipole magnets. The RF cavities accelerate the electrons whilst the dipole magnets keep the electrons in orbit around the booster ring. This is done by increasing the magnetic field produced by the dipole magnets as a function of the electrons increasing energy. Once the electron energy matches that of the electrons held within the storage ring, they can then be ejected from the booster ring into the storage ring.

4. Storage Ring:

   The storage ring at a synchrotron is not in fact circular, but actually polyhedral. A storage ring is made up of several straight sections that are connected using dipole bending magnets. The straight sections in the storage ring contain hexapole and quadrupole magnets that are utilised to corral the bunches of electrons, reducing their divergence during orbit around the ring. As the electrons enter the bending magnets they are accelerated, which causes the electrons to emit a fan of electromagnetic radiation tangential to their orbit. This radiation is then extracted from the storage ring towards a beamline. The straight section of the storage ring can also contain insertion devices that are able to generate extremely bright beams of radiation that can be sent towards a beamline.

5. Insertion Devices:
   Generally, there are two different types of insertion devices used at a synchrotron, wigglers and undulators. These devices work by disrupting the electron orbit so that electromagnetic radiation is emitted. Wigglers do this by utilising very strong magnetic fields to make the electron beam ”wiggle” along an extremely tight radius of curvature. By doing this, the X-rays generated are much harder X-rays than can be generated within the storage ring. On the other hand, undulators utilise weaker magnetic fields placed in an alternating directions. This induces sinusoidal oscillation into the electron orbit, and when the electron orbit is forces to alter direction electromagnetic radiation is emitted. This emitted radiation can then interact constructively or disruptively along the undulator to give a harmonic structure to the X-ray spectrum. The use of an undulator can result in obtaining an extremely intense beam if the harmonics are arrange correctly.

Synchrotron radiation has many benefits over those of standard lab sources. For example, the intensity of X-rays generated at a synchrotron are many magnitudes greater than those accessible with standard lab sources. This high intensity allows for experiments to be conducted on relatively dilute samples, whilst high flux provides the ability to perform *in-situ* experiments with good time resolution (data collection on ms scales for certain techniques). Generally, at a synchrotron beamline it is trivial to access different energy X-rays, meaning problems surrounding sample absorption as can negated for many experiments. X-rays at synchrotron sources are also considered to be higher ”quality” than those of lab sources. The ”quality” of an X-ray source is measured by its brilliance, which has units of photons sec^{-1} mrad^{-2} mm^{-2} 0.1% bandwidth. The brilliance combines photon flux, divergence of the beam and the cross-sectional area of the beam. High brilliance can be achieved by combining high intensity or flux, with good collimation for low divergence, with a small spot size. The brilliance that can be obtained at a synchrotron radiation facility on a bending magnet beamline can read up to 10^{14} photons sec^{-1} mrad^{-2} mm^{-2} 0.1% bandwidth, whereas wigglers and undulators can reach 10^{16} and 10^{19} photons sec^{-1} mrad^{-2} mm^{-2} 0.1% bandwidth respectively.

2.4.2 Diamond Light Source Beamline I22

Diamond Light Source it a third generation synchrotron with a medium energy storage ring. Diamond operates at 3 GeV, with a typical ring current of 250 - 300 mA, and consists of around 30 operational beamlines, each specialising in a particular experimental technique that the beamline has been specifically designed to preform. Beamline I22 a.k.a. SAPPHIRES (Small angle photons for resonant and elastic scattering) is a beamline specialising in non-crystalline diffraction. It is situated on a 2 m long undulator, that has a magnetic period of 25 mm. When the beam enters the beamline from the storage ring/undulator, it is first met by an aperture to limit the beams divergence. This is followed by a set of primary slits to define the beam size. Next along the beamline, I22 is equipped with a Si (111) double crystal monochromator, which is cooled using liquid nitrogen for dispersion of the incident white beam on the first crystal. Kirkpatrick-Baez mirrors are then utilised to focus the beam in both horizontal and vertical planes. These mirrors can have a voltage applied to the piezoelectric actuator positioned under their polished surface to change their shape, altering the focal length of the mirrors.

Next there are three sets of slits, which can be utilised to remove parasitic scatter from the upstream beamline components, something that is very important in the collection of SAXS data as any extraneous scatter can have detrimental effects on the quality of data collected. After these slits the beam enters the experimental hutch. In this hutch there is a large motorised optical sample stage for positioning

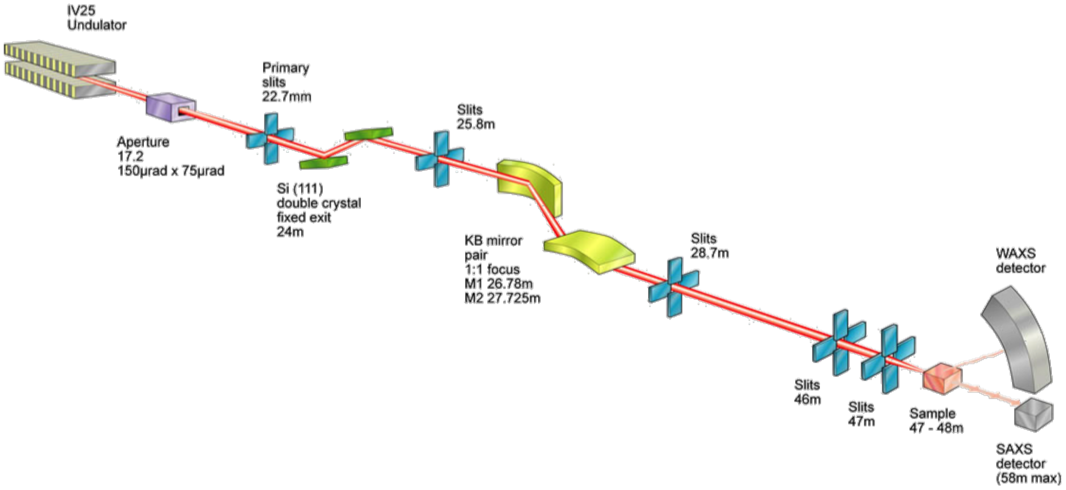

Figure 2.5: Layout of beamline I22 at Diamond Light Source.

samples within the beam. Next in line, is the first of two DECTRIS Pilatus 2M area detectors.[20] These detectors are used for the simultaneous collection of SAXS and WAXS data. These detectors are high resolution photon counting devises, with low noise and high dynamic range characteristics, allowing for the collection of good quality scattering data on short time scales from weakly scattering samples. The WAXS detector is housed within a vacuum chamber. This large chamber can be modularly extended towards the SAXS detector that is positioned on a motorised track. This allows for sample-to-detector distances of mere centimetres, for the collection of wide-angle data, and up to a possible 9.5 m for the collection of small-angle data.

2.5 Microscopy

2.5.1 Scanning Electron Microscopy (SEM)

Scanning electron microscopy (SEM) uses a high-energy electron beam to produce high-resolution images of the surface of a sample.[21] It does this by is first bombarding the samples surface with high-energy electrons, which in-turn ejects electrons from the samples surface (secondary electrons) and it produces back- scattered electrons (electrons that have undergone elastic/inelastic scattering with the sample surface). Secondary electrons, generally, have low kinetic energy in comparison to that of back-scattered electrons, which causes them to be recaptured by ionized atoms within the bulk of the sample. Hence, it is only possible for a secondary electron to escape from the sample via the surface. The intensity of back-scattered electrons, which have greater kinetic energy than that of secondary electrons, is dependent upon atomic number. With backscattered electron images, regions of the surface with greater electron density appear brighter than those of a lower electron density.

2.5.2 Transmission Electron Microscopy (TEM)

Transmission electron microscopy (TEM) is a microscopic technique in which a beam of electrons is transmitted through very thin layers of the sample material. The beam interacts with the sample as it passes through it, which can then be interpreted into an image by looking at the interactions of the electrons within the sample. This image is then magnified and focused on to a imaging device (e.g. a fluorescent screen) and then on to either a layer of photographic film, or a sensor such as a CCD camera for the images to be captured.

With TEM it is possible to obtain images with much greater resolutions than those seen with standard light microscopy due to the nature of TEM and the small de Broglie wavelengths of electrons. Hence, it is possible to observe details such as lattice planes on the surface of crystals. These capabilities of TEM make it a very important analytical technique in the determination of how particle formation occurs, as the nucleation of nano-scaled particles can be observed *ex-situ*.

2.6 SAXS & Microscopy as Complimentary Techniques

SAXS is similar to diffraction as it characterizes lengths within a sample. However, in a SAXS experiment small objects/features contribute only a small amount of scatter to large angles and large features scatter a large amount to small angles. The scattering power of an object is related to its volume, with the scattering power scaling with volume squared leading to a dominance of scattering from large objects in polydispersed systems. A large limitation of SAXS is that unlike with PXRD, a

SAXS pattern does not actually contain much information and without information on sample morphology from microscopy scattering data is open to a multitude of interpretations, which leads to the question of why not just use microscopy as an analysis technique instead? Microscopy is the obvious choice of technique when it comes to analysing small particles as it allows for the visualization of objects smaller than 1 cm in size. Optical and confocal microscopes can image objects to sub micron resolution, SEMs can comfortably measure to 100 nm and TEM on an even smaller scale to, in some cases, near atomic resolutions, and then there is scanning-probe microscopy which can probe along this entire scale. However, the biggest challenge associated with microscopy comes from sample preparation. Sample preparation becomes more and more complex when greater resolutions are sort after. It can be a time consuming process and it can impose structure on the sample from the grinding, cutting and polishing of samples that is often needed. This makes it much harder to distinguish sample structure from that of induced structural artefacts. If these difficulties can be overcome, the next problem is intrinsic to the technique, as only a small fraction of a sample can be observed, and observing samples *in-vivo* or *in-situ* is not always possible with microscopic techniques.

SAXS, on the other hand, is able to gather information on the whole of an irradiated sample containing potentially thousands of particles, to obtain parameters for the average particle within the sample. This is an advantage SAXS has over microscopy, however, microscopy dominates labs due to the challenges associated with collecting good scattering data and the difficulties of analysis. SAXS also substitutes the problems associated with microscopy with others of its own. The main challenge is associated with the analysis of the data itself. These problems lie in the ambiguity of the data collected as mentioned previously. Information is lost during the scattering process as only the scattering intensity is detected and phase information is lost. A particles shape and polydispersity are lost and both cannot be retrieved simultaneously, a very important concept in SAS. Polydispersity can only be determined when the particle shape is known and vice versa, thus, either monodisperse systems or prior knowledge of the shape distribution within the sample is needed. Hence, complimentary microscopy data is necessary to produce convincing fits of the data, which can still be a very time consuming procedure.

To fully understand the formation of any system the use of multiple analytical techniques is essential. Microscopy and scattering techniques complement each other extremely well. This is because their strengths and weaknesses do not overlap but instead complement each other, making it is possible to obtain a more complete picture of an unknown sample or process through the utilization of both techniques.

Bibliography

[1] A Fresnel, T Young, F Arago, C Huygens, and H Crew. *The Wave Theory of Light*. American Book Company, 1900.

[2] J C Maxwell. A Dynamical Theory of the Electromagnetic Field. *Philosophical Transactions of the Royal Society of London*, 155:459–512, jan 1865.

[3] W Bragg. The diffraction of X-rays by crystals. pages 370–382, Stockholm, 1922.

[4] A Guinier and G Fournet. *Small-angle scattering of X-rays*. Wiley, Michigan, 1955.

[5] H Schnablegger and Y Singh. The SAXS Guide. *Anton Paar*, 2011.

[6] M Newville. Fundamentals of XAFS. *ReVision*, page 43, 2004.

[7] J H Hubbell, W J Viegele, E A Briggs, R T Brown, D T Cromer, and R J Howerton. Atomic Form Factors, Incoherent Scattering Functions and Photon Scattering Cross Sections. *Journal of Physical and Chemical Reference Data*, 4:471, 1975.

[8] B R Pauw. Everything SAXS: Small-angle scattering pattern collection and correction. *Journal of Physics-Condensed Matter*, 25(38), 2013.

[9] B R Pauw. How to do a perfect SAXS measurement. pages 1–50, 2011.

[10] B R Pauw, A J Smith, T Snow, N J Terrill, and A F Thuenemann. The modular small-angle X-ray scattering data correction sequence. *Journal of Applied Crystallography*, 50:1800–1811, 2017.

[11] J Haug, H Kruth, M Dubiel, H Hofmeister, S Haas, D Tatchev, and a Hoell. ASAXS study on the formation of core-shell Ag/Au nanoparticles in glass. *Nanotechnology*, 20(50):505705, dec 2009.

[12] B R Pauw, J S Pedersen, S Tardif, M Takata, and B B Iversen. Improvements and considerations for size distribution retrieval from small-angle scattering

data by Monte Carlo methods. *Journal of Applied Crystallography*, 46:365–371, 2013.

[13] G K Williamson and W H Hall. X-ray Line Broadening from Filed Aluminium and Wolfram. *Acta Metall.*, 1:22–31, 1953.

[14] Y T Prabhu and K V Rao. X-Ray Analysis by Williamson-Hall and Size-Strain Plot Methods of ZnO Nanoparticles with Fuel Variation. *World Journal of Nano Science and Engineering*, 4(March):21–28, 2014.

[15] S Kitagawa, R Ryoo, and O Terasaki. Study of Argon Gas Adsorption in Ordered Mesoporous MFI Zeolite Framework. *J. Phys. Chem.*, 116:25300–25308, 2012.

[16] T M Stawski. *Understanding microstructural properties of perovskite ceramics through their wet-chemical synthesis*. 2011.

[17] A Guinier. La diffraction des rayons X aux très petits angles : application à l'étude de phénomènes ultramicroscopiques. *Ann. Phys.*, 11(12):161–237, 1939.

[18] B R Pauw, J S Pedersen, S Tardif, M Takata, and B B Iversen. Improvements and considerations for size distribution retrieval from small-angle scattering data by Monte Carlo methods. *Journal of Applied Crystallography*, 46(2):365–371, 2013.

[19] I Bressler, B R Pauw, and A F Thuenemann. McSAS : software for the retrieval of model parameter distributions from scattering patterns. *Journal of Applied Crystallography*, 48(3):962–969, 2015.

[20] C Broennimann, E F Eikenberry, B Henrich, R Horisberger, G Huelsen, E Pohl, B Schmitt, C Schulz-Briese, M Suzuki, T Tomizaki, H Toyokawa, and A Wagner. The PILATUS 1M detector. *Journal of Synchrotron Radiation*, 13:120–130, 2006.

[21] J I Goldstein, D E Newbury, P Echlin, D C Joy, C E Lyman, E Lifshin, L Sawyer, and J R Michael. *Scanning Electron Microscopy and X-ray Microanalysis*. Springer US, Boston, MA, 2003.

Chapter 3

Nucleation and Growth of Zeolites

3.1 Zeolites

The popularity of porous materials has continued to grow, as their ability to interact with atoms, ions and molecules throughout their bulk becomes more and more important. Porous materials are typically utilised in applications that can exploit the highly ordered, large internal surface area that these materials possess. The applications that these materials are used in encompass ion exchange, adsorption/separation and catalysis. The ability of porous solids to succeed in a particular field is dependent upon the distribution of the pore properties throughout the material (e.g. pore shape, size, uniformity and order). For example, zeolites are uniformly microporous and are capable of separating molecules on a basis of size through selective adsorption. This is why they are sometimes referred to as molecular sieves, as small molecules can be separated from a mixture containing larger molecules that are of greater size to that of the zeolites micropores. For these applications to work, possessing uniform pore shape and size distributions is key, but the porous materials' elemental composition can also play an important role. For example, microporous molecular sieves comprised solely of silica (SiO_2) are innately hydrophobic, hence they adsorb organic molecules from oil-water mixture, however upon the addition of aluminium into the same microporous array, creating an aluminosilicate, the reverse is observed. Controlling the uniformity of porous solids is of great importance, and only through gaining insight on how these materials are formed can their properties be utilised to their full potential. Through understanding of the underlying mechanisms which occur during the formation of these materials can control be applied to their syntheses, potentially allowing for their more desirable properties to be tuned for specific application.

3.1.1 Introduction

Zeolites are a class of microporous, metastable, crystalline oxides that were first discovered in 1756. Zeolites are composed of silicon, aluminium and oxygen atoms, that are systematically bonded together in arrays to produce over 200 differnt, well-defined, uniform zeolite structures.[1] Within zeolite structures, the silicon and aluminium atoms possess tetrahedral coordination and can be referred to as T-atoms. These T-atoms are bound together through bridging oxygen atoms located at the vertices of each tetrahedron to create TO_4 units.

Zeolitic frameworks are made up of ordered systems of pores and channels, which run throughout their uniform structures. The size of the channels are determined by the number of T-atoms within the ring structures that form the pore opening. In zeolitic solids, these openings are typically 3-12 Å in diameter.[2] Zeolite structures have been classified by their framework symmetry and given a three-letter identification by the International Zeolite Association (IZA). For example, silicalite-1 and ZSM-5 possess the same Zeolite Socony **M**obil-**Fi**ve (MFI) framework, whilst zeolite X and Y both have faujasite (FAU)frameworks.[3] Compounds, with similar structures to those of zeolites, made up of T-atoms and TO_4 units, that are not solely Si and Al, can be classed as zeotypes (eg. aluminophosphates, which have both Al^{3+} T-atoms and P^{5+} T-atoms).

Aluminosilicate zeolites, or ”true zeolites” posses negatively charged frameworks due to the discrepancy of formal charges present on the SiO_2 and AlO_2 groups within the framework. These groups have charges of 0 and -1 respectively, which are caused due to the presence of Si-atoms being in a +4 oxidation state, and Al-atoms being in a +3 oxidation state. This leaves a formal negative charge on the zeolite structure, however this is compensated through the presence of non-framework cations held within the pores of the structure.

The Si/Al ratio within aluminosilicates is very important to many of the zeo-

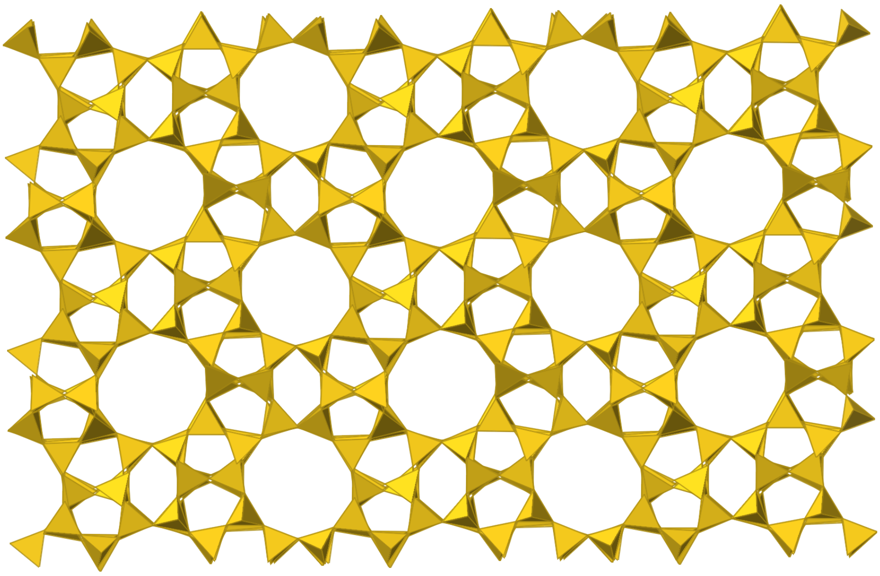

Figure 3.1: Structural representation of silicalite-1, which possesses MFI framework symmetry.

lites properties, and can influence the structure formed. The Si/Al ratio can be in anywhere between the range of one and infinity (zeolite A and silicalite-1, respectively), however, their direct connectivity is strictly controlled by the Löwenstein rule.[4] This rule states that there can be no Al-O-Al bridges within the zeolite structure due to coulombic repulsion.[5] Hence, when the Si/Al ratio tends to one, a strict alteration between SiO_4 and AlO_4 tetrahedra is observed. However, as the Si/Al ratio is increased towards infinity, the spacing between AlO_4 tetrahedra is maximized to aid in the reduction of coulombic repulsion seen within the structure, a property known by Dempseys rule.[6]

3.1.2 A Brief History of Zeolites (1756 - 1945)

Zeolites were first discovered in 1756 by a Sweedish mineralogist, Axel Fredrik Crønstedt, whom, is credited with the original discovery Stilbite, a naturally occurring mineral. The Sweedish mineralogist named his discovery zeolite from the ancient Greek words $\zeta\varepsilon\omega$, to boil', and $\lambda\iota\theta o\varsigma$, stone, as upon heating this natural mineral steam was released.[7] However, it wasnt until nearly 100 years after Crønstedts initial discovery, in the 19th century, that most of their innate properties began to be uncovered.

In 1840, Damour discovered that zeolites could reversibly hydrate, without causing any perceivable changes to the zeolite morphology or its transparency.[8] Eighteen years later, Eichhorn was the first to report upon cation exchange with zeolites. Eichhorn discovered that zeolites could successfully exchange cations from aqueous solutions, a property of zeolites that would be exploited a great deal in the furture.[9]

The next big discovery came in 1896, when Friedel expanded on Damour and Eichhorns earlier work to postulate that zeolites were in fact open spongy frameworks.[10] This conclusion came about from observation on how certain fluids, such as benzene and chloroform, are occluded by zeolites. This work was followed up, by Grandjean's 1909 study of the adsorption properties of chabazite (a naturally occurring zeolite).[11] Here, Grandjean, observed how ammonia vapours, hydrogen and other molecules could be adsorbed by zeolites, a property that would be further explored by Weigel and Steinhoff in 1925, who reported the first molecular sieving properties of zeolites.[12] By utilising dehydrated zeolite they were able to demonstrate how water, methanol, ethanol and formic acid were rapidly adsorbed by chabazite, whilst the vapours of acetone, ether and benzene were essentially omitted.

Soon after Weigel's study, Leonard described the first use of X-ray diffraction in the identification of synthesised minerals.[13] A study that would be followed up three years later, with Taylor and Pauling's initial determination of the single crystal structures for naturally occuring zeolites using X-ray diffraction, a technique that would soon catapult natural zeolites into the world of industry.[14]

These discoveries lead to the term molecular sieve being coined by McBains in 1932, when chabazites ability to selectively adsorb molecules < 5 Å in size was first presented.[15] It was then in the mid-1930s that Richard M. Barrer began his pioneering work on the adsorption properties of zeolites.[16] Barrer, in 1945, became the first to hypothesize that the selective adsorption properties of zeolites could be explained using two distinct mechanisms:

1. Selectivity by molecular size and shape:
   Where adsorption is favoured by smaller molecular species, a property that varies with pore size and the geometry of the channels running through the crystal structure.

2. Selectivity through interactions between the zeolite and a specific compound within a liquid/gaseous stream:
   Where species with a greater affinity towards the material will stay within the pores longer than those with a lower affinity.

After this discovery, Barrer, then went on to report the first definitive, readily-reproducible synthesis of a non-naturally occurring zeolite, a synthesis that would go on to revolutionize the world of zeolites.[17]

3.1.3 A Breif Industrial History of Zeolites (1948 - Present)

When stilbite was first discovered in 1756, it was believed that zeolites were only a minor component found within the vugs and cavities of basaltic and volcanic rock formations. This thought would hinder the early commercialization of zeolites, as with a perceived lack of minable quantities their commercialization was not viable. This belief, however would be proven wrong in the late 1950s, when large sedimentary deposits of zeolites were discovered in the United States of America. This discovery, can be credited to the advancement made in X-ray diffraction and the new found ability to examine fine-grained sedimentary rocks. This led to the industrialization of naturally-occurring zeolites, such as chabazite and mordenite as adsorbents. However, the thought that zeolites were not present naturally on a minable scale lead to the exploration into the synthesis of zeolites. In 1862, the first synthetic zeolite was produced by St Claire Deville.[18] Though, due to a lack of reproducibility and an inability to completely characterize synthetic zeolites at the time zeolites were not propelled into the world of industry. These problems with reliability, reproducibility and lack of appropriate characterisation techniques would be present up until the 1930s, meaning a multitude of early syntheses were reported but we not considered reliable enough to make an impact within the world of industry.

However, in the 1940/50's Richard M. Barrer and Robert Milton began work that would propel zeolite synthesis into a new era.[17, 19, 20, 21] Barrers initial work in 1948 would go on to inspire Robert Milton, of the Union Carbide Corporation, to begin the search for new materials to aid in industrial separation and purification processes. The work performed by these two scientists would lead to the development of the hydrothermal syntheses used in modern times. Barrer and Milton utilised high temperature and vapour pressures to convert amorphous reactants (silica and alumina) in a basic (high pH) medium into crystalline zeolites. These experiments would lead to the further development of hydrothermal synthesis of many different zeolites, including the first commercially significant zeolites A, X and Y.[22, 23]

Barrer and Milton's work would signify a new chapter in the history of zeolites. Their developments meant that there was a near unlimited supply of high purity synthetic zeolites available to the world, meaning research in the field began to grown. Due to this "boom" in research, it wasnt long until the catalytic properties of zeolites were uncovered. In 1959, the Union Carbide Corporation were first to market zeolite-Y as an isomerization catalyst. This would however, only be the tip of the iceberg, and it didnt take long for more catalytic zeolites to be produced through the incorporation of rare-earth metals into the structure of zeolite-X to produce zeolites for the catalytic cracking of fossil fuels.[24]

Next, zeolites would start to utilised for the hydroisomerization of hydrocarbons. Here, linear hydrocarbon chains are converted into branched isomers using doped zeolites.[25] This process was further developed by the Shell-Union Carbide Total Isomerization Process (TIP), a very important process for the production of high-octane gasoline. This process would negate the use of lead, and catalytically active zeolites would be utilised to isomerize linear hydrocarbons, before a second zeolite would then be utilised for separation processes.[26] The linear hydrocarbons would then be recycled and fed back into the feedstock to undergo further isomerization.

This commercialization of zeolites took almost 200 years, and it only became truly viable when high purity synthetic zeolites became widely available. The development of reproducible synthetic routes for the production of high purity synthetic zeolites would pave the way for multiple commercial applications ranging from ion exchange and gas separation to multiple uses in catalysis.[27] Zeolites in industry are used to separate molecules based on their shape, polarity, size and even by a molecules degree of saturation, and are conventionally used as ion exchangers, catalysts and adsorbents in industry today.[28, 29]]

3.1.4 ZSM-5 and Silicalite-1

ZSM-5 is a highly siliceous, MFI zeolite, where the Si:Al can be varied to alter its properties. This interesting property means that ZSM-5 crystals can be both hydrophilic and hydrophobic depending on the Si:Al ratio. This is in contrast to many other zeolites, such as A, X and Y which are all highly hydrophilic.[30] This variable property of ZSM-5 is, in part, a result of the number and type of cations found compensating the overall lattice charge. However, even with its variable hydrophilic/phobic properties, ZSM-5 remains very stable, both chemically and thermally. ZSM-5 also allows for the introduction of a variety of different T-atoms into its structure (e.g. Zr, Fe, Sn, Ti). This property enables the alteration of a zeolites catalytic properties, whilst retaining its structural characteristics.

ZSM-5 is most commonly used in the conversion of methanol to hydrocarbon fractions containing both aliphatic and aromatic compounds within the boiling range of gasoline. Due to its low aluminium content, and as the acid strength of a zeolite is maximised when Al T-atoms are spaced far apart, ZSM-5 can be said to posses very strong acid sites.[31] This property, in combination with the stability and molecular selectivity of ZSM-5, makes it very adaptable for catalytic applications. For example, in industry today, ZSM-5 is utilised in the conversion of methanol to gasoline (MTG), the alkylation of toluene with methanol to para-xylene, the disproportionation of toluene to benzene and p-xylene, and the selective cracking of paraffins.[32, 33, 34, 26] However, the two most common industrial uses of ZSM-5 are in the formation of para-xylene and the catalytic dewaxing of fossil fuels, two processes that utilize both ZSM-5s shape selectivity and its catalytic properties.

Para-xylene (and other para-substituted benzene species) possesses a much higher diffusion coefficient than their ortho- and meta-substituted counterparts. This means that para-xylene passes through the zeolite pores unhindered. However, both meta- and ortho-xylene traverse the pores much more slowly, allowing for isomerization to occur within the pores of ZMS-5.[26] Hence, the alkylation of toluene with methanol, and the disproportionation of toluene, produces higher yields of para-xylene than what would be expected from a thermodynamic perspective. The catalytic de-waxing of heavy oil fractions using ZSM-5, is a hydroisomerization cracking process involving linear or waxy hydrocarbon chains. These ”waxy” hydrocarbon chains can enter the pores of ZSM-5 whilst branched chains are omitted. This process produces two fraction, one with a boiling range comparable to that of the feed stock and one that is comparable to gasoline. The de-waxing process lowers the pour point of the fuel (the point at which a liquid becomes semi-solid and loses its flow characteristic), which in-turn dramatically improves the low temperature properties of the fuels.[35] The dewaxing of diesel is very important in the automobile industry, as it lowers the temperature at which fogging occurs. Fogging is a phenomenon that occurs at low temperatures, where linear paraffins within diesel fuels form ”clouds” and can block fuel lines.

Another zeolite that possess the MFI structure is silicalite-1. This zeolite is unique in the fact that it is fully siliceous, made up entirely of silicon and oxygen. It possesses the same structure as ZSM-5, with straight channels and pore openings of 5.4 x 5.6 Å along its b-axis, and sinusoidal channels with pore openings of 5.1 x 5.6 Å. Silicalite-1 pores made up of 10-membered rings and are sizable enough to permit ion exchange and diffusion of organic molecules. Due to its purely siliceous nature, silicalite-1 is non-catalytically active, however, due to its simplified make-up, it has been hypothesised, that through studying the mechanism involved in its formation, insights could be made on the formation of more complex zeolites with similar frameworks, such as ZSM-5.[36, 37, 38] Due to this idea, studies following the formation of silicalite-1 have gained a great deal of attention, with great emphasis placed upon the hydrothermal synthesis of silicalite-1. This is due partly to the simplicity of the system, and that within this ”clear-sol” synthesis there are only three components (silica, water and a structure directing agent). Upon mixing these reactants, hydrolysis reactions occur, forming a ”gel”, which upon heating crystallises. It is thought, that through determination of the role of the initially formed silica particles that a mechanistic understanding of the growth of silicalite-1 crystals may, in time, facilitate some aspect of control towards the zeolitic properties possessed by the end product. This is hypothesized to be possible through microstructural control, and by possessing the ability to control the size, shape and pore connectivity of zeolite systems, making it possible to tailor bulk properties, such as catalytic activity.[39] For example, mesoporous silicates, with pore diameters between 2-50 nm were originally targeted to overcome the pore size limitations seen within zeolites, i.e. the larger pores within mesoporous silicates would be open to a much broader range of molecules. However, with mesoporous silicates, catalytic applications are inhibited due to their poor hydrothermal stability and poor catalytic activity, in comparison to zeolites, a property attributed to the lack of crystalline order within the pore walls of mesoporous silicates.[40, 41] There is also a great deal of interest in the production of crystalline-mesoporous zeolitic systems, so that both the properties of zeolites, and mesoporous solids, can be exploited simultaneously within catalysis. Research has mainly focused on the production of crystalline mesoporous materials and gaining an understanding of zeolite nucleation and crystal growth is said to be of great interest in the production of these new materials.[42, 43, 44]

3.1.5 Nucleation and Growth in Literature

The nucleation and growth of zeolites is a complex, multi-step process where crystallization rate, morphology, and polydispersity, to name only a few, are determined by a multitude of different parameters, such as synthesis conditions (temperature, seeding, ageing, stirring), as-well as composition-dependant parameters (pH, dilution, ionic strength and ratios between templating agents and framework elements).

Even with these factors effecting nucleation, the formation processes involved in a typical zeolitic synthesis can be broken up into five distinctive steps:[39]

1. Amorphous precursors containing the necessary building blocks for the formation of a zeolitic structure (e.g. Si, Al, Ti, Ge, Zn, etc.) are, most commonly, placed within a basic medium, where a heterogeneous phase begins to form, known in general, as the primary amorphous phase. This gel-like colloid is then often left to age for a specific length of time, which can influence the characteristics of the final product.

2. The primary amorphous phase is then heated at autogenic pressures, within a sealed vessel to temperatures $> 100°$C. This facilitates the formation of a secondary amorphous phase (that may or may not possess some short-range order), which is in pseudo equilibrium with the solution phase.[45, 46, 47]

3. After an initial induction period, zeolitic nuclei begin to form, which can be related to equation 1.10 where the relaxation time (t_r) is the time needed for the above steps to occur, whilst t_n and t_g are equal.

4. Growth of zeolitic materials then begins at the expense of the amorphous solid phase.

The above steps have been identified in a number of different zeolitic systems, however differentiating between them has proven difficult. This has been attributed to the complexity of the probed systems, where multiple processes can occur simultaneously.[39] The steps involved in zeolite nucleation encompasses the transformation of amorphous reactants to ordered crystalline networks. It is thought that this process includes the formation of a secondary amorphous phase that may possess short-range order. However, the number of sites, with short-range order, that are able to grow into critical nuclei and then grow further into macroscopic crystals has been investigated a great deal through the calculation of nucleation rates as an inverse of the induction period. However, many studies have shown that zeolite crystallisation may not follow the traditional nucleation paths observed within a large majority of condensed matter, which has led to some suggestions that these non-traditional paths stem from the increased surface area seen within zeolites.[48]

Historically, the in-depth study of zeolite nucleation has been hindered by the difficulties associated with collecting representative *in-situ* data. However, this blockade meant that there was a heavy reliance upon computational investigations into the nucleation of zeolites, in particularly, work looking at the effects of ageing and seeding of zeolite gels.[39, 49, 50] These studies revealed that ageing can influence the distribution of crystals in the final product and provided a great deal of insight into the mechanics of zeolites nucleation. However, many of these mechanisms are still greatly debated, with many disagreeing on whether the processes are homo- or heterogeneous, and some have argued that zeolite nucleation may even be a crystal induced, secondary nucleation process.[39, 51, 52, 53] However, the problems associated with distinguishing between these mechanisms stems, in part, from an inability to differentiate between colloidal-sized gel particles and the aqueous phase in the crystallisation of zeolites from clear solution. There have, however, been a growing number of studies claiming that primary nucleation occurs mainly within the gel, at the solution-gel interface where nutrient concentrations are said to be greatest. Some of these studies have also indicated that nucleation may occur within the colloidal-sized gel particles themselves in clear solution systems.[53, 54, 55] It is thought that the mechanistic aspects of nucleation in zeolites is progressive and comprised of a reversible mechanism, where bonds are broken and reformed in a reaction catalysed by hydroxyl ions, whilst cations and templating agents are surrounded by metal-oxide species in preferential geometries due to van der Waals and electrostatic forces.[56] There has been a great deal of interest in the nucleation of zeolitic materials, and it is generally agreed that for the vast majority of systems that zeolite growth is thought to be linear throughout the crystallization process, though it has been shown that zeolite growth is effected by a great deal of parameters, including synthesis composition, ageing, and synthesis temperature.[39]

Great effort has been put into revealing the formation mechanisms of zeolites. These studies have predominantly focused on identifying the building blocks present in the early stages of zeolite growth. Iler, has shown that the formation of silica nanoparticles in a aqueous basic environment occurs *via* a base catalysed hydroxylation:

$$Si(C_2H_5O)_4 + 2H_2O \longrightarrow SiO_2 + 4C_2H_5OH \tag{3.1}$$

$$SiO_2 + 2H_2O \longrightarrow Si(OH)_4 \tag{3.2}$$

The water-soluble $Si(OH)_4$ can then react with hydroxide ions to form additional ionic species:

$$Si(OH)_4 + OH^- \longrightarrow HSiO_3^- + 2H_2O \tag{3.3}$$

$$HSiO_3^- + OH^- \longrightarrow SiO_3^{2-} + H_2O \tag{3.4}$$

This reaction scheme aided in determining when the concentration of silica surpasses the solubility limits of the ionic and monomeric silica species from the reaction of TEOS with NaOH. From this, Iler was able to determine that the excess silica in a water soluble form ($Si(OH)_4$) is polymerised and oligomeric species or nanoparticles are formed.[57] This process can be broken up into the consumption of OH^-:

$$Si(OH)_4 + OH^- \longrightarrow (HO)_3SiO^- + H_2O \tag{3.5}$$

$$(HO)_3SiO^- + OH^- \longrightarrow (HO)_2SiO_2^{2-} + H_2O \tag{3.6}$$

and the subsequent polymerization reaction:

$$nSi(OH)_4 \longrightarrow Si_nO_{\frac{4n-nx}{2}}(OH)_{nx} + \frac{4n-nx}{2}H_2O \tag{3.7}$$

Where x is the total ratio of OH^- to Si, and n is the degree of polymerization, and as n increases, the OH^- to Si ratio decreases. This showed how the polymeric silicate ions were in a solubility equilibrium with the monomeric species.[57] This work was later confirmed and extended by Fedeyko who showed that Ilers results were also valid when using organic templates such as TPAOH, instead of NaOH, and defined a critical aggregation concentration (CAC), at which nanoparticles form and where below silica is present as monomeric species.[58] The CAC was determined through titration of silica into a TPA-water mixture and measuring changes in the pH level. It was found that OH^- species are consumed by the silicic acid ($Si(OH)_4$) up until the CAC is reached, where additional amounts of silica added are polymerized:

$$nSi(OH)_4 + m(TPA^+Si(OH)_3O^- \longrightarrow Si_{n+m}O_{\frac{3}{2}(n+m)}(OH)_n(O_m)^{m-}(TPA^+)_m + \frac{3}{2}(n+m)H_2O \quad (3.8)$$

This reaction is said to proceed without seeing any change in pH, and the CAC is defined as the point at which no pH change is observed upon the addition of more silica. In clear sols it is also believed that TPA^+ adsorb onto the surface of these silica particles creating what has been termed an electric double layer that is thought to prevent the growth of new particles by aggregation at room temperature due to electrostatic repulsions.[59]

The initial formation of primary TPA-Silicate nanoparticles is widely supported throughout the zeolite community, however, their role in the formation of zeolitic crystals is still a greatly debated issue. Schoeman proposed that ethoxy groups, within TEOS, are subject to base-catalysed hydrolysis to produce a stabilised silicate suspension.[3, 36] This suspension contains both monomeric and oligomeric silicate species in a dynamic equilibrium alongside polymeric silicate species. These polymeric silicates are described as being 2-4 nm in size, and containing TPA^+, which helps to stabilise the particles, however, Schoeman also emphasises that the presence of TPA^+ within these particles is not sufficient to claim that there is a presence of short-rage order. Though he does state that this produces suitable growth sites for incoming nutrients, hence, sub-colloidal particles of a suitable structure will grow aided by monomeric species, and to a lesser extent oligomeric species, with temperature, whilst the growth rate is maintained by the equilibrium soluble silica concentration.[3, 60, 61]

Schoeman has also utilised Derjaguin-Landau and Verwey-Overbeek (DVLO) theory to propose that the primary nanoparticles grow by aggregation.[36, 60] This model shows how reaction limited cluster-cluster aggregation can form larger secondary aggregates of hydrated TPA^+-silicate clusters. These clusters can then densify and aggregate into secondary crystalline fractal aggregates ($>$ 52 nm). However, Mark E. Davis disagrees with this idea of nucleation, stating that the aggregation of primary particles cannot account for the observations that certain phases display intergrowths as the formation of intergrowths ocurs layer-by-layer, hence larger entities are envisages as the nuclei that template crystal growth.[62] This has been investigated through TEM studies that have shown grain boundaries found in large crystals but not in small ones, hence each nucleus is said to be a new crystal domain.[62, 57, 36]

Aerts came to the conclusion that silicalite-1 forms through the oriented aggregation of nanoparticles with zeolitic frameworks.[63, 64, 62] Here it is proposed that a discrete population of nanoparticles with different framework connectivities grow from a clear sol containing monomeric and oligomeric silica species. The oligomors and nanoparticles (2 nm) with low silica framework connectivity do not participate in the crystallization and only nanoparticles with highly connected silicate frameworks that resemble the final zeolite grow to form larger nanoparticles (6 nm), which are the units for further nucleation and aggregative growth of colloidal silicalite-1 crystals.

Other studies of silicalite-1 have hypothesised that crystal formation occurs through the assembly of silicate building blocks that possess similar structural characteristics to that of the final zeolitic material. This process is directed by interaction with template molecules.[36] Initially, monomer addition leads to the formation of the solid material and small clusters begin to form from condensation reactions and growth through Ostwald ripening. A narrow population of amorphous particles in clear precursor suspensions was also observed by this study, and it is thought that the homogeneity and high degree of super-saturation in the suspension, that nucleation processes can occur as a single event, resulting in the formation of nuclei, which can subsequently grow uniformly.

Figure 3.2: Model for the formation of silicalite-1 crystals from clear precursor suspensions.[65, 66]

Similar studies of silicalite-1 from clear precursor suspensions have also show that template rich silicate species form prior to the formation of crystalline species.[66] This was shown using MAS-NMR, where Q^3 and Q^4 silicate interactions were observed after heating of precursor species, hence it was determined that the organic-organic structures were actually amorphous nuclei.

These studies essentially broke down the formation of silicalite-1 into six stages:

1. The initial mixing of organic template with a silicate species;
2. The subsequent formation of initial amorphous silicate species;
3. The aggregation of the amorphous species (1 - 10 nm), to form primary fractal amorphous aggregates;
4. These primary fractals then undergo densification, and form secondary amorphous aggregates ($<$ 10 nm)
5. Further densification occurs, creating secondary fractal structures ($<$ 50 nm)
6. Then there is crystal growth (zeolite crystals $>$ 50 nm).

Other studies on the formation of zeolites form clear suspensions have provided evidence for a slightly different model for zeolite formation.[67, 68] The proposed sequence for the formation of zeolites begins with the formation of an amorphous phase that transforms to crystalline matter:

1. The mixing of organic template with a silicate aluminate species;
2. The formation of initial amorphous species;
3. The agglomeration of these initial amorphous particles to form larger, amorphous particles (5 - 100 nm);
4. The nucleation and growth of zeolite nuclei within the amorphous particles (5 - 100 nm);
5. The full conversion of the amorphous particle to crystalline zeolite (5 - 100 nm);
6. Further crystal growth (1 - 5 μm).

Figure 3.3: Model for the formation of zeolite crystals /nanocrystals from colloidal precursor suspensions.[65, 67, 68]

This proposed mechanism is based on observations on the initial, intermediate and final materials through microscopic and spectroscopic studies. First, amorphous aluminosilicate suspensions containing 5 nm particles were observed, and it is thought that these particles agglomerate upon mixing with an organic templating agent. This template addition results in the formation of larger amorphous particles 40 - 80 nm in size, and in the case of zeolite-X and -Y, the zeolitic material nucleates within the amorphous particles.

The main differences between these two proposed mechanisms comes from how the amorphous particles become the crystalline zeolitic material. The second mechanism, proposed by Mintova, only a single zeolite crystal nucleates per amorphous particle, hence the aggregation of several nuclei is not required for crystallisation/the formation of zeolites.[67, 68] This idea relies on the presence of high super saturation within the amorphous gel particles, and it is thought that this teamed with reorganization within the sealed solution, may be the driving force for zeolite nucleation. The preservation of small particle sizes was observed with the amorphous gel/zeolite particles, until their complete conversion into denser zeolitic material was observed, hence it was hypothesised that mass-transport dominants substantial crystal growth with the same zeolite suspensions at elevated temperatures.

A third mechanism has also been proposed, by T. M. Davis *et al*, for the formation of silicalite-1:[59]

1. Mixing of organic template with a silicate species;
2. Formation of precursor amorphous particles;
3. These amorphous particles evolve into *n* intermediate amorphous particles (where *n* essentially denotes the number of intermediate particles the initial amorphous precursor particles go through prior to the nucleation of silicalite-1 particles, hence can be denoted as n_1 - n_∞);
4. The agglomeration and nucleation of intermediate particles, and hence, there are again, *n* amorphous particles with zeolite nuclei (5 - 100 nm) are formed;
5. Crystal growth through agglomeration, hence the presence of amorphous particles containing zeolite aggregated nuclei ($>$ 100 nm);
6. Further crystal growth.

Here, the amorphous precursor particles are said to be TPA-silica core-shell particles that contribute to crystal growth through aggregate-like processes, and it is also stated that the later stages of crystal growth is dominated by aggregation of zeolite nuclei. It is said that the aggregate-like appearance of zeolite crystals is the most obvious evidence that there the nanoparticles contribute to the formation of nuclei and the overall crystallization process. Davis describes how aggregative growth dominates the early crystallisation processes, and presents that the precursor nanoparticles have a constant size for first several hours of hydrothermal treatment,

Figure 3.4: Model for the formation of zeolite crystals, describing the growth of silicalite-1 propsed by T. M. Davis *et al* where n denotes the number of intermediate, amorphous particles.[65, 59]

before they begin to evolve with respect to their colloidal stability. It is also proposed that a kinetic mechanisms, supported by mass-action kinetics for the evolution of precursor nanoparticles, results in the formation of silicalite-1 crystals.

Davis also made observations of how the amorphous particles have relatively fast dissolution dynamics and increased colloidal stability, in comparison to that seen with the zeolite-like particles, which was explained to be due to the negative surface charge and steric stabilization from adsorbed structural-directing agents. The intermediate particles were also said to contribute to the development of silicalite-1 nuclei through attachment processes. What can be considered as the most novel part of Davis' proposed mechanism is the elimination of zeolite dissolution, growth by crystal-crystal aggregation and Ostwald ripening.

This chapter will focus on probing the formation of silicalite-1 from three commonly used silica precursors. The system will be probed using two complementary techniques, so that a full picture of the formation process can be investigated. The use of complementary techniques makes it possible to obtain information that is representative of the system as a whole. *Ex-situ* TEM microscopy will provide information on the finer details of the parts of the system, whereas *in-situ* SAXS will provide information that is representative of the overall system as a whole.

3.2 Experimental

silicalite-1 samples were prepared using three different silica sources:

1. Tetraethyl Orthosilicate (TEOS)
2. Colloidal Silica (Ludox AS-40, c.a. 22nm)
3. Fumed Silica (c.a. 11nm)

Each silica source was mixed with tetrapropylammonium hydroxide (TPAOH) and water for 20 minutes, prior to being subjected to hydrothermal conditions. The synthesis gels were produced in a 25:8:590 SiO2:TPA+:H2O molar ratio. *Ex-situ* samples for microscopy studies were prepared using stainless-steel autoclaves at 180°C, whilst *in-situ* samples were prepared within the UCL hydrothermal *in-situ* cell at 160°C.The *in-situ* cell was equipped with a 2 mm pathlength and sealed using two, 50 μm mica windows. *In-situ* SAXS experiments were performed at both Diamlond light source beamline I22 and at the ESRF beamline BM26b. At I22, data was recorded at 12.4 keV, using a Pilatus3 2M detector with a sample-to-detector distance of 9.44 m. At BM26b, data was recorded at 14 keV using a Pilatus2 2M detector with a sample-to-detector distance of 0.9 m. Data reduction was performed using the DAWN software package provided by Diamond Light Source and data analysis was performed using McSAS software package.[69] TEM images were taken using a Jeol 2100 HRTEM with a LaB6 source operating at an acceleration voltage of 200 kv at the Department of Chemistry, University College London.

3.3 Results and Discussions

3.3.1 Formation of Silicalite-1 from TEOS

The formation of silicalite-1 from TEOS was initially studied *ex-situ* using TEM microscopy. TEOS was first mixed with TPAOH and water for 20 minutes prior to being exposed to hydrothermal conditions. After 15 minutes (3.5 a and b), microscopy was performed on the sample, revealing the presence of small nanoparticels ($<$ 20 nm) with a globular morphology. The observed nanoparticles are polydispersed and found within large agglomerated clusters.

After 30 minutes of hydrothermal treatment (figure 3.5 c and d) three distinct populations of particles are observed. The clusters of nanoparticles seen after 15 minutes are still present, but are found to be creating an interconnected network of particles. The other two populations of particles can be found supported within this network. The largest observed particles (c.a. 250 - 400 nm in length) are of a typical morphology often associated with crystalline silicalite-1. These particles have rough and rounded edges that appear to be formed from smaller, $<$ 20 nm, particles from the network of silica. The final population of particles observed possess a pseudo-spherical morphology and appear in a range of size from 30 150 nm in diameter. These particles, like the larger particles, are again contained within the network of $<$ 20 nm particles, and are observed in close proximity to the larger particles (250 - 400 nm), and in places, look to be attached to the surface of these larger particles with crystal-like morphologies.

With a further 15 minutes of hydrothermal treatment (figure 3.5 e and f) a change in particle population is again observed. Larger crystal-like particles are again observed, however they possess a slightly different morphology than previously observed, where the particles are now less elongated along a single axis, giving them a squarer appearance. These crystal-like particles are of a similar size to those observed after 30 minutes of hydrothermal treatment, however the edges of the particles are better defined. The number of observed pseudo-spherical particles has also increased drastically over this period of time. These particles are observed with varying particles sizes (up to 150 nm) and are again found within a network of

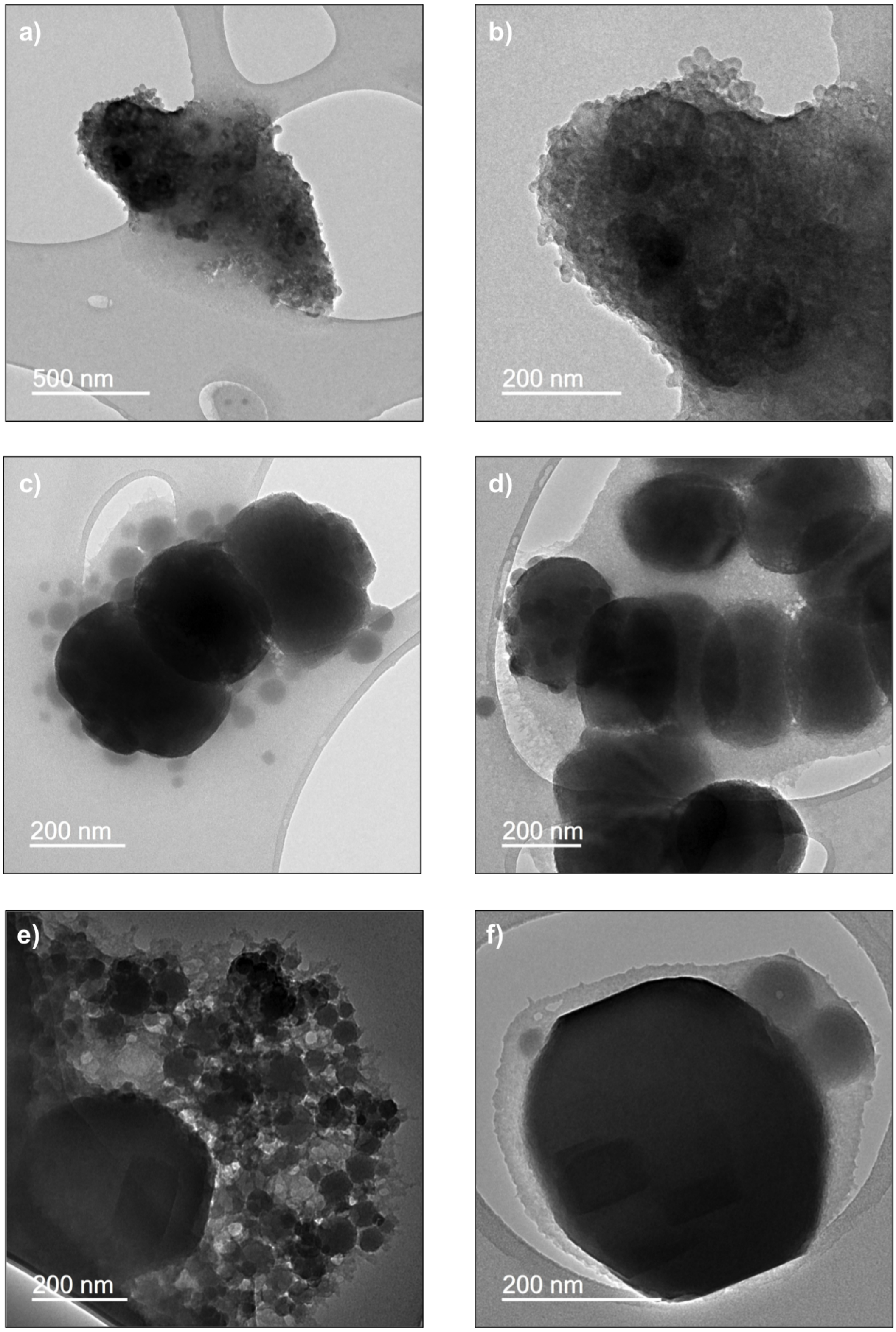

Figure 3.5: TEM images of a time sequence study of the formation of silicalite-1 from TEOS at 180°C. Images taken after 15 (a. & b.), 30 (c. & d.), 45 minutes (e. & f.)

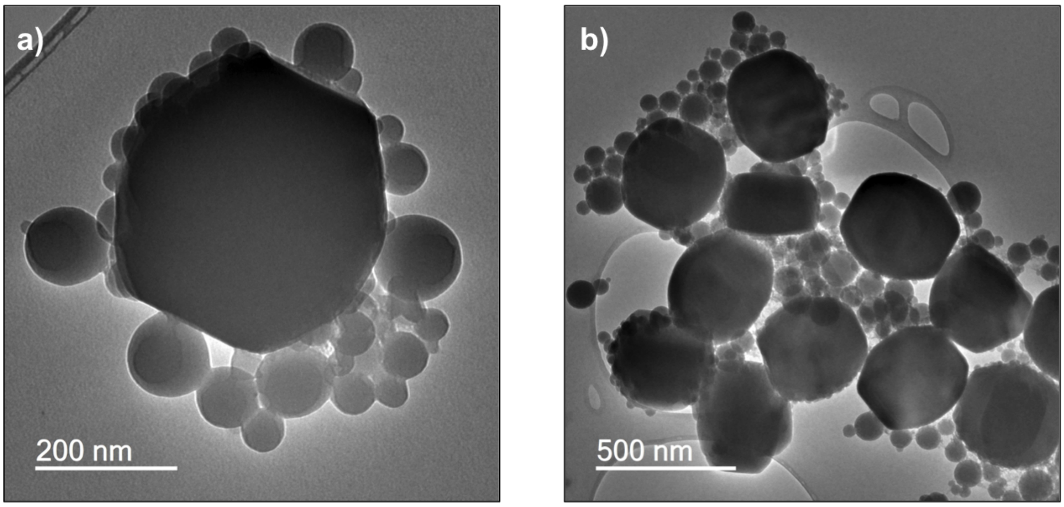

Figure 3.6: TEM images of the time sequence study of the formation of silicalite-1 from TEOS at 180°C. Images taken after 60 minutes of hydrothermal treatment.

smaller particles as previously observed.

Figure 3.6 shows TEM images taken after 60 minutes of hydrothermal treatment. After this period of time many more large particles with a typical silcialite-1 morphology are observed. These particles are now c.a. 400 nm in length and have a more well-defined appearance than previously observed. The network of smaller $<$ 20 nm particles is now present in much smaller amounts and only observed between the pseudo-spherical particles. Figure 3.6 a) shows the pseudo-spherical particles more clearly, revealing that they are actually core-shell particles observed with sizes up to 150 nm. These particles are observed with only a single core per particle, however, it can also be seen that the cores interact with one another through interconnected bridges, which could be indicative of how these particles grow. It can also be seen that the cores interact with the larger crystal-like particles in this same manner, as the cores look to attached themselves to the surface of the larger particles.

Figure 3.7 a) give a closer look at the core-shell particles, also revealing that the cores of the larger particles interact with the smaller non-core-shell particles, as they look to flow into one another. Aggregative interactions are also observed where the shells of the particles touch, whist it can also be seen that some of the particles seem rougher and could be made from multiple smaller particles. Figure 3.7 b) shows the larger crystal-like particles with the core-shell particles present upon its

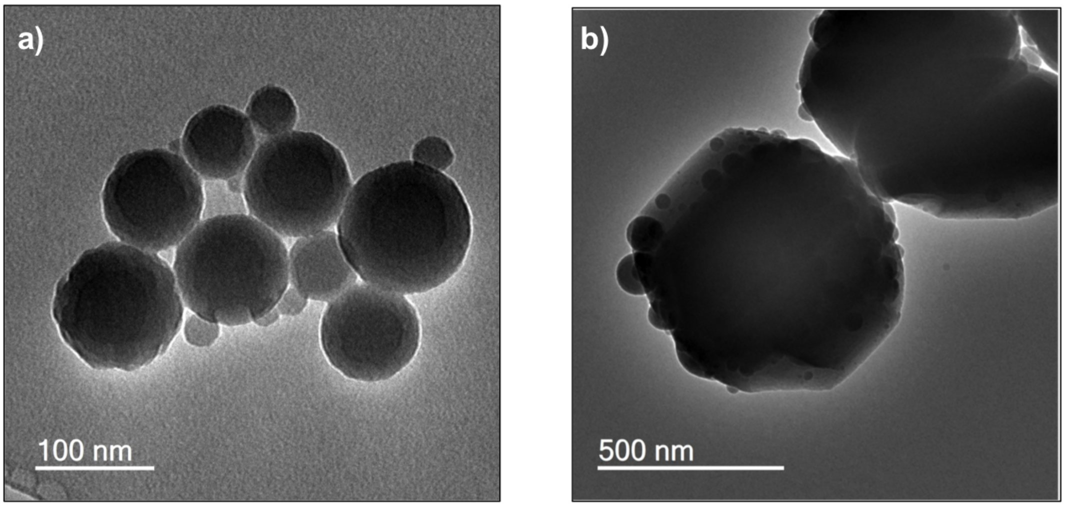

Figure 3.7: TEM images of the time sequence study of the formation of silicalite-1 from TEOS at 180°C.

surface, indicating that these particles may contribute directly to crystal growth.

Figure 3.8 shows the *in-situ* SAXS data collected on the formation of silicalite-1 where TEOS is used as a silica precursor. Over the first 8 minutes (c.a. 500 seconds) of hydrothermal treatment, very little change is observed in the scattering cuvres. This indicating that the zeolite precursor gel has undergone little change over this period of time. However, after 8 minutes (c.a. 500 seconds) changes are observed in the SAXS data, with fits of the data indicating the presence of particles upto 4.6 nm in size, but with an average particle size of 2.96 nm ± 0.24 (see appendix A.1.2 for fit data).

However, after 10 minutes (600 seconds) of hydrothermal treatment it can be seen that this population of particles begins to grow, with fits indicating a slight increase in the average particle size found within the system (3.12 nm ± 0.24), and the largest observed particles now being 5.1 nm in diameter. This population can then be seen to grow in terms of particle size and volume fraction over the next 5 minutes (c.a. 900 seconds), where the population contains particles up to 10 nm in diameter. This growth continues again over the next 5 minutes (c.a. 1200 seconds), where the average particle size slowly increases from 3.85 nm ± 0.14, to 5.66 nm ± 0.22. This growth again continues over the next 5 minutes (c.a. 1500 seconds) until particles upto c.a. 18 nm are observed. The particles found from fits of the SAXS

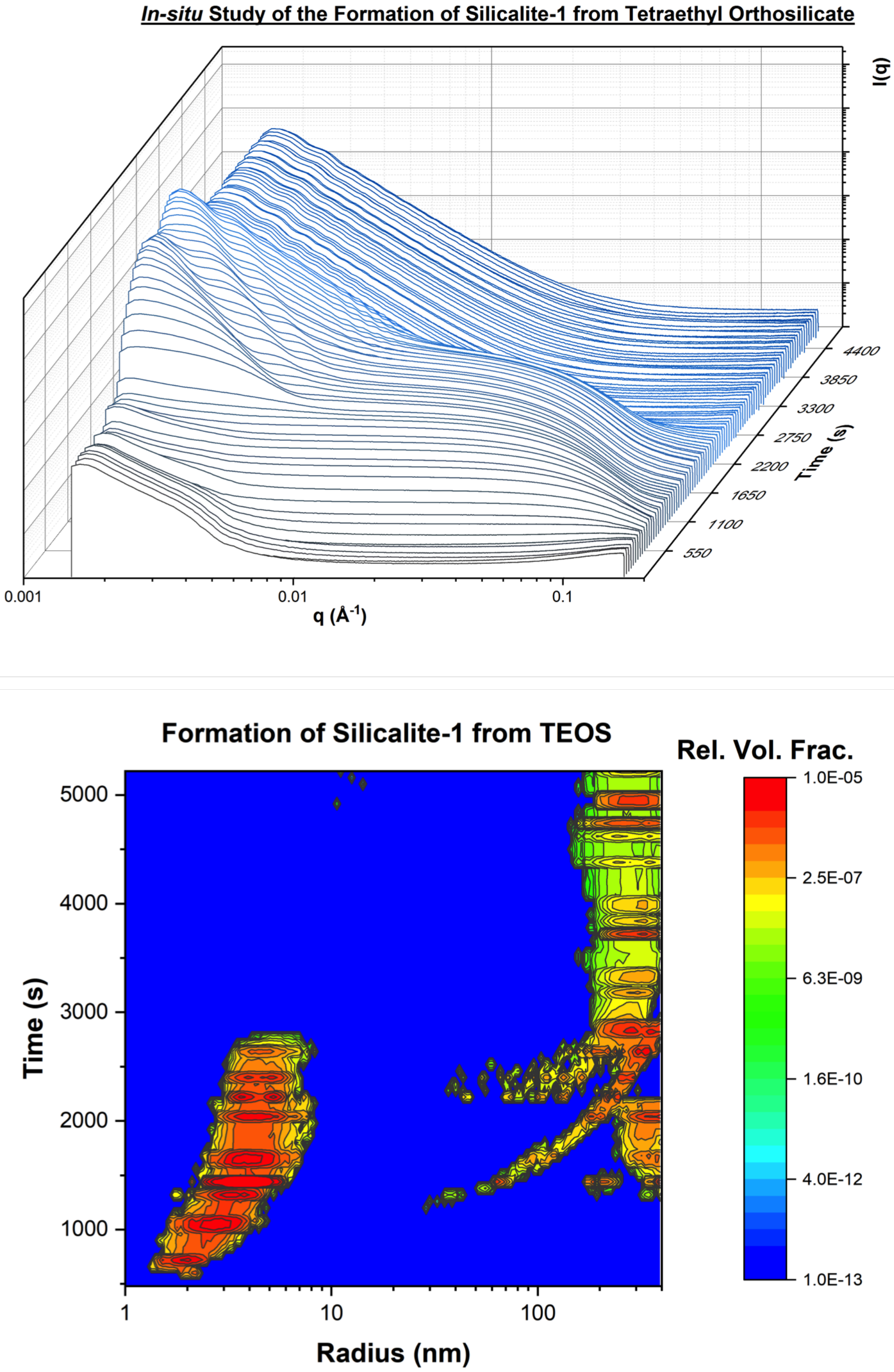

Figure 3.8: *In-situ* SAXS data on the formation of silicalite-1 from TEOS at 160°C (top), and results from Monte Carlo fitting (bottom).

data at this time correspond quite well with the observations seen from the *ex-situ* TEM study after 15 minutes of hydrothermal treatment, where particles upto 20 nm were observed.

After 21 minutes (c.a. 1200 seconds) of hydrothermal treatment, The relative volume fraction of the 18 nm particles begins to decrease, however a second population of larger particles is now observed. This secondary population of particles are observed to be 45 - 90 nm in size, and whilst this population is only small in comparison to that of the smaller particles, their presence is easily observed in the SAXS data with the change in gradient observed at $q < 0.1 nm^{-1}$ (figure 3.8). The appearance of the secondary population of larger particles seems to come at the expense of the c.a. 18 nm particles which could be inductive of a change in favourable growth mechanics, where a point of saturation has been reached with the formation of the $<$ 20 nm particles, opening up different pathways for further growth to become more favourable.

After 23 minutes (c.a. 1400 seconds), an average particle size of 10.2 nm ± 0.25 if obtain for the system as a whole. However, at this stage in the process the average particle size of the system begins to provide little information on the system as a third larger population is now observed. The initial population of small nanoparticles now contains particles upto c.a. 15.5 nm, with the majority of particles observed within this population between 5.4 - 9.7 nm. A second population observed, consists of particles 40 - 60 nm in diameter, whilst the third population represents much larger particles 100 - 140 nm in size.

After 25 minutes (1500 seconds) the population of the smallest particles continues to slowly decrease in terms of relative volume fraction, whilst the relative volume fraction of the larger population increases. The larger particles continue to grow (now c.a. 120 - 185 nm in size), but the presence of particles $>$ 300 nm are also observed within the system. Over the next five minutes, the population of 120 - 185 nm particles almost doubles in size, with particles between 240 - 340 nm now being observed. The formation of these larger particles lines up well with observation from *ex-situ* TEM measurements taken after 30 minutes of hydrothermal treatment. It is also around this time where the form factor of the larger particles begins to be observed more easily in the SAXS data at $q < 0.1$ nm^{-1} (figure 3.8).

After 37 minutes (c.a. 2200 seconds) of hydrothermal treatment, the SAXS data begins to change dramatically (figure 3.8). It is at this point that a decline of the relative volume fraction of the smallest particles is observed in the SAXS fits. This shift is observed alongside the appearance of other population of larger particles 87 - 102 nm, 130 - 200 nm, 240 - 280 and particles over 420 nm. This sudden decline in the volume fraction of the smallest nanoparticle population occurs rapidly, however it also comes with an observed increase in crystallinity of the system (see appendix A.1.1 for low-q SAXS data).

After a further 3 minutes of hydrothermal treatment (2400 seconds), the relative volume fractions observed between larger and smaller particle population becomes much more similar, indicating the loss of the smallest particles is connected to the increasing growth of the larger particles, which could again represent a shift in favourable growth mechanics. This trend of increasing and decreasing population continues until after 45 minutes (2700 seconds) of hydrothermal treatment, the hump observed in the SAXS data at $q > 0.1$ nm^{-1} (figure 3.8) is no longer visible, corresponds to the ultimate demise of population of small particles within the system. After an hour (3600 seconds) of hydrothermal treatment no particles bellow 10 nm in size are observed, whilst only very few particles between 10 - 160 nm are observed, alongside the growing population of particles $>$ 250 nm. This growing population continues to grow in terms of particle size until the end of the experiment where they are $>$ 400 nm is size. The smaller population of particles also grows in terms of size, with the population encompassing particles 10 - 200 nm at the end of the experiment, though the volume fraction occupied by these particles is continually decreasing towards the end of the experiment (see appendix A.1.1 for low-q SAXS data).

From comparing both the *ex-situ* microscopy data, and the *in-situ* SAXS data a good representation of the system as a whole, for the formation of silicalite-1 from TEOS, can be obtained. The *ex-situ* data provides unique, unambiguous results that are not necessarily representative of the systems as a whole, whilst the *in-situ* SAXS data provides somewhat ambiguous but representative data. Hence, when used together these two techniques complement each other greatly, making it easier for the formation of a hypothesis for growth that can be said to be representative of the probed system.

When looking at the presented data as a whole, it can be seen that initially particles are formed within the synthesis gel (present at the start of the SAXS experiments). These particles are roughly $<$ 5 nm in size, and over time these amorphous precursors particle grow into secondary amorphous particles, c.a. 5 - 20 nm in size. After this stage in the reaction there is then evidence for two distinct pathways for the nucleation of silicalite-1. The first is the conversion of these secondary amorphous particles to zeolite through aggregation processes. There is evidence for this shown in both the TEM images and the SAXS data. Figure 3.5 d shows that after 30 minutes of hydrothermal treatment, large particles with morphologies typical of silicalite-1 are observed within a network of the secondary amorphous particles. The majority of particles observed at this stage are visibly longer along one axis, and appear to be made up of much smaller particles, giving rise to the hypothesis that these large particles are formed through aggregative processes. The SAXS data shows that after 21 minutes (c.a. 1200 seconds) of hydrothermal treatment the largest of the secondary amorphous particles disappear, with the introduction of larger particles. These larger particles could be formed in a multitude of ways, however basing the hypothesis on both the SAXS data and microscopy, aggregation processes present the most likely scenario. Soon after this point of crystal nucleation seen in the SAXS data, it is observed that these larger particles grown in size gradually over the next 5 - 10 minutes to a size $>$ 300 nm. This gradual increase in size also indicates that the secondary amorphous particles may contribute directly to crystal growth, due to the lack of presence of intermediate sized particles at this stage. This nucleation path and crystal growth can be summarised as:

1. Template (organic) + Silica source

    - Mixing

2. Formation of amorphous precursor nanoparticles (< 5 nm)
    - Evolution and Agglomeration
3. Secondary amorphous nanoparticles (5 - 20 nm), present within clusters creating a network of particles
    - Aggregation and Nucleation
4. Amorphous particles and Zeolite Crystals (200 - 400 nm)
    - Further Crystal Growth
5. Zeolite Crystals

However, it is after this point that we see that other routes for crystal growth and nucleation may be present. Figure 3.5 e shows the presence of intermediate particles after 45 minutes of hydrothermal treatment. The formation of these particles is also observed after 37 minutes (c.a. 2200 seconds) in the SAXS data. The SAXS data also provides information on how these particles are formed very quickly at the expense of the secondary amorphous particles. These are observed in the TEM micrograph as pseudo-spherical particles with diameters between 20 - 150 nm. TEM images also show the evidence that these intermediate particles are core-shell particles, which would indicate the nucleation of zeolitic material within the cores of these particles, a hypothesis that is again backed up by evidence in the SAXS data, whereas upon the formation of these particles the crystallinity of the system increases dramatically (see appendix A.1.1). The formation of core-shell like particles has previously been proposed in many other studies, however it is often thought that the colloidal-like particles initially formed are core-shell particles, though many studies have also hypothesis the formation of zeolite nuclei witin amorphous particles at later stages.[53, 54, 55, 65] The formation of these intermediate particles coincided well with T. M. Davis *et al* hypothesis, where *n* intermediates are formed and these intermediates can all contribute to further crystal growth.[59]

At this stage in the experiments we also see large crystal-like particles int the TEM micrographs. These large particles are of a similar size to the larger particles observed earlier in the *ex-situ* TEM study, however they have a slightly different morphology. The particles formed at this later stage, after the appearance of the intermediate particles, are much broader in appearance, which could be indicative that they were formed through different mechanism. These broader particles, are hypothesised to be formed form the intermediate core-shell particles, rather than from the secondary amorphous particles. However, it must be noted that the remaining secondary amorphous particles left within the reaction medium can contribute to the growth of these broader crystalline particles.

After this point the data indicates that there are much fewer secondary amorphous particles, some intermediate particles and a growing amount of larger zeolite crystals. In TEM images taken after 60 minutes, primarily only the intermediate particles and crystal particles are observed with very few secondary amorphous particles present. It is at this stage where we see more clearly the interaction between the intermediate particles and the crysalline particles. Figure 3.6 shows that, in places, the cores of the intermediate particles are attracted to the crystalline particles and, in some cases, are through thin bridges of what is assumed to be the core material. This is also observed between cores within separate intermediate particles, which could be evidence of Ostwald ripening.[36, 70] Overall, this second path for the formation of silicalite-1 from TEOS can be summarised as:

1. Template (organic) + Silica source
    - Mixing
2. Formation of amorphous precursor nanoparticles ($<$ 5 nm)
    - Evolution and Agglomeration
3. Secondary amorphous nanoparticles (5 - 20 nm), present within clusters creating a network of particles
    - Agglomeration and Nucleation
4. Intermediate nanoparticles with ”core-shell” morphologies with amorphous shell and zeolite nuclei core (20 - 150 nm)

  - Ostwald ripening and Crystal growth

5. Secondary intermediate ”core-shell” particles with larger zeolite nuclei cores (150 nm), and zeolite crystals ($>$ 200 nm)

  - Crystal Growth

6. Zeolite Crystals

This is similar to the mechanism proposed by T. M. Davis *et al*, which neglects zeolite dissolution, growth by crystalcrystal aggregation, and Ostwald ripening involving monomeric or oligomeric species.[59] With the proposed paths for the formation of silicalite-1 from TEOS, it is also emphasised that the secondary amorphous particles and all intermediate particles can contribute to crystal growth directly as a nutrient source for growing crystalline species.

3.3.2 Formation of Silicalite-1 from Ludox AS-40

Figure 3.9 shows a TEM image of Ludox AS-40 particles. It can be seen that the particles are polydispersed, with particle diameters in the region of 15 30 nm.

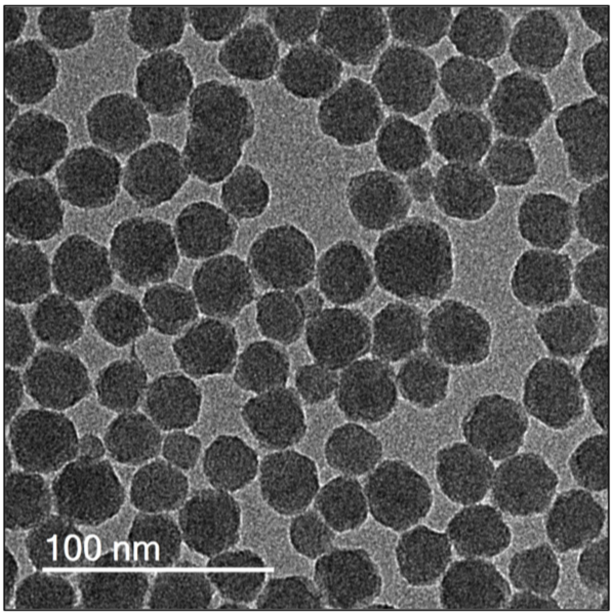

Figure 3.9: TEM images of the Ludox AS-40.

Figure 3.10 a and b show TEM images of large clusters of ludox particles once they have been mixed with TPAOH and water and subjected to hydrothermal conditions for 15 minutes. The observed particles are of similar size to that of the starting ludox material, however these particles show signs of dissolution, as individual particles appear rougher, and there is a presence of smaller particles creating a network around the ludox particles. Within some parts of the large clusters, it is hard to identify individual particles and seems as though some particles may be interconnected and have undergone densification. This is reminiscent of observation previously seen when using TEOS as a silica precursor in the formation of Silcalite-1, however these observations occur much faster using the ludox precursor.

After a further 15 minutes of hydrothermal treatment (figure 3.10 c and d) the presence of much larger particles (up to c.a. 500 nm) with a similar morphology to that of crystalline silicalite-1 are observed. These particles are suspended in a network of ludox-sized particles, and have rough edges that are covered by particles of similar size to that of the initial Ludox particles. Figure 3.10 e and f show TEM images obtain after 45 minutes of hydrothermal treatment. After this period of time particles of up to 800nm (figure 3.10 e) in size are observed. However, smaller particles with silicalite-1 morphologies are still observed within the sample (c.a. 300 nm, figure 3.10 f), however these particles have broader appearance than those previously seen, but posses the coffin-shaped morphology expected from silicalite-1 crystals.

Figure 3.11 also shows particles found after 45 minutes of hydrothermal treatment. Two distinct morphologies are observed here, with one population of particles being the roughened ludox-sized particles, and the second population being much larger particles (c.a. 200 nm) with crystal-like morphologies. It can be seen that the large crystal-like particles are made up from the smaller ludox particles, and even though they do not have the final expected morphology of silicalite-1 crystals it can be seen that these particles are at least partially crystalline, due to the presence of a visible crystalline lattice in the TEM images.

Figure 3.12 shows the *in-situ* SAXS data collected on the formation of silicalite-1 from ludox AS-40. It can be seen that at the start of the experiment, the form factor from the ludox particles is observed. From fits of the data (see ap-

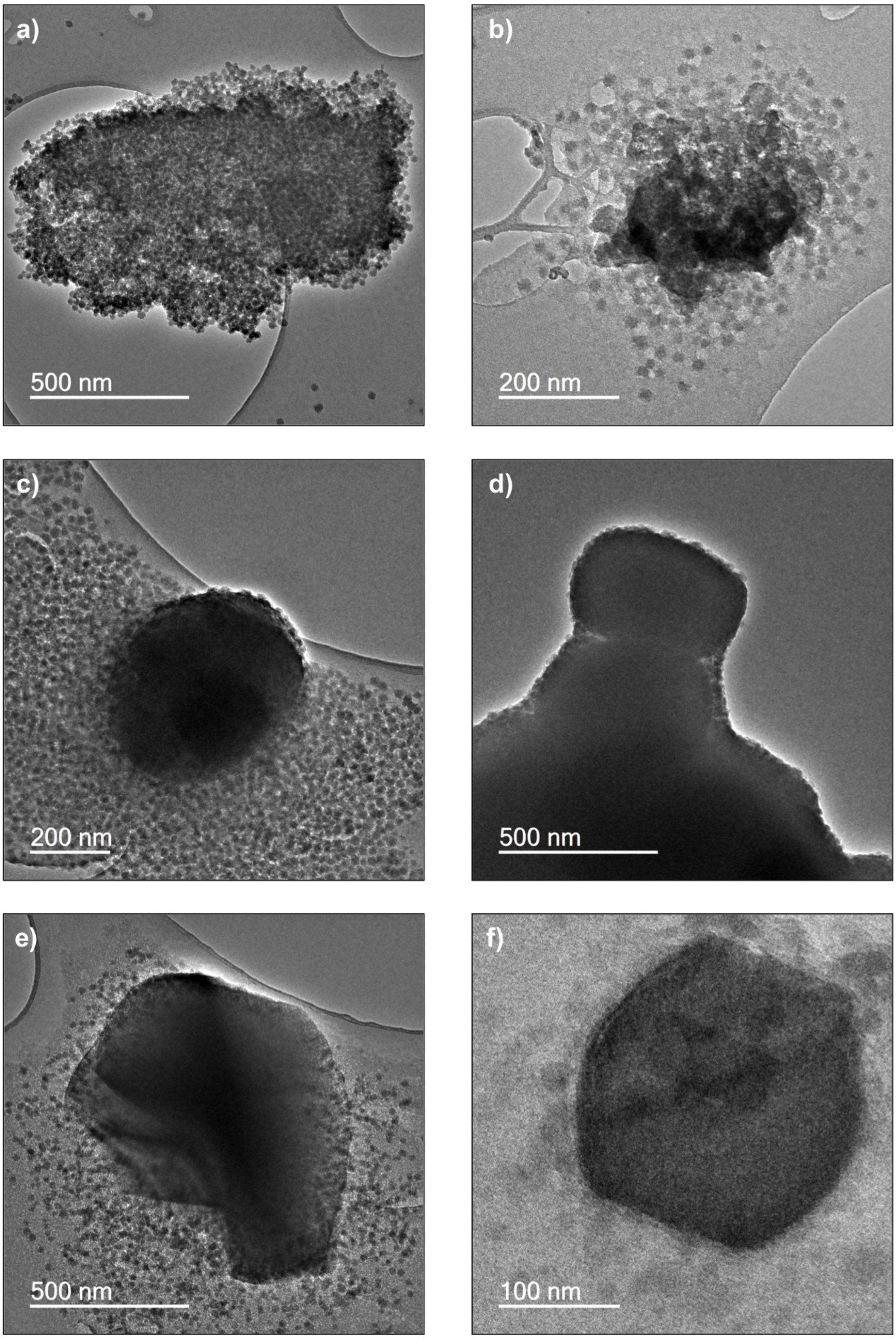

Figure 3.10: TEM images of a time sequence study of the formation of silicalite-1 from Ludox at 180°C. Images taken after 15 (a. & b.), 30 (c. & d.), 45 minutes (e. & f.)

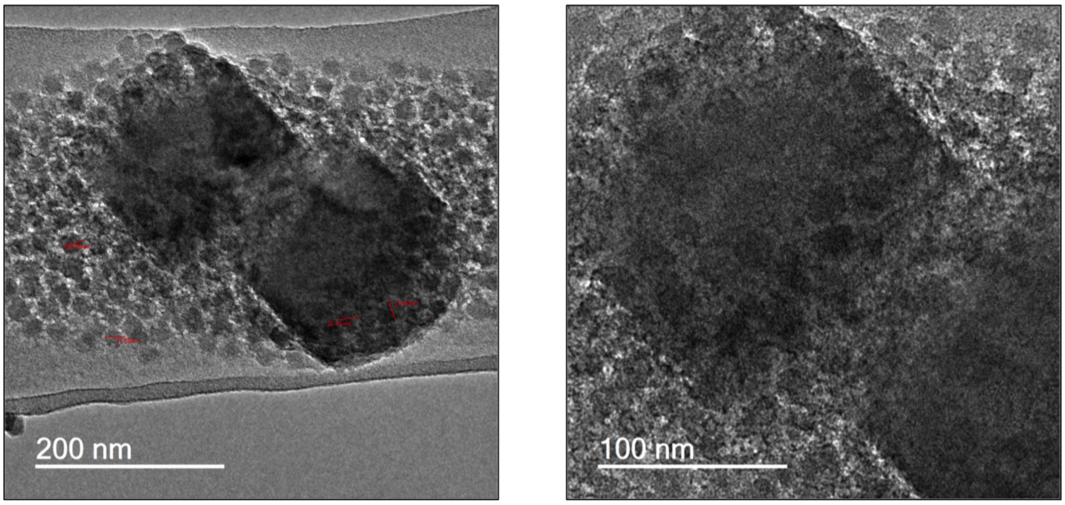

Figure 3.11: TEM images of the time sequence study of the formation of silicalite-1 from Ludox at 180°C. Images taken after 45 minutes of hydrothermal treatment.

pendix A.2.2), it can be seen that the ludox particles have an average particle size of 26.48 nm ± 0.04, with the majority of particles sized between 25.67 - 30.47 nm. After 3 minutes (180 seconds) of hydrothermal treatment the average particles size has decrease only slightly (26.26 nm ± 0.05), however the overall population of particles is becoming broader, encompassing particles between 21.64 - 31.34 nm. This indicates both growth and dissolution is occurring within the system. The dissolution of the ludox particles is also backed up by the observation of a very broad population of smaller particles. This indicates that there maybe multiple processes occurring simultaneously within the system even at this early stage.

After 7 minutes (c.a. 400 seconds) little change is observed with respect to the observed particles sizes, however the population of smaller particles is growing in terms of volume fraction. Three minutes later (600 seconds), a shift in the distribution of particle sizes is observed with the ludox-sized particles, where the particles are seen to shrink in size from a range of 21.64 - 31.34 nm to 18.76 - 28.78 nm. This shift is also represented in the change in average particle size to 23.36 nm ± 0.06, but more importantly this change in particle size is also accompanied by the the appearance of a population of c.a. 40 nm particles.

After 15 minutes (900 seconds) of hydrothermal treatment, the average particle size is still decreasing, 22.28 nm ± 0.05. The population of ludox-sized particles

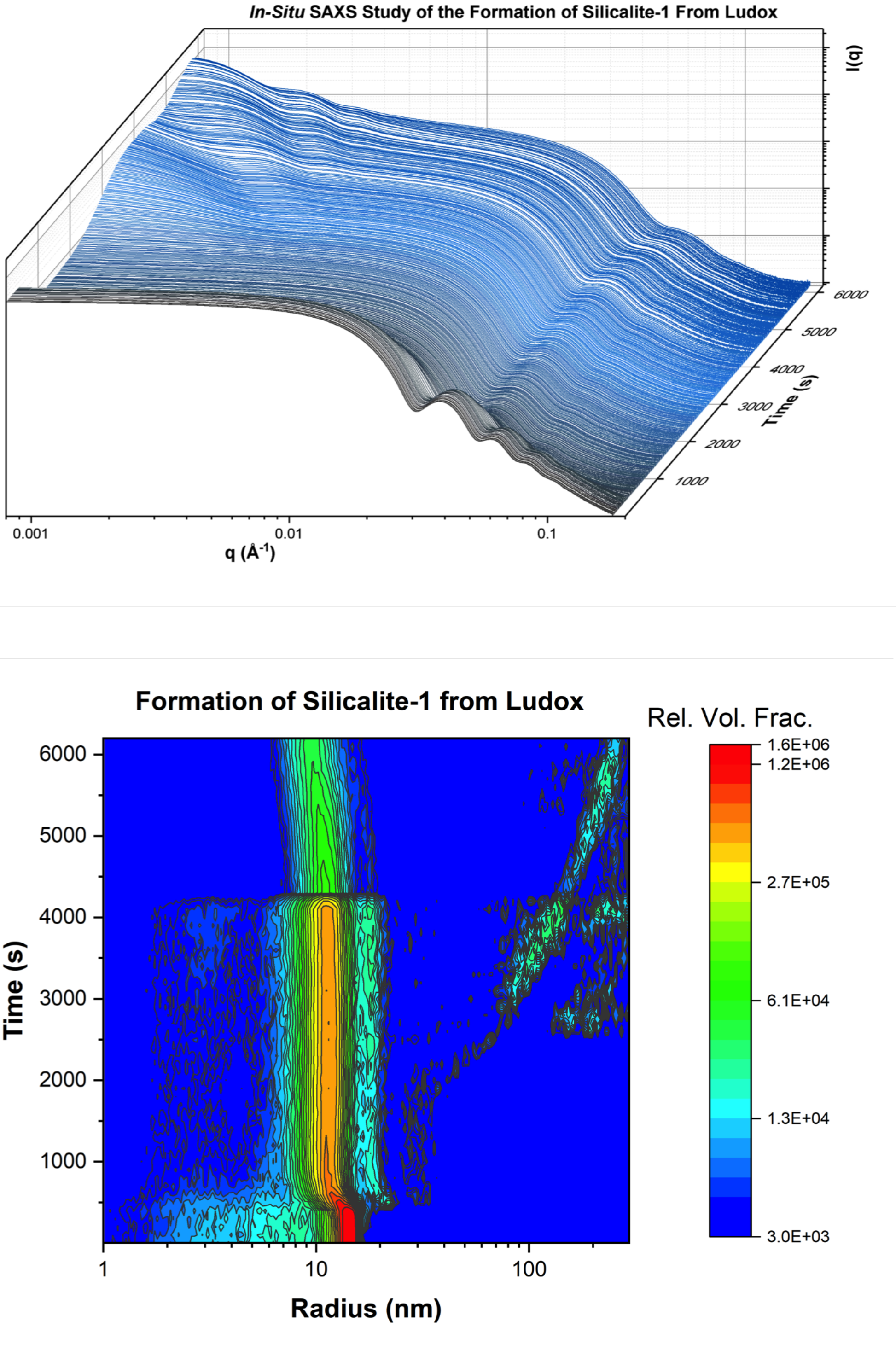

Figure 3.12: *In-situ* SAXS data on the formation of silicalite-1 from Ludox AS-40 at 160°C (top), and results from Monte Carlo fitting (bottom).

has remained relatively the same over the past 5 minutes, however the growing population of larger particles has increased in overall volume fraction and is made up of particles between 46 - 63 nm. It is also around this stage that a visible change in the SAXS data at $q < 0.01\ \AA^{-1}$ (figure 3.12, where the data tends towards a steeper gradient, indicating the increased scattering from larger particles within the system. After 20 minutes (1200 seconds) the ludox-sized particles are still the largest population in terms of relative volume fraction, though in general, they are still decreasing in overall size, now 17.72 - 28.18 nm. Again, the larger particles are still growing in both overall volume fraction and size, with this population encompassing particles 50 - 66 nm.

After 25 minutes (1500 seconds) the majority of particles are again observed between 17.22 - 28 nm, whilst the secondary group of larger particles is still growing in size, now 50 - 75 nm. Ten minutes later (2100 seconds), little change is seen with the 17.22 - 28 nm population, however the secondary population has again become broader to include particles upto 100 nm in size, which again grow over the next 5 minutes (2400 seconds) to encompass particles upto 140 nm. After 50 minutes (3000 seconds) of hydrothermal synthesis, a change in the gradient at $q < 0.05\ \AA^{-1}$ is observed (figure 3.12), indicating the presence of larger particles. This is also indicated by the fits of the data, with the observation of three distinct population. The initial population of Ludox-size particles are still present with a broad population of particles 17.2 - 28.78 nm in size. This population is accompanied by a broad population of particles 92 - 185 nm in size, along with a third population, consisting of particles greater than 300 nm. Ten minutes later (3600 seconds) the Ludox-like particles have again not changed, whilst the other population have grown and are made up of particles 168 - 244 nm and $>$ 340 nm. After, 70 minutes (4200 seconds), a significant drop in the relative volume fraction of the ludox-sized particles (now 17 - 27 nm) is then observed, alongside further growth of the larger particle populations now observed in the range of 225 - 300 nm and $>$ 350 nm.

After 80 minutes (4800 seconds) the Ludox-like particles have again begun to become smaller, now 15.8 - 27.18 nm. This trend continues towards the end of the experiment where their final particles size distribution is between 14.67 - 24.94 nm. At the end of the experiment particles $>$ 200 nm are also observed with the majority of particles being 270 - 520 nm. It is also important to mention that throughout this experiment (from 3 minutes onwards) there has been a presence of $<$ 5 nm nanoparticles, though the volume fraction of these particles is small they are still present throughout the experiment.

Comparing the results form both experiments a clearer picture of the system as a whole can be obtained. Initial observation made from the *ex-situ* TEM study over the first 30 minutes of hydrothermal treatment are similar to what is observed when using TEOS as the silica source. However, the crystal like particles formed after 30 minutes in each experiment are much larger in the ludox experiments. This suggests that an aggregative growth process is taking place early on in the experiments where silicalite-1 particles are nucleated from clusters of smaller particles, which are observed in the surface of the crystals. This hypothesis of aggregative grow is also backed up by SAXS with the presence of the form factor from the ludox particles being ever present throughout the experiment, as well as the larger particles that grow iteratively, and constantly over the first 50 minutes (3000 seconds) of the experiment. This would indicate that the ludox particles can directly participate in crystal growth and that the formation of intermediate stages is not necessary. After this stage in the SAXS experiment, only the ludox-like particles (c.a. 15 - 30 nm) and much larger particles are observed ($>$ 90 nm). This again corresponds well with observation in TEM, where only the ludox-like particles and larger crystal particles are observed. This leads to the hypothesis that the formation of silicalite-1 occurs primarily through the aggregation ludox particles:

1. Template (organic) + Ludox
    - Mixing and Agglomeration
2. Clusters of template infused ludox particles
    - Aggregation and Nucleation
3. Amorphous particles and Zeolite Crystals (200 - 400 nm)

    - Further Crystal Growth

4. Zeolite Crystals

From the observation made from both *ex-situ* microscopy and *in-situ* scattering experiments, the above proposed mechanism is thought to be the dominant formation mechanism. However, dissolution also occurs within this system, and from this dissolution comes the formation of < 5 nm particles. The formation of these particles is similar to the early stages of growth observed when using TEOS as a silica source. This would indicate that there could be the presence of a second, less favourable formation mechanism present within the system similar to the main growth mechanism proposed for growth with TEOS. This could also explain the appearance of smaller silicalite-1 particles in the later stages of the experiments, with slightly different morphologies (figure 3.10 f). However, when looking at TEM and SAXS data, the infusion of ludox particles with TPAOH and their subsequent aggregation and nucleation is clearly the most dominant path for the formation of silicalite-1.

3.3.3 Formation of Silicalite-1 from Fumed Silica

Figure 3.13 a and b, show TEM images of the fumed silica precursor used in the formation of silicalite-1. These images show that the particles are aggregated, and are not uniform in either size or shape, though they possess a relatively smooth form. The observed particles are very polydisperse, with particle sizes between 10 - 40 nm. Figure 3.13 c and d shows samples that have been subjected to hydrothermal conditions for 15 minutes. Here, it can be seen that the fumed silica particles have become much rougher after this period of time. The particles are again observed clustered together, however individual particles are now harder to defined as independent particles, as the particle look to have aggregated to some extent. After a further 15 minutes of hydrothermal treatment (Figure 3.13 e and f) the aggregated fumed silica particles with the rougher surface appearance are still observed, alongside the first indications of crystallisation, with the presence of a c.a. 130 nm particle, with a early-stage crystal-like morphology. The particle is held within a

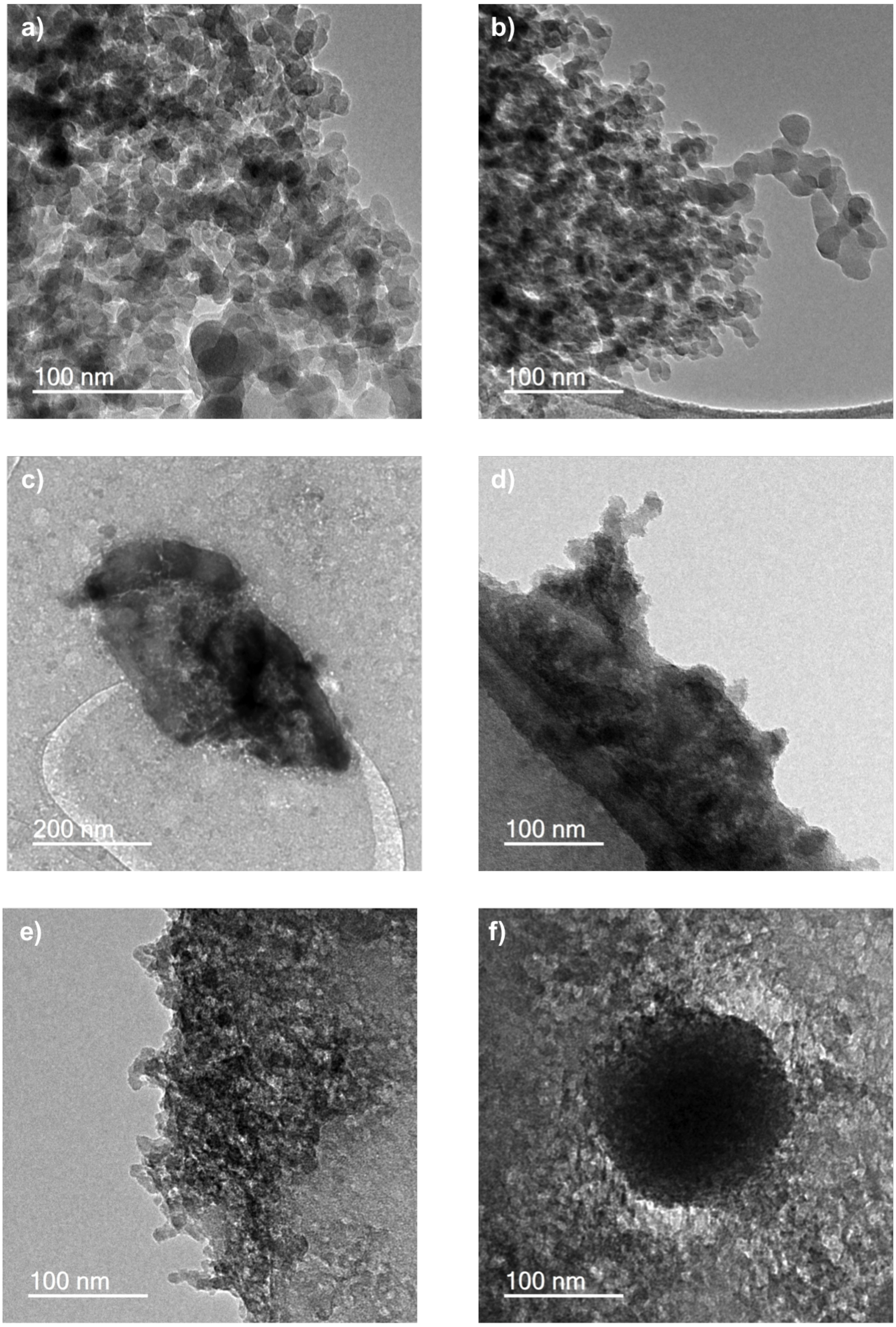

Figure 3.13: TEM images of the time sequence study of the formation of silicalite-1 from fumed silica at 180°C. Images taken of fumed silica (a. & b.) and after 15 (c. & d.) and 30 minutes (e. & f.) of hydrothermal treatment.

network of the smaller particles, and its surface looks to be rough, and formed of these smaller particles, bluring some of the edges with the network particles. This is reminiscent of the crystal growth observed in both TEOS and ludox experiments.

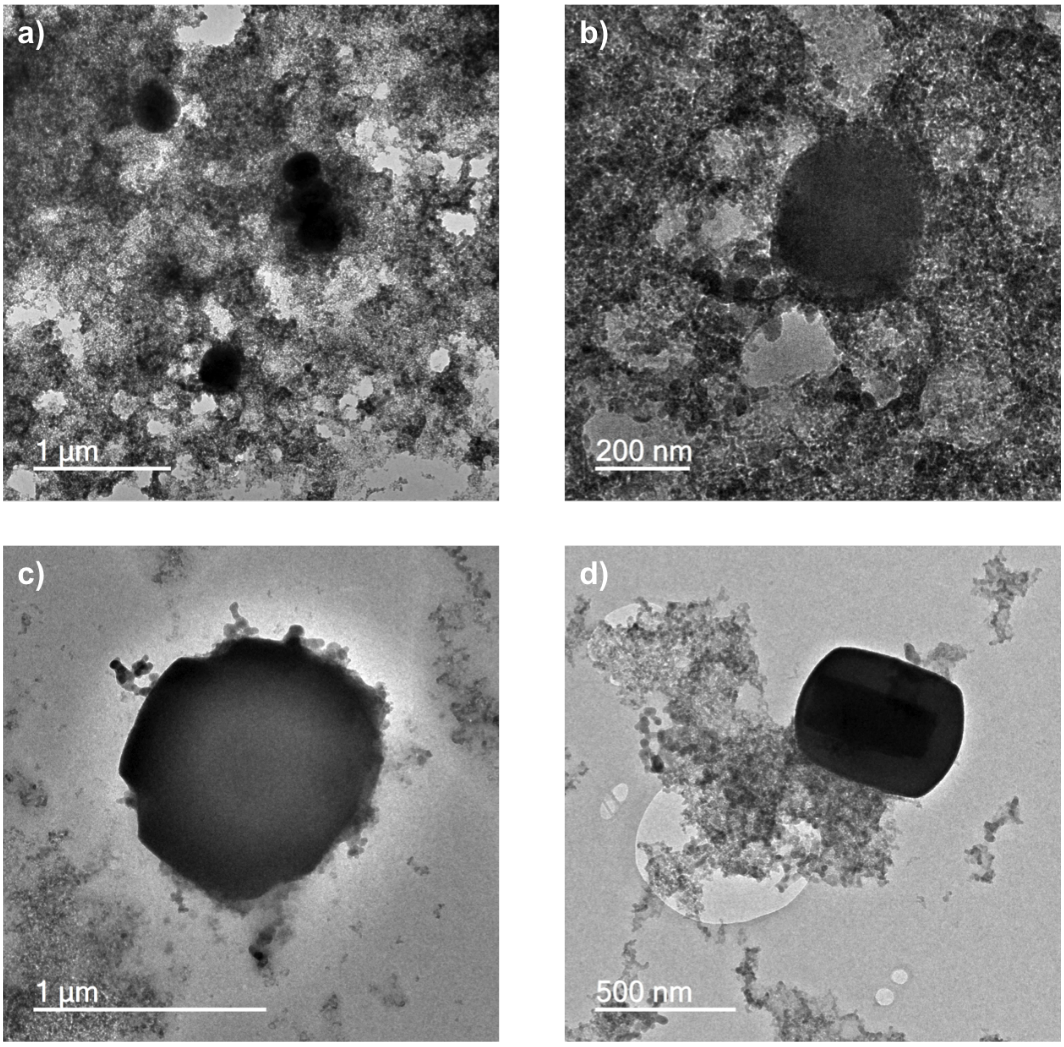

Figure 3.14: TEM images of the time sequence study of the formation of silicalite-1 from fumed silica at 180°C. Images taken after 45 minutes of hydrothermal treatment.

After 45 minutes of hydrothermal treatment (figure 3.14) the presence of relatively large crystal-like particles are observed. These large particles are suspended within a network of smaller particles, which range in size and shape. In figure 3.14 c and d it is possible to see the different size and morphologies of the crystal-like particles found within the system. The particle in 3.14 c is much larger than that seen in d, but it is of a much less well-defined morphology, again this is reminiscent of structures observed when using ludox as a silica precursor (figure 3.10 e).

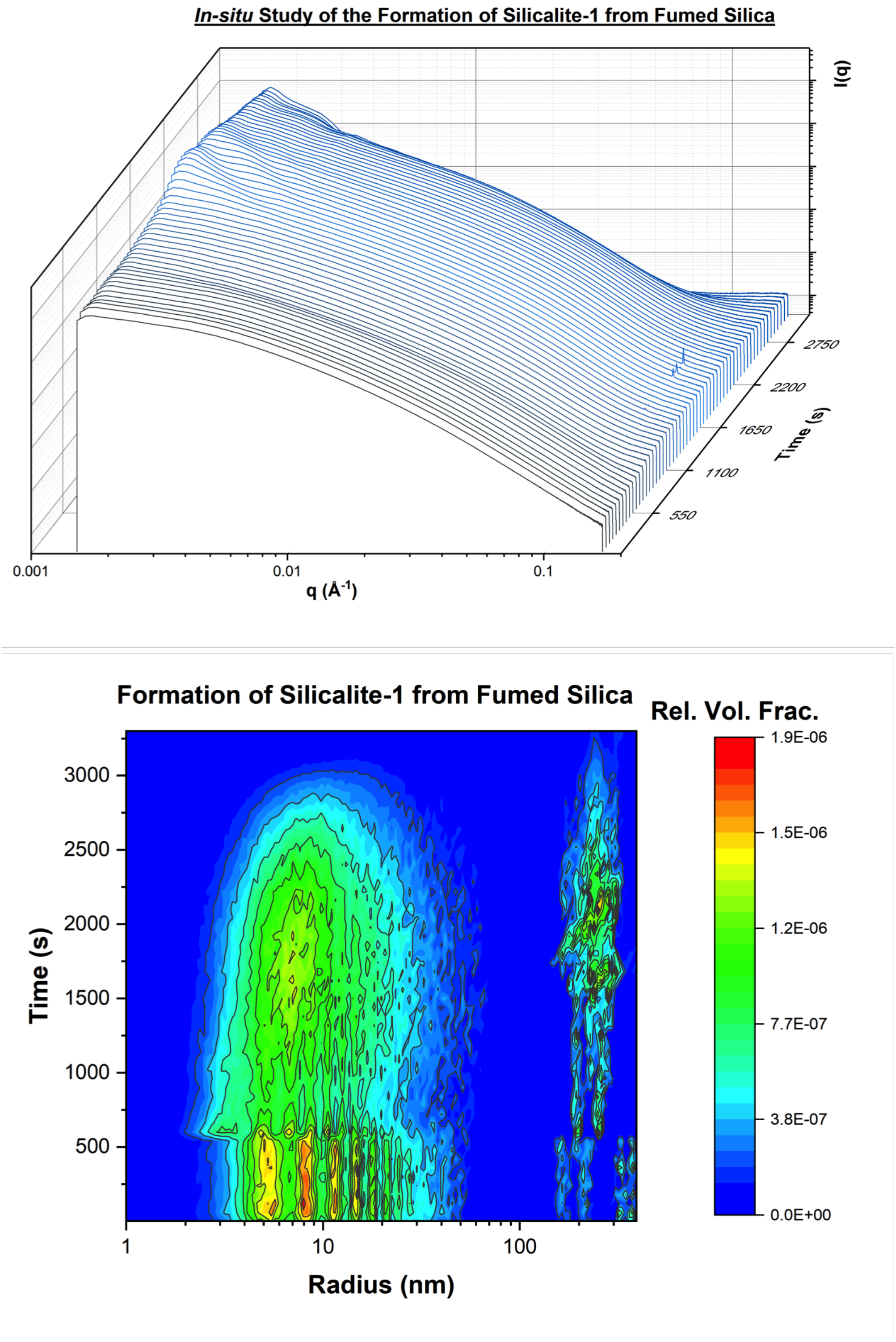

Figure 3.15: *In-situ* SAXS data on the formation of silicalite-1 from fumed silica at 160°C (top), and results from Monte Carlo fitting (bottom).

Time-resolved SAXS data (figure 3.15) gives an overlook at how the reaction proceeds on a much finer time-scale than with *ex-situ* microscopy study. At the start of the experiment, an average particle size of 57.48 nm ± 10 is observed. From fits of the data (see appendix A.3.1) it is possible to see that there is a broad spread of particle diameter observed, with the majority of particles found between 7.8 - 36.4 nm. However, particles as large as 120 nm and as small as 3.8 nm are also observed. There is also a small population of particles $>$ 300 nm, observable from the start of the experiment, which are most likely from the presence of larger clusters of fumed silica particles.

After 10 minutes (600 seconds), the average particle size has not changed greatly (58.5 nm ± 9.98 nm), however the largest population of particles is found to span a slightly smaller distribution of sizes, between 8 - 31 nm, though this population is still very polydisperse with particles ranging from 3.6 - 120 nm. The larger particles are still present but have grown in both number and size (300 - 420 nm). Five minutes later (900 seconds), a change in the shape of the SAXS curve is observed at 0.05 $\AA^{-1}$ (figure 3.15), and the average particle size has decreased to 52.94 nm ± 9.09. It is possible to see that the large polydisperse population of smaller particles has shrunk slightly in terms of particle size distribution. This trend continues over the next five minutes (1200 seconds), however slight changes can be seen in the SAXS data (figure 3.15) at a q value of c.a. 0.1 $\AA^{-1}$, where the data begins to flatten, indicating the presence of particle growth (the hump observed within the SAXS data is propagating toward lower q). Over this period of time, the population of larger particles, which are now 360 - 500 nm in size, is growing in terms of volume fraction, in comparison to that of the decreasing volume fraction seen for the sub 100 nm particles.

After 30 minutes (1800 seconds) of hydrothermal treatment a drastic increase in the average particle size is observed (now 103.8 nm ± 8.3). This is due to the increased population size of the larger particles, which in terms of total volume fraction, has almost doubled over the last 10 minutes of hydrothermal treatment.This is observed alongside, a shift in the distribution of smaller particles, which now encompasses particles $<$ 140 nm, though the majority of particles are observed in the range of 10 - 25 nm. The flattening of the SAXS curve (figure 3.15) tends towards lower values of q, indicating further growth within the system, whilst the observed increase in gradient from 0.003 $\AA^{-1}$ towards lower values of q indicates the presence of much larger particles within the system. This trend is observed over the next 10 minutes (2400 seconds) of hydrothermal treatment, where at this point the population of smaller particles again spans a broader size range then previously observed, encompassing particles $<$ 154 nm, though the majority of particles remain in the range of 9 - 27 nm. Whilst at this time, the larger particles in the system are, in general, $>$ 310 nm in size with the majority of particles falling in the range of 440 - 500 nm.

After 50 minutes (3000 seconds) of hydrothermal treatment, the two populations are of equal size in terms of relative volume fraction, with the smaller particles now encompassing particles $<$ 155 nm, whilst the growing population is made up of particles $>$ 300 nm. The decreasing population has the majority of particles between 9 - 60 nm now, which indicates a net growth in terms of overall particle size within this polydisperse population. After this point in the SAXS data, it can be seen that the population of smaller particles begins to reduce rapidly, with the relative volume fraction decreasing by a factor of 10 over a two minute period. This population continues to decrease until it is almost undetectable after 56 minutes (c.a. 3400 seconds) of hydrothermal synthesis. This decrease in volume fraction comes with the broadening of the distribution of the larger particles present, which can now be said to encompass particles $>$ 200 nm. This is very similar to observation made when using TEOS as a silica source, however the decline in the population of smaller particles here, does not come with a surge in the formation of intermediate sized particles, but a more iterative growth is observed.

The observation made from experiments using fumed silica as a starting material are very reminiscent of the observation made when ludox is utilised. In both SAXS and microscopy studies, evidence for the dissolution of the fumed silica particles is observed, with the roughening of particle surfaces observed with TEM and the observed decrease in overall particle size in the SAXS data. Both TEM and SAXS studies also show little evidence for the formation of intermediate species, with only two distinct particle populations observed within both sets of data. This also provides evidence that crystal growth may occur through aggregative processes, similar to that observed with the ludox experiments. However, the dissolution of the fumed silica particles does not introduce many $<$ 5 nm particles as previously observed. This could be because the fumed silica particles are less porous than the mesoporous ludox particles, meaning that dissolution primarily occurs only at the outer surface of the particles, leading to less dissolution in comparison to that observed when utilising mesoporous ludox particles for the synthesis of silicalite-1. These observations lead to the hypothesis that the formation of silicalite-1 occurs primarily through the aggregation of fumed silica particles:

1. Template (organic) + Fumed Silica
    - Mixing and Aggregation
2. Clusters of template infused Fumed silica particles
    - Further Aggregation and Nucleation
3. Amorphous particles and Zeolite Crystals (150 - 400 nm)
    - Further Crystal Growth
4. Zeolite Crystals

The formation of silicalite-1 from fumed silica is very similar to the path observed with ludox, and partially with TEOS. The presence of intermediate species is not observed in microscopy, and little evidence of their formation is observed within the SAXS data. Though the above path of formation is thought to be the most dominant process, due to the evidence of dissolution processes occurring, other pathways with the formation of intermediate species should not be ruled out.

3.4 Summary

The formation of silicalite-1 was probed using three different silica precursors, to observe the effects that precursor choice can have on these nucleation of zeolites. These studies were performed using complimentary *in-situ* and *ex-situ* techniques. *Ex-situ* microscopy was utilised to provide unique details on the local structure only available from the investigating individual particles, whilst *in-situ* SAXS experiements were able to provide greater in sights on the formation process as a whole, giving representative observations on the average structures found throughout the crystallisation process. All three precursors (TEOS, Ludox and fumed silica) showed similar formation mechanisms that are somewhat intertwined, hence, the proposed routes of crystallisation can be considered branches of the same tree. The use of TEOS led to the observations of a formation mechanism with strong similarities to the model proposed by T. M. Davis *et al.*[59] However, no single route for the crystallisation of silicalite-1 can explain all observations, hence the proposal of secondary, less dominant routes has also been proposed for the formation of silicalite-1 from TEOS. However, this less dominant route of formation observed with TEOS, does incorporate aspects from some of the other proposed mechanisms detailed earlier in this chapter.[65, 66, 67, 68] However, it is also thought that this route describes the most dominant route for crystallisation and growth when utilising either ludox or fumed silica as a precursor. The observation made from these experiments, using three different silica precursors, however does not show evidence for the presence of a single route of formation that is mutually exclusive from the rest. Hence, it is suggested that certain routes can be made more favourable through precursor choice, and potentially through the tailoring of synthesis conditions.[39, 65]

Bibliography

[1] C Baerlocher and L McCusker. Database of Zeolite Structures.

[2] C Baerlocher, W Meier, and D Olson. *Atlas of Zeolite Framework Types*. Elsevier Science Inc., Amsterdam, 5th editio edition, 2001.

[3] B J Schoeman and O Regev. A study of the initial stage in the crystallization of TPA-silicalite-1. *Zeolites*, 17(5-6):447–456, nov 1996.

[4] W Lowenstein. -. *American Mineralogist*, 39:92, 1954.

[5] E Dempsey, G H Kuehl, and D H Olson. Variation of the lattice parameter with aluminum content in synthetic sodium faujasites. Evidence for ordering of the framework ions. *The Journal of Physical Chemistry*, 73(2):387–390, feb 1969.

[6] E Dempsey. Molecular Sieves. *Society of the Chemical Industry*, 1968.

[7] D Vollath. Nanomaterials and Nanocomposites. *Nanomaterials An Introduction to Synthesis, Properties, and Applications*, pages 5–18, 2013.

[8] M A Damour. Sur quelques min{é}raux connus sous Le nom de quartz r{é}sinite. *Annales Des Mines*, 17:202, 1840.

[9] H Eichhorn. -. *Poggendorf Ann. Phys. Chem.*, 105:126, 1858.

[10] G Friedel. -. *Bull. Soc. Fr. Mineral. Cristallogr.*, 19(14):96, 1896.

[11] F Grandjean. -. *Compt. Rendu.*, 149:866, 1909.

[12] O Weigel and E Steinhoff. Adsorption of organic liquid vapors by chabazite. *Zeitschrift für Kristallographie*, 61:125–154, 1925.

[13] R J Leonard. The hydrothermal alteration of certain silicate minerals. *Economic Geology*, 22(1):18–43, jan 1927.

[14] W H Taylor. The structure of analcime. *Zeitschrift für Kristallographie*, 74:1–19, 1930.

[15] J W McBain. The Sorption of Gases and Vapours by Solids. *Angewandte Chemie*, 45(21):365–365, may 1932.

[16] R M Barrer. -. *Journal of the Society of Chemical Industry*, 44:130, 1945.

[17] R M Barrer and D W Riley. Sorptive and molecular-sieve properties of a new zeolitic mineral. *Journal of the Chemical Society (Resumed)*, page 133, 1948.

[18] H Sainte-Claire Deville. -. *Comptes rendus des séances de l'Académie des sciences*, 54:324, 1862.

[19] R M Barrer. Synthesis of a zeolitic mineral with chabazite-like sorptive properties. *Journal of the Chemical Society (Resumed)*, page 127, 1948.

[20] R M Barrer and C Marcilly. Hydrothermal chemistry of silicates. Part XV. Synthesis and nature of some salt-bearing aluminosilicates. *Journal of the Chemical Society A: Inorganic, Physical, Theoretical*, page 2735, 1970.

[21] M Milton. Molecular Sieve Science and Technology. In M Occelli and H Robson, editors, *Zeolite Synthesis*, chapter Chapter 1, page 1. 1989.

[22] R M Milton. U.S. Patent 2.882.244, 1959.

[23] R M Milton. U.S. Patent 2.882.243, 1959.

[24] R M Milton. Molecular Sieves. *Society of Chemical Industry*, page 199, 1968.

[25] H W Kouwenhoven. Molecular Sieves. *Adv. Chem. Ser.*, 121:529, 1973.

[26] I E Maxwell. -. *Inclusion Phenom.*, 4(1):1–29, 1986.

[27] J Weitkamp. Zeolites and catalysis. *Solid State Ionics*, 131(1-2):175–188, jun 2000.

[28] M E Davis. Ordered porous materials for emerging applications. *Nature*, 417(6891):813–21, jun 2002.

[29] W O Haag, R M Lago, and P B Weisz. The active site of acidic aluminosilicate catalysts. *Nature*, 309(5969):589–591, jun 1984.

[30] R J Argauer and G R Landolt. US Patent 3.702,886, 1972.

[31] D Barthomeuf. -. *Materials Chemistry and Physics*, 17:4, 1987.

[32] C D Chang, C Chu, P Perkins, and E Valyocsik. Olefins from methanol and/or dimethyl ether (US4476338 A), 1983.

[33] L B Young, S A Butter, and W Kaeding. -. *Journal of catalysis*, 76:418, 1982.

[34] N R Meshram, S G Hegde, and S B Kulkarni. Active sites on ZSM5 zeolites for toluene disproportionation. *Zeolites*, 6(6):434–438, 1986.

[35] S P Donnelly and J R Green. -. *Oil Gas Journal*, 78(43):77–84, 1980.

[36] B J Schoeman. Analysis of the nucleation and growth of TPA-silicalite-1 at elevated temperatures with the emphasis on colloidal stability. *Microporous and Mesoporous Materials*, 22:9–22, 1998.

[37] V Nikolakis, M Tirrell, M Tsapatsis, and D G Vlachos. Zeolite Growth by Addition of Subcolloidal Particles: Modeling and Experimental Validation. *Chemistry of Materials*, 12(3):845–853, mar 2000.

[38] S P Naik, A S T Chiang, R W Thompson, and F C Huang. Formation of Silicalite-1 Hollow Spheres by the Self-assembly of Nanocrystals. *Chemistry of Materials*, 15(3):787–792, feb 2003.

[39] C S Cundy and P A Cox. The hydrothermal synthesis of zeolites: Precursors, intermediates and reaction mechanism. *Microporous and Mesoporous Materials*, 82(1-2):1–78, jul 2005.

[40] Z Feng, Y Li, D Niu, L Li, W Zhao, H Chen, L Li, J Gao, M Ruan, and J Shi. A facile route to hollow nanospheres of mesoporous silica with tunable size. *Chemical communications (Cambridge, England)*, (23):2629–31, jun 2008.

[41] J F Chen, H M Ding, J X Wang, and L Shao. Preparation and characterization of porous hollow silica nanoparticles for drug delivery application. *Biomaterials*, 25(4):723–727, feb 2004.

[42] L Han, J Yao, D Li, J Ho, X Zhang, C H Kong, Z M Zong, X Y Wei, and H Wang. Hollow zeolite structures formed by crystallization in crosslinked polyacrylamide hydrogels. *Journal of Materials Chemistry*, 18(28):3337, 2008.

[43] J Jiang, J Yao, C Zeng, L Zhang, and N Xu. Preparation of magnetic hollow ZSM-5/Ni composite spheres. *Microporous and Mesoporous Materials*, 112(1-3):450–457, jul 2008.

[44] J Jiang, Y Yang, C Duanmu, Y Xu, L Feng, X Gu, and J Chen. Preparation of hollow ZSM-5 crystals in the presence of polyacrylamide. *Microporous and Mesoporous Materials*, 163:11–20, nov 2012.

[45] H Yang, R I Walton, S Antonijevic, S Wimperis, and A C Hannon. Local order of amorphous zeolite precursors from 29Si{ 1H} CPMAS and 27Al and 23Na MQMAS NMR and evidence for the nature of medium-range order from neutron diffraction. *Journal of Physical Chemistry B*, 108(24):8208–8217, 2004.

[46] R I Walton and D O'Hare. An X-ray absorption fine structure study of amorphous precursors of a gallium silicate zeolite. *Journal of Physics and Chemistry of Solids*, 62(8):1469–1479, 2001.

[47] T Wakihara, S Kohara, G Sankar, S Saito, M Sanchez-Sanchez, A R Overweg, W Fan, M Ogura, and T Okubo. A new approach to the determination of atomic-architecture of amorphous zeolite precursors by high-energy X-ray diffraction technique. *Physical chemistry chemical physics : PCCP*, 8(2):224–227, 2006.

[48] C Pope. Nucleation and growth theory in zeolite synthesis. *Microporous and Mesoporous Materials*, 21(4-6):333–336, 1998.

[49] R M Barrer. *Hydrothermal Chemistry of Zeolites*. Academic Press, London, 1982.

[50] A Giaya and R W Thompson. Recovering the Crystal Size Distribution from the Moment Equations. *AIChE Journal*, 50(4):879–882, 2004.

[51] T Brar, P France, and P G Smirniotis. Control of Crystal Size and Distribution of Zeolite A. *Industrial & Engineering Chemistry Research*, 40(4):1133–1139, 2001.

[52] R W Thompson and A Dyer. Mathematical analyses of zeolite crystallization. *Zeolites*, 5(4):202–210, 1985.

[53] J Warzywoda, R D Edelman, and R W Thompson. Crystallization of high-silica ZSM-5 in the presence of seeds, 1991.

[54] Z Kajcsos, L Liszkay, G Duplatre, L Varga, L Lohonyai, C Kosanovic, S Bosnar, B Subotic, K Lzr, D Bosnar, K Havancsk, and P M Gordo. Critical parameters of positron and positronium annihilation in grainy and porous solids: Ionic crystals and zeolites. *physica status solidi (c)*, 6(11):2540–2545, 2009.

[55] S Mintova and V Valtchev. Effect of the silica source on the formation of nanosized silicalite-1 : An in situ dynamic light scattering study. *Microporous and Mesoporous Materials*, 55:171–179, 2002.

[56] T Wakihara and T Okubo. Hydrothermal Synthesis and Characterization of Zeolites, 2005.

[57] R K Iler. *The Chemistry of Silica: solubility, polymerization, colloid and surface properties and biochemistry*. Wiley, New York, 1979.

[58] J M Fedeyko, J D Rimer, R F Lobo, and D G Vlachos. Spontaneous Formation of Silica Nanoparticles in Basic Solutions of Small Tetraalkylammonium Cations. *J. Phys. Chem. B*, 108:12271–12275, 2004.

[59] T M Davis, T O Drews, H Ramanan, C He, J Dong, H Schnablegger, M A Katsoulakis, E Kokkoli, A V McCormick, R L Penn, and M Tsapatsis. Mechanis-

tic principles of nanoparticle evolution to zeolite crystals. *Nature materials*, 5(5):400–8, may 2006.

[60] S Kumar, T M Davis, H Ramanan, R L Penn, and M Tsapatsis. Aggregative growth of silicalite-1. *The Journal of Physical Chemistry. B*, 111(13):3398–403, apr 2007.

[61] J D Rimer, D G Vlachos, and R F Lobo. Evolution of self-assembled silica-tetrapropylammonium nanoparticles at elevated temperatures. *The journal of physical chemistry. B*, 109(26):12762–71, jul 2005.

[62] M E Davis. *Zeolites: A Refined Tool for Designing Catalytic Sites*. Elsevier, Amsterdam, 1995.

[63] A Aerts, M Haouas, T P Caremans, L R A Follens, T S van Erp, F Taulelle, J Vermant, J A Martens, and C E A Kirschhock. Investigation of the mechanism of colloidal silicalite-1 crystallization by using DLS, SAXS, and 29Si NMR spectroscopy. *Chemistry (Weinheim an der Bergstrasse, Germany)*, 16(9):2764–74, mar 2010.

[64] A Persson, B Schoeman, J Sterte, and J Otterstedt. -. *Zeolites*, (14):141, 1999.

[65] J Grand, H Awala, and S Mintova. Mechanism of zeolites crystal growth: new findings and open questions. *CrystEngComm*, 18(5):650–664, 2016.

[66] S L Burkett and M E Davis. Mechanism of Structure Direction in the Synthesis of Si-ZSM-5 : An Investigation by. *J. Phys. Chem.*, 98:4647–4653, 1994.

[67] S Mintova, N H Olson, V Valtchev, and T Bein. Mechanism of Zeolite A Nanocrystal Growth from Colloids at Room Temperature. *Science*, 283(5405):958–960, 1999.

[68] S Mintova, N H Olson, and T Bein. Electron Microscopy Reveals the Nucleation Mechanism of Zeolite Y from Precursor Colloids **. *Angew. Chem. Int. Ed.*, 38(21):3201–3204, 1999.

[69] I Bressler, B R Pauw, and A F Thuenemann. McSAS: Software for the retrieval of model parameter distributions from scattering patterns. *Journal of Applied Crystallography*, 48:962–969, 2015.

[70] J M Fedeyko, D G Vlachos, and R F Lobo. Formation and Structure of Self-Assembled Silica Nanoparticles in Basic Solutions of Organic and Inorganic Cations. *Langmuir*, (16):5197–5206, 2005.

Chapter 4

Synthesis of Hierarchical Zeolites

4.1 Introduction

Hierarchical structures can be found in nature, where they are most commonly deployed in structural application, in materials such as bone and those found in the stems of trees. Hierarchical structures are also common in fluid transport applications within nature where, for example, the structures found within the lungs of many animals can be considered hierarchical.[1, 2] Multimodal porous structures are found within these structures as they are able to maximise the efficiency of transport processes, a function that has provided good evidence of the efficiency of these structures in transport applications for them to gain a great deal of interest from their adaptation into a multitude of industrial applications in watering systems and catalysis.[3, 4, 5]

Zeolites are well-known catalytic materials, with large surface areas and sieve like properties. In industrial applications such as catalysis, the efficiency of zeolites tends to be limited by the slow transport of reactive species throughout the zeolites microporous structure. One way of minimising transport limitation, is the use of nano-sized zeolite materials, which can reduce diffusion paths significantly, however, in practice the use of nano-sized zeolites has shown to have a few drawbacks. For example, the mesoporosity seen with nano-sized zeolite structures is primarily intercrystalline, some structures have also been shown to have poor thermal and hydrothermal stability, whilst the use of nano-sized zeolites also means that catalyst recovery becomes much more difficult.[6] An alternative to the use of nano-sized zeolites for minimising diffusion paths is the introduction of meso- and/or macropores into zeolitic materials, as multimodal pore systems have the ability to mimic similar structural properties seen with nano-sized zeolites.[7, 8, 9, 10] In general, it is thought that the use of macroporous zeolites could diminish transport limitations to a greater effect than the introduction of mesopores, whilst also introducing an increased resistance to coking, and therefore the effective catalytic lifetime of the material.[11]

4.2 Synthesis of Hierarchical Zeolites

There is a plethora of different methods for introducing secondary porosity into zeolites, with new methods and new variations being developed constantly.[7, 11] In general, these introduction of secondary porosity into zeolites can be split into two main groups, bottom-up synthesis and top-down methods. With bottom-up methods, pores are incorporated into the growing zeolite structure through the addition of templates in synthesis gels. These pore templates can then be removed form the final zeolite structure leaving voids behind. Top-down approaches take synthesised zeolite structures and introduce secondary porosity into these crystals through a variety of post-synthesis treatments.

4.2.1 Removal of Framework Components

The removal of framework components is one of the most common top-down approaches for the synthesis of hierarchical zeolites. This methodology encompasses three different methods for introducing mesoporosity into zeolite structures through the removal of T-atoms with varying degrees of control. However, these methodologies are hindered by the the significant drawback of large loss of zeolitic mass.

4.2.1.1 Dealumination

The dealumination of zeolites is a well-known, post-synthesis treatment originally utilised to increase Si/Al ratios in zeolite systems where this was not possible directly from synthesis control, for example, creating high Si/Al ratio faujasite.[12, 13] The dealumination of zeolites can be *via* using a variety of different methods, however these different methodologies can be grouped in to two broad groups; those that utilise chemical agents (e.g. acid leaching) and those that use hydrothermal treatments (e.g. high temperature steaming). With both methods, the extraction of aluminium T-atoms from the zeolite structure creates vacancies, which add to the materials overall porosity. However, this method can also lead to partial collapses of the zeolite structure and can also have consequences on the materials acidity.[14]

In 1993, Sulikowski utilised ethylenediaminetetraacetic acid (EDTA) to leach aluminium T-atoms from zeolite Na-Y under reflux at 800°C.[15] This method resulted in the removal of aluminium from the external surface of the zeolite structure, in-turn creating a heterogeneous distribution of aluminium within the crystals. The use of acid in the dealumination of zeolites would soon evolve into the multi-step process made famous by Van Oers in 2009.[16] In this process, Van Oers aged zeolite Beta nanoparticles at 140°C within an aqueous solution containing both TEAOH and HCl. This solution was then quenched before being acidified further with 12 M HCl and then subsequently subjected to hydrothermal conditions for 72 hours. Through this study it was shown that the rate at which the aged solution is quenched can have a significant impact upon the resulting properties of the zeolite crystals. For example, if the solution is cooled slowly higher crystallinity was observed in comparison to those that were crash cooled. It was also discovered that crash cooling negatively impacts the overall microporosity of the zeolite, but facilitated the creation of 10 nm mesopores within the crystal structure, where as with slower cooling regimes, smaller 6 nm pores were discovered.

Another route for the dealumination is through steaming, a method originally applied to the dealumination of zeolite-Y.[17] This process starts by first substituting Na^+ ions with NH_4^+ ions and then subsequently steaming the zeolite at high temperatures (600 - 800°C). The steaming process induces the hydrolysis of Al-O-Si bonds, causing Al atoms to be expelled from the framework, leaving vacancies behind in the structure. This process does however cause partial amorphisation of the zeolite structure. Some of the vacancies are thought to be filled by Si atoms supplied by amorphised materials, whilst others vacancies are thought to grow into larger mesopores.[18] It is also thought that if the formation of mesopores occurs in a significant concentration, channels can be formed through coalescence of pores.[19] The initial steam treatment of zeolites is often followed by a mild acid leaching process to remove excess aluminium species that have been deposited as extra-framework aluminium species on the external and internal surfaces of the crystals, and it is this process that opens up the internal and external surface of the zeolite crystals.[20]

It has been shown that the dealumination of zeolites thought steam treatment at temperatures above 750°C can also increase a zeolites hydrophobicity, when framework aluminium is first extracted it is subsequently morphed into Al-O-Si species and not alumina (Al_2O_3).[21] The steam treatment of zeolites is also known to cause desilication. Malola, showed this computationally, using DFT calculation to simulate the steaming process on the chabazite structures.[22] This study did, however show that the dealumination process is more favourable than desilication, with calculated energy barriers of 190 and 240 kj mol^{-1} respectively. Electron microscopy studies also showed another drawback to the steaming of zeolites.[23, 24] These studies showed that the creation of mesopores through steam treatment did not create an interconnecting network of pores, meaning that the observed intracrystalline diffusion rates between treated and untreated samples showed little to no difference.

4.2.1.2 Desilication

Desilication is a very common method for creating secondary porosity into zeolitic systems. This method utilises alkaline environments to selectively remove silicon from zeolite structures. An advantage to using this method is that it is possible to retain a zeolites acidic properties, whilst incorporating mesoporosity into the structure.

The first alkaline desilication treatment on a zeolite was performed by Ogura in 2000. By treating ZSM-5 with an NaOH, it was observed that the materials overall crystallinity was retained, whilst its mesopore volume increase by nearly 400

Suzuki and Okuhara completed similar experiments to those of Ogura *et al.* however, lower concentrations of NaOH were utilised (0.05 M) for the creation of smaller super-micropores (c.a. 1.8 nm) instead of the creation of the larger mesopores (c.a. 4 nm) seen in Ogura's work.[25] It was also later shown through the use of ^{27}Al NMR studies that the amount of dealumination occurring during the desilication process is actually very low/negligible.[26]

In 2004, it was discovered that the Si/Al atomic ratio can play an important role in desilication through alkaline treatment. Groen studied the desilication of ZSM-5 samples with varying Si/Al atomic ratios, and it was discovered that after alkaline treatment the Si/Al ratios for all samples increased confirming that Si was preferentially removed using this method.[27] It was discovered that for lower Si/Al atomic ratios (< 25) that the presence of greater quantities of Al, had adverse effects upon the removal of silica and, hence, the observed mesoporosity from such samples was much lower than those seen in samples with higher Si/Al atomic ratios. It was also shown that for samples with high Si/Al atomic ratios (> 50) the dissolution of silica is much less controlled, leading to the development of larger pores and lower overall mesoporosity.[27] Groen also showed that no additional framework aluminium was present in these samples through the use of FTIR and ^{27}Al NMR, alongside results from NH_3 TPD measurements showing that the treated materials acidity had been preserved. This is however, a somewhat controversial topic as other authors have reported reductions in Brønsted acidity with alkali treated samples.[28, 29]

Predominantly, the focus of alkaline treatment studies have focused on ZSM-5, however this method can also been applied to many other zeolite structures (MOR, CHA, FAU, BEA, FER and many more).[30, 31, 32, 33, 34] Due to this methods diversity, desilication is generally considered a highly versatile technique for the introducing mesoporosity into zeolites. However, alkaline treatment does not always induce the similar mesoporous characteristics in every zeolite systems. For example, Beta zeolites lower framework aluminium stability (in comparison to ZSM-5) results in an higher removal of silicon, resulting in greater mesoporosity at the expense of microporosity, crystallinity and acidity.[33] For zeolites such as ZSM-22 and ferrierite, which generally possess smaller crystal sizes (< 100 nm) as well as needle-like and platelet crystal morphologies, much lower mesopore volumes are observed post treatment. The crystal size and morphology of these structure are ascribed to cause these observations, whilst the observed mesoporosity is attributed to be intercrystalline rather than intracrystalline mesoporosity.[35]

Studies have shown that when zeolite-Y, which possess a Si/Al ratio between 2.4 - 3.1, is subjected to alkaline treatment only low mesoporosity is observed in the resulting product (< 65 m^2 g^{-1}).[36] For zeolite-USY (Si/Al ratio = 2.6) standard desilication processes yield little improvements in mesoporosity (< 50 m^2 g^{-1}), however if USY zeolite is dealuminated prior to undergoing alkaline treatment, a large mesoporous surface area increase is observed (c.a. 275 m^2 g^{-1}).[35] However, this large increase comes at the high cost of losing nearly 60% of the materials micropore volume and large reductions in the overall crystallinity of the product, indicative of the occurrence of amorphization. It has been proposed that the differences seen between these two systems and ZSM-5 can be explained by the presence of twelve membered rings, which are more easily desilicated than the ten membered rings found in systems such as ZSM-5.

These discoveries have lead to the development of an ”accessibility index” that can be utilised for comparing hierarchical zeolites.[37] The index primarily uses FTIR spectrography to determine and quantify the accessibility of enhanced acid sites within hierarchical zeolites. The accessibility index is defined by the ratio between the number of Brønsted acid sites, found in the parent zeolite, and that of the desilicated samples, where the values are determined from through FTIR measurements obtained after the adsorption of substituted alkylpyridines (pyridine, 2, 6-lutidine and 2, 4, 6-collidine). Due to the different sizes of the substituted alkylpyridines (0.57, 0.57 and 0.74 nm respectfully) they have access to different acid sites, hence the accessibility index increases with accessible mesoporous surface area.

In general, the desilication and the introduction of mesoporosity using standard alkaline treatment methods comes at the high cost of microporosity, which is a very undesirable side-effect. Hence, there has been a great deal of interest in maximising mesoporosity, whilst minimizing loss of microporosity. The substitution of NaOH with organic bases, such as TPAOH and TBAOH, have been studied in the desilication of ZSM-5. The use of these organic bases reduced desilication rates, leading to lower mesoporosity, and the formation of smaller mesopores than those seen when using NaOH, however this comes with much less of an effect to the materials micropore volume (a 20% loss instead of the 50% loss observed with NaOH).[38, 35]

This new knowledge paved the way for the development of ”pore growth moderators.”[39] The use of organic and inorganic bases together for desilication lead to an element of control, with respect to mesopore size, through the regulation of the organic/inorganic ratios of bases used in the alkaline treatment of zeolites. For example, if the concentration of OH^- is kept constant and the TPA^+/OH ratio is altered between zero and 0.4, pore size can be tuned between 10 nm and 4 nm respectively. Hence, the use of tetraalkylammonium cations is said to be highly effective in tuning the development of mesoporosity of zeolites when deployed as pore growth moderators in desilication processes, as they are effective in controlling mesopore growth, and in-turn preserving the microporosity present in the parent zeolites.[39]

4.2.1.3 Irradiation

Developed initially by Valtchev in 2011, the irradiation of zeolite crystals with heavy ions for the formation of oriented meso-/macropores has proven to be a novel, top-down approach for introducing hierarchical porosity into zeolites.[40] In this process, zeolite crystals are exposed to swift heavy ions (e.g. ^{238}U) which possess energies in the hundreds of MeV, and masses above 100. During this process an irreversible material transformation occurs along each projectile path, creating a region of damaged material which is termed the ”latent track” or ”nuclear track.” These tracks are cylindrical in shape, with pore dimension ranging from a few nanometers to a few tens of nanometers in diameter. The size of the pore openings can be increased depending upon the energy and mass of the projectiles used in the irradiation process. After this initial processing with swift heavy ions, the material is then treated with HF acid before then being washed with water. The process has been shown to successfully introduce uniformly sized, parallel arrays of 50 nm macropores into ZSM-5 crystals.[40] In comparison to other top-down methodologies for the creation of hierarchical zeolites, this method facilitates a remarkable amount control. As it is possible to create parallel arrays of meso-/macropores within the zeolite crystals, the resultant hierarchical structures showed little to no change in their crystallinity or their microporosity. However, the formation of hierarchical zeolites through irradiation has its own drawbacks especially with the techniques accessibility and reliance on the use of heavy ions such as ^{238}U.

4.2.2 Surfactant-Assisted Recrystallisation

It has been shown that mesoporosity can be incorporated into zeolite structures with the use of cation surfactants such as cetyltrimethylammonium bromide (CTAB) under mild synthesis conditions. The use of mild synthesis conditions facilitates the recrystallization of microporous zeolites to micro-, mesoporous zeolites. In this method, dissolution processes are avoided due to surfactant-zeolite interactions, allowing for the reorganization of the zeolitic network around surfactant micelles.[8, 41] The mechanism of the recrystallisation process has been probed using XRD, MAS-NMR and TGA, and it has been proposed that Si-O-Si bonds are initially broken within the alkaline environment (provided under general the zeolite synthesis), and during this desilication process, and larger inter- and intracrystalline pores begin to form.[42] The surfactant molecules involved can diffuse into these areas, and ion exchange can occur, which in-turn aids in the formation of the micelles. After this agglomeration of silica around the micelles occurs, encapsulating them and creating a single-phase zeolite with bimodal porous structure.[43] In general, this method of mesopore formation is relatively less destructive to the micropore structure of the material than desilication methodologies.[7]

4.2.3 Dual-Templating

One of the most commonly used methods for the formation of hierarchical structures is dual-templating. It is a common syntheses method utilised for the formation of materials such as MCM-41, which posses long-range ordering of hexagonal arrangements of mesopores within its structure. Dual-templating, in general utilises different surfactants that are capable of forming micelle structures within aqueous solutions alongside zeolite templating agents. The surfactant micelles act as templates for mesopores (as seen with the surfactant-assisted recrystallisation methods), whilst the zeolite template agent acts as the template for micropores. These templates work in tandem to form hierarchical structures, however initial studies utilising this approach showed that having both templates present within the starting reaction mixture lead to the segregation of phases, resulting in the formation of either zeolites, mesoporous silica materials or their physical mixtures.[44]

To combat the formation of these less desirable products, dual templating and initiating growth with the introduction of zeolite seeds to the synthesis mixture has been explored with more positive results.[45] This methodology proved successful in introducing mesoporosity into aluminosilicate zeolites, which showed both increased stability and catalytic activities in comparison to their conventionally synthesised zeolites counterparts.[45, 46, 47]

The use of organic ammonium salts has also been explored. The organic ammonium salts can act as structure-directing agents for both the zeolite structure and that of the mesoporosity through the introduction use of cationic polymers.[48] This method has been utilised to create hierarchical Beta zeolite with the use of polydiallyldimethyammonium chloride as a cationic polymer. Similar studies have also shown how the use of cationic polymers can dictate mesopore size, and how altering the amounts of polymer can provide some form of pore control, where adding large amounts of polymer can facilitate the introduction of larger pores into the materials on macro-scale.[49] However, drawbacks to this methodology are that, in general, lower crystallinity products are obtained, as well as some multiphase products.

4.2.4 Zeolitization

The zeolitization of meso-/macro-porous materials is another method for synthesising hierarchical zeolites. The methods used for the conversion of preformed solids was first presented by Xu in the 1990s, with the steaming aluminosilcate dry gels.[50] This ultimately resulted in the development of the alternative, non-conventional, hydrothermal synthesis methods known as vapour phase transport (VPT) and steam-assisted conversion (SAC):

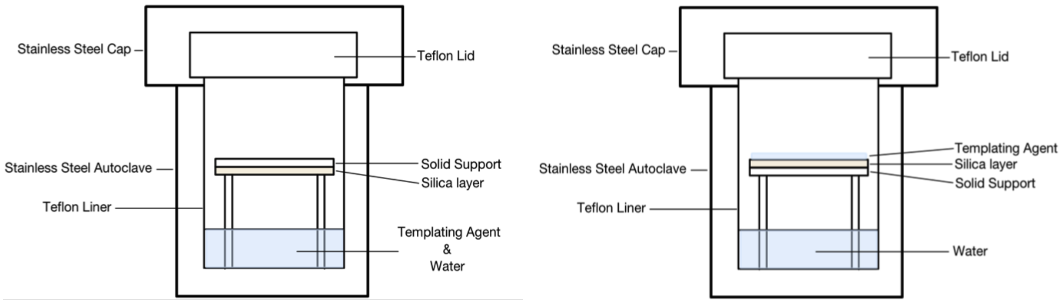

Figure 4.1: Schematic diagrams of autoclaves set up for the conversion of silica thin films (supported on alumina substrates) to zeolites using VPT (left) and SAC (right) hydrothermal methods.

1. VPT is where the templating agent is not contained within the gel, or when converting a thin film the substrate is not in direct contact with the templating agent. In the case of zeolites, the template is mixed with water and placed below the ”gel” or thin film and upon heating, the template is transported to the nutrient source, within steam vapours, where the conversion of amorphous silica to crystalline zeolitic solid can begin.[50]

2. The SAC methodology has the templating agent and the silica nutrient source in directly contact. Here, only the water is vaporised and the steaming of the nutrient source/template mix results in the formation of zeolitic solids.[51]

The development of these methodologies presented many advantages in the world of zeolite synthesis. Firstly, it was thought that zeolitic materials with the same SiO_2/M_xO_y ratios within the precursor gels could be obtained. Another advantage is the consumption of expensive templating agents could be minimised, and the fact that crystallisation time was reduced are all very favourable characteristics. Both, SAC and VPT, methodologies have been applied to the synthesis of hierarchical zeolites, where nanoparticle silicas, meso-structured solids, dry gels and macroscopic hierarchical amorphous solids have all been utilised.[52, 53, 54, 55]

In 2011, SAC methodologies were utilised by Moller in synthesising hierarchical zeolite Beta.[54] Moller utilised concentrated zeolite precursor gels, so that the large numbers of individual nuclei would be formed initially, which would then crystallise to form zeolite Beta nanocrystals. These nanocrystals would then aggregate, creating a intercrystalline mesoporous network. The resulting nanocrystals synthesised in this study were roughly 20 nm in size, with BET surface areas up to 730 m^2 g^{-1}. This surface area, was said to have high contributions from the mesoporous network created through the utilisation of the SAC methodology. The mesopores found between crystals were reported as having diameters of 13 nm, and it was discovered that the amount of water used in the SAC synthesis could be altered to speed up the formation of the zeolitic solid to have obtain full crystallinity in only a few hours.

The use of VPT and SAC methodologies for zeolitization can also be applied with the hard-templating of zeolites, if the hard template being used is made up of materials appropriate for conversion to zeolite (generally silica or aluminosilicas). For example, Li used SAC methodologies to convert silica nanospheres to create microspheres of MFI zeolite, which possessed both meso- and microporosity.[52] Yue, utilized zeolitization methods for the conversion of MCM-41 materials (both silicate and aluminosilicates) by ageing the material in a solution of TAPOH and ethanol. This resulting mixture was subsequently dried then the subjected to hydrothermal conditions using a SAC methodology to form hierarchical zeolites. It was found that with longer hydrothermal treatment zeolite crystallinity increased, however the mesoporous structure found within the MCM-41 materials was increasingly damaged over time, meaning that the mesoporous structure was not well preserved when highly crystalline samples were produced.

VPT methodologies have been utilised to synthesise silicalite-1 from seeded Diatomite.[56] The seeds in this synthetic approach are used to induce the zeolitization process. This study showed that after 10 days of VPT treatment around half of the starting material had been converted to silicalite-1, with a morphology resembling that of the Diatomite, and possessing macropores.

Silica and Aluminosilica monoliths prepared *via* hydrolysing tetramethoxysiline have also been subjected to zeolitization.[57] This is done within a solution containing soluble polymers to induce phase separation during the polymerization of silica. The resulting silica gel is then mixed with zeolite precursors and subjected to hydrothermal condition using SAC methodologies.[58] The silica gels created from the polymerization step have a web-like morphology, consisting of strands of silica that interconnect to create a network of macropores throughout its structure. The zeolitization of these structures has been successful in producing hierarchical zeolites with BEA and MFI frameworks, with the preservation of the web-like morphology inherited in the precursor monoliths.[55, 58, 57] Alongside the micropores (from the zeolite structure) and the bicontinuous macropores (from the precursor monolith structure), mesopores are also formed. These are introduced into the material as voids that are formed between growing zeolite nanocrystals. This trimodal porosity gives these materials very large surface areas, however, it has been shown that zeolitized structures tend to show lower acidity in comparison to their non-hierarchical, conventionally synthesised counterparts, indicating that the monolith structures used in zeolitazation process may not be completely converted to zeolite.[57, 58]

4.2.5 Hard-Templating

Hard-templating is a bottom-up approach to synthesising hierarchical zeolites, where porous, hollow or even solid materials are used as scaffolds for pores and/or the growth of inorganic solids. This methodology for creating hierarchical zeolites begins by mixing the hard template with the zeolite precursors, the resulting solution is then subjected to the conventional hydrothermal conditions used for the fabrication of zeolites. The resulting mixture of zeolitic solid and embedded hard templates is then calcined at high temperatures to remove the hard template, leaving behind hierarchical zeolite structures. Alternatively, depending on the hard template used, dissolution processes can also be utilised to remove the template, again leaving behind a hierarchical zeolite structure.

An example of herd-templating is the use of small amorphous carbon nanoparticles or polystyrene spheres dispersed within a zeolite synthesis gel. During the synthesis/crystallisation process the carbon particles become trapped and incorporated within the zeolite structure. These particles are then removed upon calcination, along with the templating agent used to form the micropores within the zeolite structure. The removal of the carbon hard-template leaves behind voids that possess the same morphology as that of the carbon particles within the zeolite structure.[59] However, this methodology has only been successfully adapted to produce hierarchical zeolites with MFI structures, and it has been suggested to only be successful with MFI structures due to their high structural stability, and tolerance for impurities during crystallisation.[60, 61, 62, 63]

Another method for hard-templating involves synthesising zeolites within the voids of a porous carbon materials, effectively infusing the hard-template with zeolite before it is subsequently burned away.[64] This is formally known as a confined-space synthetic strategy, where the continuous carbon phase that is utilised as a scaffold for the growth of the hierarchical zeolites, is generally synthesised through the use of other templating methods such as surfactant micelles, that create the initial porosity within the carbon scaffolds that is exploited for the growth of hierarchical zeolites. For example, porous carbon based materials (e.g.g Black Pearls 700 and 2000) have been used as hard templates for the synthesis of hierarchical zeolites.[61, 62, 64, 63] With this synthetic approach, the zeolite precursors and the porous carbon scaffolds are mixed together and aged at room temperature before they are steamed under hydrothermal conditions at 180°C. The crystalline product is then washed with ethanol and water, before the scaffolds are removed through combustion by calcining samples at 550°C. The resulting products contained highly crystalline nano-sized zeolite and BET results have shown the presence of mesopres, which have been ascribed to the intercrystalline spacings from the packing of the zeolite crystals.[60] This confined-space synthetic strategy has been successful used to synthesise a broader range of zeolite structures (MFI, LTA, FAU, BEA, CHA and LTL).[59, 61, 62, 64, 63, 65]

Use of carbon nanotubes and nanofibers as hard templates for the generation of mesopores in zeolite systems has also been explored.[66, 67] Again, the carbon templates are utilised to induce intraparticle mesoporosity, similar to that seen with the confined-space synthetic strategies. Hence, is is essential for the nucleation of the zeolitic material to occur between the voids in the carbon templating agent. To make this happen, sequential impregnation of the individual components of the precursor gel in needed. It has been shown that the use of carbon nanotubes and nanofibres creates cylindrical mesopore formation, with lower porosity in comparison to the mesopores formed through the use of carbon black.[67]

Mesoporous carbons with highly ordered pore structures have been utilised as hard-templates. The use of mesoporous carbons is very desirable for the formation of pores in the final zeolite, due to the simplicity of their removal from the final product. The hierarchical zeolites obtained through the used of mesoporous carbon templates, generally, exhibit more regularity in mesopore distribution, with smaller sized crystals than those templated using commercially available carbons. Another advantage is that the final zeolitic product's mesoporosity can be tailored, through the tuning of synthesis paramaters for the production of the mesoporous carbon scaffolds.[68] The use of mesoporous carbon temples, however, has its drawback, especially when it comes to cost and time of preparation. Hence, research has begun on trying to make the synthesis of these materials cheaper through using alternate, less expensive carbon source such as carbohydrates and sugars.[69, 70]

Carbon templates have also been used to introduce macropores into zeolite crystals. Carbon based aerogel monoliths, carbonized rice husks and pyrolysed wood have all been utilised successfully.[71, 59, 72, 73, 74]

4.2.6 Direct-Synthesis

The direct-synthesis of hierarchical zeolite structures has proven to be one of the more difficult routes, due to the lack of simple accessible methods for introduction of macropores into crystalline zeolite structures without the use of macropore templates. However, synthesis of stacked structures, aka "house-of-cards" structures, have been possible without the use of templates. These structures are formed through the creation of MFI nanosheet structures, with twinned crystals. The twinned crystal intergrowths appear at 90° angles to the nanosheet allowing for the sheets to be stacked, whilst incorporating mesoporosity between nanosheets.[75] This unique method for introducing mesoporosity has been seen with MFI zeolites, due to the orthogonal intergrowths of MFI crystals, which is induced by the higher symmetry framework segments found at the twin bondaries. The house-of-cards approach is relatively simple and effective for creating mesoporosity but is limited to only few zeolite frameworks due to its reliance on the repetitive rotation of intergrowths. The house-of-cards structural approach has also been successfully applied to FAU and EMT zeolite stuctures.[76]

The utilization of macroporous zeolites, where macropores are embedded within the structure itself, has been limited in industrial application due to the lack of simple direct methods for the formation of macropores within material structures. Some most common methods for the introduction of macropores into zeolite structures include the use of sacrificial templates, post-synthesis modifications and the zeolitization of amorphous macroporous structures. However, the drawback to many of these methods is the introduction of complex multi-step processes. This chapter presents a simple method for the direct synthesis of hierarchical silicalite-1 using conventional hydrothermal methods. The formation of the resulting hierarchical zeolites is explored using *in-situ* SAXS and *ex-situ* microscopy studies. *Ex-situ* microscopy will provide a unique insight to the system at certain points in the formation these hierarchical structures, whilst *in-situ* SAXS measurement will provide a fuller picture of the system as a whole, making it is possible to see multiple population of particles, whilst being able to simultaneously see their growth and decline in reference to one another.

4.3 Experimental

Macroporous silicalite-1 samples were prepared using 500 nm silica spheres, tetrapropylammonium hydroxide (TPAOH) and water, which were mixed together for 20 minutes prior to being subjected to hydrothermal conditions. The synthesis ”gels” were produced in a 25:8:590 SiO_2:TPA+:H_2O molar ratio. *Ex-situ* samples for microscopy studies were prepared using stainless-steel autoclaves at 180°C, whilst *in-situ* samples were prepared within the UCL hydrothermal *in-situ* cell at 160°C. The *in-situ* cell was equipped with a 2 mm pathlength and sealed using two, 50 μm mica windows. *In-situ* SAXS experiments were performed at both Diamond light source beamline I22 and at the ESRF beamline BM26b. At I22, data was recorded at 12.4 keV, using a Pilatus3 2M detector with a sample-to-detector distance of 9.44 m. At BM26b, data was recorded at 14 keV using a Pilatus2 2M detector with a sample-to-detector distance of 0.9 m. Data reduction was performed using the DAWN software package provided by Diamond Light Source and data analysis was performed using McSAS software package.[77] TEM images were taken using a Jeol 2100 HRTEM with a LaB6 source operating at an acceleration voltage of 200 kv, whilst SEM images were obtained using a Jeol 7401 high resolution Field Emission Scanning Electron Microscope at the Department of Chemistry, University College London.

4.4 Results and Discussions

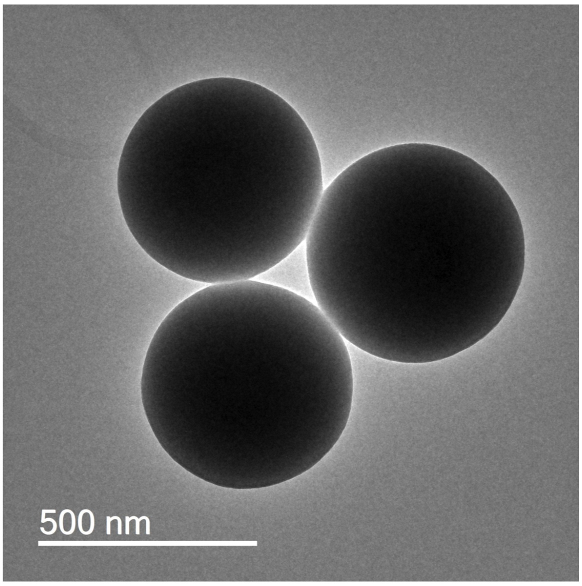

Figure 4.2: TEM image of 500 nm silica nanospheres.

Figure 4.2 shows the 500 nm silica spheres utilised for the synthesis of macroporous silicalite-1. It can be seen that the silica spheres vary slightly in size, though are roughly 450 - 485 nm in diameter. Figure 4.3 shows the species visible after the silica spheres have been exposed to hydrothermal conditions in the presence of TPAOH and water for 15 minutes. Figure 4.3 a and b show that after this period of time, the silica spheres have become much rougher in appearance, and shows the spheres vary in size greatly. It is clear that the silica spheres are actually multimodal, with the presence of smaller particles 50 - 100 nm in size particles with similar morphologies to that of the silica spheres. It can also be seen that the spheres are held within a network of smaller particles, which can also be seen within figure 4.3 c, which shows a roughened sphere, 385 nm in diameter, surrounded by this network of smaller particles. This network of particles is similar to that observed in the formation of TEOS under the same conditions (Chapter 2), however the network seems to radiate away from the silica sphere. The presence of these smaller particles creating the network of particles, is indicative of dissolution and nucleation processes occurring within the system. Figure 4.3 d, also shows signs of dissolution, however it is observed in a much more aggressive manner, where the surface of the silica particle has been torn away in layers. This is thought to be due to the mesoporous nature of the silica spheres, where the basic templating agent can access the inner surface area of the spheres, causing dissolution to occur from within. Figure 4.3 e and f, again show very different species found within reaction mixture after 15 minutes of hydrothermal synthesis. These TEM images show the presence of core-shell species, where the core is less dense than the shell it resides within. The size of the core shell particles are of similar size to that of the roughened spheres. The formation of such species could be indicative of the pore forming mechanism within the system.

Figure 4.4 a and b shows the network of particles, made up of c.a. 20 nm particles, again very similar to observation made from experiment on the formation of silicalite-1 from TEOS (Chapter 2. Figure 4.4 c, shows that the silica spheres are still present after 30 minutes of hydrothermal treatment, however the observed spheres have a rougher outer appearance than originally observed. It can also be seen that these particles are considerably smaller than the untreated silica spheres,

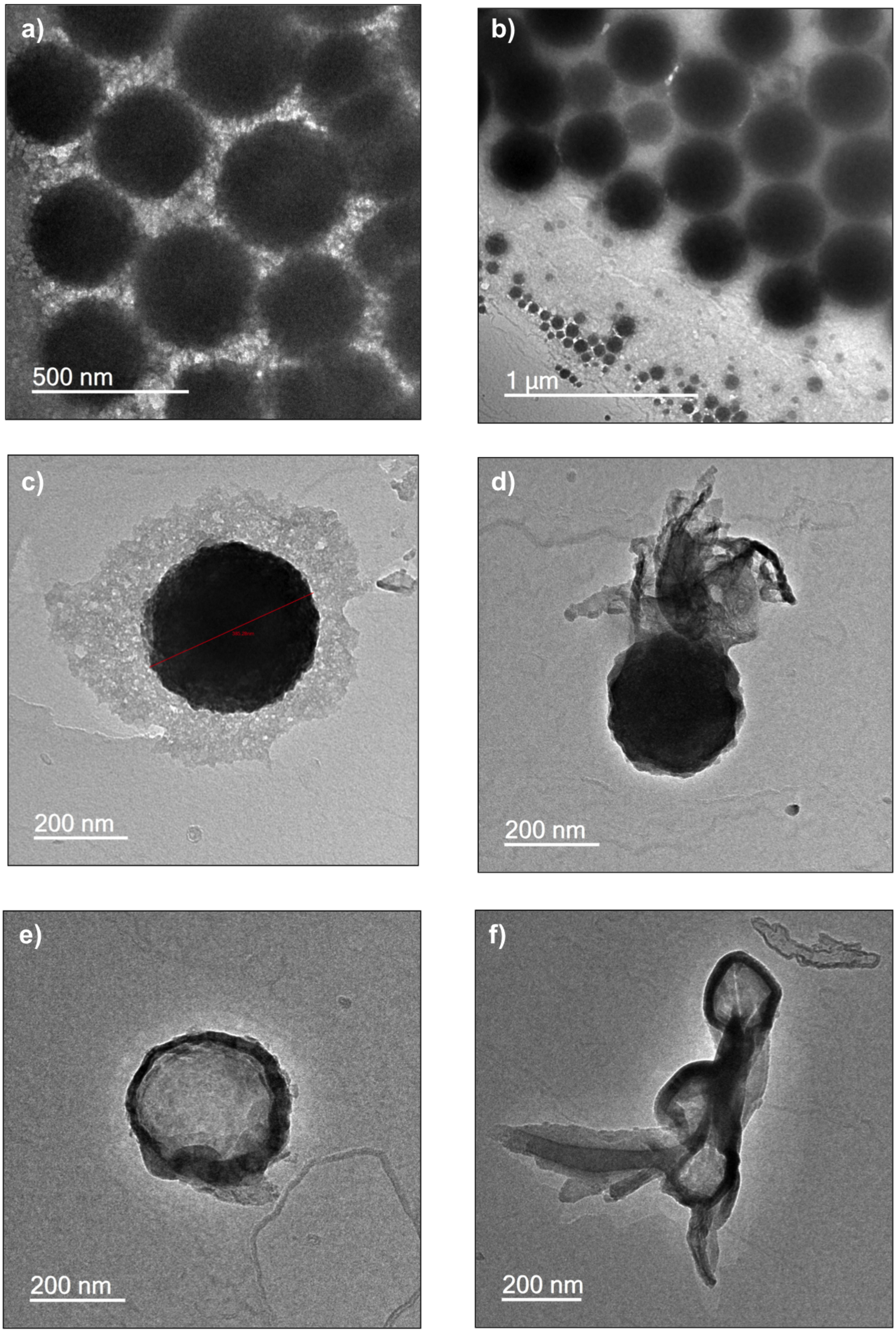

Figure 4.3: TEM images from a time sequence study of the formation of hierarchical silicalite-1 from 500 nm silica nanospheres at 180°C. Images taken after 15 minutes of hydrothermal treatment.

however this could also be due to there being a range of sphere sizes present from the start of the experiment. Figure 4.4 d, shows that some of the spherical particles are interconnected forming aggregated structures, thought it should be noted that the material at the surface of the spheres and the material bridging the particles together has a morphology similar to that of the network particles. Figure 4.4 e, again shows the large silica spheres, however many smaller particles, 50 - 150 nm, are also observed within a network of smaller particles. The large number of these particles observed at this stage would give the impression that these particles may have nucleated from the smaller network particles, however due to the presence of smaller silica spheres from earlier stages of the experiment, their nucleation and growth cannot be confirmed. Figure 4.4 f shows that the presence of large particles with morphologies similar to that expected from silicalite-1 (c.a. 600 nm in length).

After a further 15 minutes of hydrothermal treatment, many more larger species are observed (figure 4.5). Large clusters of silica spheres (c.a. 1.5 μm) can be seen in both figure 4.5 a and b. At the center of these clusters it becomes difficult to distinguish between individual particles, however, spherical particles can be seen at the edges of these particles. Figure 4.5 c, again shows large particles possessing similar morphologies to those that could be expected from silicalite-1 crystals, however at the edges of many of these particles voids can be seen. These voids give the large particles a ”swiss-cheese” like appearance, and the voids are os similar sizes the other of the spheres observed at this stage of the experiment. Figure 4.5 d, shows a particle with typical silicalite-1 morphology, which is atypical of the probed system. This could indicate the presence of different formation paths within the probed system. Figure 4.5 e and f, again show large particles that have evidence that they are hierarchical structures. Figure 4.5 e, shows a large crystal with inhomogeneities, which are thought to be voids within the structure. Figure 4.5 f, also exhibits similar inhomogeneities, however the voids can be seen to be of a similar size to that of the spheres present within the system, provides some evidence that the external voids created on the surface of these large particles could be templated by the sphere within the system.

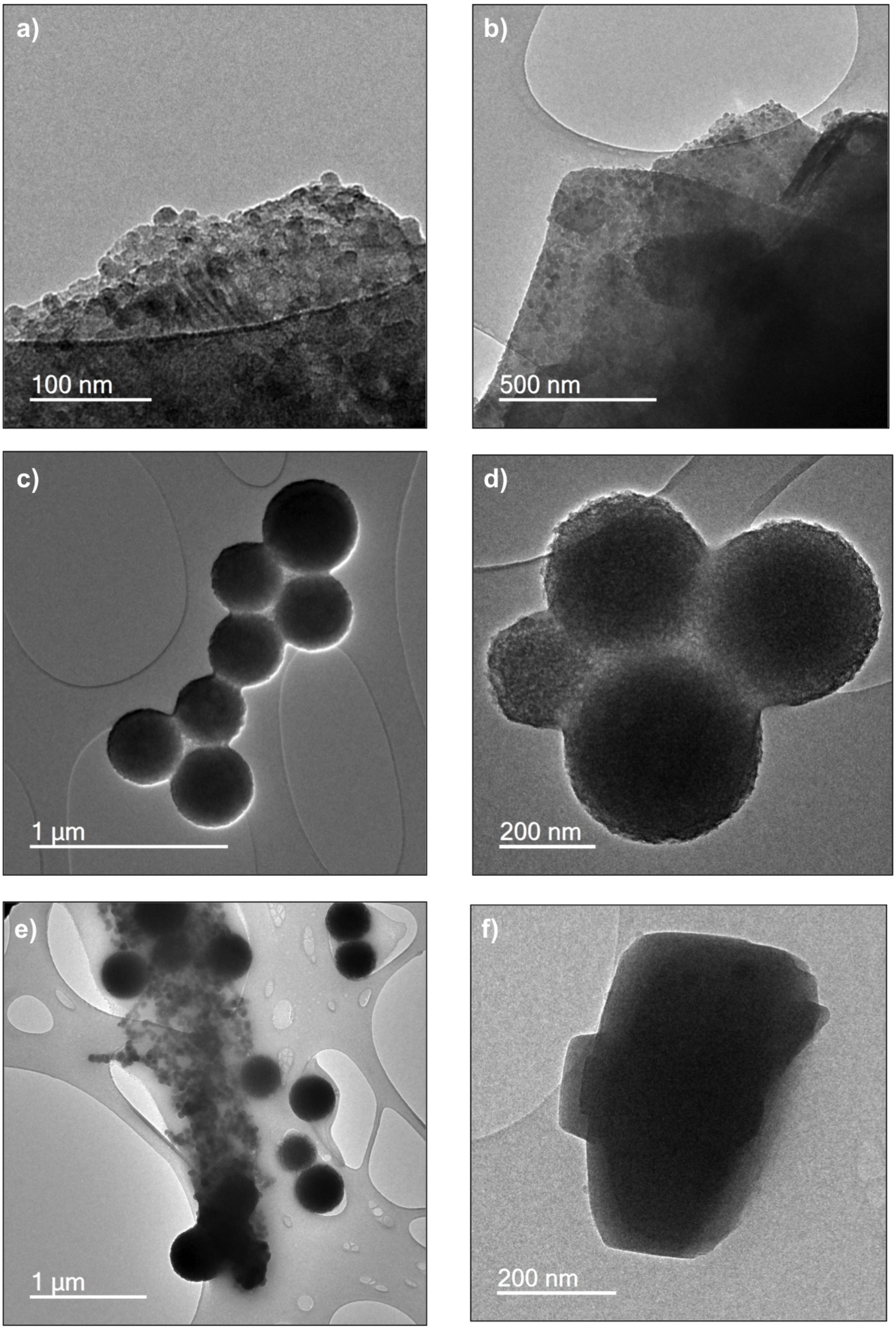

Figure 4.4: TEM images from a time sequence study of the formation of hierarchical silicalite-1 from 500 nm silica nanospheres at 180°C. Images taken after 30 minutes of hydrothermal treatment.

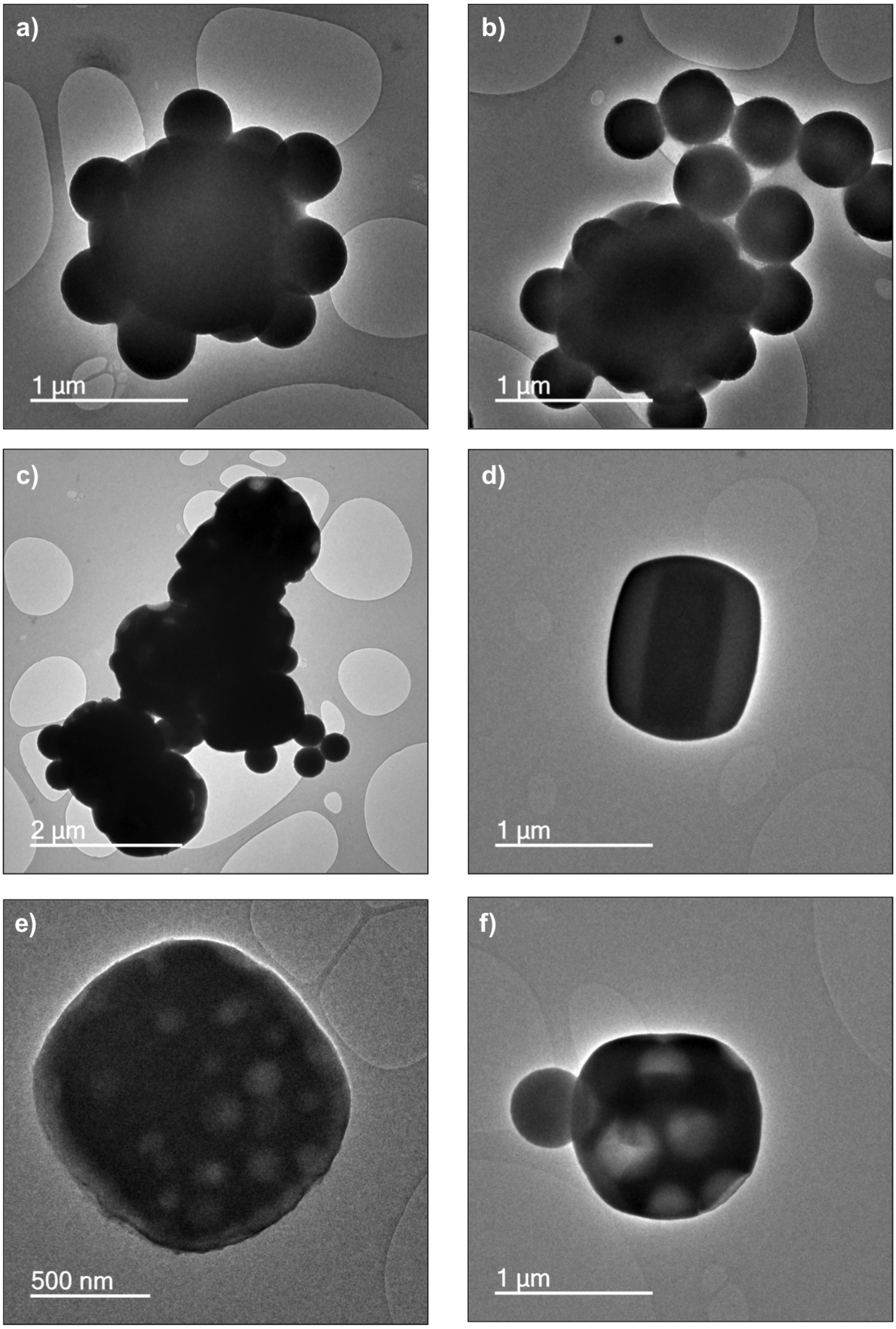

Figure 4.5: TEM images from a time sequence study of the formation of hierarchical silicalite-1 from 500 nm silica nanospheres at 180°C. Images taken after 45 minutes of hydrothermal treatment.

Figure 4.6 shows SEM images taken after 120 minutes of hydrothermal synthesis. It can be seen that the particles present have a typical morphology associated with twinned silicalite-1 crystals, however voids can be seen in the surface of the particles. These voids vary in size across the surface of these particles, however it is not possible to see if the voids are only found on the surface or are present throughout the whole of the structure.

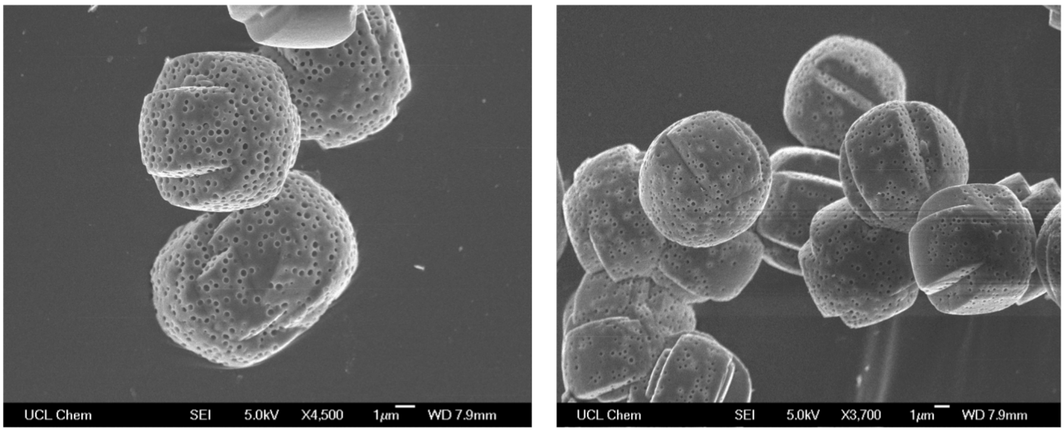

Figure 4.6: SEM images from a time sequence study of the formation of hierarchical silicalite-1 from 500 nm silica nanospheres at 180°C. Images taken after 2 hours of hydrothermal treatment.

Some evidence for the mechanism behind the formation of the surface pores is observed in figure 4.7. The first SEM image shows silicalite-1 crystals with a surface covered with silica spheres, alongside half-sphere shaped voids within the surface of the large particle. This gives the impression that the surface morphology is templated by these spheres, and as they are partially incorporated into the crystal before they become detached, leaving behind a void. It is also important to note that at this stage of the experiment that this sample is only participially crystalline (figure 4.8). The other SEM image shows the system after 8 hours of hydrothermal treatment. The voids on the observed crystal are much smaller that previously seen, whilst the surface of the crystal also have evidence of its formation, with the presence grain boundaries indicating that the crystal has formed from multiple smaller particles. Also, it is possible to see the presence of smaller particles with silicalite-1 morphology within these SEM images, which could indicate the presence of multiple paths for nucleation and crystal growth.

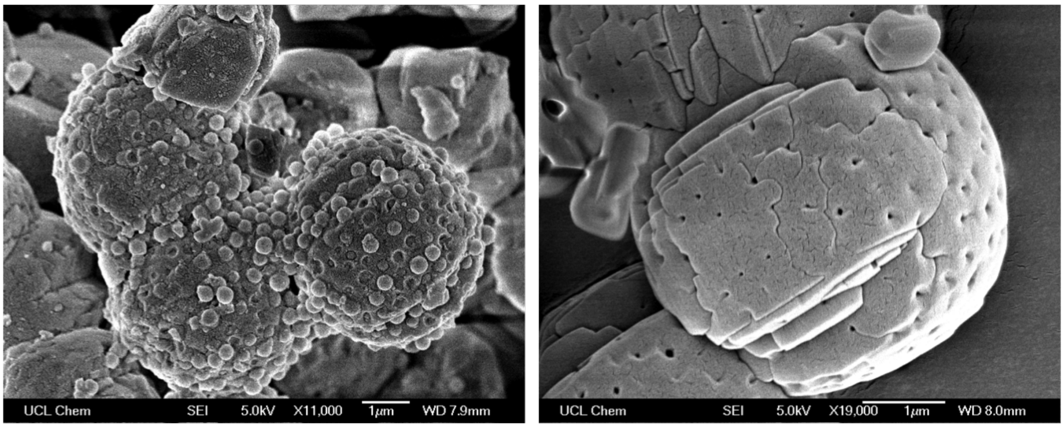

Figure 4.7: SEM images from a time sequence study of the formation of hierarchical silicalite-1 from 500 nm silica nanospheres at 180°C. Images taken after 4 (left) and 8 (right) hours

In-situ SAXS data reveals that the silica spheres at the start of the experiment are on average 480 nm in diameter (figure 4.9). The data shows that the majority of the silica nanospheres are c.a. 465 nm, however the nanospheres vary in size with some as small as 330 nm, and as large as 720 nm observed. Figure 4.10 shows the SAXS data collected at a shorter sample-detector distance, providing information on the smaller particles found within the system. It can be seen that at the start of the experiment that there are very few $<$ 5 nm particles observed, however particle ranging between 16 - 200 nm are observed within the data, which could correspond to the particles observed in figure 4.3 b, meaning that these particles observed in the *ex-situ* TEM study after 15 minutes may have been present from the start of the experiment.

As the experiments proceed, it can be seen that a population of small $<$ 5 nm particles begins to grown, in both volume fraction and size. This observed growth is observed alongside the loss of the larger particle observed between 16 - 200 nm in size, and the shrinking of the ”500 nm” spheres. It can be seen in Figure 4.10 that when the $<$ 5 nm particles reaches a peak in population size the 16 - 200 nm population reaches its lowest point in terms of volume fraction. However, after this point when the $<$ 5 nm population begins to decline, a population of particles, 16 - 50 nm in size begins to increase in volume fraction. This is observed alongside the formation of c.a. 90 nm particles. From this point onwards in the data it can

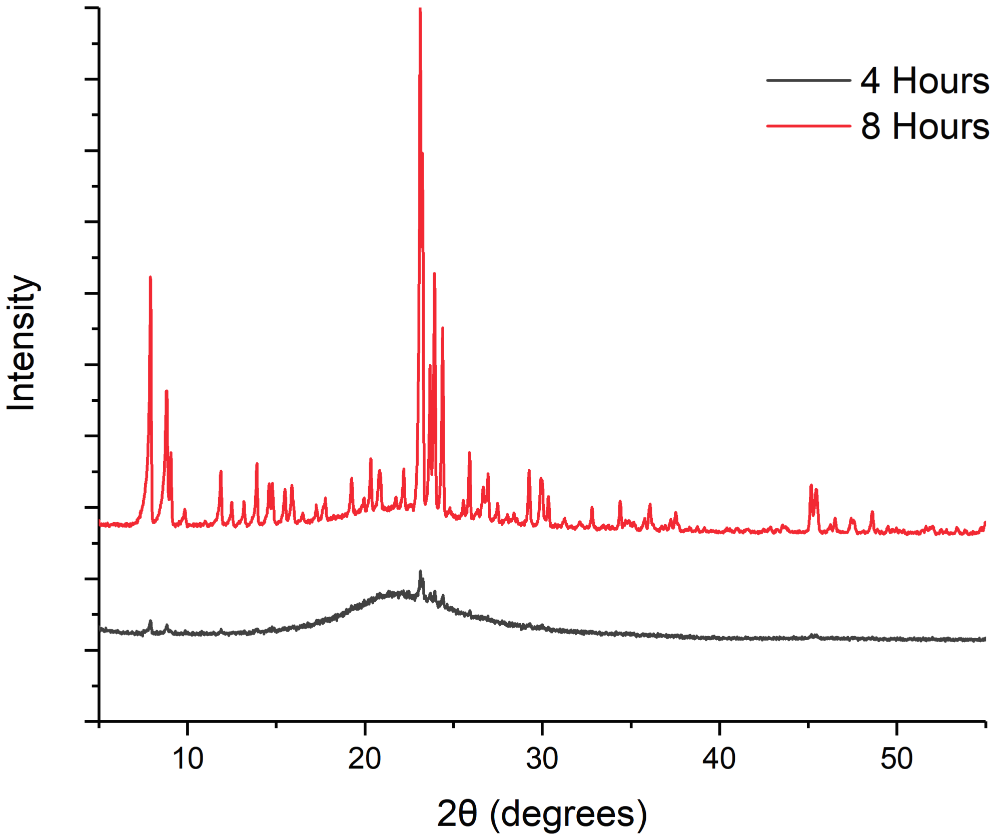

Figure 4.8: PXRD patterns of hierarchical silicalite-1 samples formed from 500 nm silica nanospheres at 180°C, after they have been subjected to hydrothermal conditions for 4 and 8 hours.

be seen that the population of < 5 nm particles continues to decline, the 16 - 50 nm population continues to grown, and the c.a. 90 nm particles are joined by the formation of particles up to 160 nm. These observation correspond to the *ex-situ* TEM study well, as at the start of the experiment evidence of dissolution is observed, followed by the formation of small particles that from a network around the silica nanospheres, where the smaller particles are c.a. 20 nm in size. At this point a population of larger 50 - 150 nm particles are observed in the *ex-situ* microscopy study. The formation of this population mid-sized population is observed in the SAXS, alongside the decline of the population of smaller particles, giving evidence that these mid-sized particles have grown from these smaller particles. The appear-

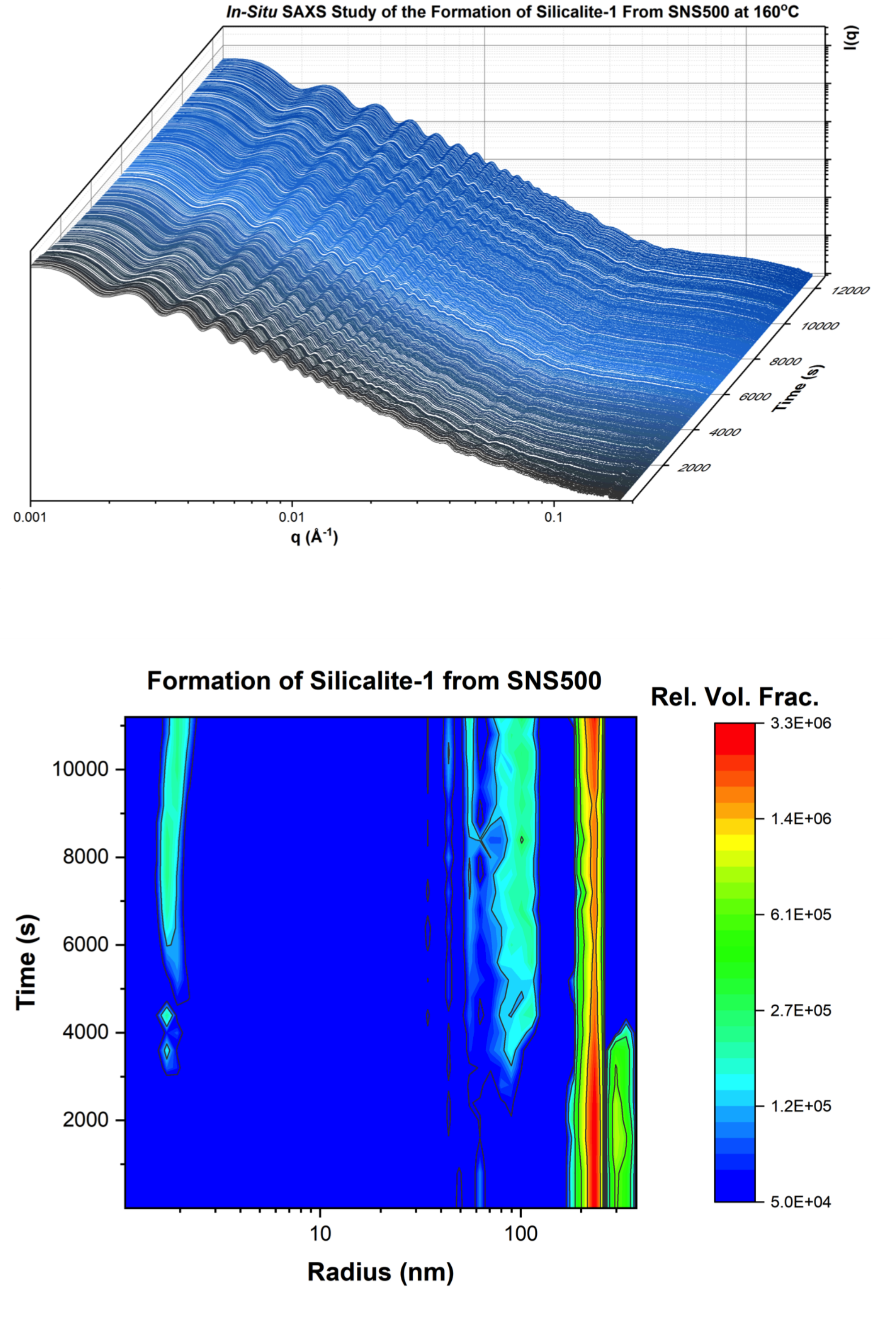

Figure 4.9: *In-situ* SAXS data on the formation of Hierarchical silicalite-1 from 500 nm silica nanospheres at 160°C recorded at Diamond Light Source (top), and results from Monte Carlo fitting (bottom).

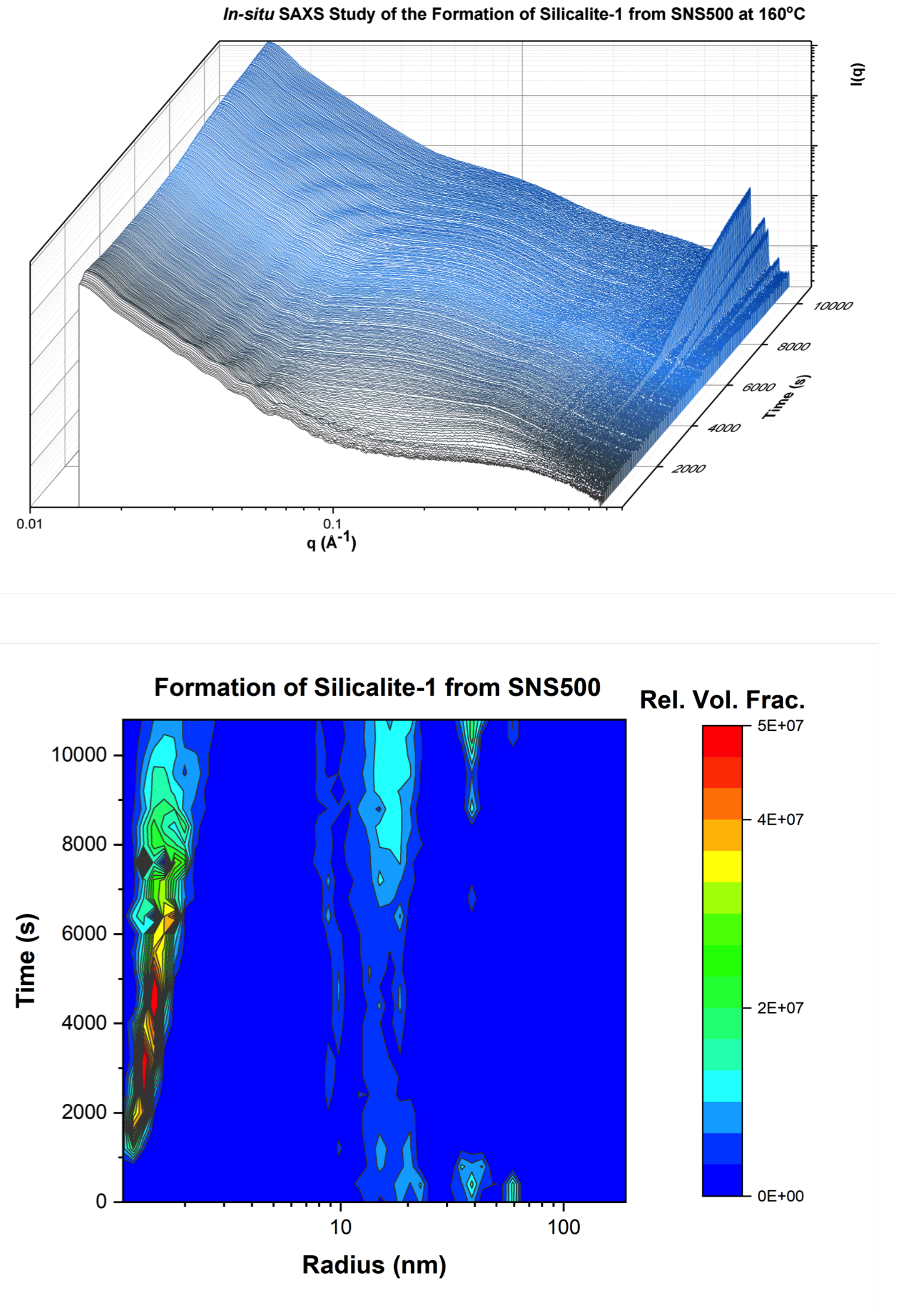

Figure 4.10: *In-situ* SAXS data on the formation of Hierarchical silicalite-1 from 500 nm silica nanospheres at 160°C recorded at the ESRF (top), and results from Monte Carlo fitting (bottom).

ance of the mid-sized particles also comes at the point where diffraction peaks are started to be observed in the system, and as the number of these particles increases so does the overall crystallinity of the system. This would indicate that these particles are atleast partially crystalline. These observations made in the high-q SAXS data, is also reminiscent of observation made when using other silica sources in the formation of silicalite-1 (Chapter 1).

Though there is a hub of activity occurring in the high-q SAXS data, little change is observed in the low-q data (figure 4.9). This data shows that the form factor from the 500 nm silica spheres is present throughout the experiment, whilst the overall size of the silica spheres has only decreased slightly. These observation indicate that some dissolution has taken place, however in correspondence to observed made in the *ex-situ* TEM study, the 500 nm silica spheres should still be visible even after long exposure to hydrothermal conditions (figure 4.7.

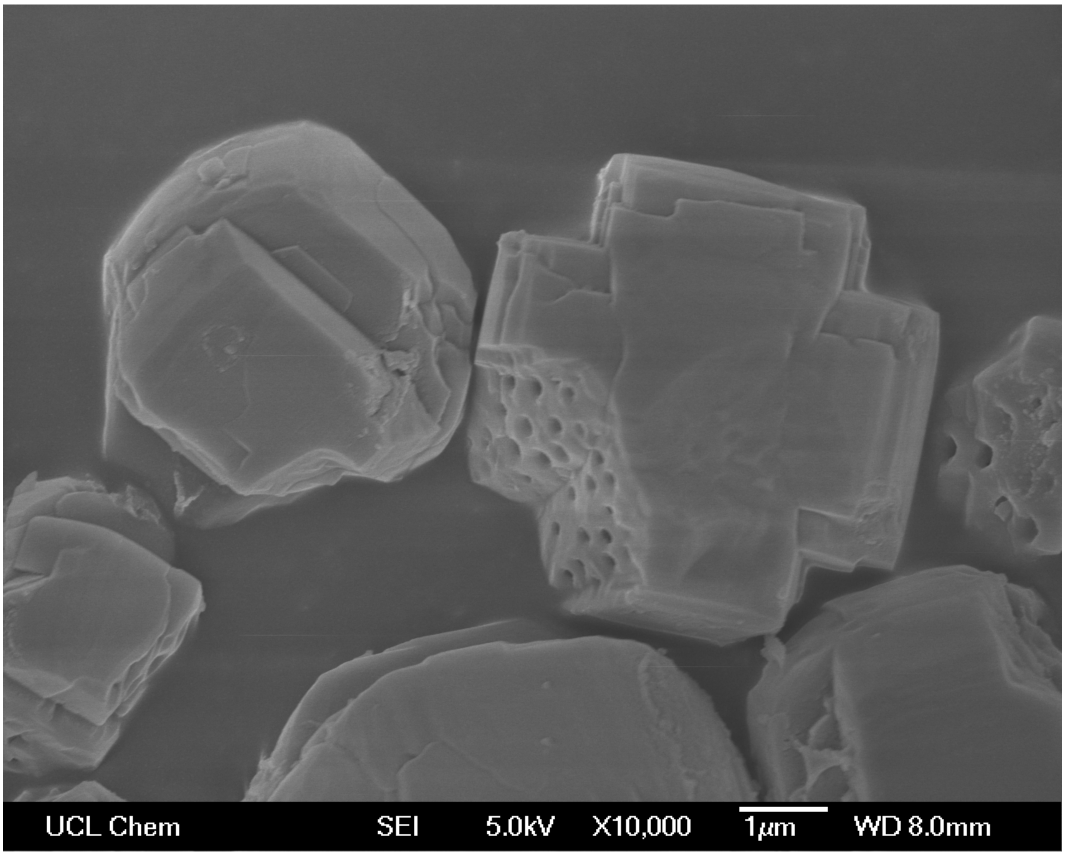

Figure 4.11: SEM image of hierarchical silicalite-1 formed from 500 nm silica nanospheres at 180°C over a 24 hour synthesis period.

Figure 4.12 shows the PXRD patterns obtained from samples exposed to 24 hours of hydrothermal treatment, alongside data taken from conventionally synthesises silicalite-1. The PXRD data shows that after 24 hours of hydrothermal treatment that using 500 nm silica spheres, good crystallinity is observed in comparison to conventionally synthesised silicalite-1 (synthesised from TEOS under the same conditions using the same synthesis ratios). Figure 4.11, shows SEM images of the Silialite-1 sample synthesised using the 500 nm silica nanospheres. It can be seen that a much smoother outer surface is observed than previously seen, however, the external surface of the crystals does not show the voids present at earlier stages, though the presence of internal macropores can be seen. These macropores are observed to be roughly half the size of the silica nanospheres used in the synthesis (figure 4.13).

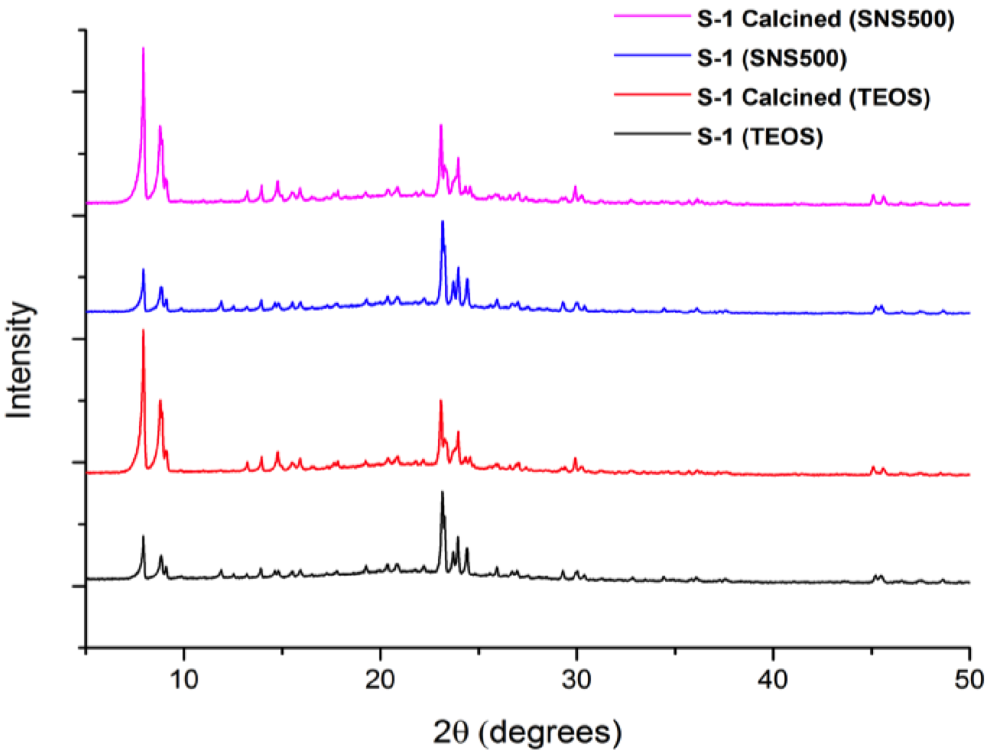

Figure 4.12: PXRD patterns of hierarchical silicalite-1, formed from 500 nm silica nanospheres at 180°C, and of conventional silicalite-1 formed under that same conditions. XRD patterns taken after samples had been subjected to hydrothermal conditions for 24 hours.

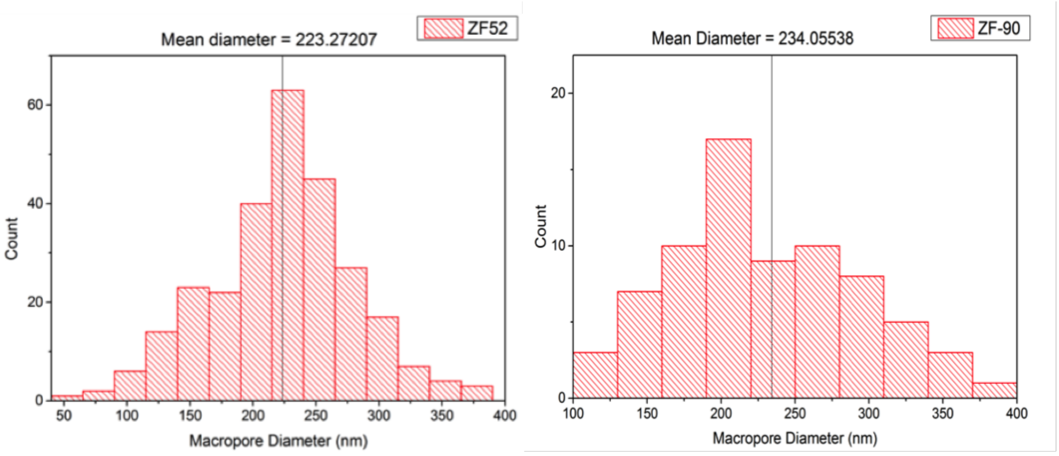

Figure 4.13: Histogram showing macropore size observed in hierarchical silicalite-1 samples formed from 500 nm silica nanospheres at 180°C for 16 hours (left), and 24 hours (right)

See a decrease in macropore size with increasing synthesis time from 16 to 24 hours (figure 4.13. This decrease in pore size could be mechanistic of the crystallisation process, and could be evidence of the presence of a reverse crystallisation, where a zeolitic shell is first formed around a nutrient source, which is then slowly converted to the crystalline solid, leaving behind a void. As the conversion of amorphous nutrient to crystalline zeolite proceeds the void becomes larger up to the point where there is no more amorphous material available for conversion to crystalline solid.

BET measurements were used to probe the internal porosity of the macroporous silicalite-1 crystals after 24 hours of hydrothermal treatment. Figure 4.14 shows N_2 BET data collected from both macroporous silicalite-1 samples and conventionally synthesised silicalite-1. From looking at the shape of the nitrogen adsorption and desorption isotherm it is possible to gain important information of the presence of pores within the structure. By looking at isotherm for the calcined conventional synthesised silicalite-1 sample, a type I isotherm is observed, where as the isotherm observed for the macroporous sample is much less commonly observed with zeolite systems. It can be seen that for the calcined macroporous silicalite-1 sample (550° for 8 hours) that the nitrogen sorption isotherms show uptake in three steps: below $P/P_0 = 0.2$, due to the filling of micropores or capillary condensation

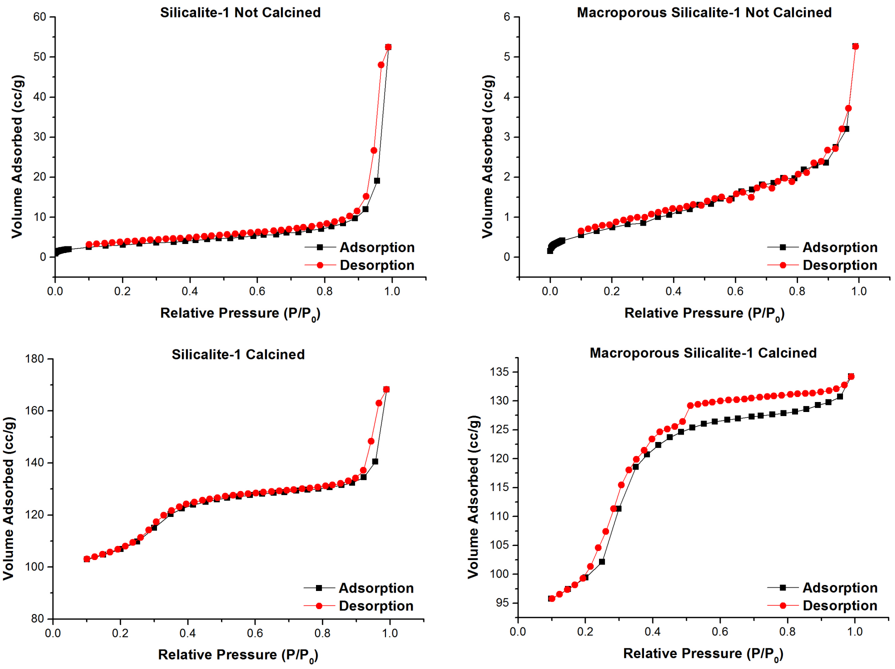

Figure 4.14: N_2 adsorption-desorption isotherms on macroporous silicalie-1 (right) and conventional silicalite-1 (left).

(also present in the conventionally synthesised silicalite-1 sample), the hysteresis loop at low relative pressure above P/P_0 = 0.2, and in the range of P/P_0 = 0.4 - 1.0. It is widely accepted that the the presence of hysteresis loops in gas sorption isotherms, are observed due to non-coincidence between capillary condensation and evaporation processes, and therefore can possess valuable information on the connectivity of pores within a probed system.[71, 78, 79, 7] The observed hysteresis at a relative pressure of roughly 0.2 is said to not be associated with pore filling, or pore condensation, however it is believed to be caused from a phase transition of the liquid-like adsorbate within the zeolite channels, that is forming a less disordered solid-like state.[80] The hysteresis loop observed at relative pressures between P/P_0 = 0.4 1.0 is of type IV, accompanied by H4 characteristics, which indicates there is a more random distribution of mesopores, within an interconnected pore system. The BET of the macorpoous system formed from these experiments are very similar to those formed when using a sacrificial mesoporous carbon tamplates which are subsequently removed from the zeolite system through calicnation.[80] The total surface area of these two samples differed only slightly with the conventional silicalite-1 having a measured surface are of 334.689 m^2 $g-1$, and the macroporous silicalite-1 having a slightly lower surface area of 324.043 m^2g-1, which is expected from the introduction of macropores into the system.

When looking at the presented data, the formation of macroporous silicalite-1 from 500 nm silica nanospheres, occurs predominantly through the aggregation of the silica precursor particles. Upon mixing the silica nanospheres with the template agent, dissolution proceeds and the majority of nanospheres develop rougher exteriors. These template infused silica nanospheres then begin to aggregate. Next, at the surface of these amorphous aggregates, nucleation proceeds. This nucleation continues until a crystalline shell is formed around the outside of the silica nanospheres. Macropore formation can then begin, as the amorphous interior of the silica nanospheres acts as a nutrient source for further crystal growth. When this amorphous core is slowly converted to silicalite-1, a void is left behind roughly equal to half the size of the silica spheres used in the synthesis. The formation of macroporous silicalite-1 can be summarised as:

1. Template (organic) + 500 nm Silica Nanospheres
    - Mixing
2. Template Infused Silica nanospheres
    - Aggregation
3. Amorphous Aggregates
    - Further Aggregation and Nucleation
4. Amorphous-Crystalline ”Core-shell” aggregates
    - Crystal Growth (and ”reverse” crystallisation)
5. Amorphous-Crystalline ”Core-shell” aggregates with voids
    - Further Crystal Growth (and ”reverse” crystallisation)

However, the presence of dissolution gives rise to secondary processes for the nucleation of silicalite-1, which have been discussed previously in chapter 1. Both the SAXS data and TEM data show evidence of the formation of intermediate species, which can either contribute directly to crystal growth of the macroporous silicalite-1 particles, or alternatively they can go on to form non-hierarchical silicalite-1 structures, which have also been observed in smaller amount in SEM images taken towards the end of the synthesis process. This would indicate that the formation of non-hierarchical silicalite-1 structures is less favourable than the formation of the macroporous silicalite-1 structures.

4.5 Summary

The formation of hierarchical silicalite-1, synthesised using simple conventional methods for the direct synthesis of hierarchical silicalite-1 from 500nm silica nanospheres. The formation of the micro-macroporous crystalline product was probed using complimentary *in-situ* SAXS and *ex-situ* microscopy. The *in-situ* SAXS experiements were able to provide in sights on the formation process as a whole, giving representative observations on the average structures found throughout the crystallisation process, whilst *ex-situ* microscopy was utilised to provide unique details on the local structure only available from the investigating individual particles. From these investigations, the presence of two distinct, competing mechanism for the crystallisation of silicalite-1 were observed, with the dominant mechanism yielding the formation of macroporous silicalite-1 when using silica nanospheres as a precursor.

Bibliography

[1] P Fratzl and R Weinkamer. Nature's hierarchical materials. *Progress in Materials Science*, 52(8):1263–1334, 2007.

[2] M O Coppens. A nature-inspired approach to reactor and catalysis engineering. *Current Opinion in Chemical Engineering*, 32:1–9, 2012.

[3] A G Machoke, A M Beltrán, A Inayat, B Winter, T Weissenberger, N Kruse, R Güttel, E Spiecker, and W Schwieger. Micro/Macroporous System: MFI-Type Zeolite Crystals with Embedded Macropores. *Advanced materials (Deerfield Beach, Fla.)*, pages 1–5, 2014.

[4] E J W Crossland, N Noel, V Sivaram, T Leijtens, J A Alexander-Webber, and H J Snaith. Mesoporous TiO 2 single crystals delivering enhanced mobility and optoelectronic device performance. *Nature*, 495(7440):215–219, 2013.

[5] K Na, C Jo, J Kim, K Cho, J Jung, Y Seo, R J Messinger, B F Chmelka, and R Ryoo. Directing zeolite structures into hierarchically nanoporous architectures. *Science*, 333(6040):328–332, 2011.

[6] M A Camblor, A Corma, and S Valencia. Characterization of nanocrystalline zeolite Beta. *Microporous and Mesoporous Materials*, 25:59–74, 1998.

[7] D P Serrano, J M Escola, and P Pizarro. Synthesis strategies in the search for hierarchical zeolites. *Chem. Soc. Rev.*, 42(9):4004–4035, 2013.

[8] C Martinez, J Pérez-Pariente, G Sankar, and A J Smith. *ZEOLITES AND ORDERED POROUS SOLIDS : Fundamentals and applications*. 2011.

[9] S Mintova, N H Olson, V Valtchev, and T Bein. Mechanism of Zeolite A Nanocrystal Growth from Colloids at Room Temperature. *Science*, 283(5405):958–960, 1999.

[10] V Nikolakis, M Tirrell, M Tsapatsis, and D G Vlachos. Zeolite Growth by Addition of Subcolloidal Particles: Modeling and Experimental Validation. *Chemistry of Materials*, 12(3):845–853, mar 2000.

[11] L H Chen, X Y Li, J C Rooke, Y H Zhang, X Y Yang, S Y Tang, F S Xiao, and B L Su. Hierarchically structured zeolites: synthesis, mass transport properties and applications. *Journal of Materials Chemistry*, 22:17381, 2012.

[12] G T Kerr. The Intracrystalline Rearrangement of Constitutive Water in Hydrogen Zeolite Y. *The Journal of Physical Chemistry*, 71(12):4155–4156, 1967.

[13] G T Kerr. Chemistry of crystalline aluminosilicates. V. Preparation of aluminum-deficient faujasites. *Journal of Physical Chemistry*, 72(7):2594–2596, 1968.

[14] C S Triantafillidis, A G Vlessidis, and N P Evmiridis. Dealuminated H-Y zeolites: Influence of the degree and the type of dealumination method on the structural and acidic characteristics of H-Y zeolites. *Industrial and Engineering Chemistry Research*, 39(2):307–319, 2000.

[15] B Sulikowski. The fractal dimension in molecular sieves: Synthetic faujasite and related solids. *Journal of Physical Chemistry*, 97(7):1420–1425, 1993.

[16] C J Van Oers, W J J Stevens, E Bruijn, M Mertens, O I Lebedev, G Van Tendeloo, V Meynen, and P Cool. Formation of a combined micro- and mesoporous material using zeolite Beta nanoparticles. *Microporous and Mesoporous Materials*, 120(1-2):29–34, 2009.

[17] R Szostak. Modified Zeolites. In H. van Bekkum, E. M. Flanigen, and J. C. Jansen, editors, *Studies in Surface Science and Catalysis*, chapter 5, pages 153–199. Elsevier B. V., 58 edition, 1991.

[18] D Verboekend, T C Keller, S Mitchell, and J Pérez-Ramírez. Hierarchical FAU- and LTA-type zeolites by post-synthetic design: A new generation of highly efficient base catalysts. *Advanced Functional Materials*, 23(15):1923–1934, 2013.

[19] R A Beyerlein, C Choi-feng, J B Hall, B J Huggins, and G J Ray. Effect of steaming on the defect structure and acid catalysis of protonated zeolites. *Topics in Catalysis*, 4:27–42, 1997.

[20] S Van Donk, A H Janssen, J H Bitter, and K P De Jong. Generation, characterization, and impact of mesopores in zeolite catalysts. *Catalysis Reviews - Science and Engineering*, 45(2):297–319, 2003.

[21] L Yingcai, J Mingyang, S Yaojun, W Tailliu, W Liping, and F Lun. State of aluminium in hydrothermally dealuminated MFI zeolite. *Journal of the Chemical Society, Faraday Transactions*, 92(9):1647–1651, 1996.

[22] S Malola, S Svelle, F L Bleken, and O Swang. Detailed reaction paths for zeolite dealumination and desilication from density functional calculations. *Angewandte Chemie - International Edition*, 51(3):652–655, 2012.

[23] P Kortunov, S Vasenkov, J Kärger, R Valiullin, P Gottschalk, M F Elía, M Perez, M Stöcker, B Drescher, G McElhiney, C Berger, R Gläser, and J Weitkamp. The role of mesopores in intracrystalline transport in USY zeolite: PFG NMR diffusion study on various length scales. *Journal of the American Chemical Society*, 127(37):13055–13059, 2005.

[24] A H Janssen, A J Koster, and K P de Jong. Three-Dimensional Transmission Electron Microscopic Observations of Mesopores in Dealuminated Zeolite Y. *Angewandte Chemie*, 113(6):1136–1138, mar 2001.

[25] T Suzuki and T Okuhara. Change in pore structure of MFI zeolite by treatment with NaOH aqueous solution. *Microporous and Mesoporous Materials*, 43(1):83–89, 2001.

[26] L Su, L Liu, J Zhuang, H Wang, Y Li, W Shen, Y Xu, and X Bao. Creating mesopores in ZSM-5 zeolite by alkali treatment: A new way to enhance the catalytic performance of methane dehydroaromatization on Mo/HZSM-5 catalysts. *Catalysis Letters*, 91(3-4):155–168, 2003.

[27] J C Groen, J C Jansen, J A Moulijn, and J Pérez-Ramírez. Optimal aluminum-assisted mesoporosity development in MFI zeolites by desilication. *Journal of Physical Chemistry B*, 108(35):13062–13065, 2004.

[28] S Svelle, L Sommer, K Barbera, P N R Vennestrøm, U Olsbye, K P Lillerud, S Bordiga, Y H Pan, and P Beato. How defects and crystal morphology control the effects of desilication. *Catalysis Today*, 168(1):38–47, 2011.

[29] S Yang, C Yu, L Yu, S Miao, M Zou, C Jin, D Zhang, L Xu, and S Huang. Bridging Dealumination and Desilication for the Synthesis of Hierarchical MFI Zeolites. *Angewandte Chemie - International Edition*, 56(41):12553–12556, 2017.

[30] J C Groen, T Sano, J A Moulijn, and J Pérez-Ramírez. Alkaline-mediated mesoporous mordenite zeolites for acid-catalyzed conversions. *Journal of Catalysis*, 251(1):21–27, 2007.

[31] L Sommer, D Mores, S Svelle, M Stöcker, B M Weckhuysen, and U Olsbye. Mesopore formation in zeolite H-SSZ-13 by desilication with NaOH. *Microporous and Mesoporous Materials*, 132(3):384–394, 2010.

[32] K P De Jong, J Zečević, H Friedrich, P E De Jongh, M Bulut, S Van Donk, R Kenmogne, A Finiels, V Hulea, and F Fajula. Zeolite y crystals with trimodal porosity as ideal hydrocracking catalysts. *Angewandte Chemie - International Edition*, 49(52):10074–10078, 2010.

[33] J C Groen, S Abelló, L A Villaescusa, and J Pérez-Ramírez. Mesoporous beta zeolite obtained by desilication. *Microporous and Mesoporous Materials*, 114(1-3):93–102, 2008.

[34] A Bonilla, D Baudouin, and J Pérez-Ramírez. Desilication of ferrierite zeolite for porosity generation and improved effectiveness in polyethylene pyrolysis. *Journal of Catalysis*, 265(2):170–180, 2009.

[35] D Verboekend, G Vilé, and J Pérez-Ramírez. Hierarchical y and USY zeolites designed by post-synthetic strategies. *Advanced Functional Materials*, 22(5):916–928, 2012.

[36] Z Qin, B Shen, X Gao, F Lin, B Wang, and C Xu. Mesoporous y zeolite with homogeneous aluminum distribution obtained by sequential desilication-dealumination and its performance in the catalytic cracking of cumene and 1,3,5-triisopropylbenzene. *Journal of Catalysis*, 278(2):266–275, 2011.

[37] F Thibault-Starzyk, I Stan, S Abelló, A Bonilla, K Thomas, C Fernandez, J P Gilson, and J Pérez-Ramírez. Quantification of enhanced acid site accessibility in hierarchical zeolites - The accessibility index. *Journal of Catalysis*, 264(1):11–14, 2009.

[38] S Abelló, A Bonilla, and J Pérez-Ramírez. Mesoporous ZSM-5 zeolite catalysts prepared by desilication with organic hydroxides and comparison with NaOH leaching. *Applied Catalysis A: General*, 364(1-2):191–198, 2009.

[39] J Peréz-Ramírez, D Verboekend, A Bonilla, and S Abelló. Zeolite catalysts with tunable hierarchy factor by pore-growth moderators. *Advanced Functional Materials*, 19(24):3972–3979, 2009.

[40] V Valtchev, E Balanzat, V Mavrodinova, I Diaz, J El Fallah, and J M Goupil. High energy ion irradiation-induced ordered macropores in zeolite crystals. *Journal of the American Chemical Society*, 133(46):18950–18956, 2011.

[41] K Li, J Valla, and J Garcia-martinez. Realizing the Commercial Potential of Hierarchical Zeolites : New Opportunities in Catalytic Cracking. *Chem cat chem*, 6(1):46–66, 2014.

[42] I I Ivanova, I A Kasyanov, A A Maerle, and V I Zaikovskii. Mechanistic study of zeolites recrystallization into micro-mesoporous materials. *Microporous and Mesoporous Materials*, 189:163–172, 2014.

[43] F Ngoye, L Lakiss, Z Qin, S Laforge, C Canaff, M Tarighi, V Valtchev, K Thomas, A Vicente, J P Gilson, Y Pouilloux, C Fernandez, and L Pinard. Mitigating coking during methylcyclohexane transformation on HZSM-5 zeolites with additional porosity. *Journal of Catalysis*, 320:118–126, 2014.

[44] N Petkov, M Ho, T H Metzger, S Mintova, and T Bein. Ordered Micro / Mesoporous Composite Prepared as Thin Films. *J. Phys. Chem. B*, 109:4485–4491, 2005.

[45] Y Liu, W Zhang, and T J Pinnavaia. Steam-Stable MSU-S Aluminosilicate Mesostructures Assembled from Zeolite ZSM-5 and Zeolite Beta Seeds. *Angew. Chem. Int. Ed.*, 40(7):1255–1258, 2001.

[46] D P Serrano, G Vicente, and M Linares. Acidic and catalytic properties of hierarchical zeolites and hybrid ordered mesoporous materials assembled from MFI protozeolitic units. 279:366–380, 2011.

[47] K Song, J Guan, S Wu, and Q Kan. Synthesis and characterization of strong acidic mesoporous alumino-silicates constructed of zeolite MCM-22 precursors. *Catalysis Communications*, 10(5):631–634, 2009.

[48] F S Xiao, L Wang, C Yin, D S Su, R Schlögl, and T Yokoi. Catalytic Properties of Hierarchical Mesoporous Zeolites Templated with a Mixture of Small Organic Ammonium Salts and Mesoscale Cationic Polymers. *Angew. Chem. Int. Ed.*, 45:3090–3093, 2006.

[49] M Karin, B Yilmaz, M Ulrich, and T Bein. Hierarchical Zeolite Beta via Nanoparticle Assembly with a Cationic Polymer. *Chem. Mater.*, 23:4301–4310, 2011.

[50] W Xu, J Dong, J Li, J Li, and F Wub. A Novel Method for the Preparation of Zeolite ZSM-5. *J. Chem. Soc. Chem. Commun.*, pages 755–756, 1990.

[51] J Coronas and J Santamaria. State-of-the-Art in Zeolite Membrane Reactors. *Topics in Catalysis*, 29(1/2):29–44, may 2004.

[52] C Li, Y Wang, B Shi, J Ren, X Liu, Y Wang, Y Guo, Y Guo, and G Lu. Synthesis of hierarchical MFI zeolite microspheres with stacking nanocrystals. *Microporous and Mesoporous Materials*, 117(1-2):104–110, 2009.

[53] C Xue, F Zhang, L Wu, and D Zhao. Vapor assisted ”in situ” transformation of mesoporous carbon-silica composite for hierarchically porous zeolites. *Microporous and Mesoporous Materials*, 151:495–500, 2012.

[54] K Möller, B Yilmaz, R M Jacubinas, U Müller, and T Bein. One-step synthesis of hierarchical zeolite beta via network formation of uniform nanocrystals. *Journal of the American Chemical Society*, 133(14):5284–5295, 2011.

[55] Q Lei, T Zhao, F Li, L Zhang, and Y Wang. Catalytic cracking of large molecules over hierarchical zeolites. *Chemical Communications*, (16):1769, 2006.

[56] Y Wang, Y Tang, A Dong, X Wang, N Ren, and Z Gao. Zeolitization of diatomite to prepare hierarchical porous zeolite materials through a vapor-phase transport process. *Journal of Materials Chemistry*, 12(6):1812–1818, 2002.

[57] T Zhao, X Xu, Y Tong, Q Lei, F Li, and L Zhang. The synthesis of novel hierarchical zeolites and their performances in cracking large molecules. *Catalysis Letters*, 136(3-4):266–270, 2010.

[58] H Yang, Z Liu, H Gao, and Z Xie. Transalkylation of diisopropylbenzenes with benzene over hierarchical beta zeolite. *”Applied Catalysis A, General”*, 379(1-2):166–171, 2010.

[59] O Sel, A Brandt, D Wallacher, M Thommes, and B Smarsly. Pore Hierarchy in Mesoporous Silicas Evidenced by In-Situ SANS during Nitrogen Physisorption. (9):4724–4727, 2007.

[60] I Schmidt, C Madsen, and C J H Jacobsen. Confined space synthesis. A novel route to nanosized zeolites. *Inorganic Chemistry*, 39(11):2279–2283, 2000.

[61] C Madsen, C Madsen, and C J H Jacobsen. Nanosized zeolite crystalsconvenient control of crystal size distribution by confined space synthesis. *Chemical Communications*, (8):673–674, 1999.

[62] H S Cho and R Ryoo. Synthesis of ordered mesoporous MFI zeolite using CMK carbon templates. *Microporous and Mesoporous Materials*, 151:107–112, 2012.

[63] C J H Jacobsen, C Madsen, J Houzvicka, I Schmidt, and A Carlsson. Mesoporous zeolite single crystals [2]. *Journal of the American Chemical Society*, 122(29):7116–7117, 2000.

[64] H Chen, J Wydra, X Zhang, P S Lee, Z Wang, W Fan, and M Tsapatsis. Hydrothermal synthesis of zeolites with three-dimensionally ordered mesoporous-imprinted structure. *Journal of the American Chemical Society*, 133(32):12390–12393, 2011.

[65] I Schmidt, A Krogh, K Wienberg, A Carlsson, M Brorson, and C J H Jacobsen. Catalytic epoxidation of alkenes with hydrogen peroxide over first mesoporous titanium-containing zeolite. *Chemical Communications*, (21):2157–2158, 2000.

[66] I Schmidt, A Boisen, E Gustavsson, K Ståhl, S Pehrson, S Dahl, A Carlsson, and C J H Jacobsen. Carbon nanotube templated growth of mesoporous zeolite single crystals. *Chemistry of Materials*, 13(12):4416–4418, 2001.

[67] A H Janssen, I Schmidt, C J H Jacobsen, A J Koster, and K P de Jong. Exploratory study of mesopore templating with carbon during zeolite synthesis. *Microporous and Mesoporous Materials*, 65(1):59–75, 2003.

[68] Z X Yang, Y D Xia, and R Mokaya. Zeolite ZSM-5 with Unique Supermicropores Synthesized Using Mesoporous Carbon as a Template. *Advanced Materials*, 16(8):727–732, 2004.

[69] K Zhu, K Egeblad, and C H Christensen. Mesoporous carbon prepared from carbohydrate as hard template for hierarchical zeolites. *European Journal of Inorganic Chemistry*, (25):3955–3960, 2007.

[70] X Wang, G Li, W Wang, C Jin, and Y Chen. Synthesis, characterization and catalytic performance of hierarchical TS-1 with carbon template from sucrose carbonization. *Microporous and Mesoporous Materials*, 142(2-3):494–502, 2011.

[71] M Thommes, B Smarsly, M Groenewolt, P I Ravikovitch, and A V Neimark. Adsorption Hysteresis of Nitrogen and Argon in Pore Networks and Characterization of Novel Micro- and Mesoporous Silicas. (22):756–764, 2006.

[72] Y Tao, H Kanoh, and K Kaneko. ZSM-5 monolith of uniform mesoporous channels. *Journal of the American Chemical Society*, 125(20):6044–6045, 2003.

[73] H Katsuki, S Furuta, T Watari, and S Komarneni. ZSM-5 zeolite/porous carbon composite: Conventional- and microwave-hydrothermal synthesis from carbonized rice husk. *Microporous and Mesoporous Materials*, 86(1-3):145–151, 2005.

[74] O De La Iglesia, J L Sánchez, and J Coronas. Hierarchical silicalite-1 structures based on pyrolized materials. *Materials Letters*, 65(19-20):3124–3127, 2011.

[75] X Zhang, D Liu, D Xu, S Asahina, K A Cychosz, K V Agrawal, Y Al Wahedi, A Bhan, S Al Hashimi, O Terasaki, M Thommes, and M Tsapatsis. Synthesis of self-pillared zeolite nanosheets by repetitive branching. *Science*, 336(6089):1684–1687, 2012.

[76] M Khaleel, A J Wagner, K A Mkhoyan, and M Tsapatsis. On the rotational intergrowth of hierarchical FAU/EMT zeolites. *Angewandte Chemie - International Edition*, 53(36):9456–9461, 2014.

[77] I Bressler, B R Pauw, and A F Thuenemann. McSAS: Software for the retrieval of model parameter distributions from scattering patterns. *Journal of Applied Crystallography*, 48:962–969, 2015.

[78] S van Donk, A H Janssen, J H Bitter, and K P de Jong. Generation, Characterization, and Impact of Mesopores in Zeolite Catalysts. *Catal. Rev.*, 45:297, 2003.

[79] J C Groen, S Brouwer, L A Peffer, and J Pérez-Ramírez. Application of mercury intrusion porosimetry for characterization of combined micro- and mesoporous zeolites. *Particle and Particle Systems Characterization*, 23(1):101–106, 2006.

[80] H Li, Y Sakamoto, Z Liu, T Ohsuna, and O Terasaki. Mesoporous silicalite-1 zeolite crystals with unique pore shapes analogous to the morphology. *Microporous and Mesoporous Materials*, 106:174–179, 2007.

Chapter 5

Nucleation and Growth of Metal Organic Frameworks

5.1 Metal-Organic Frameworks

5.1.1 Introduction

A little over 20 years ago, the term metal-organic framework (MOF) was first proposed in literature, for a group of coordiantion polymers, some of which can be dated back to the 1960s. [1, 2] MOFs are a class of crystalline materials possessing structures with classical coordination bonds between metal cations (e.g. Zn^{2+}) and electron donating organic linker molecules (e.g. carboxylates or amines). As there are inorganic and organic components within these systems, the pore size and chemical environments can be tailored towards specific applications or desirable properties and it is this feature that sets them apart from other porous materials such as zeolites. The topology of a MOFs intimately related to the coordination environment favoured by the metal ions and the geometry of the organic linker groups that make up its structure. The metal ion and its surrounding linkers, can be considered as building blocks and it is these blocks that establish the network of symmetry throughout its structure.

In recent years, MOFs have gained a great deal of attraction within a diverse range of research areas, due to the versatility nad large range of potential structures. This diversity also means that MOFs have the potential to be tailored to specific tasks and through obtaining a greater understanding of the formation mechanisms of different MOF systems, it is thought that application specific MOFs can be developed.[3] The properties that MOFs can possess are observed in a great deal of micro- and mesoporous materials used commercially today, making them equally desirable in a great deal of applications. These potential applications include gas storage, adsorption, separation, drug storage and delivery, flame retardants and in catalysis.[4, 5, 1, 6, 7, 8, 9, 10, 11] However, work is still needed to push MOFs fully into the world of large scale industrial applications, and there are many limitation that need to be overcome before this can occur. Some of the setbacks include poor stability to temperature, humidity, pH change and the removal of solvents from pores. One of the other major setbacks for MOFs has been that the optimization and scale-up of synthesis has proven challenging. It has been shown for a great number of systems that the relationship between synthesis parameters and final products can be difficult to predict, and has lead to many trial and error, or large-scale screenings of syntheses rather than through rational experimental design.[3, 12] Hence, more research has started to go into trying to understand the link between reaction parameters and synthetic outcome to aid in creating targeted MOF structures and to obtain a greater understanding of the processes involved in their formation.[3, 12, 13, 14, 15, 16]

5.1.2 Nucleation and Growth of MOFs

5.1.2.1 Theories of Nucleation

Classical nucleation is thought to occur homogeneous through the rearrangement of atoms, ions or molecules to form crystalline nuclei that will eventually become large enough to grow irreversibly.[17, 18] The homogeneous nucleation of particles occurs when crystallisation becomes thermodynamically favourable under conditions of supersaturation. However, this nucleation incurs a change in the free energy of the system:

$$\Delta G = 4\pi r^2 \gamma - \frac{4}{3}\pi r^3 \Delta\mu \tag{5.1}$$

where $\Delta\mu$ is the difference in chemical potential between the crystalline and liquid phases, γ is the free energy between the different phases, and r is the radius of the nuclei formed. The change in the free energy of the systems can be either negative, due to the contributions from the difference in chemical potential, or positive due to contribution from the presence of unfavourable interfacial free energy between the different phases. The theory of homogeneous nucleation can be considered an activated process, where the kinetics are determined, in part, by the critical size of the nuclei and the size at which free energy is maximised. Classical nucleation theory also infers that the most thermodynamically favourable state is obtained directly, without the formation of intermediates or amorphous species, whereas non-classical nucleation allows for the formation of metastable phases and intermediates through multiple nucleation stages.[18]

Nucleation can also occur heterogeneously in the presence of foreign objects within a solution, such as dust, bubbles or anything that can create a solid interface, and the presence of these foreign bodies means that nucleation can occur at lower levels of supersaturation.[18] This means that nucleation occurring heterogeneously is more favourable, making a larger contribution to the overall nucleation of the system, in comparison to homogeneous nucleation. This also means that nucleation processes can be influenced through the addition of foreign bodies to a system, such as substrates and seed particles to promote the formation of nuclei through heterogeneous means.[19] This is performed regularly in the world of MOFs with the introduction of modulators and capping agents into a system to alter the nucleation and growth characteristics, which can influence the obtained crystal morphology and even be used to create new structures entirely.[12, 20]

Many of the hypotheses for the nucleation of MOFs, have a strong basis zeolite in crystallisation. This, in part, is due to the fact that many MOF systems share similar structures to zeolites.[21] One of these theories proposes the nucleation of zeolites through monomer addition. This follows the idea that there is an equilibrium between forming bonds and breaking bonds within the zeolite precursor gel. These bonds will continually form and break until a thermodynamically more stable state is reached, which in general is the formation of a stable crystalline structure.

This is thought of as a classical model of nucleation, though in the case of zeolites, as the the monomeric species are present within the zeolite gel, a heterogeneous system, the formation of additional monomer species is not required, making it significantly different to the traditinoal classical nucleation model.[16, 19]

Another zeolite model that has been applied to the nucleation of MOFs is the introduction of secondary building unit. In essence, this model is an extension of monomer addition, through the formation of secondary building blocks, which are defined as the smallest structural units of the crystalline product. With this model, the amorphous gel can act as a reservoir for the secondary building blocks to form, as well as being a site for heterogeneous nucleation to occur.[22, 23] One of the major differences between monomeric addition and secondary building unit theories is that with monomeric addition, nucleation occurs within the amorphous gel, whereas with secondary building unit theory, nucleation can occur at either the surface of the gel or homogeneously.[22, 23] With the secondary building units theory, it is also important to note that, traditionally, only the final crystalline phase is produced without the formation of intermediates, meaning that the building blocks are of the same structure as that of the final crystalline product.

Essentially, when it comes to the nucleation of MOFs there are two main ideas, the first being that monomeric species, the metal ions and organic linkers, contribute to nucleation directly, or that nucleations occcurs through the formation of intermediate units, prior to the nucleation of the crystalline MOF. [24, 25, 26]

5.1.2.2 Theories of Growth

Again, the theories surrounding the mechanics of crystal growth can also be separated into classical and non-classical ideologies. Classical growth models encompass theories that indicate that upon the formation of stable nuclei, they can then grow larger through unit-cell replication and without the formation of intermediate species, hence only the formation of the final structure is observed.[27] This essentially means that both the growing nuclei and the final crystalline product are the of the same structure, and growth occurs through the attachment of smaller the species. This theory stems from the idea that under supersaturated conditions, growth is thermodynamically favourable and will yield the formation of crystalline morphologies that reduce the total Gibbs surface free energy.[16] The growth of larger particles, that further minimise the Gibbs surface free energy, is also favoured, hence the dissolution of smaller particles and the subsequent deposition on the surface of the larger particles (Ostwald ripening) is observed.[28] Classical growth ideologies also tend to rely upon the assumption that growth from a solution occurs *via* diffusion and the subsequent incorporation of monomeric species into a crystalline surface.[19, 29, 30, 31] Hence, classical growth models can be either diffusion-limited or dependent upon the rate of surface integration. When surface integration processes are favoured, the mechanism of crystal growth can occur *via* multiple different paths and is greatly dependent upon the systems level of supersaturation. For example, at lower levels of supersaturation the crystal surface tend to be smooth and growth occurs through the attachment of adsorbed units, forming energetically favourable sites of growth. This form of growth can also become self-perpetuating at very low levels of supersaturation, resulting in the formation of defects and dislocations, encouraging spiral growth or the formation of screw dislocations.[32] At higher levels of supersaturation, steps and kinks can form through birth and spread mechanisms, and as the level of supersaturation increases, growth becomes more and more favourable, resulting in the integration of growth units into the crystal surface at a greater number of sites.[30] This process is known as rough or continuous growth, and it can have and effect upon the overall appearance of the final crystalline product.

Non-classical growth models treat growth quite differently, with the main divergence of the two models being the introduction of growth through forms other than that of the attachment of smaller units, which possess the same structure as the final product. For many systems a variety of intermediate species have been observed, where they have been shown to take on a multitude of different forms, including gels, and both amorphous and crystalline metastable phases.[22, 33, 34, 35, 36] This opens up the world of growth to a multitude of possibility, with the formation of various isomers and intermediates becoming possible. This in-turn, means that reaction parameters can have a great influence upon the formation of intermediate species, and the mechanisms that are taking place throughout the formation of crystalline products. This opens up the potential for multi-step processes taking place, leading to the formation and growth through Ostwald's rule of stages.[18, 19, 37]

The main principle behind Ostwald's step rule is that the phase with the lowest free energy barrier, in relation to the solution it is within, will nucleate and grow, even if that phase is not the thermodynamically most stable, however the formation of these phases will persist until the most thermodynamically stable phase is reached. This, in essence, takes a classical growth model and adds an iterative element, meaning that the classical model can still be followed, but through the formation of multiple products.[38]

Two formation models that follow Ostwald's step rule are the solid-solid transformations and dissolution-recrystallisation models.[23] Solid-solid transformations occur through the rearrangements of solid phases, without the involvement of dissolution processes or solution-phase intermediates. This means that solid-solid transformations are limited to forming structurally related products as new building blocks cannot be created due to the lack of dissolution processes. However, dissolution-recrystallisation involves the dissolution of the reactant phases, creating a reactive solution that can form a more thermodynamically stable product. This process involves solution based intermediates and can cause dramatic changes between reactants and products.

The formation of crystalline products through the aggregation of smaller particles is also not covered by classical growth theories.[19, 27]. Aggregation is the process where smaller units come together to form a larger crystalline product that posses a morphology that is dictated by the particles it is made from. This process is generally considered to occur under kinetically controlled growth conditions, and the final obtained morphologies can be contradictory to the surface energy minimization of the systems, which again goes against the classical model of growth.

5.1.3 The Formation of Metal-Organic Frameworks

Both classical and non-classical nucleation and growth models have been reported with respect to the formation of MOFs.[39] The use of kinetic models to gain greater understanding of MOF crystallisation have been performed to great extent.[39] Avrami models are commonly utilised in the solvothermal crystallisation of MOFs, though the Avrami model was originally created for describing solid-state transformations.[40, 41, 42] The Avrami-Erofeev equation can be expressed as:

$$\alpha = 1 - e^{[-(kt)^n]} \tag{5.2}$$

Here, α is the extent of crystallisation, k is the rate constant for crystal growth, t is the reaction time, and n is the Avrami exponent, which is said to contain information on the dimensionality and mechanism of growth. For example, when $n \approx 0.54 - 0.62$, growth is said to be through diffusion mechanisms, when $n \approx 1 - 1.24$ growth occurs *via* first order or phase boundary mechanisms, and when $n \approx 2 - 3$, nucleation or growth mechanisms are observed.[43, 44] However, the use of the Avrami-Erofeev model has some limitations.[45] For example, growth and nucleation processes are undistinguishable from one another, meaning no detailed information on the the crystallisation process can be obtained. The model also assumes that crystallization occurs *via* the stepwise addition of individual molecules at a constant rate, and as the model was originally created for use with solid-state reaction, ambiguities can rise in the interpretation of the parameters within the context of solvothermal reactions. However, many XRD studies have been preformed on the formation of MOFs, and the Avrami-Erofeev model have been utilised to obtain nucleation and growth rate constants, where for the majority of probed MOFs values between 0.5 - 1.5 have been observed.[39, 46, 47, 48, 34] These values indicate that diffusion and phase-boundary controlled mechanisms prevail, however as such a wide range of values have been observed, this highlights the difficulty in finding a generalized ”one fits all” model for MOFs as a whole.[44]

Time-resolved XRD studies have also been utilised to probe the mechanistic formation of MOFs. Angle-dispersive XRD studies, along with Rietveld refinements, have provided insight on the formation of rare-earth MOFs, suggesting that in the early stages of crystallisation, they form water-rich structures that are subsequently dehydrated as the water is exchanged with organic ligands towards the later stages of formation.[34] These observation are said to show the formation of secondary building units in MOF systems. The secondary building units are thought to assemble within solution from monomeric metal precursors, something that has been probed using X-ray absorption spectroscopy (XAS).[35] XAS was utilised to follow the formation of MIL-89 from trimeric Fe^{3+} acetate, and it was found that Fe trimers remained present throughout the entire crystallisation process.[35] This includes the formation of amorphous intermediate species and the final product, providing strong evidence towards the hypothesis of secondary building units. Similar evidence has also been observed with the formation of Mn-MIL-100, where during crystallisation, where Mn^{3+} species are formed from Mn^{2+} precursors prior to formation the final product.[49] This again showed that the mechanism of formation occurred in two stages, with the initial formation of Mn^{3+} secondary building units, and then subsequent formation of the crystalline product.

Non-classical growth in MOFs has also been presented in a variety of studies.[39, 50, 51, 52] In 2010, Walton *et al*, utilised time-resolved energy-dispersive XRD methods to follow the crystallisation of HKUST-1 and MIL-53. Whilst results from the study on HKUST-1 revealed classical growth mechanics, a different story was observed with MIL-53.[39] The growth of MIL-53 was more consistent with Ostwald's step rule, with the formation of MOF-235 as an intermediate phase prior to the formation of MIL-53. In this synthesis.[36] However, the formation of the MOF-235 as an intermediate phase only occurs when MIL-53 is synthesised in protic solvents, and the presence of an intermediate phase is not observed when preforming the synthesis in water.[50, 51, 52]

The formation of crystalline intermediates has also been observed in the formation of lithium tartrate MOFs, where the formation of three competing intermediate phases has been reported.[53] This study shows the formation of two low-density intermediates prior to the formation of the thermodynamic product. Kinetic analysis of the system suggested that the thermodynamic product possesses a much greater activation energy than that of the intermediate species, hence the formation of the final product is more favourable as it requires a transformation of the ligand conformation.

The formation of MOF-5 has proven to be a complex system, with a variety of time-resolved studies being performed on the system.[54, 55] These studies have unveiled that the formation of MOF-5 proceeded *via* the formation of at least one intermediate phase, however the formation of this intermediate depends greatly upon the physical paramaters implemented (time, temperature and the presence of mechanical stirring).[54] With higher temperature syntheses (140°C), the intermediate formed was observed to be MOF-69c, which would then form MOF-5 through the reaction with additional terephthalic acid. Other studies found that when synthesised at 110°C, a layered Zn(BDC)(DMF) intermediate structure formed alongside dimeric secondary building units.[55] This observation was made upon quenching samples for *ex-situ* measurements to be taken, though when *in-situ* experiments were preformed, a layered $Zn_3(BDC)_3(H_2O)_3$ compound with trimeric secondary building units were observed. Neither of these layered structures correspond to the MOF-69c observed in the study preformed by Wu *et al*, and the formation of these different intermediates is thought to be down to the differences in synthesis parameters used. [55]

Studies have also provided evidence for dissolution-recrystallization mechanisms, when going from crystalline intermediates to the final product.[56] In dissolution-recrystallization mechanisms, the intermediate species transform into the final product through the rapid dissolution and subsequent recrystallisation of a crystalline intermediate species to produce larger particles with a different crystalline structure.[56] It has also been shown that some desirable products are not necessarily the thermodynamic product but are a metastable intermediate form. This has been in many MOF systems where the thermodynamic product can often be non-porous. This illustrates some of the difficulties associated with the synthesis of MOFs, and one of the main reasons for studying the formation of these systems is to obtain a better understanding on how to easily synthesise materials with desirable properties, and without the formation of non-desirable intermediates, or in certain cases the thermodynamic product.

A good example of an intermediate phase being the desirable product is observed witht the formation and collapse of MOF-14.[57] When MOF-14 is exposed to higher temperatures for prolonged periods of time the structure collapses into Cu_2O. This process shows the importance in tailoring of synthesis parameters for desirable products to be formed. Other studies have also shown, that heating zinc oxalate and piperazine together at increasing temperatures, can yield a variety of different structures with increasing dimensionality.[58, 59] It was shown that 1D helical chains, 2D honeycomb structures and 3D layered pillars can all formed depending upon the heating regime used, and at the highest temperatures the 3D layered pillar structures formed through the progressive build-up of the forms with lower dimensionality. Similar findings have also been observed with *ex-situ* time-resolved XRD studies on manganese oxy-bis(benzoate) structures, where it was found that upon increasing the temperature of the system, 1D wire-like structures would form and would transition into 2D layered structures before finally forming a 3D network.[60] The structures also showed increasing levels of dehydration leading to the conclusion that the change in dimensionality may have been driven by entropy of dehydration.

It has also been shown that the formation of MOFs can be effected by the method of heating used at synthesis.[36, 61, 62, 63, 64] For example, MIL-53 was synthesised using a two-step procedure to probe nucleation and growth processes independently, and it was shown that nucleation and growth rates change depending on the form of heat applied to the system.[64] Of the three heating methods used, ultrasonic heating was shown to be the fastest, closely followed by microwave heating, whilst conventional heating was significatly slower, with significant drops observed in the speed of nucleation and growth.[36, 61, 62, 63, 64]

5.1.4 Formation of Zeolitic imidazolate frameworks (ZIFs) from solution

ZIFs are a class of MOFs compromised of imidazolate linkers and metal cations arranged in tetrehedral coordinated frameworks. The structures formed by ZIFs are similar to those observed in zeolites, and they are intrinsically porous, and have been shown to have good thermal and chemical stabilities. These properties have lead to much interest from the scientific community to harness the properties of ZIFs, and exploit them in commercial applications.

XRD has shown to be a popular technique for probing the formation of ZIFs.[48, 65, 66] Studies performed on the formation of ZIF-8 have observed the formation of small clusters prior to crystallisation. Time-resolved XRD studies have been deployed to probe the nature and formation of these clusters to better understand their nature. Such studies have shown that these clusters are either amorphous or only possess medium-range order, before transitioning into the final crystalline form.

The formation of partially ordered intermediates has also been probed using using XRD with ZIF-67, which is a cobalt-substituted structure analogous to ZIF-8.[48, 65] This study followed both nucleation and growth phases, revealing that after only short synthesis times, peaks in the data were observed. It was suggested that these observations could result from the formation of low crystallinity ZIF-67 species with medium-range order, which the author deemed to be a metastable intermediate phase.

Light scattering experiments have also played a key role in helping to understand the formation of MOFs *in-situ*. Static light scattering (SLS), which measures the scattered intensity as a function of angle, which can be related to the radius of gyration, has been utilised to follow the formation of ZIF-8 in methanol, where the rapid formation of c.a. 50 nm particles was obsereved within the first few minutes of the reaction.[68, 69] It was also hypothesised that the presence of larger particles within the system was due to the aggregation/agglomeration of smaller nanocrystals. Similar observations have been made using dynamic light scattering (DLS),

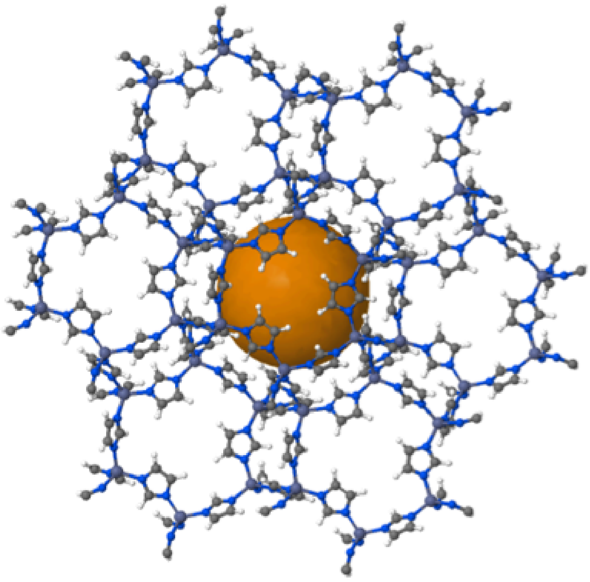

Figure 5.1: Structural representation of ZIF-8.[67]

within other ZIF structures. DLS is used to estimate particle diffusion through the Stokes-Einstein relation, which can be related to a particles hydrodynamic radius, and experiments preformed on the formatoin of ZIF-zni (a dense zinc imidazolate framework), using DLS revealed that the formation occurs through two distinct steps.[70] The formation of 120 nm primary particles is observed first, which is subsequently followed by the formation of aggregated secondary particles, similar to observation made with SLS experiments on ZIF-8.[69]

Combined SLS/DLS and SAXS/WAXS studies have also been utilised for probing the formation of ZIF-71.[71] The authors, initially observed the formation of amorphous clusters followed by subsequent growth through aggregation to form larger amorphous particles, prior to the formation of crystalline ZIF-71, which was proposed to occur *via* particle reorganization. *In-situ* SAXS/WAXS studies have also been deployed to observe the formation of ZIF-8, where the formation of amorphous intermediates was probed.[15] This study observed the initial formation of c.a. 1 nm clusters, which subsequently disappeared with the formation of larger particles. Other SAXS/WAXS studies have probed the growth of ZIF-71, with the authors suggesting that growth proceeds through the formation of small clusters, prior to the formation of larger amorphous particles and the subsequent formation of crystalline ZIF-71, whihc is said to occur through a solid-solid transformation.[71, 23] It was proposed that growth occurs *via* monomer addition, where the monomers could be either the small clusters observed in the early stages of the synthesis, oligomers or individual metals and linkers.

Atomic force microscopy (AFM) studies has also proven helpful in exploring the formation of ZIFs.[72, 73, 74, 75] AFM studies have shown that the formation can occur *via* more classical routes at low levels of supersaturation. *In-situ* AFM was deployed to probe the growth of ZIF-8 in DMF, giving indications that growth can occur through the classical birth and spread mechanism with spiral growth occuring simultaneously at the (110) crystal face.[72] However, *in-situ* studies on ZIF-76 and ZIFs with LTA structures have resulted in the observations of high nucleation rates proceeding through the birth and spread mechanism, though as the level of supersaturation begins to decrease, spiral growth is subsequently observed. It was also shown that growth proceeds *via* step wise, two-dimensional nucleation and the further spreading of metastable sublayers, and it was noted that the sublayers were temporarily bridged, and stabilised through non-framework species prior to the formation of stable terraces, a finding that would also be observed is other MOF systems.[73, 74, 75]

The step heights of growing MOF crystal interfaces have also been probed using AFM, identifying fundamental growth units.[72, 73, 76, 75, 77] Step height analysis has revealed the presence of monomeric species, and not the presence of full secondary building units, alongside non-framework species acting as stabilisers for partially formed layers. It was also found that the observed growth mechanism was highly dependent upon the relative metal:ligand concentrations. Many of these studies share the idea that the simple solvated metal ions and linkers, instead of larger units, should be considered as the fundamental growth units.

TEM studies have also been used to probe the growth of ZIF-8 in real-time.[78, 46] The study preformed by Patterson *et al*, concluded that the formation of ZIF-8 does not actually occur through the aggregation of particles, but from the growth of subunits within solution. This result is consistent with some results obatined from SAXS/WAXS experiments, where nucleation is said to be limited by the depletion of reactants from the solution, resulting in limited growth.[33] Other high-resolution TEM studies have also shown the formation of armchair and zigzag termination along the (110) face of the ZIF-8 crystals.[79] It was also shown that coherent interfacial structures were found between crystals.

The formation of small pre-nucleation clusters has also been explored using TEM studies, where it was shown that the formation of crystalline ZIF-8 occurs in four stages.[46] First nucleation occurs, followed by crystallisation, growth and stationary periods. The authors proposed that the formation of ZIF-8 proceeds from a gel solution, where crystalline growth occurs at the expense of the gel, similar to hypotheses seen in the world of zeolites.[23, 80] The authors also indicated that the formation of medium-range ordered ZIF-8 intermediates occurs prior to the formation of crystalline particles through either solution or solid mediated mechanisms.[46]

This chapter focuses on probing the formation of ZIF-8 using time-resolved *in-situ* SAXS/WAXS techniques to monitor the nucleation and growth of crystalline ZIF-8 in flow. The use of simultaneous SAXS/WAXS measurements allows for particle size and shape to be monitored, alongside crystallinity and allows for the easy observation of any intermediate stages (crystalline or amorphous) that may produced during the formation of ZIF-8.

5.2 Experimental

In-situ SAXS/WAXS studies were preformed on the formation of ZIF-8 samples in-flow at Diamond Light Source beamline I22 (figure 5.2). Two precursor solutions were prepared, one containing zinc nitrate hexahydrate, and the other containing 2-methylimidazole in methanol. The 2-methylimidazole solution was placed within a PTFE round bottom flask and flowed through PTFE tubing and a glass capillary using a peristalitic pump. The round bottom flask was placed within an oil bath so that the temperature could be regulated during experiments. The zinc nitrate solution was placed within a syringe, which was subsequently placed in a syringe

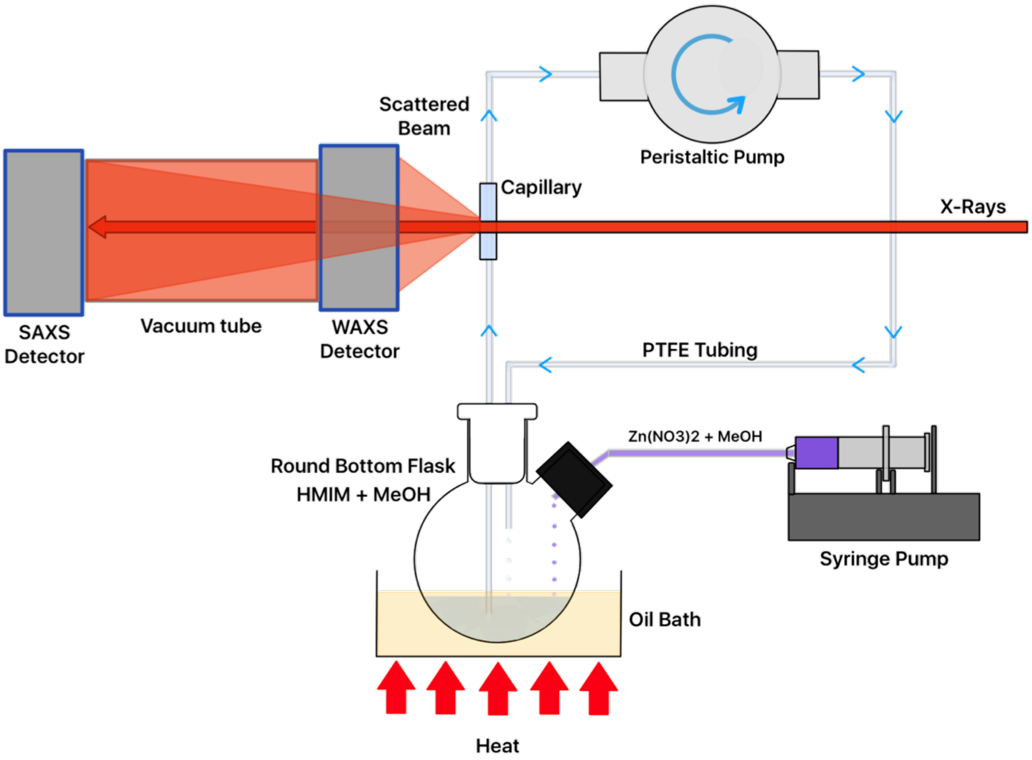

Figure 5.2: Diagram of the experimental set-up used at beamline I22 at Diamond light source for preforming *in-situ* SAXS measurements on the formation of ZIF-8.

pump that could be controlled remotely, so the reaction could be triggered simultaneously with data collection. ZIF-8 samples were prepared with a total molar ratio of Zn:Hmim:MeOH 1:8:550. Both SAXS and WAXS data was collected simultaneously providing a total accessible q-range of 0.003 - 3 $Å^{-1}$ using two Dectris Pilatus 2M detectors.

5.3 Results and Discussions

Figures 5.3 and 5.4 shows the *in-situ* WAXS data collected on the formation of ZIF-8 at three different temperatures. All observed Bragg reflections correspond to the body centred cubic lattice of ZIF-8, without the presence of other phases throughout the crystallisation process. This indicates that ZIF-8 is the only crystalline product formed under these conditions, with the formation of any transient crystalline phases. It can also be seen that temperature can have a great upon the speed that crystallisation occurs, with crystalline products observed after c.a. 400,

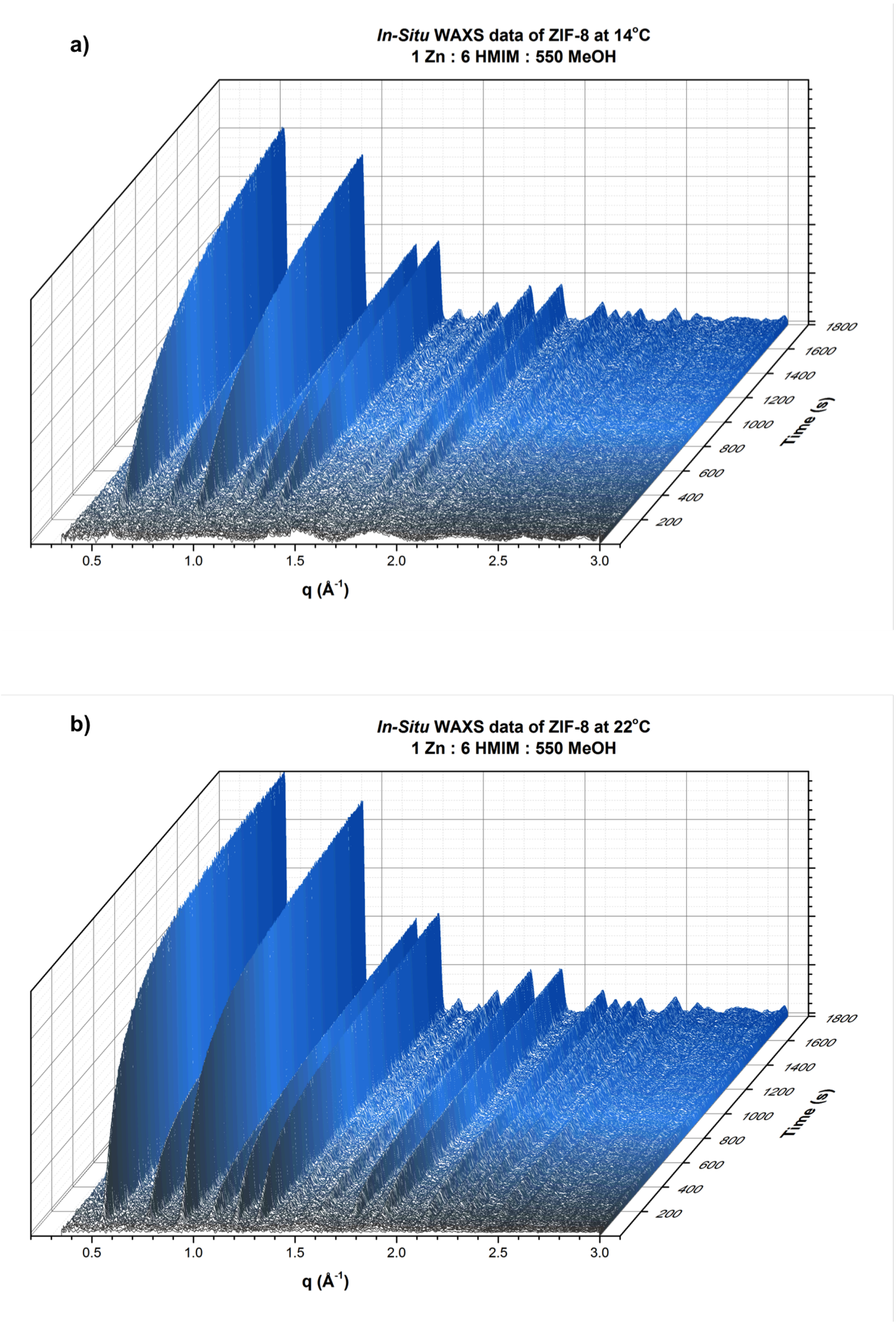

Figure 5.3: Waterfall plots of the *in-situ* WAXS data collected on the formation of ZIF-8 at 14 (a), 22°C (b)

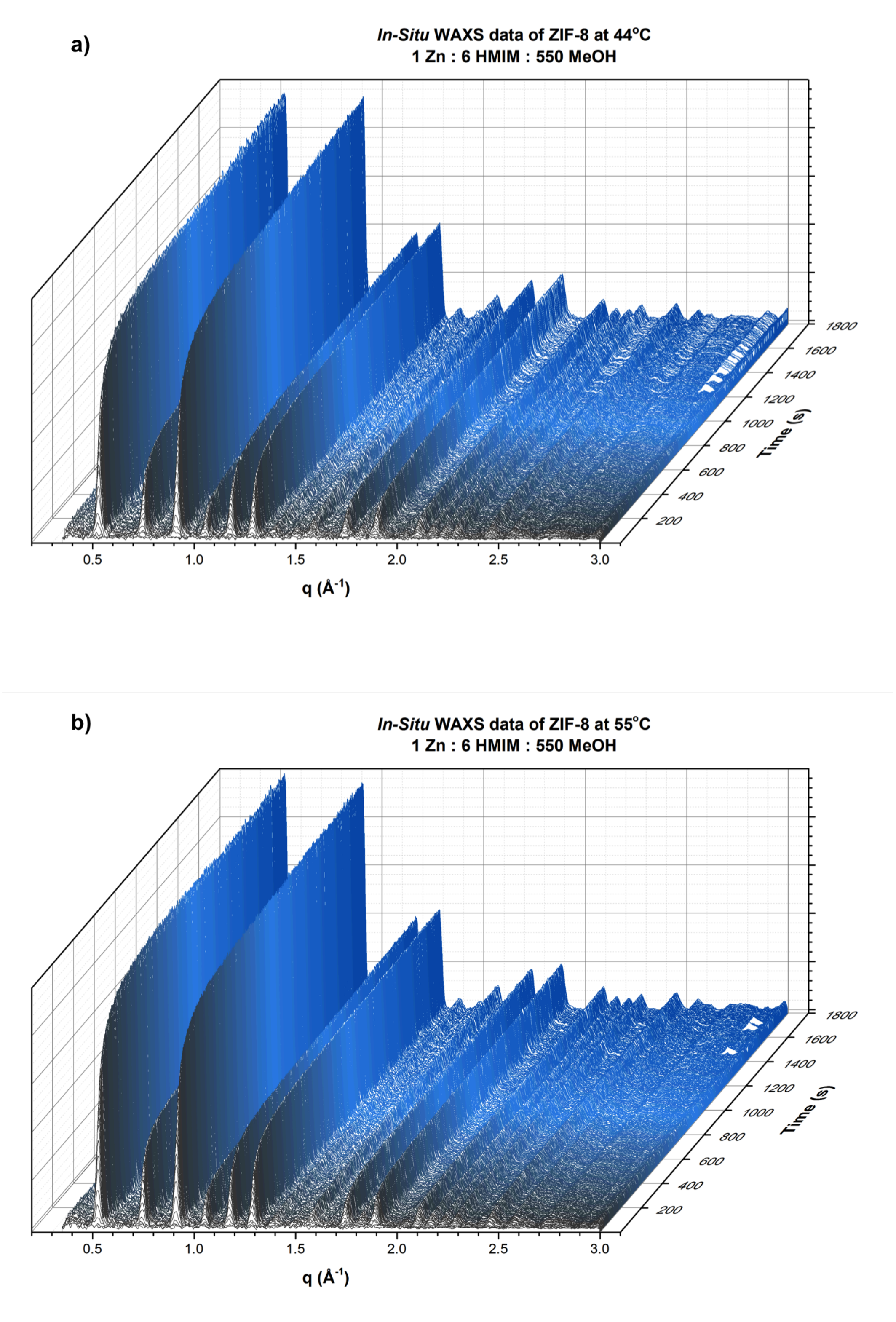

Figure 5.4: Waterfall plots of the *in-situ* WAXS data collected on the formation of ZIF-8 at 44 (a) and 55°C (b)

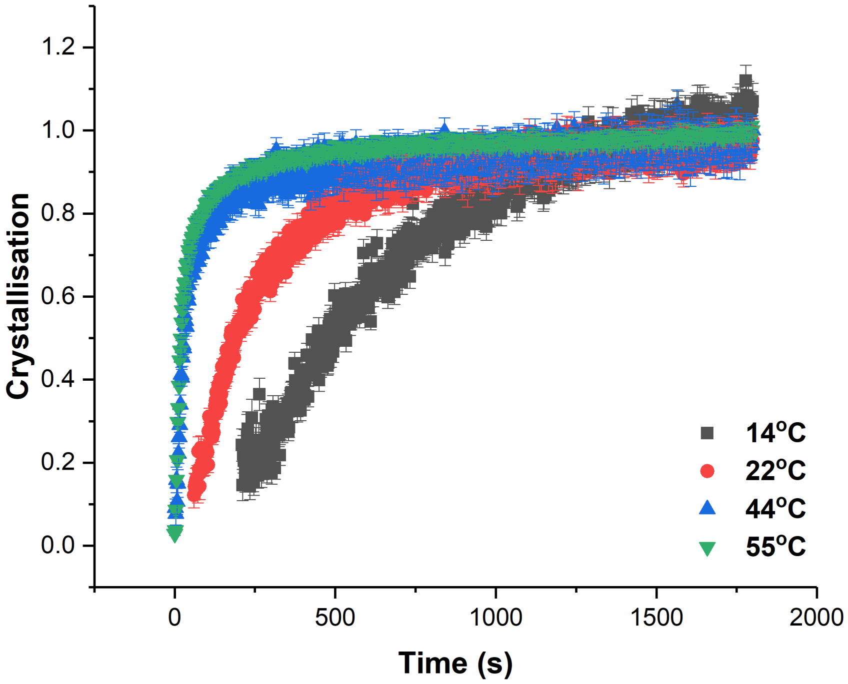

Figure 5.5: Rate of crystallisation of ZIF-8 at 14, 22, 44 and 55°C.

100, 4 and 2 seconds at 14, 22, 44 and 55°C respectively.

Figure 5.5 shows a plot of crystallisation versus time, where the intensity of the 211 reflection was normalised to the the intensity observed at the end of the experiment. It can be seen that at higher temperatures the crystallization process initially occurs rapidly, before slowing, which could be indicative of a different crystallisation mechanisms become more prevalent, such as Ostwald ripening.

From the *in-situ* WAXS data crystallite size was estimated using the Williamson-Hall method (figure 5.6). This shows that, in general, with increasing synthesis temperature, smaller crystallites are observed. This could indicate that at increased temperatures, nucleation is more favourable, leading to the formation of a greater number of nuclei, limiting their overall growth due to the lack of nutrients in the later stages of the experiment. However, when comparing estimated crystallite size from experiments at 44 and 55°C the reverse is observed, with larger estimates for crystallite size observed at the highest temperature. However, from the WAXS data no obvious explanation for this change in trend can be deduced.

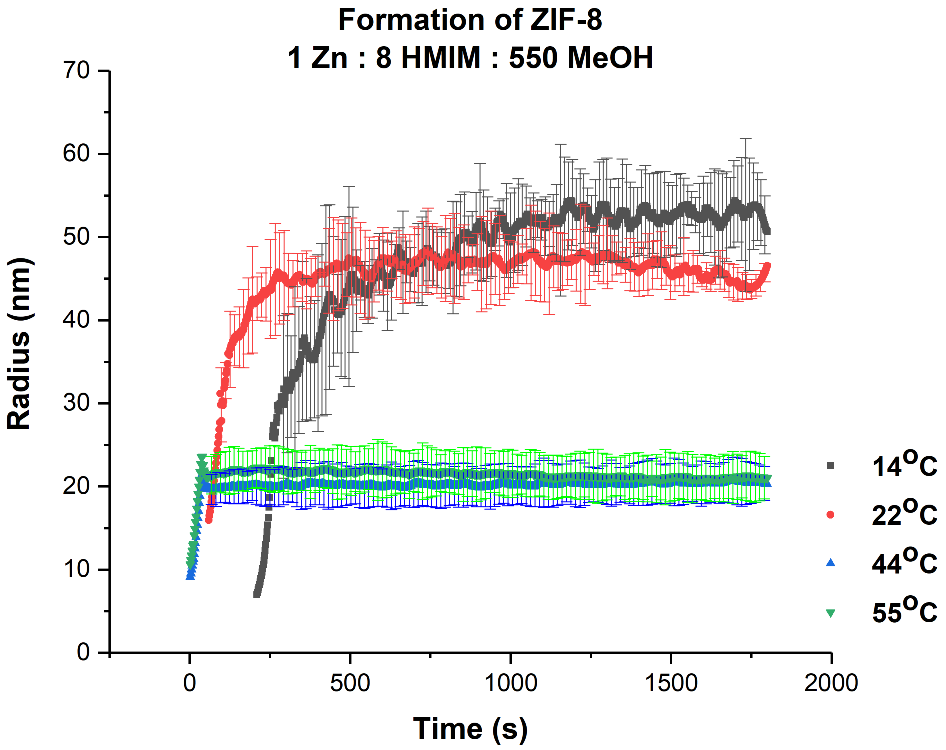

Figure 5.6: Crystallite sizes obtained from Williamson-Hall plot on the WAXS data obtained from on the formation of ZIF-8 at 14, 22, 44 and 55°C.

Figures 5.7 and 5.8 shows the *in-situ* SAXS data recorded simultaneously with the corresponding *in-situ* WAXS data (figures 5.3 and 5.4) on the formation of ZIF-8 at four different temperatures. It can be seen that altering the synthesis temperatures can have a significant effect on the size and polydispersity of the particles formed.

The first thing that becomes visible in the data is that at the start of the reaction there are no visible population of particles observed. However, after a few seconds in each reaction small clusters of particles are observed. These clusters are observed in the data at $q > 0.1\ \mathring{A}^{-1}$, after 12, 6, 2 and 1 seconds at 14, 22, 44 and 55°C respectively. Figure 5.9 shows fits of the SAXS data at high-q where it can be seen that the size of these clusters appears to be temperature dependent, with an average size of 1.12 nm observed at 14°C and 2.3 nm at 55°C. It can also be seen that the distribution of these clusters is relatively narrow, and they are visible in the background subtracted SAXS data for different periods of time, again depending

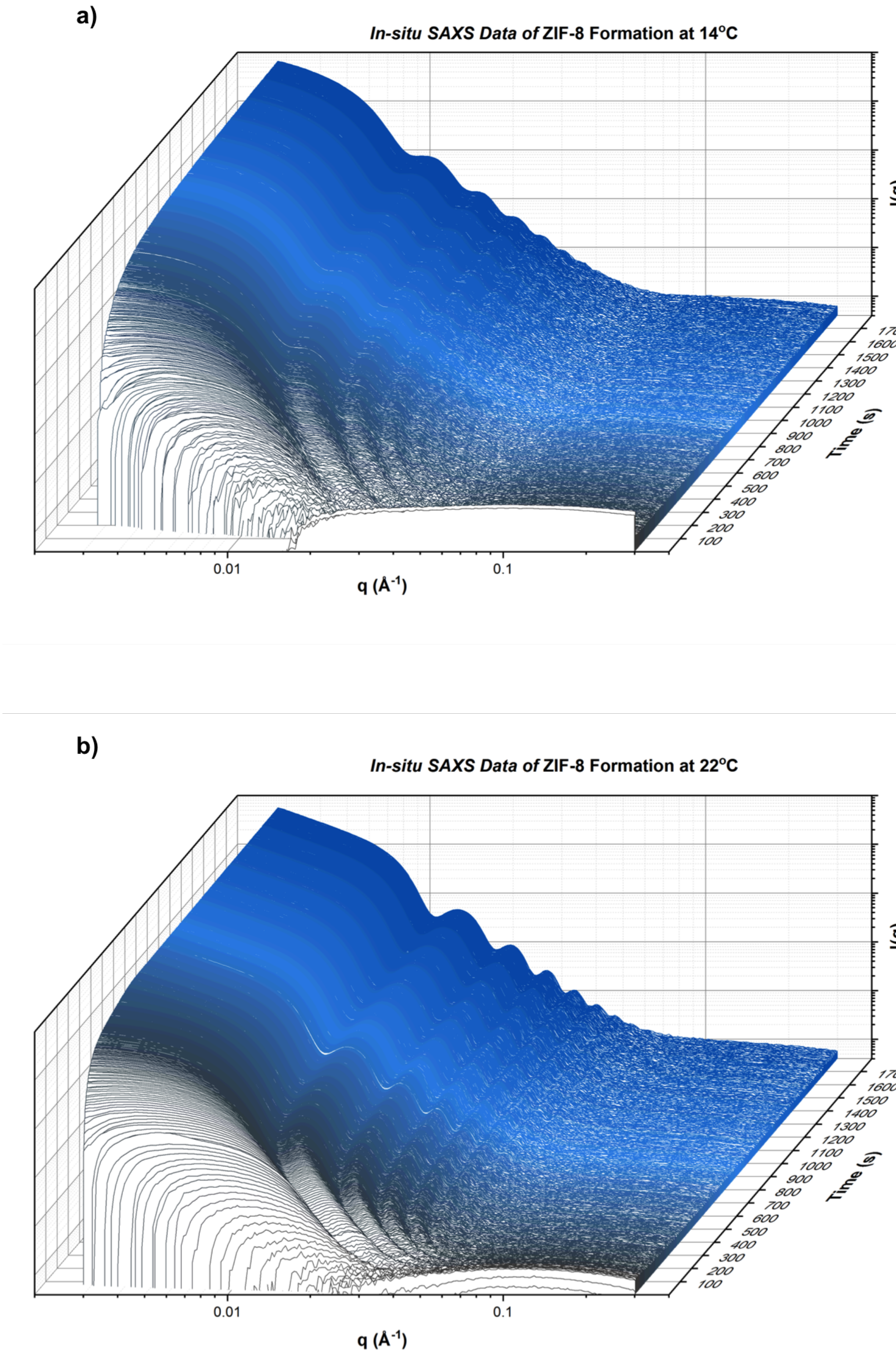

Figure 5.7: Waterfall plots of the *in-situ* SAXS data collected on the formation of ZIF-8 at 14 (a) and 22°C (b).

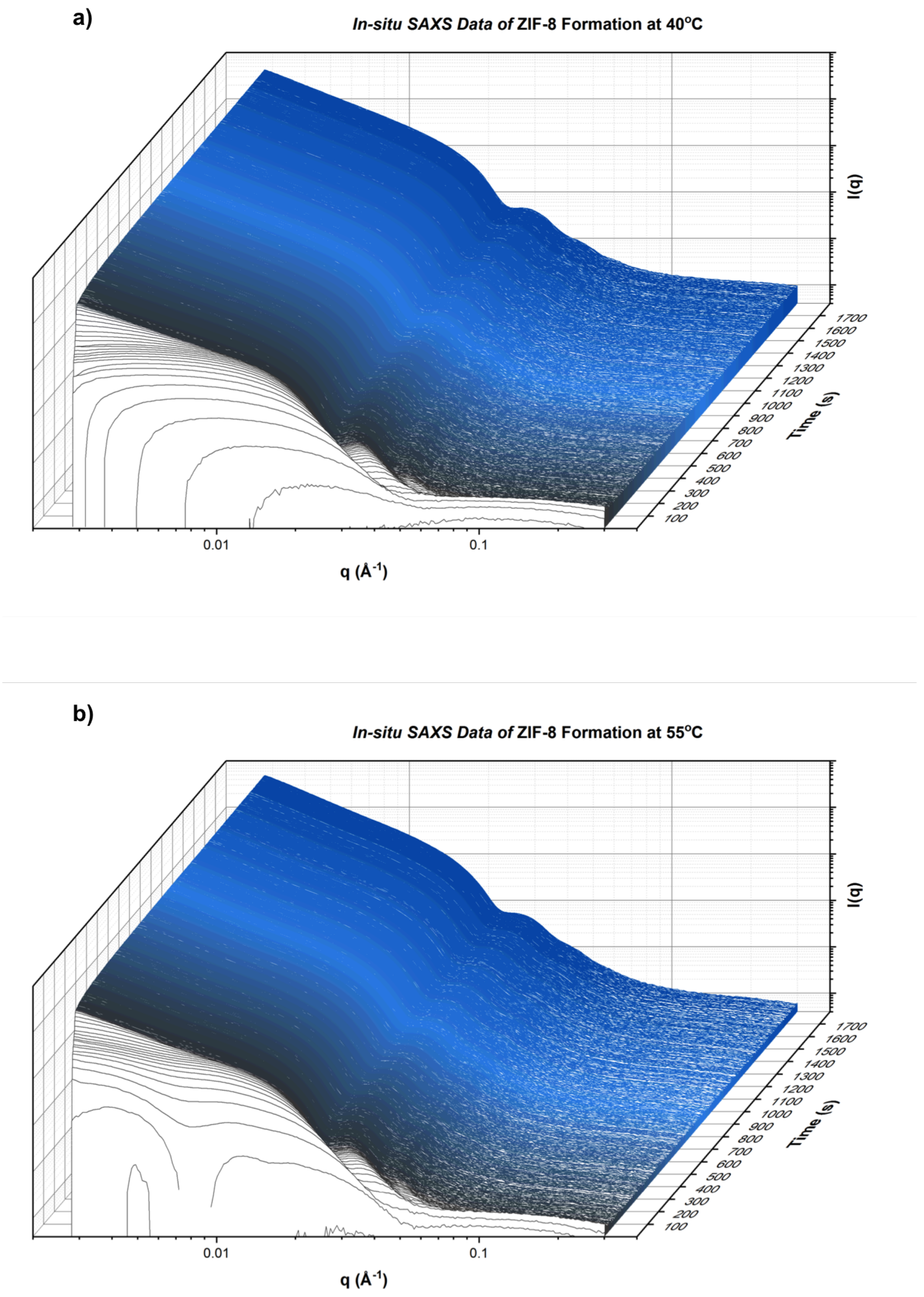

Figure 5.8: Waterfall plots of the *in-situ* SAXS data collected on the formation of ZIF-8 at 44 (a) and 55°C (b).

upon the synthesis temperature (figures

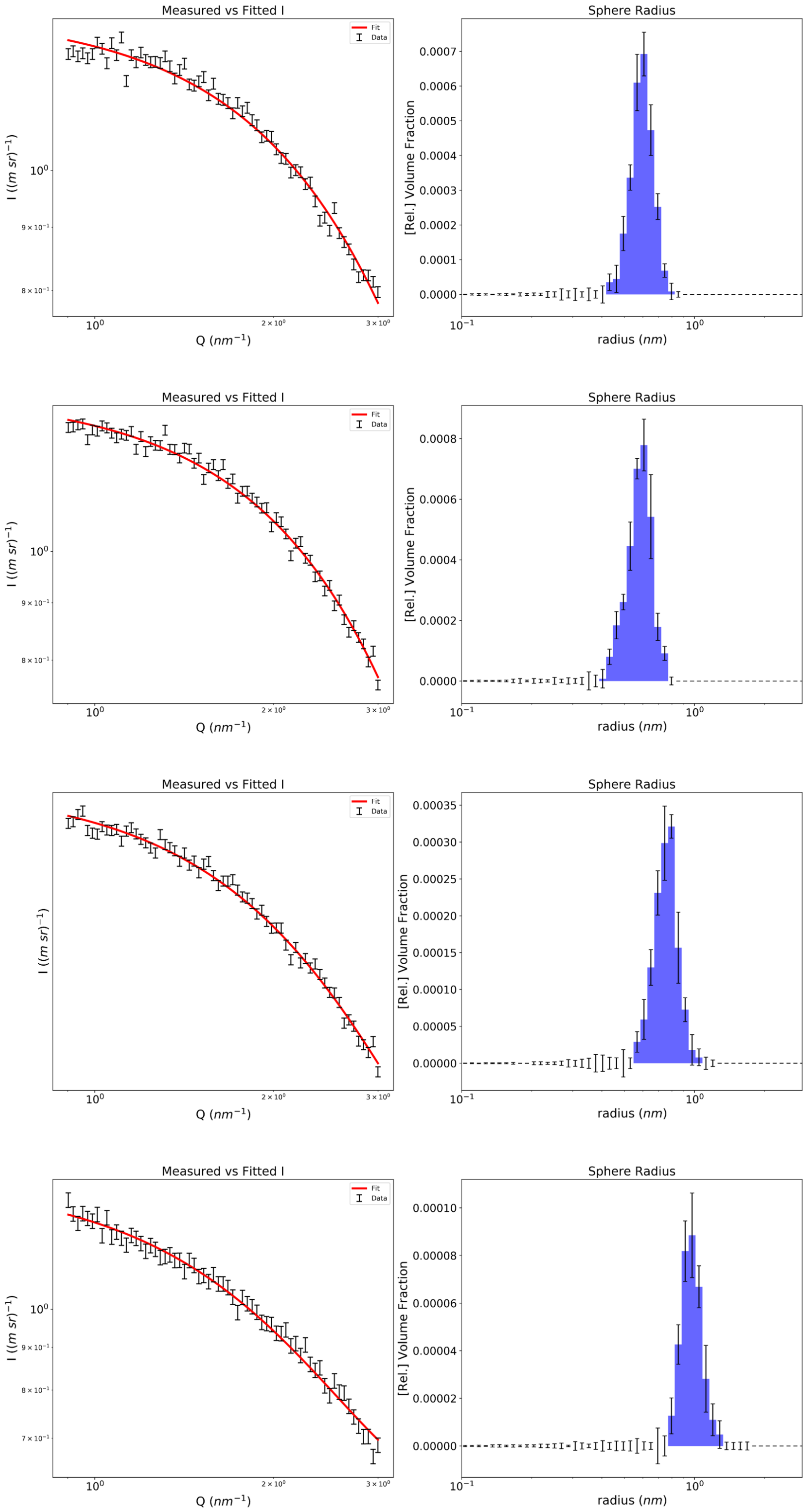

Figure 5.9: Monte Carlo fits of SAXS data for the formation of small particles formed initially in the formation of ZIF-8 at 14 (a), 22 (b) 44 (c), and 55°C (d).

This figure also shows the presence of an isosbestic, which is only observed within SAXS when two solid states dominate the scattering during growth, where the scattering of smaller particles is observed towards higher-q and that from the larger particles is observed towards lower-q.[81] The presence of an isosbestic point strongly indicates that the larger particles are formed from these smaller clusters, and it provides evidence that no intermediate stage or stages are formed between that of the clusters and the larger particles. This is because an isosbestic point indicates that whilst the concentration of the large scatterers increases over time, the opposite is observed with the small clusters. It should also be noted that the appearance of the larger particles also coincides with the first observations of Bragg peaks in the *in-situ* WAXS data, indicating that these larger particles are actually crystalline ZIF-8 particles.

It can also be seen in figures 5.10 and 5.11, that the isosbestic point shifts to higher-q with increasing temperature, indicating at lower temperatures there is a larger average volume between the two physical states, indicating that at lower temperatures the smaller particles cluster together more efficiently. This would result in the observation of larger particles at lower temperatures. It is also possible to see in figures 5.10 and 5.11 that as the scattering increases for the larger particles, a decrease in scattering is observed for the cluster particles, which is a good indication that the clusters are directly involved with the nucleation of the larger ZIF-8 particles.

From fits of the SAXS data (figures 5.12 and 5.13), it can be seen that synthesis temperature can have a large impact in the overall particle distribution observed (appendix c). At 14°C it can be seen that a much broader distribution of particles is observed in comparison to other synthesis temperatures. It can be seen that the population of ZIF-8 particles is polydisperse with the largest observed particles being c.a. 60 nm by the end of the experiment. The growth of particles can be observed over time, and it can be seen that at 14°C the initial growth of particles occurs much slower than at higher temperatures. The broad range of observed particles could be indicative of a low rate of nucleation, which results in the formation of a broader

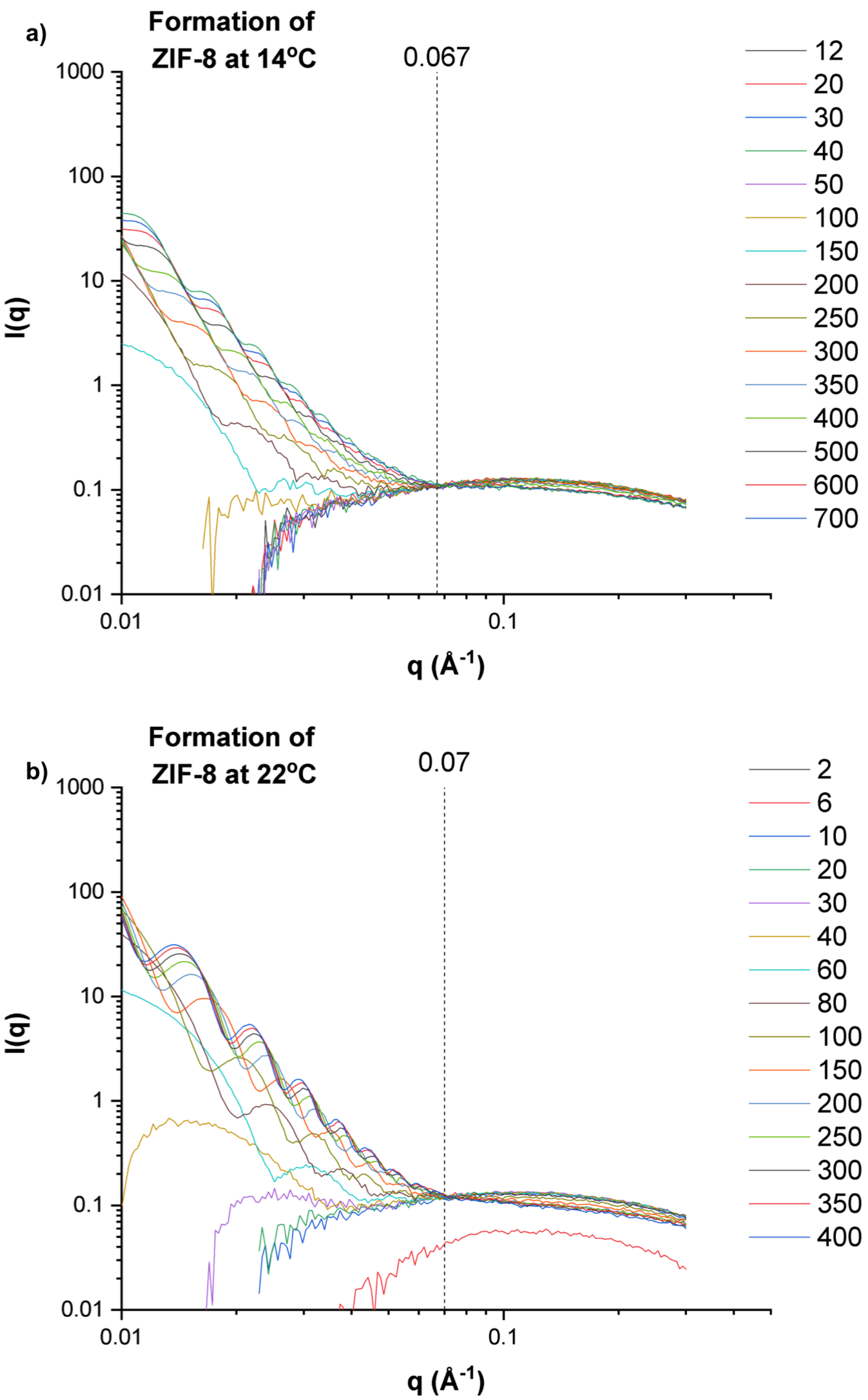

Figure 5.10: Background subtracted time-resolved SAXS plots for the formation of ZIF-8 at 14 (a) and 22°C (b) showing the isosbestic point. The numbers within the legend represent time in seconds.

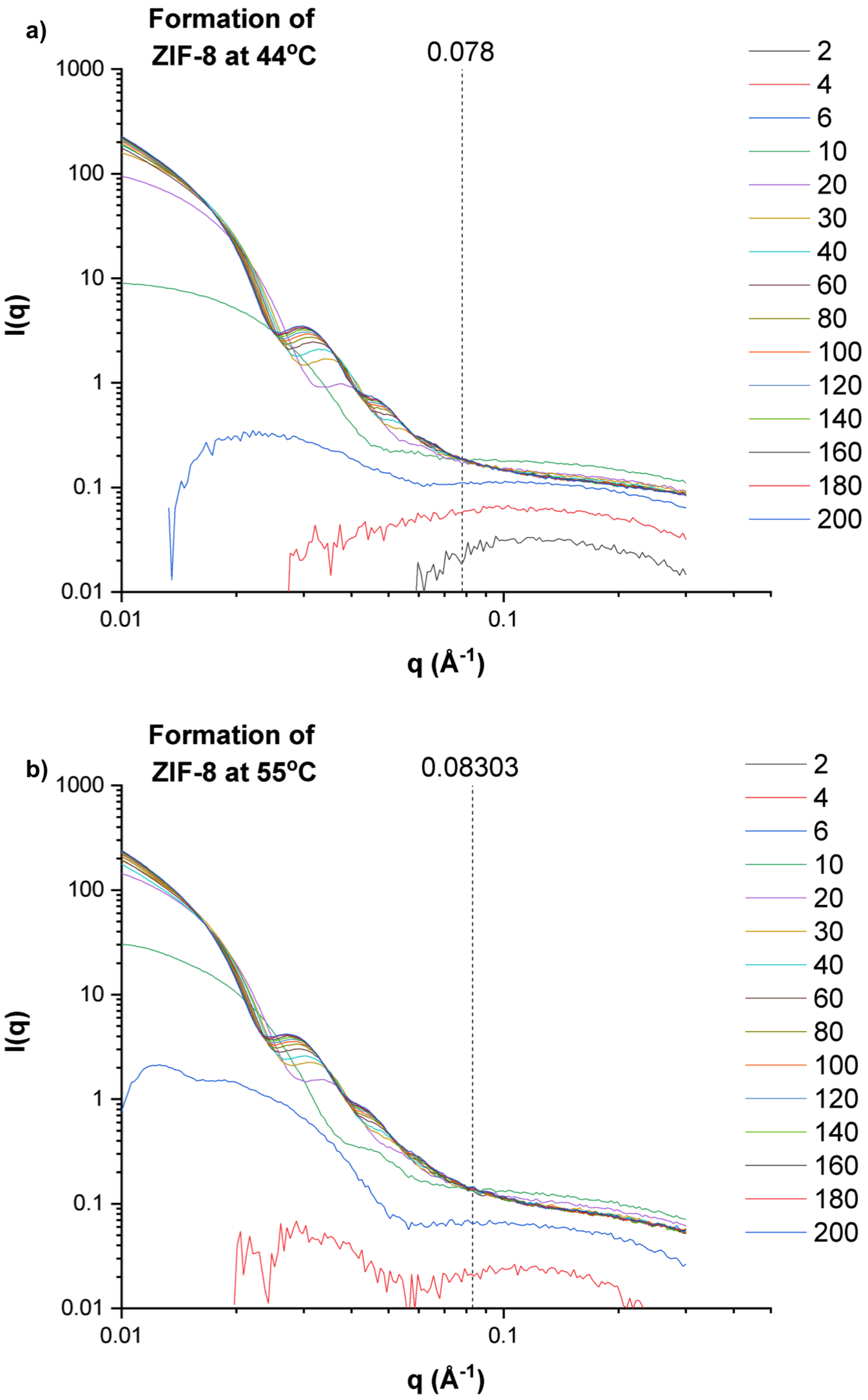

Figure 5.11: Background subtracted time-resolved SAXS plots for the formation of ZIF-8 at 44 (a) and 55°C (b) showing the isosbestic point. The numbers within the legend represent time in seconds.

range of particles with larger average particles size.

At 22°C a much more monodisperse population of particles is observed, with a final particle size of c.a. 45 nm observed. It can be seen that, in comparison to a synthesis temperature of 14°C, the growth of particles occurs much faster. It can also be seen that after the initial growth of particles, the growth begins to slow rapidly after 300 seconds.

At 44°C a relatively narrow population of particles is observed c.a. 20 nm after 1800 seconds. It can be seen that the initial growth of particles is very rapid, however, at this temperature secondary populations of larger particles are observed. These larger particles do not grow from the smaller particles, indicating that they are most likely formed from aggregates. These aggregated particles are also observed growing similar to that of the primary population of particles. The presence of these larger aggregate particles can also be seen in the SAXS data (figures 5.7 and 5.8) as towards the end of the experiment the SAXS data at low-q tends towards a gradient of q^{-4}, indicating the presence of larger structures.

At 55°C a relatively narrow population of particles is initially observed, whilst the presence of larger aggregates is observed after c.a. 100 seconds. The volume fraction occupied by these aggregate particles is more than previously seen with a synthesis temperature of 44°C, and the presence of multiple larger population is also visible at this higher temperature. However, the aggregates are also observed to grow independently. At a synthesis temperature of 55°C the observed particles are slightly larger than those observed at 44°C. This goes against the trend observed with higher temperatures resulting in the formation of smaller particles. This can be better observed in figure 5.14 that shows the average particle sizes obtained from fits of the *in-situ* SAXS data.

Figure 5.14 shows the average particles sizes obtained from Monte Carlo fits of the *in-situ* SAXS data at each temperature. It can be seen that, in general, that at higher temperatures smaller particles are formed, however this does not hold true when comparing the synthesis at 44 and 55°C. The observed increase in average particle size at 55°C could be due to the presence of larger aggregated particles

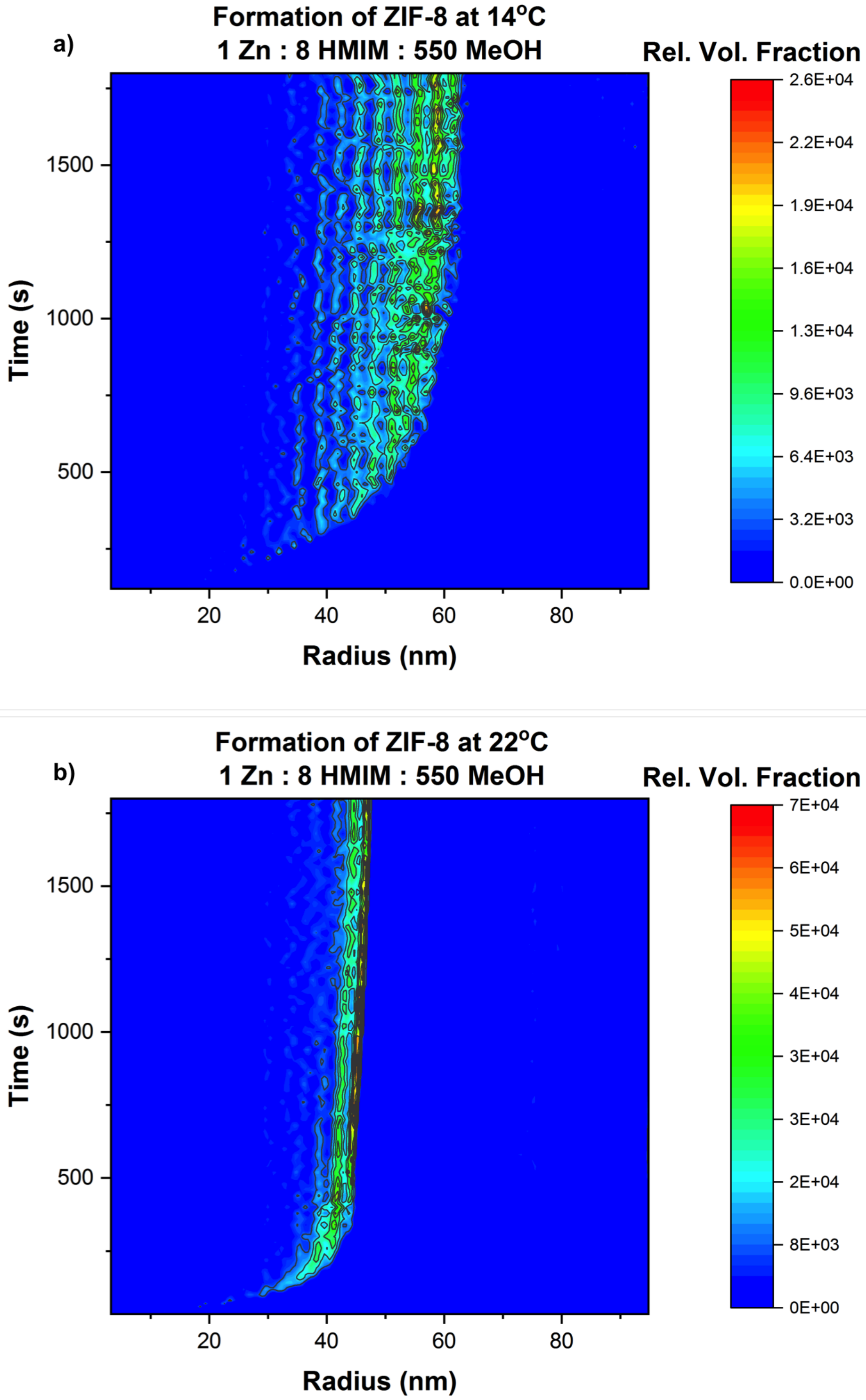

Figure 5.12: Colour contour plots of the SAXS fit data for the formation of ZIF-8 at 14 (a) and 22°C (b).

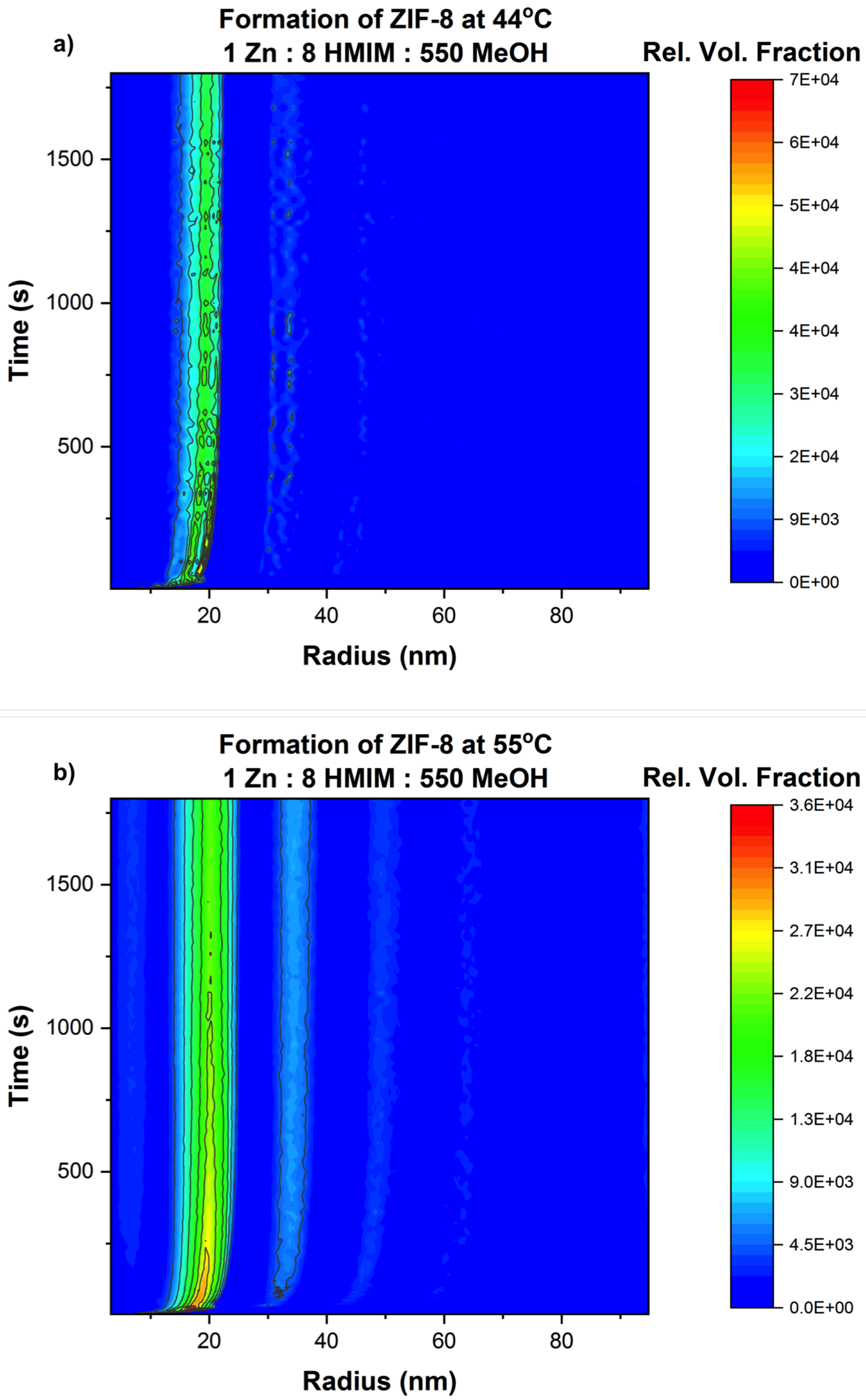

Figure 5.13: Colour contour plots of the SAXS fit data for the formation of ZIF-8 at 44 (a) and 55°C (b).

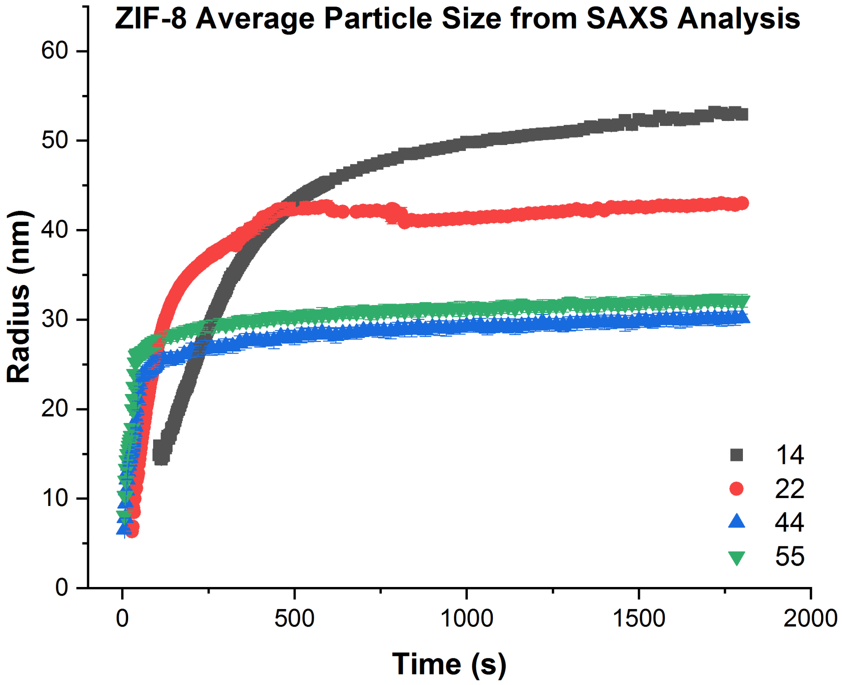

Figure 5.14: Average particle radius obtained from Monte Carlo fitting of SAXS data obtained from following the formation of ZIF-8 at 14, 22, 44 and 55°C.

being present at higher temperatures, however when looking at the data presented in figure 5.13, it can be seen that the primary group of particles are of a greater size than those observed at 44°C.

If the values obtained for average size from Monte Carlo fits of the *in-situ* SAXS data are looked at more closely (figure 5.15) it can be seen that growth does not occur continuously, but looks to occur in steps. This can be seen most prominently at higher temperatures but can also be seen at 22°C, where the steps occur over an elongated period of time. This trend is not observed at 14°C, however it is thought that the trend may not be visible due to the slower formation times smearing the trend.

Figure 5.15 shows that at 55°C, the particles that are formed initially are slightly larger than those observed at 44°C, this could be attributed to the presence of larger pre-nucleation clusters being present at higher temperatures, however it can also be seen that the initial growth at 55°C occurs slightly faster than at 44°C.

This is then followed by a secondary phase of rapid growth observed after c.a. 25 seconds of synthesis at 55°C.

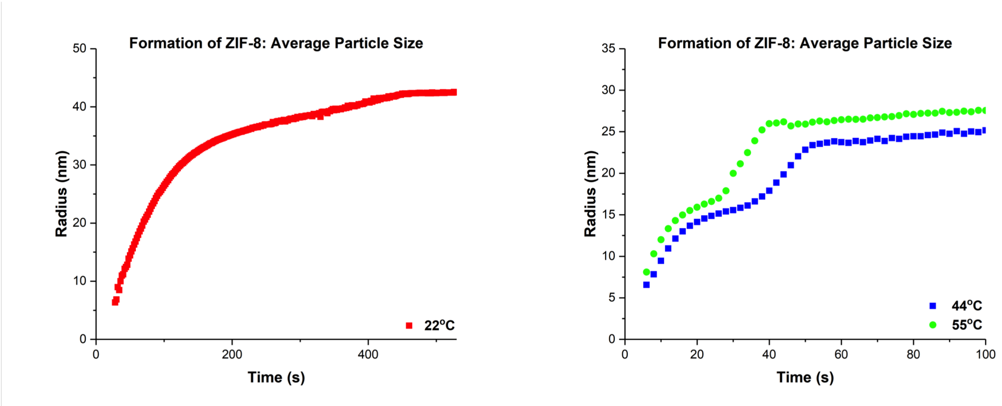

Figure 5.15: Average particle radius obtained from Monte Carlo fitting of SAXS data obtained from following the formation of ZIF-8 at 22 (a), 44 and 55°C (b).

When this trend is looked at with respect to the rest of the data presented in this chapter, the different steps can be attributed to significant moments observed in the formation of ZIF-8. Initially, the formation of small amorphous clusters occurs this is then followed by the nucleation and growth of crystalline ZIF-8, which is thought to proceeds by the following steps (figure 5.16):

1. Nucleation of crystalline ZIF-8 begins, in tandem with cluster formation.

2. The isosbestic point is then reached, where formation of clusters ends, but the nucleation and growth of crystalline ZIF-8 particles continues at the expense of the decreasing population of cluster particles. This correlates to the presence of an isosbestic point, which indicates that there is a conversion between no more than two phases, meaning that the clusters are directly converted into crystalline ZIF-8.

3. Population of cluster particles is fully depleted at this point, and the nucleation of crystalline ZIF-8 becomes less favourable in comparison to growth (*via* monomer addition).

4. Particle growth begins to slow as levels of available nutrients decreases. At this point further growth *via* aggregation becomes more favourable at higher

temperatures.

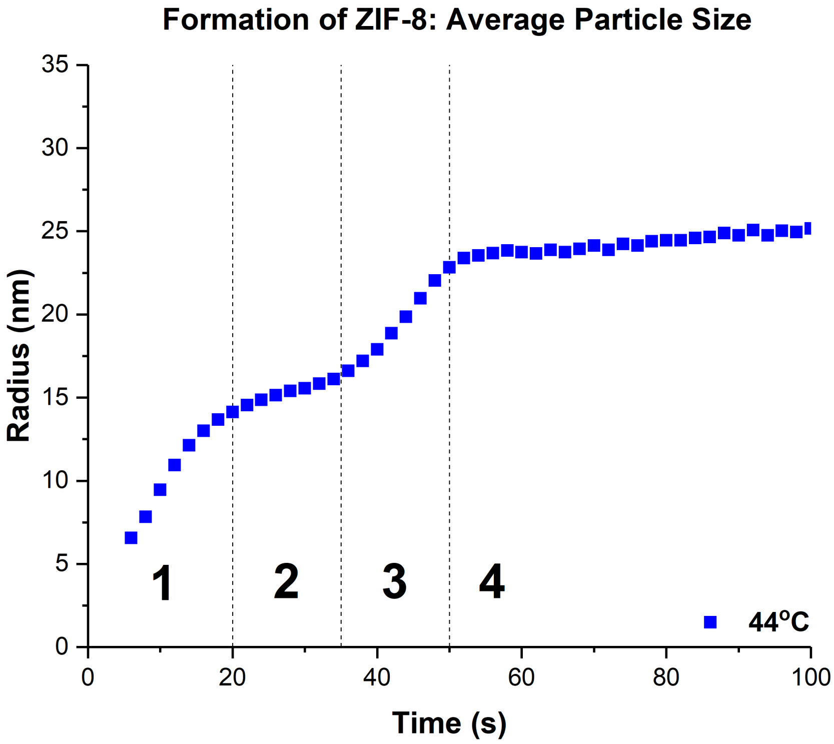

Figure 5.16: Average particle radius obtained from Monte Carlo fitting of SAXS data obtained from following the formation of ZIF-8 at 44°C, split into sections to emphasize different stages of growth.

At 55°C larger pre-nucleation clusters form, which allows for the formation of larger ZIF-8 nuclei than observed at 44°C. The nucleation phase can be seen to be more rapid at higher temperatures, and also means that the isosbestic point is reached much more quickly at higher temperatures than at lower temperatures. This means that nucleation at the expense of the pre-nucleation clusters occurs more rapidly at 55°C than at 44°C, and once this nucleation phase has ended growth continues to occur *via* monomer addition, which is more favourable at 55°C than at 44°C, hence larger particles are observed at 55°C than at 44°C.

This formation mechanism can also be used to explain the higher polydispersity observed at 14°C. At low synthesis temperatures, a lower rate of nucleation is observed. Due to this the ordered packing of the pre-nucleation clusters is much greater, hence larger particles are formed in general, though due to the low rates of nucleation the observed product yields are also much lower. At 14°C the broader range of particles observed can also be explained by the presence of simultaneous nucleation and growth within the system. As particle nucleation is slow, it occurs over a much longer period of time, allowing for nuclei formed early on in the synthesis to grow to a larger size, whilst other nuclei are still forming. This occurs until all the pre-nucleation cluster particles are gone, at which point a variety of different sized particles are present within the synthesis medium, when only growth can then occur. This is observed at 14°C with a slight narrowing of the particle size towards the end of the experiment (figure 5.12).

5.4 Summary

In-situ SAXS and WAXS experiments, with high temporal resolution, were preformed to probe the formation of ZIF-8 at four different synthesis temperatures. This studied provides evidence that the nucleation of crystalline ZIF-8 particles occurs *via* a non-classical route, where the pre-nucleation clusters evolve into larger ZIF-8 particles, which is subsequently followed by growth *via* monomer addition, and aggregation. Initially, pre-nucleation clusters were observed prior to the formation of crystalline ZIF-8 particles. These clusters were observed to form within a matter of seconds, depending on the synthesis conditions and the size of the pre-nucleation clusters formed was shown to be temperature dependent, with higher temperatures yielding larger sized clusters. After the formation of these clusters, ZIF-8 particles then begin to form and it is thought that the pre-nucleation clusters play a prominent role in the nucleation of these crystalline particles. After the initial formation of crystalline ZIF-8 particles, the pre-nucleation clusters can also serve as a reservoir of nutrients for subsequent growth of the crystalline particles. However, once this nutrient resource becomes spent, growth *via* monomer addition and aggregation processes is thought to be favoured.

Bibliography

[1] O M Yaghi and H Li. Hydrothermal Synthesis of a Metal-Organic Framework Containing Large Rectangular Channels. *Journal of the American Chemical Society*, 117(41):10401–10402, 1995.

[2] C Janiak. Engineering coordination polymers towards applications. *Dalton Transactions*, (14):2781, 2003.

[3] J L C Rowsell and O M Yaghi. MetalOrganic Frameworks : a new class of porous materials. *Microporous and Mesoporous Materials*, 73:3–14, 2004.

[4] H Li, M Eddaoudi, M O'Keeffe, and O M Yaghi. Design and synthesis of an exceptionally stable and highly porous metal-organic framework. *Nature*, 402(November):276–279, 1999.

[5] O M Yaghi, M O'Keeffe, N W Ockwig, H K Chae, M Eddaoudi, and J Kim. Reticular synthesis and the design of new materials. *Nature*, 423(6941):705–714, 2003.

[6] K S Park, Z Ni, A P Côté, J Y Choi, R Huang, F J Uribe-Romo, H K Chae, M O'Keeffe, and O M Yaghi. Exceptional chemical and thermal stability of zeolitic imidazolate frameworks. *Proceedings of the National Academy of Sciences of the United States of America*, 103(27):10186–91, 2006.

[7] J R Li, J Yu, W Lu, L B Sun, J Sculley, P B Balbuena, and H C Zhou. Porous materials with pre-designed single-molecule traps for CO 2 selective adsorption. *Nature Communications*, 4:1538, 2013.

[8] P Horcajada, T Chalati, C Serre, B Gillet, C Sebrie, T Baati, J F Eubank, D Heurtaux, P Clayette, C Kreuz, J S Chang, Y K Hwang, V Marsaud, P N Bories, L Cynober, S Gil, G Férey, P Couvreur, and R Gref. Porous metal-organic-framework nanoscale carriers as a potential platform for drug deliveryand imaging. *Nature Materials*, 9(2):172–178, 2010.

[9] Y Hou, W Hu, Z Gui, and Y Hu. Preparation of Metal-Organic Frameworks and Their Application as Flame Retardants for Polystyrene. *Industrial and Engineering Chemistry Research*, 56(8):2036–2045, 2017.

[10] H Wang, J Tian, Z Y Xu, D W Zhang, H Wang, S H Xie, D W Xu, Y H Ren, Y Liu, and Z T Li. Supramolecular metal-organic frameworks that display high homogeneous and heterogeneous photocatalytic activity for H2 production. *Nature Communications*, 7(May):1–9, 2016.

[11] K Shen, L Zhang, X Chen, L Liu, D Zhang, and Y Han. Ordered macro-microporous metal- organic framework single crystals. 210(January):206–210, 2018.

[12] N Stock and S Biswas. Synthesis of Metal-Organic Frameworks (MOFs): Routes to Various MOF Topologies, Morphologies, and Composites. *Chemical Reviews*, 112(2):933–969, feb 2012.

[13] Y Sun and H C Zhou. Recent progress in the synthesis of metal-organic frameworks. *Science and Technology of Advanced Materials*, 16(5):54202, 2015.

[14] K Kida, M Okita, K Fujita, S Tanaka, and Y Miyake. Formation of high crystalline ZIF-8 in an aqueous solution. *CrystEngComm*, 15(9):1794, 2013.

[15] J Cravillon, C A Schrçder, R Nayuk, J Gummel, K Huber, and M Wiebcke. Fast Nucleation and Growth of ZIF-8 Nanocrystals Monitored by Time-Resolved In Situ Small-Angle and Wide-Angle X-Ray Scattering. *Angew. Chem. Int. Ed.*, 50:8067–8071, 2011.

[16] M J V Vleet, T Weng, X Li, and J R Schmidt. In Situ , Time-Resolved , and Mechanistic Studies of Metal Organic Framework Nucleation and Growth. *Chem. Rev.*, 118(7):3681–3721, 2018.

[17] G C Sosso, J Chen, S J Cox, M Fitzner, P Pedevilla, A Zen, and A Michaelides. Crystal Nucleation in Liquids: Open Questions and Future Challenges in

Molecular Dynamics Simulations. *Chemical Reviews*, 116(12):7078–7116, 2016.

[18] S Karthika, T K Radhakrishnan, and P Kalaichelvi. A Review of Classical and Nonclassical Nucleation Theories. *Crystal Growth and Design*, 16(11):6663–6681, 2016.

[19] J J De Yoreo, P U P A Gilbert, N A J M Sommerdijk, R L Penn, S Whitelam, D Joester, H Zhang, J D Rimer, A Navrotsky, J F Banfield, A F Wallace, F M Michel, F C Meldrum, H Cölfen, and P M Dove. Crystallization by particle attachment in synthetic, biogenic, and geologic environments. *Science*, 349(6247), 2015.

[20] S Furukawa, J Reboul, S Diring, K Sumida, and S Kitagawa. Structuring of metalorganic frameworks at the mesoscopic/macroscopic scale. *Chem. Soc. Rev.*, 43(16):5700–5734, 2014.

[21] M Eddaoudi, D F Sava, J F Eubank, K Adil, and V Guillerm. Zeolite-like metal-organic frameworks (ZMOFs): Design, synthesis, and properties. *Chemical Society Reviews*, 44(1):228–249, 2015.

[22] J D Rimer and M Tsapatsis. Nucleation of open framework materials: Navigating the voids. *MRS Bulletin*, 41(5):393–398, 2016.

[23] C S Cundy and P A Cox. The hydrothermal synthesis of zeolites: Precursors, intermediates and reaction mechanism. *Microporous and Mesoporous Materials*, 82(1-2):1–78, jul 2005.

[24] M P Attfield and P Cubillas. Crystal growth of nanoporous metal organic frameworks. *Dalton Trans.*, 41(14):3869–3878, 2012.

[25] A Ramanan and M S Whittingham. How molecules turn into solids: The case of self-assembled metal-organic frameworks. *Crystal Growth and Design*, 6(11):2419–2421, 2006.

[26] M Singh, D Kumar, J Thomas, and A Ramanan. Crystallization of copper(II) sulfate based minerals and MOF from solution: Chemical insights into the supramolecular interactions. *Journal of Chemical Sciences*, 122(5):757–769, 2010.

[27] H Cölfen and S Mann. Higher-order organization by mesoscale self-assembly and transformation of hybrid nanostructures. *Angewandte Chemie - International Edition*, 42(21):2350–2365, 2003.

[28] P W Voorhees. The theory of Ostwald ripening. *Journal of Statistical Physics*, 38(1-2):231–252, jan 1985.

[29] R W Thompson. *Verified Syntheses of Zeolitic Materials*. Elsevier, 2001.

[30] P Cubillas and M W Anderson. Synthesis Mechanism: Crystal Growth and Nucleation. In *Zeolites and Catalysis: Synthesis, Reactions and Applications*, pages 1–66. 2010.

[31] R J Kirkpatrick. Crystal growth from the melt: a review. *Am. Mineral.*, 60:798–814, 1975.

[32] W K Burton, N Cabrera, and F C Frank. The Growth of Crystals and the Equilibrium Structure of their Surfaces. *Philosophical Transactions of the Royal Society A: Mathematical, Physical and Engineering Sciences*, 243(866):299–358, 1951.

[33] J Cravillon, C A Schröder, R Nayuk, J Gummel, K Huber, and M Wiebcke. Fast nucleation and growth of ZIF-8 nanocrystals monitored by time-resolved in situ small-angle and wide-angle X-ray scattering. *Angewandte Chemie - International Edition*, 50(35):8067–8071, 2011.

[34] Y Wu, M I Breeze, G J Clarkson, F Millange, D O'Hare, and R I Walton. Exchange of Coordinated Solvent during Crystallization of a Metal-Organic Framework Observed by in Situ High-Energy X-ray Diffraction. *Angewandte Chemie - International Edition*, 55(16):4992–4996, 2016.

[35] S Surblé, F Millange, C Serre, G Férey, and R I Walton. An EXAFS study of the formation of a nanoporous metal-organic framework: Evidence for the retention of secondary building units during synthesis. *Chemical Communications*, (14):1518–1520, 2006.

[36] E Haque and S H Jhung. Synthesis of isostructural metal-organic frameworks, CPO-27s, with ultrasound, microwave, and conventional heating: Effect of synthesis methods and metal ions. *Chemical Engineering Journal*, 173(3):866–872, 2011.

[37] W Ostwald. Studies on the Formation and Transformation of Solid Compounds: Report I. Supersaturation and Practicing Cooling. *Z. Phys. Ch.*, 22:289330, 1897.

[38] A R Patel and A Venkateswara Rao. Crystal growth in gel media. *Bulletin of Materials Science*, 4(5):527–548, 1982.

[39] F Millange, M I Medina, N Guillou, G Férey, K M Golden, and R I Walton. Time-resolved in situ diffraction study of the solvothermal crystallization of some prototypical metal-organic frameworks. *Angewandte Chemie - International Edition*, 49(4):763–766, 2010.

[40] M Avrami. Kinetics of phase change. I: General theory. *The Journal of Chemical Physics*, 7(12):1103–1112, 1939.

[41] M Avrami. Kinetics of phase change. II Transformation-time relations for random distribution of nuclei. *The Journal of Chemical Physics*, 8(2):212–224, 1940.

[42] M Avrami. Granulation, phase change, and microstructure kinetics of phase change. III. *The Journal of Chemical Physics*, 9(2):177–184, 1941.

[43] J D Hancock and J H Sharp. Method of Comparing SolidState Kinetic Data and Its Application to the Decomposition of Kaolinite, Brucite, and BaCO3. *Journal of the American Ceramic Society*, 55(2):74–77, 1972.

[44] K M O Jensen, C Tyrsted, M Bremholm, and B B Iversen. In Situ studies of solvothermal synthesis of energy materials. *ChemSusChem*, 7(6):1594–1611, 2014.

[45] E E Finney and R G Finke. Nanocluster nucleation and growth kinetic and mechanistic studies: A review emphasizing transition-metal nanoclusters. *Journal of Colloid and Interface Science*, 317(2):351–374, 2008.

[46] S R Venna, J B Jasinski, and M A Carreon. Structural Evolution of Zeolitic Imidazolate Framework-8. *Journal of the American Chemical Society*, 132(51):1–6, 2010.

[47] J Cravillon, C A Schröder, H Bux, A Rothkirch, J Caro, and M Wiebcke. Formate modulated solvothermal synthesis of ZIF-8 investigated using time-resolved in situ X-ray diffraction and scanning electron microscopy. *CrystEngComm*, 14(2):492–498, 2012.

[48] X Feng and M A Carreon. Kinetics of transformation on ZIF-67 crystals. *Journal of Crystal Growth*, 418:158–162, 2015.

[49] H Reinsch and N Stock. Formation and Characterisation of Mn-MIL-10. *CrystEngComm*, 15:544–550, 2013.

[50] J Juan-Alcañiz, M Goesten, A Martinez-Joaristi, E Stavitski, A V Petukhov, J Gascon, and F Kapteijn. Live encapsulation of a Keggin polyanion in NH 2-MIL-101(Al) observed by in situ time resolved X-ray scattering. *Chemical Communications*, 47(30):8578–8580, 2011.

[51] E Stavitski, M Goesten, J Juan-Alcañiz, A Martinez-Joaristi, P Serra-Crespo, A V Petukhov, J Gascon, and F Kapteijn. Kinetic control of metal-organic framework crystallization investigated by time-resolved in situ X-ray scattering. *Angewandte Chemie - International Edition*, 50:9624–9628, 2011.

[52] M G Goesten, E Stavitski, J Juan-Alcañiz, A Martiñez-Joaristi, A V Petukhov, F Kapteijn, and J Gascon. Small-angle X-ray scattering documents the growth of metal-organic frameworks. *Catalysis Today*, 205:120–127, 2013.

[53] H H Yeung, Y Wu, S Henke, A K Cheetham, D O'Hare, and R I Walton. Crystal Growth In Situ Observation of Successive Crystallizations and Metastable Intermediates in the Formation of Metal Organic Frameworks. *Angewandte Chemie - International Edition*, 55:2012–2016, 2016.

[54] Y Wu, M I Breeze, D O'Hare, and R I Walton. High energy X-rays for following metal-organic framework formation: Identifying intermediates in interpenetrated MOF-5 crystallisation. *Microporous and Mesoporous Materials*, 254:178–183, 2017.

[55] C McKinstry, E J Cussen, A J Fletcher, S V Patwardhan, and J Sefcik. Effect of synthesis conditions on formation pathways of metal organic framework (MOF-5) crystals. *Crystal Growth and Design*, 13(12):5481–5486, 2013.

[56] Y Wu, S J Moorhouse, and D O'Hare. Time-Resolved in Situ Diffraction Reveals a Solid-State Rearrangement During Solvothermal MOF Synthesis. *Chemistry of Materials*, 27:7236, 2015.

[57] F Millange, R El Osta, M E Medina, and R I Walton. A time-resolved diffraction study of a window of stability in the synthesis of a copper carboxylate metal-organic framework. *CrystEngComm*, 13(1):103–108, 2011.

[58] M Dan and C N R Rao. A Building-Up Process in Open-Framework Metal Carboxylates that Involves a Progressive Increase in Dimensionality. *Angewandte Chemie*, 118(2):287–291, 2006.

[59] A Thirumurugan and C N R Rao. 1,2-, 1,3- and 1,4-benzenedicarboxylates of Cd and Zn of different dimensionalities: Process of formation of the three-dimensional structure. *Journal of Materials Chemistry*, 15(35-36):3852–3858, 2005.

[60] P Mahata, A Sundaresan, and S Natarajan. The role of temperature on the structure and dimensionality of MOFs: An illustrative study of the formation of manganese oxy-bis(benzoate) structures. *Chemical Communications*, (43):4471–4473, 2007.

[61] N A Khan, M M Haque, and S H Jhung. Accelerated syntheses of porous isostructural lanthanide- benzenetricarboxylates (Ln-BTC) under ultrasound at room temperature. *European Journal of Inorganic Chemistry*, 2(31):4975–4981, 2010.

[62] N A Khan, E Haque, and S H Jhung. Rapid syntheses of a metalorganic framework material Cu3(BTC)2(H2O)3 under microwave: a quantitative analysis of accelerated syntheses. *Physical Chemistry Chemical Physics*, 12(11):2625, 2010.

[63] E Haque, N A Khan, C M Kim, and S H Jhung. Syntheses of metal-organic frameworks and aluminophosphates under microwave heating: Quantitative analysis of accelerations. *Crystal Growth and Design*, 11(10):4413–4421, 2011.

[64] E Haque, N A Khan, H J Park, and S H Jhung. Synthesis of a metal-organic framework material, iron terephthalate, by ultrasound, microwave, and conventional electric heating: A kinetic study. *Chemistry - A European Journal*, 16(3):1046–1052, 2010.

[65] X Feng, T Wu, and M A Carreon. Synthesis of ZIF-67 and ZIF-8 crystals using DMSO (Dimethyl Sulfoxide) as solvent and kinetic transformation studies. *Journal of Crystal Growth*, 455(July):152–156, 2016.

[66] P Y Moh, M Brenda, M W Anderson, and M P Attfield. Crystallisation of solvothermally synthesised ZIF-8 investigated at the bulk, single crystal and surface level. *CrystEngComm*, 15(45):9672–9678, 2013.

[67] N Greeves. ChemTube3D. *The University of Liverpool*, 2018.

[68] J Cravillon, R Nayuk, S Springer, A Feldhoff, K Huber, and M Wiebcke. Controlling zeolitic imidazolate framework nano- and microcrystal formation: Insight into crystal growth by time-resolved in situ static light scattering. *Chemistry of Materials*, 23(8):2130–2141, 2011.

[69] J Cravillon, S Münzer, S J Lohmeier, A Feldhoff, K Huber, and M Wiebcke. Rapid room-temperature synthesis and characterization of nanocrystals of a prototypical zeolitic imidazolate framework. *Chemistry of Materials*, 21(8):1410–1412, 2009.

[70] T Hikov, C A Schröder, J Cravillon, M Wiebcke, and K Huber. In situ static and dynamic light scattering and scanning electron microscopy study on the crystallization of the dense zinc imidazolate framework ZIF-zni. *Physical Chemistry Chemical Physics*, 14(2):511–521, 2012.

[71] S Saha, M Wiebcke, and K Huber. Insight into Fast Nucleation and Growth of Zeolitic Imidazolate Framework-71 by in Situ Static Light Scattering at Variable Temperature and Kinetic Modeling. *Crystal Growth and Design*, 18(8):4653–4661, 2018.

[72] P Y Moh, P Cubillas, M W Anderson, and M P Attfield. Revelation of the molecular assembly of the nanoporous metal organic framework ZIF-8. *Journal of the American Chemical Society*, 133(34):13304–13307, 2011.

[73] M Shoaee, M W Anderson, and M P Attfield. Crystal growth of the nanoporous metal-organic framework HKUST-1 revealed by in situ atomic force microscopy. *Angewandte Chemie - International Edition*, 47(44):8525–8528, 2008.

[74] N S John, C Scherb, M Shöâeè, M W Anderson, M P Attfield, and T Bein. Single layer growth of sub-micron metal-organic framework crystals observed by in situ atomic force microscopy. *Chemical Communications*, 2(41):6294–6296, 2009.

[75] P Cubillas, M W Anderson, and M P Attfield. Crystal growth mechanisms and morphological control of the prototypical metal-organic framework MOF-5 revealed by atomic force microscopy. *Chemistry - A European Journal*, 18(48):15406–15415, 2012.

[76] P Cubillas, M W Anderson, and M P Attfield. Materials discovery and crystal growth of zeolite A type zeolitic-imidazolate frameworks revealed by atomic force microscopy. *Chemistry - A European Journal*, 19(25):8236–8243, 2013.

[77] M Shöâeè, J R Agger, M W Anderson, and M P Attfield. Crystal form, defects and growth of the metal organic framework HKUST-1 revealed by atomic force microscopy. *CrystEngComm*, 10(6):646, 2008.

[78] J P Patterson, P Abellan, M S Denny, C Park, N D Browning, S M Cohen, J E Evans, and N C Gianneschi. Observing the Growth of MetalOrganic Frameworks by in Situ Liquid Cell Transmission Electron Microscopy. *Journal of the American Chemical Society*, 137(23):7322–7328, jun 2015.

[79] Y Zhu, J Ciston, B Zheng, X Miao, C Czarnik, Y Pan, R Sougrat, Z Lai, C E Hsiung, K Yao, I Pinnau, M Pan, and Y Han. Unravelling surface and interfacial structures of a metal-organic framework by transmission electron microscopy. *Nature Materials*, 16(5):532–536, 2017.

[80] J Grand, H Awala, and S Mintova. Mechanism of zeolites crystal growth: new findings and open questions. *CrystEngComm*, 18(5):650–664, 2016.

[81] M Goesten, E Stavitski, E A Pidko, C Gücüyener, B Boshuizen, S N Ehrlich, E J M Hensen, F Kapteijn, and J Gascon. The molecular pathway to ZIF-7 microrods revealed by in situ time-resolved small- and wide-angle x-ray scattering, quick-scanning extended X-ray absorption spectroscopy, and DFT calculations. *Chemistry - A European Journal*, 19(24):7809–7816, 2013.

Chapter 6

In-situ Hydrothermal Cell Development

6.1 Introduction

Solvothermal processes are utilised in a great number of syntheses involved in the formation and transformation of heterogeneous catalytic materials, for example most zeolitic solids are commonly formed under hydrothermal conditions. Similarly, dense framework oxides, metals oxides, sulphides and many other systems are synthesised using solution based processing methods so that morphology, specific particle shape and size can be controlled efficiently.

When studying the processes involved in the formation of these materials the prevention of sedimentation becomes very important. This is especially so when conducting *in-situ* experiments on dynamic heterogeneous systems, where particles can nucleate and subsequently sediment within the sample environment. This can greatly hinder the collection of good, representative data on particle growth as events can be partially, or even completely missed.

This chapter describes the history of hydrothermal synthesis and *in-situ* hydrothermal experiments, focusing on the experimental set ups and the equipment used. The difficulties associated with the collection of *in-situ* data on hydrothermal systems and strategies for overcoming these issues. This chapter also covers the design and development of a new *in-situ* hydrothermal cell, designed to prevent the sedimentation of nucleating and growing particles within heterogeneous systems, for the collection of high quality, representative data.

6.2 Hydrothermal Synthesis

Hydrothermal synthesis, generally, refers to any heterogeneous reaction occurring in the presence of a solvent/mineralizer under high pressures and temperatures. This allows dissolution and recrystallization to occur in materials that would normally be considered to be relatively insoluble under ambient conditions.

However, this has not always been the definition of hydrothermal synthesis, for example, in 1913 it was described as the conditions that reactants are to under the action of water, at temperatures near or above its critical point (c.a. 370°C), when held within a sealed vessel to subsequently create an high pressure environment.[1] Another definition came from Lobachev, where he states that hydrothermal synthesis is actually a group of methods encompassing crystallisation from superheated aqueous solutions at high pressures.[2] This definition has evolved over time, essentially lowering the temperature and pressure requirements than in previous definitions. For example, hydrothermal synthesis has been defined as an heterogeneous reaction occurring within an aqueous medium at temperature greater than 100°C and 1 bar of pressure, or a water catalysed reactions taking place at temperatures ¿100°C and at pressures greater than a few atmospheres [3, 4, 5]

Essentially, the term has grown over time to encompass nearly any heterogeneous reaction occurring in an aqueous medium carried out at temperatures and pressure above those considered to be ambient.[6] The definition can also be broadened to encompass any homo- or heterogeneous reaction in the presence of a solvent (aqueous or not) occurring within a closed system at temperatures and pressures above those of ambient conditions.[7] This includes the use of gels and solution based precursors in the formation of nanomaterials and many other reactions performed within closed vessels. Due to this broader, more encompassing, modern definition for hydrothermal synthesis other terms, such as solvothermal, ammonothermal, carbonothermal and alcothermal synthesis to name only a few, have become commonly used to describe different off-shoots of hydrothermal synthesis.

6.3 Hydrothemal Synthesis

6.3.1 The Early History of Hydrothermal Synthesis

The success and popularity of Hydrothermal synthesis can be largely associated with advancements in technical capabilities, especially, those associated with improvements in the machining and fabrication of materials with the suitable characteristics to withstand the high temperatures and pressures produced during hydrothermal treatments. However, the adoption of hydrothermal methods by chemists, as a common synthesis practice for the production of crystalline materials also played its roles the overall success of the technique.

The origins of the term ”hydrothermal synthesis” can be ascribed to the field of geology, and specifically, the British geologist Roderick Murchison, who in the early nineteenth century described it as the actions of water, at elevated temperatures and pressures, that can bring about changes in the Earth’s crust and is responsible for the formation of many rocks and minerals.[1, 8, 6] From this description it was determined that minerals formed during postmagmatic and metasomatic stages, in the presence of water and at elevated temperatures and pressures, can be considered to have been formed hydrothermally. To begin with hydrothermal conditions were known to occur naturally, typically emanating from cooling magmas, and other heated exogenic sources, capable of initiating petrogenetic processes, which would in-turn trigger the formation of the metasomatic facies found naturally in large rock formation. The origins and importance of hydrothermal processes were well known in the field of geology in the early nineteenth century, however, the processes itself was still to be examined in great detail, leaving lots of questions to be answered. This quest for answers would quickly lead to a great deal of research into the inner workings of hydrothermal processes and the development of studies looking at how these conditions could be replicated and controlled within a lab environment.

The first lab based hydrothermal experiments are widely credited to have been performed in 1839, by Robert Bunsen.[9] Bunsen began using sealed thick walled glass tubes to heat aqueous solutions upto 200°C, which in turn put these solutions under 100-150 atmospheres of pressures. These initial experiments were then followed up when Bunsen began to grow barium and strontium carbonate crystals within aqueous ammonium chloride solutions under the same conditions, and it is these experiments that are considered, by many, as some of the first hydrothermal experiments to utilise aqueous solvents as a synthesis medium.[3, 10] The idea of synthesising crystaline materials under high temperatures and pressures, quickly began to spread and was soon adopted by another German scientist, Karl Emil von Schafhäutl, whom in 1845 began to grow quartz crystals from freshly precipitated silicic acid.[11] Schafhautl, performed his experiments within a Papin's digester (high pressures cooker) and this method would also soon be widely adopted by many European mineralogists later in the nineteenth century, a technique that would eventually overtaking the use of sealed glass tubes.

It was the success of these early experiments that made hydrothermal synthesis what it is today. Without the early adoption of this technique, as a method for simulating the conditions found naturally within the Earth's crust, the push for the synthesis of many naturally occurring crystalline materials would not have been so strong, and it wasn't long after these initial experimental reports that other naturally occurring crystalline materials were synthesized for the first time.

In 1848, Wohler recrystallized Apophyllite, in aqueous solutions at 180°C under 10 atm of pressure.[12] This work was soon followed up by De Senarmont's hydrothermal synthesis focusing on silica gels, in 1851, where a variety of different solvents were utilised at temperatures ranging from 200 - 300°C. These experiments resulted in the formation of six-sided prisms possessing pyramidal terminations, and is one of the earliest known successful syntheses of quartz crystals.[13, 14] In the same year, De Senarmont also published his designs for a hydrothermal vessel, where the sealed glass tubes, that are used to hold the synthesis mixture, are subsequently held within fused gun barrels.[15] This design would soon be iterated on by Daurree, in 1859, for the synthesis of quartz at 400°C in an aqueous medium. This iteration would be the first to introduce a pressure balance arrangement between the glass tube and the steel housing.[16, 17]

In 1862, St Claire Deville attempted to convert bauxite to corundum under hydrothermal conditions using sodium hydroxide as a mineralizer, however the results obtained were not particularly definitive.[18] This lack of definite results was quite common in the early history of hydrothermal synthesis. For example, a great deal of the early work performed on hydrothermal synthesis was conducted in sealed glass tubes, but these tubes were effected by the hydrothermal conditions. However, it wasn't until 1873 when preventative measures were proposed by von Chroustshoff, which consisted of lining the autoclaves with gold/noble metals, and it was this break through that allowed von Chroustshoff to synthesize tridymite phase quartz.[19]

With the introduction of steel autoclaves, with noble metal linings, higher temperatures and pressures became accessible for the first time, however, work primarily remained focused on developing the syntheses of quartz, feldspar and a few other related silicates. This lead to some early definitions of hydrothermal synthesis being specifically tied to the synthesis of silicates, however, there were still attempts by people to synthesise other materials. For example, Hannay, in 1880 claimed to synthesise artificial diamonds, a claim that could have aided in fuelling more research into hydrothermal synthesis, especially the development of higher pressure techniques.[20]

The synthesis of large (2-3mm) crystals of potassium silicate, obtained whilst growing orthoclase and feldspar as an additional phase was the next significant development for hydrothermal methods, alongside Friedel's coining of the term hydrothermal "bomb" in 1881.[21] The availability of new alloys and metals in the late 1870s and early 1880s lead to the development of newer hydrothermal set-ups, including De Schulten's copper "bomb," which was used to synthesise analcite at 180°C in 18 hours, and Ramsay's cast iron autoclaves.[22, 23]

Many long term hydrothermal experiments were performed, including Chroustshoff's synthesis of quartz, in 1887, where initially four experiments were set up in glass tubes, with three of the tubes burst during the heating process, however the fourth remained in tact and large (8 x 3 mm) quartz crystals were eventually obtained six months later.[24]

A couple years later, Bruhns designed a platinum-lined, steel autoclave that utilised steel screws and copper washers to hold down the cover.[25] This design would grow to be very popular in Europe. It was also around this time, when Doetler was able to synthesise chabazite and analcite utilising an iterative gun-barrel autoclave design, where a nickel coated gun barrel enclosure was used in conjunction with sealed silver-lined steel tubes (”bullets”).[26] In the same year, Chroustshoff, used thick wall evacuated glass tubes to produce large (1 x 0.5 mm) dark green iron-magnesium silicate crystals (hornblende) in 3 months.[27]

In 1892, Karl Josef Bayer, was first to commercialise hydrothermal technologies for the extraction of Alumina from bauxite using sodium hydroxide, a process that is still used to the modern day.[28, 6]

The popularity of hydrothermal synthesis finally made its way from Europe to a second continent when, in 1898, Barus became the first North American to publish work on the impregnation of glass through the utilisation of steel autoclaves.[1]

Throughout most of the 19th century, it can be seen that there were a great deal of studies concentrating on the formation of naturally occurring minerals and other crystalline materials. However, in these early years of synthetic crystal growth by hydrothermal synthesis it is easy to see that there was little consideration given to solvent chemistry, kinetics and solubility of the probed systems.[29, 1] Nonetheless, around 80 different mineral syntheses were discovered in the nineteenth century alone.[1] The largest problems that effected these early hydrothermal experiments were from experimental uncertainties. These arose predominantly from the lack of suitable synthesis equipment, for example, many experiments failed due to poor sealing of vessels, causing leakages and pressure fluctuations.

Another problem with earlier experiments was a lack of adequate characterisation techniques. Initially, it was only possible to obtain small amounts of sample, partly due to the limitations the most commonly used hydrothermal vessels possessed. For example, sealed glass tubes would often corrode during the hydrothermal process adding silica to the reactants, creating a great deal of problems when trying to perform accurate chemical and phase analysis on products. Many early syntheses also produced small crystal sizes making optical microscopy difficult, and it was these technological road blocks that hindered the progress of hydrothermal synthesis in its early days. This, in-turn, lead to more focused research into the synthesis of large bulk crystals, meaning that many experiments yielding smaller sized crystals and small amounts of product were cast aside and considered failures. This was predominantly due to the lack of available X-ray techniques at the time, hence, chemical analysis had to be relied upon. This meant that many of the experiments that were considered to be failures, may well not have been. This led to some poorly informed assumptions being made on the solubility of materials, and the subsequent labelling of materials as not suitable for crystal growth.[6]

This would soon change though, when more systematic studies began to be undertaken, such as Spezia's seminal work on seeded growth of α-quartz.[30] Spezia's work shows that subjecting samples to high pressure alone was not enough to influence the growth or solubility of quartz. He then looked at the influence of sodium silicate on quartz crystals at temperature and found that in the presence of a basic medium, that the quartz crystal's rhombohedral faces were attacked, whilst on the other faces large masses of deposited silica was found. This explained observations of rapid growth along the *c*-axis of quartz crystals.[31] Soon after, Allen was then able to synthesise quartz at c.a. 400°C in 3 days using a steel autoclave sealed with a large copper disk, kept in place by a screw on a steel cap (an iterative design of Bruhns' earlier autoclave).[1]

Next, came some important developments in autoclave designs to reach even higher temperatures and pressures. First, test tube-like pressure vessels that could reach pressures as high at 5 kbar and temperatures upto 750°C for extended periods of time. This design was followed up by Boeke and Tammann's newly designed autoclaves capable of reaching even higher pressures, through the utilisation of CO_2 pressures. The experiments performed by Boeke and Tammann can be considered some of the first solvothermal experiments ever performed (though the term 'solvothermal' would not be introduced for another 60 years).[32, 33, 34] These autoclaves were made of steel rods, 25 cm in diameter, and 45 cm long. The design utilized soft metal gaskets which act as seals when compressed and the heating was performed internally using a resistance furnace.

In 1914, Morey, also designed a simple gasket sealed autoclave that could contain 25 - 100 ml. This became a very popular design due to its simplicity, ease of use, and the fact that they could withstand temperatures up to 450°C and pressures of 2 kbar.[35] Morey and Fenner, also looked at the pressure and temperature conditions used in hydrothermal synthesis more in-depth, by using high purity reactants, meaning product composition could be known with a higher degree of accuracy than before.[36] With the results of these experiments, Morey and Fenner, were able to form a mechanism for the crystallisation of pegmatite.[10] They determined that various stable solid phases can coexist within the solution over specific temperature ranges, corresponding to a three-phase pressure system. A systematic approach to studying phase equilibria at high temperatures was also taken by Bowen in 1922 for silicates, a study that would eventually lead to Bowen's famous reaction series.[37] It was also around this time that X-ray techniques became much more readily available, meaning that there was no longer a reliance on producing large bulk crystals and a more systematic understanding of the products obtained from hydrothermal synthesis could begin.

In 1931, there were further developments in hydrothermal vessel designs when Goranson designed an autoclave that was internally heated but also externally cooled using circulating water.[28] These designs were and iteration of a earlier design by Adams and Smyth, however the the internal and external heating a cooling elements enabled these autoclaves to reach higher pressures and temperatures than those previously seen.[38] It was also around this time where the hydrothermal synthesis of inorganic compounds, similar to those found in nature could be called well established. However, in general crystal growth at this time would be considered very slow due to the lack of understanding of solvent chemistry at the time. This would soon change due to an unlikely source. As a consequence of World War II (WWII) there became a large demand for high-quality quartz crystals. High perfection α-quartz crystals were used in for piezoelectric applications at the time, as when subjected to mechanical stress, quartz generates an electrical polarisation.[39] Hence, during the war quartz was used in submarine detection systems due to their anisotropic properties, in oscillators, were frequency is highly dependent upon crystal orientation. These crystals were previously supplied from Brazil, however and embargo halted the supply of high-quality quartz from Brazil, this lack of supply also had an effect on telecommunication applications during WWII. However, in the history of hydrothermal synthesis this embargo lead to huge developments in the synthesis of large quartz crystals at faster rates then previously possible, though the accomplishments at this time had to wait for the war to end before any publications could be made, though progress was shared through intelligence reports between allies at the time. One of the first publications after WWII, in the field of hydrothermal synthesis, came from Nacken, in 1946, where it was shown how natural α-quartz can be used to seed growth in an isothermal system to obtain large quartz crystals.[40, 41]. The autoclaves used during war time were generally of a design reminiscent of Doetler's earlier 1890s gun-barrel design.

After WWII, more hydrothermal syntheses were commercialized including the large-scale synthesis of single crystal quartz using the methods described by Nacken in 1946.[40, 42] Soon after this, the first non-naturally occurring zeolite was next to be synthesised by Barrer in 1948, which would again cause a surge of excitement around hydrothermal synthesis.[43, 44] Barrer was already a well known name in the world of zeolites and hydrothermal synthesis with the commercialization of his earlier natural zeolite syntheses in the late 1930s.[45, 46] However, his discovery of the first non-naturally occurring zeolite would soon be follow up with there characterisation and his pioneering on the adsorption properties of zeolites.[47]

In the same year, Tuttle came out with a new autoclave design.[48] He designed a threadless cold-cone seal, though this first iteration of the design was not capable of reaching the high temperatures and pressures required for most syntheses. However, this design was soon adapted by Roy into the test-tube like bomb design manufactured from mixed alloy rods with a hole drilled down the middle. These test tubes were c.a. 20 cm long and c.a. 2 cm in diameter in size, with one end being threaded and sealed with a cone seated against where a pressure pump could be connected.[10] This design was able to reach temperatures up to 1000°C, depending on the alloy used, and with its direct connection to a pressure pumps, pressure was no longer coupled to temperature. Gold or platinum tubes could be housed within the test-tube bomb housings and experimentalist could have a much more precise control of pressures (up to 5 kbar) than ever before. One other advantage of this design was that multiple vessels could be used simultaneously using a single pressure source. The noble metal capsules used were welded shut with the nutrients inside, and during the experiments these capsules would collapse when pressurised, but remain sealed, and as the vessel was heated to the desired temperature, whilst being kept at a constant pressure, capsule would expand back to its original volume. The Tuttle-Roy design would be successful in initiating a great number of studies on the phase relations in several systems that required greater pressure and temperature ranges than had been previously inaccessible in labs around the world. [49, 50, 51, 52]

In the 1950s, Walker and Buehler contributed significantly to hydrothermal synthesis by developing methods for producing large crystals within welded steel autoclaves, and even more progress came from Laudise's and Sullivan's contribution from undertaking systematic kinetic studies of crystal growth that lead to significant improvements in overall growth rates.[53, 54, 55]

By the 1970s hydrothermal research began to stagnate and declined due to there being minimal scope for new research in making large-size single crystals of quartz (its main use at the time), and the growth of large-scale crystals of many other compounds had been attempted and determined to be failures. This also came with a stigma that the crystal growth of large crystals was more of an art form than an actual science.[10] This stagnation came even though little to no work had been done to probe solvent chemistry or the kinetic processes involved with hydrothermal synthesis. However, hydrothermal synthesis was finally ready to start reaching its full potential and have its renaissance when work done by Franck in the late 1950s began to gained some attention. This research started probing solvent chemistry and system kinetics within hydrothermal synthesis.[56, 57, 58, 59] This work and its delayed popularity could be considered one of the main reasons that hydrothermal synthesis is what it is today.

Finally, in 1982, the first international Hydrothermal Symposium was held in Japan marking over 100 years of research in hydrothermal synthesis.[60]

6.3.2 Hydrothemal Equipment

6.3.2.1 Glass-Tube Autoclave

The use of thick-walled glass-tube autoclaves was very common in the relative cheapness and easy of use. The use of sealed glass-tubes came with the advantage of being able to observe the reaction taking place and the materials resistance to acidic environments. However, these advantages come with the disadvantages of only being able to be used at relatively temperatures and pressures, in comparison to later designs and also not being resistant to attack from basic solutions. The use of quartz tubes autoclaves would eventually be the direct successor to thick-walled glass-tube autoclaves.[61]

6.3.2.2 Steel autoclaves

Flat-Plate Closure Autoclaves, also known as Morey-Autoclaves, were initially designed in 1913 to incorporate a Bridgman unsupported area seal gasket.[1, 62] Essentially, a Bridgman seal consists of a cylindrical driving piston that can be subjected to an external force to pressurise a vessel. The piston is pressed into the vessel that has a solid base, and the piston sits within the vessel on top of a compressible material (generally softer metals). The gaskets were commonly made from copper, silver or teflon, with the autoclave itself being made from hard steel. These autoclaves were sealed through compression of the gasket when tightening of a nut (see figure 6.1). For the Morey-Autoclave, maximum obtainable temperatures wre in the region of 450°C, with a maximum pressure of 2 kbar.[63]

In 1948, Tuttle designed a small thread-less hydrothermal vessel (figure 6.2). The use of threaded sealing mechanism in hydrothermal equipment had previously caused some problems with the sealing/opening of the vessels, especially after mul-

Figure 6.1: Morey Autoclave design from 1949 (patent US3201209A).[64]

tiple uses, do the the seizing of the mechanisms after the vessels had been subjected to multiple heating/cooling cycles. This design could reach higher temperatures the previously seen and had the advantage of being able to control the pressure within the vessel.[48] The ”Tuttle apparatus,” was made from steel cells that were closed using a cone-in-cone seal. The seal was closed using weights placed above the vessel to press the cones together. The cones would be machined to 59° and 60° so that the seal. could be made. These autoclaves were heated externally and were capable of reaching 800°C and 2 Kbar, however, the cones would need to be machined for each and every experiment.

Figure 6.2: Tuttle Autoclave from patent US7374616B2.[65]

A year after its initial invention, the ”Tuttle apparatus” was developed further in a quest to make the design simpler to use.[64] The cone seal was moved outside of vessel, hence, the seal was renamed the use cold-cone seal. The initial 1949 design was made from a cobalt-based alloy, and pressure could be applied to the samples through a hole in the external closure. This design was capable of reaching 900°C and 1 kbar or 750°C at 3 kbar for long duration experiments. This vessels design would be altered and tweaked a great deal in the coming years. For example, in 1952, a universal pressure intensifier for compressing gasses and liquids was designed by Roy and Osborn.[66] This initiated the use of test-tube hydrothermal racks, where a single compressor could be used with multiple hydrothermal vessels making it much easier to perform large scale experiments or multiple experiments at a time. The original design by Tuttle would also be iterated on with availability of newer alloys. These new materials were able to extend the temperature and pressure ranges of the cells to over 1000°C and 10 kbar.[67, 68, 69]

Roy, again, modified Tuttle’s original designs to make what is known as the ”test-tube bomb.” This was a design that would prove to be simpler to use than the original, by using only a single threaded closure and decoupling the pressure and temperature dependencies through the use of an external pressure system. For performing experiments, samples would be sealed within noble metal tubes that would then be placed within the test-tube cell that would utilise the cold-cone seal design. Due to this designs simplicity, its ability to be used with multiple vessels using a single pressure pump, and its inexpense, made this design one of the most popular in the history of hydrothermal synthesis.

Welded closures, designed by Walker and Buehler, were capable to reaching temperatures up to c.a. 400°C and pressures up to 3 kbar. These were first introduced in the early 1950s, and use disposable liners, that were welded closed at both ends. These sealed liners would then be placed within an outer tube made of a heavier construction.[53, 70] These designs were generally used for dealing with corrosive environments as the use of sacrificial liners means that the heavier and more expensive external construct could be saved. After each experiment, the liners would need to be sawn open, meaning that this design required a great deal of machining to use these autoclaves. Though this heavy reliance on machining was relatively inexpensive in comparison to having to replace entire autoclaves when using corrosive environments which was not an uncommon practice in the early days of hydrothermal synthesis.

Next, came the Unsupported area closures or the modified Bridgman high pressure autoclave.[71] These were sealed through the mechanical tightening of a plunger against a deformable gasket (similar to that of the original Tuttle design). The pressure generated upon sealing these vessels would force a piston to push upwards against the deformable gasket creating a hermetic seal. This design could be used at 500°C and was capable of creating 3.7 kbar. Generally, the external encloses would be made from stainless steel, and these autoclaves were used primarily for the synthesis of quartz crystals. As there is no liner for the prevention of corrosion used with these autoclaves, they would be attacked by the mineralizers used in the synthesis of quartz. With the initial experiments sodium iron silicates would then form on the inner walls of the autoclaves, which would then inhibit any further corrosion of the autoclave. The corroded iron that would be present in the reactants mixture is on a scale of a few parts per million, hence, high-acoustic and watch-quality quartz can still be obtained with these levels of impurities.[72, 69]

Many other experiments require the use of low-carbon steel or the use of noble metal liners to reduce the amount of impurities in the final products. However, with these liners pressures are counterbalanced with that of the inner walls of the autoclave. Due to this, the liners are only filled with a specific amount to prevent over pressuring the liners, in-turn preventing any ruptures. This style of autoclave has also undergone other modifications for easy of scale-up making them more useful for industrial scale applications and for growing large single crystals.[73] One of the most important design feature of these autoclaves is the self-energized flange closures, which utilize a sealing gasket or plastic materials, such as teflon, depending on desired experimental temperatures. Further modifications to the sealing mechanism allowed for the production of large capacity autoclaves which use modified GreyLoc seals.[60, 74]

6.3.3 *In-situ* Hydrothermal Equipment

Crystallisation studies were originally limited to static measurements where it was only possible to take periodic snapshots of the reaction by probing *ex-situ* samples. This process is not very efficient, and can incorporation artefacts into the data obtained. For example, when preparing samples for measurements, products and reactants need to be separated, changing the state of the system, in turn limiting the usability of the information obtained from the samples. However, with the introduction and development of X-ray based techniques, the ability to prove sample *in-situ* became more feasible. The ability to perform *in-situ* experiments took a huge leap with the introduction and fast expansion of synchrotron radiation sources.

The first *in-situ* experiments were performed during the 1980s. These experiments focused on studying solid state reactions due to a lack of adequate time resolution, which can be negated, for example, when probing temperature related phase transformations. Hence, why these types of reactions were initially probed. However, the first *in-situ* hydrothermal reactions were performed in 1990 by Polak using neutron diffraction techniques to study the formation of zeolites.[75] The first synchrotron X-ray study on the formation of zeolites was later performed by Barnes in 1992, using energy-dispersive diffraction.[76, 77]

For studying hydrothermal reaction *in-situ* generally two types of experimental set-ups have been utilised in studying the crystallisation of solids.[78] The first, an autoclave-esque set-up used for energy dispersive studies, and the second, capillary reactors that are preferred for angularly resolved studies. Energy dispersive methods have been used for the study of zeolites by Bensch,[79, 80] O'Hare,[81, 82, 83, 84] Sankar,[85, 86, 87, 88] and Walton.[89, 90]

The autoclave cells used for *in-situ* studies are generally similar to those used with a standard synthesis lab. However, the walls of the autoclaves need to be thinned in two places (one on each side of the autoclave), to essentially act as small windows for the X-rays to enter and exit the cell.[91] Like most simple modern autoclaves, heating conducted externally, and data acquisition using energy-dispersive techniques can be on the scale of milliseconds to minutes depending on experimental parameters and beamline capabilities. An advantage of these set ups is their physical size, as the reactants can be stirred *in-situ* to prevent sedimentation, and keeping the sample in a homogenised suspension. Cells like these however, come with the drawbacks that the ”windows” need to be kept small, to preserve the structural integrity of the autoclave which in turn limits the accessible q-range. Also, when using this type of *in-situ* cell X-ray absorption can become a problem, hence, they are only really suitable for energy dispersive studies using white beam. These autoclave-like cells has been successfully utilised to obtain valuable information on the crystallisation of layered double hydroxides,[92] metal-organic frameworks,[90] and many other systems.[80, 93] One example of a *in-situ* autoclave type cell is the Oxford/Daresbury hydrothermal cell. This cell has been utilised for studying the crystallisation of a wide range of inorganic materials, including microporous solids (zeolites), layered materials (layered tin sulfides), and open framework materials (gallium fluorophosphates) alongside many others.[94, 81, 93, 82, 78, 95, 96] The use of this cell has shed light on the existence of many previously unknown intermediate crystalline phases that occur only under specific reaction conditions and not others. For example, when studying the crystallisation of gallium fluorophosphates, unknown intermediate crystalline phases were observed prior to the formation of the expected microporous phase.

6.3.3.1 Capillary cells

The use of a narrow capillary as hydrothermal reactors, has been utilised for numerous *in-situ* experiments. First pioneered by Norby in the 1990s, capillary reactors need needed to use capillaries made from a material capable of withstanding the temperatures and pressures produced during hydrothermal synthesis, as well as being chemically inert (to the reactants in the probed reaction) and relatively transparent to X-rays.[97, 98, 99] Due to these requirements, quartz, sapphire, diamond and thinned steel tubes have been used depending on reaction and technique used to probe the synthesis.[6, 100, 78, 94, 99] Capillary cells have the advantage that their length provides, as probing the reactions are not limited to a specific window area, and samples can be probed along with length of capillary. As the scattered beam is not limited to a specific window area and scattered X-rays can escape from the entirety of the reaction volume, means that capillary cells are well suited for use in angular resolved studies. The design of capillary based cells has been adapted many times since its initial development in the 1990s.[101, 102, 103, 104, 105] For hydrothermal experiments, capillaries are sealed with once the reaction precursors have been injected into the cell. The capillary is then mounted on a goniometer head so it can be placed directly into the beam. The use of the goniometer head also means that the capillaries can be spun for better data acquisition. Heating is commonly done *via* a hot air blower and with some designed pressures can be applied externally. Capillary cells do, however, have certain drawbacks. For one, no *in-situ* stirring can be applied to the reactants, this can cause problems with the homogeneity of samples and reaction mixtures. Another draw back is the very small probed volume within these reactors, which can cause problems with repeatability and also introduce artefacts into obtained results.

6.3.3.2 UCL *in-situ* Hydrothermal cell

This cell was designed to mimic conditions produced within an autoclave with the incorporation of large windows to allow the passage of X-rays through the sample. Heating is provided from four cartridge heaters built into the cell stand, and the heat is transferred though the brass body of the cell, to a polyether ether ketone (PEEK) sample holder. PEEK is utilized in this cell primarily for its high chemical inertness and its ability to withstand moderate temperatures (up to 240°C). The cell is sealed using two large (25 cm in diameter) windows placed on either side of the PEEK sample holder. Typically the windows used would be made out of mica or kapton, however, the window material can be altered to better suit the technique being used to probe the experiments or to better withstand the conditions that the experiments are conducted under. The advantages of using a cell with this sort of design are the larger accessible q-ranges in comparison to the autoclave set up due to the incorporation of large windows. Using changeable window materials is also an advantage as it can be tailored to better suit experimental requirements. This cell also has a much larger probed volume in-comparison to capillary cells, however there is still a lack of space for sufficient stirring. This means sedimentation can become an issue. Also, the indirect heating of the sample means that the sample temperature in the cell needs to calibrated/calculated. Other issue can occur from improper sealing as this design utilises a large screw threaded seal that can bow the large windows.

6.4 Designing a New Hydrothermal Cell

6.4.1 Introduction

Design a *in-situ* cell capable of synthesising materials under hydrothermal conditions on a beamline at a synchrotron. The cell will be primarily designed for use when collecting scattering experiments and for preventing the sedimentation of particles during data acquisition.

6.4.2 Prevention of Sedimentation

The sedimentation of particles can be a large problem when performing *in-situ* experiments on heterogeneous solution, as it becomes harder to assess if the data collected is relevant or not. For example, when trying to look at the nucleation and growth of nanoparticles, nucleating from within a solution, the repeated nucleation of particles can be easily observed, whilst their growth can be easily missed due to particle sedimentation. The sedimentation of particles is a sizeable problem when performing such experiments *in-situ*, but also when collecting data on any heterogeneous systems. Hence, the prevention of particle sedimentation becomes very important for collecting data that is representative of the sample as a whole.

Stokes' law is, in its essence, a description of how drag forces act upon a spherical object within a fluid and it can be used to determine the rate at which a particle, of known size, sediments within a fluid of known viscosity and density.[106] It is generally written as:

$$F_d = 6\pi \cdot \eta \cdot R \cdot \upsilon \tag{6.1}$$

where, F_d is the frictional force acting upon the interface between the particles and the fluid (Stokes' drag), η is the dynamic viscosity of the fluid, R is the radius of the spherical particles and υ is the flow velocity of the particles.[107] There are a few assumption made with this equation such as the homogeneity of the materials involved, the particles are spherical with smooth surfaces and the particles do not interact with each other. Stokes Law can be used to obtain the terminal velocity of spherical particles in a fluid by utilising differences in weights and buoyancies of the spheres in the fluid:

$$F_g = \Delta\rho \cdot g \cdot \frac{4}{3} \cdot \pi \cdot R^3 \tag{6.2}$$

where $\Delta\rho$ is the difference in densities between the particles and the fluid and

g is the gravitational acceleration.[108] From using equations 6.1 and 6.2 a force balance can be derived so that $F_d = F_g$ meaning that the velocity, υ, can be derived:

$$\upsilon = \frac{2 \cdot \Delta\rho \cdot R^2}{9 \cdot \eta} \tag{6.3}$$

where η is the dynamic viscosity. As the excess force increases with R^3 and Stokes' drag increases with R, the terminal velocity increases with R^2 meaning that it is greatly dependent upon particle size.[109] For example, 500 nm silica spheres held within water will sediment at a rate of c.a. 4 mm $hour^{-1}$ at $25°C$. For 250, and 100 nm silica spheres, under the same conditions, sediment at $c.a.$1 and 0.1 mm $hour^{-1}$ respectively. For systems with greater $\Delta\rho$ values sedimentation becomes much more of a problem, for example, 100 nm gold nanoparticles in water under the same conditions as above sediment x20 faster than silica particles, at a rate of c.a. 2 mm $hour^{-1}$. Heat is also a factor to consider when thinking about sedimentation and performing *in-situ* experiments. With increasing heat sedimentation also increases. For example, 100 nm silica spheres in water at $80°C$ sediment at a rate of 0.42 mm $hour^{-1}$, in comparison to 0.15 mm $hour^{-1}$ at $25°C$, and 100 nm gold nanoparticles sediment at a rate of 4.7 mm $hour^{-1}$, in comparison to 1.66 mm $hour^{-1}$ at $25°C$. This temperature increase results in a substantial change in sedimentation rates (see table 6.1). The rates of sedimentation may not seem that large at first, but when considering the size of sample environments used for SAXS measurements and the size of the X-ray beam the problems become more apparent. For example, the X-ray beam at Diamond beamline I22 is only 0.2 mm in height, hence, for many *in-situ* experiments, especially at high temperatures the sedimentation of particles can be a very big issue. This is again an significant problem for lab SAXS and SANS experiments due to the longer exposure times that are needed for data collection.

6.4.3 Design Specification

When designing an *in-situ* hydrothermal cell for performing scattering experiments at a synchrotron there are many things that need to be taken into account. First, the

Material	**Particle Size** (nm)	**Sedimentation** ($mm \cdot h^{-1}$)
	$25°C$	
Silica	500	3.74
Silica	250	0.94
Silica	100	0.15
Silica	50	0.04
Gold	250	10.39
Gold	100	1.66
Gold	50	0.42
	$80°C$	
Silica	500	10.57
Silica	250	2.64
Silica	100	0.42
Silica	50	0.11
Gold	250	29.35
Gold	100	4.70
Gold	50	1.17

Table 6.1: Rate of sedimentation for spherical nanoparticles in water.

experimental conditions for temperatures, pressures etc. need to be met, but also requirements from the probing technique also need to be considered, and only if the design can meet the criteria from both can be considered a success. For this project a hydrothermal cell was developed, primarily for collecting *in-situ* SAXS data from heterogeneous solutions. This means that the cells needs to be capable of creating hydrothermal conditions, but also allow for good data acquisition over a large q-scale.

The attractive features for the use of hydrothermal synthesis is that material growth can occur below a material's melting point, and often at a temperature below that of a destructive phase transformation (e.g. α-quartz for silicas). As hydrothermal systems are sealed the atmosphere can be altered to suit that of the growing material (e.g. creating an oxidising or reducing environment). Hence, for designing an hydrothermal cell there are some specific criteria that needs to be met. The good hydrothermal cell needs to be:

1. Inert to acids, bases and oxidising agents

2. Easy to seal and be leak proof

3. Capable of reaching the high temperatures and pressures required for hydrothermal synthesis
4. Able to withstand hydrothermal conditions for extended periods of time
5. Rugged enough to withstand multiple heating and cooling cycles

The requirements for an *in-situ* cell from the point of view of scattering experiments are quite different. A good *in-situ* cell for collecting SAXS data needs:

1. Changeable path-lengths
2. Changeable window materials (also useful for other techniques such as XAS)
3. Large windows for obtaining large q-range
4. The prevention of sample sedimentation
5. Integration into beamline systems (for remote control of temperature etc.)

Changeable path-lengths are important to be able to perform experiments on different material systems where the probed sample has a greater or lesser X-ray absorption coefficient. Changeable windows are advantageous as there is a lower chance of contamination between experiments, whilst the ability to use different window materials means that the window material can be tailored to different experimental set-ups.

The criteria for the hydrothermal capabilities of the cell are very much material based, whilst the data collection criteria are primarily design focused. This, in a way, partially decouples material choice and design aspects of this project at its initial stages, however, both need to be considered when it comes to component fabrication and overall cost. Safety also needs to be considered a each stages of the design process.

6.4.4 Choice of Materials and Parts

Due to the requirements, discussed above, the choice of materials used for the construction of an autoclave is very important to be able to perform hydrothermal experiments successfully. Material choice is especially important when considering where the sample will be held within the cell (an initial design prototype can be seen in figure 6.3). Overall, the external enclosure need to be made from a strong material to withstand the high temperatures and pressures produced within the cell, however, there are very few materials that are strong and also inert to acidic and basic conditions.

Also for use with sensitive synchrotron techniques the presence of impurities can not be tolerated, hence, manufacturing the sample chamber from metal and using similar methods to prevent corrosion of the walls that were utilised with modified Bridgman high pressure autoclave (mentioned above) are not applicable here. The use of such methods would also limit the use of the *in-situ* cell to only a few specific experiments and, hence, the use of a material with good chemical inertness is therefore a necessity. The solution to this problem is therefore to use at least two materials for the cell, one strong material for the external enclosure, and a second for containing the sample. Materials such as Polyether ether ketone (PEEK) and Polytetrafluoroethylene (PTFE) are some of the best choices for being in direct contact with the sample due to their high chemical resistance. PEEK is a high temperature thermoplastic, that retains its physical properties upto temperatures of around 240°C.[110, 111] It absorbs little moisture, has good wear characteristics and is easily machined. PTFE, on the other hand, is a crystalline polymer with a melting point of around 250 - 300°C (depending on purity) and possess many of the same attributes as PEEK, though it is not as easily machined, or as strong as PEEK, though it is more elastic. However, the unique characteristics associated with PTFE make it the idea material for use as liners in modern autoclaves, where PTFE's ability to expand with rising temperatures can be exploited in forming an hermitic seal within modern metal autoclaves.[72] For the design of an *in-situ* hydrothermal cell, where a hermetic seal will not be used, PEEK is generally a better choice, where ease of machining, good wear characteristics, strength and low levels of deformation are more valuable.

A wide variety of window materials can be incorporated into the cell's design to make the cell suitable for different experimental conditions and for different char-

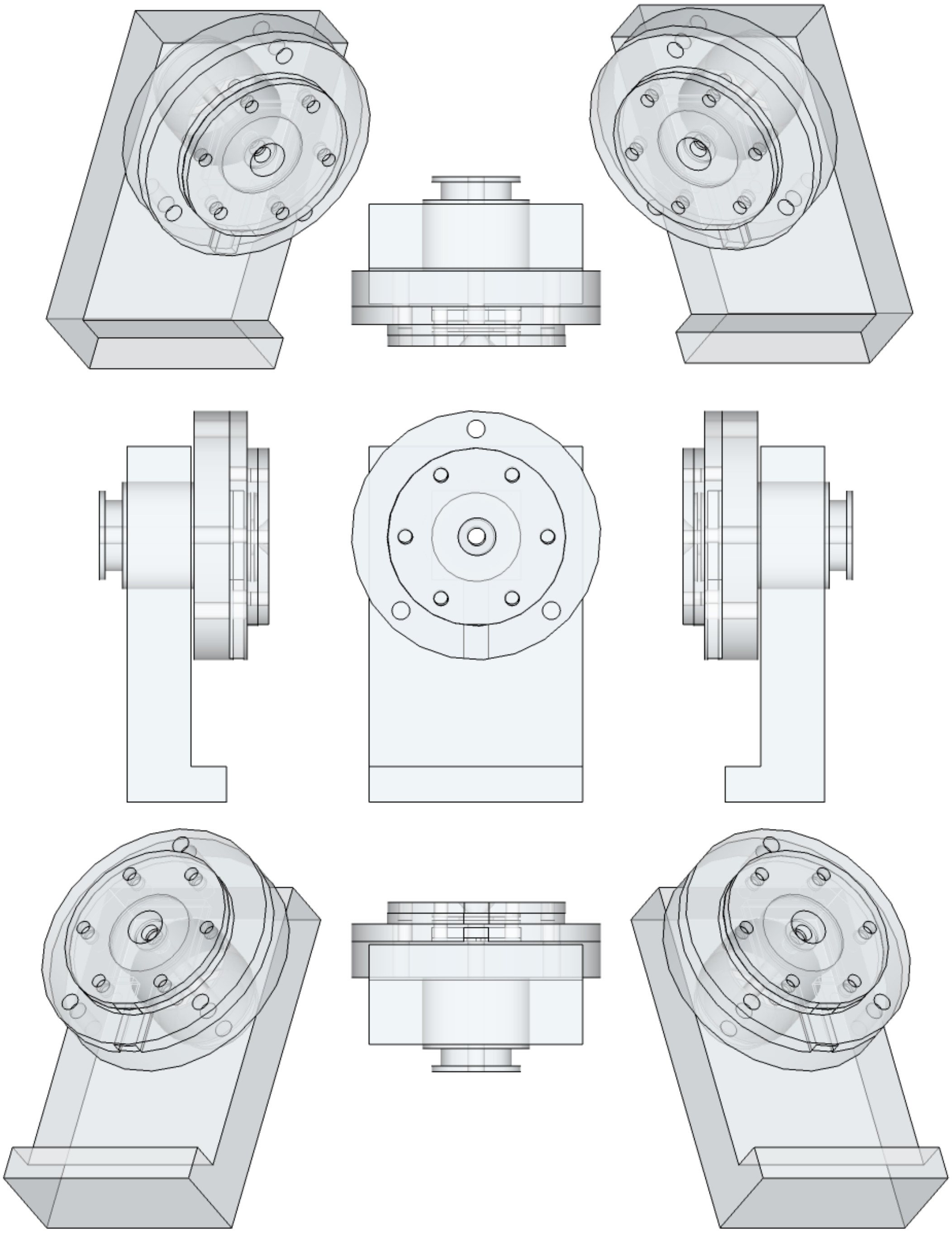

Figure 6.3: Orthographic representations of the initial design for the *in-situ* rotating hydrothermal cell that were 3D printed to aid in the design process.

acterisation techniques. The windows need to be between 6 - 25 mm in diameter and window material should be chosen for specific experiments as window materials themselves have their own pros and cons that are experimentally dependent.

For example, mica can be a good window choice for SAXS experiments as they are strong and scatter little at small angles, however, mica cannot be used for SAXS experiments where data collection is occurring simultaneously with a 2D WAXS detectors, due to the presence of high intensity single crystal spots on the detector potentially damaging the detector. Hence, window material is very experiment dependent, though some example window materials are: mica, mylar, kapton, sapphire, diamond, PTFE, amorphous glass.

As for the external enclosure strong materials are required that have good thermal characteristics, and are easy to machine. The ease of machining characteristic removes a lot of potential materials such as the use of stainless steel, however, metals such as aluminium and brass are still valid options. Both materials have similar thermal characteristics (depending on compositions) and both are easily machined, however, aluminium is much cheaper than brass making it the more obvious choice for the external enclosure.

For heating the sample, the heater needs to be capable of reaching temperatures in excess of 200°C. It also needs to be able to incorporated into the design so that heating of the sample is done as directly as possible. Due to these requirements a ceramic heater was chosen due to the diversity of shapes readily available on the market. The Watlow Ultramic 600 advanced ceramic heater was chosen due to its small form factor (25 x 25 mm square) that has a 5 mm diameter mounting hole in the centre of the heater, which will be utilised as a path for the X-rays to access the sample.[110] The heater is capable of reaching 400°C and has a build in k-type thermocouple for accurate temperatures reading.

For the prevention of sedimentation the *in-situ* cell required a motor and bearing for the rotation of the sample enclosure. The motor needs to have accurate, reproducible positions, variable speeds, be able to rotate both clockwise and anti-clockwise directions and quickly switch between rotation directions without issue. Hence, the Quicksilver motor QCI-A23K3 was chosen for its broad range of controllable parameters, its simple set up and detailed software package making in-depth motor control relatively simple.[112]

The bearing used for smooth rotation of the sample, in general, needs to be able to withstand some high temperatures, be of a standardised size that is readily available and relatively inexpensive. For the bearing the standard 6305 form factor was chosen due to its 25 mm and 62 mm internal and external diameters that could be easily incorporated into the design. The 6305 form factor also has a wide range or bearings available that are self lubricating, can withstand high temperatures and remain stable at high temperatures to prevent off axis rotation that could effect data collections.[113]

6.4.5 Description of Final Design

The cell is designed for the primary purpose of preventing the sedimentation of particles within heterogeneous systems. The cell is a versatile hydrothermal reactor with large, interchangeable windows that allow the passage of X-rays through the sample. For sample loading (figure 6.4), a PEEK ring of desirable pathlength is chosen and fitted with a window made from a suitable material, tailored for the experiments being performed. A 2 mm silicon rubber seal (24mm O.D, 18mm I.D) is then placed on the window and attached to the aluminium heater mounting using six M3 x 5mm countersunk internal hex screws. This unit is then placed on a flat working surface, PEEK sample ring facing up, so that the sample can be added (2mm path length with 10 mm diameter opening holds c.a. 120-140μl, 1mm path length c.a. 60-70μl). Next a second window is carefully placed over the sample, making sure no liquid is pushed between the PEEK ring and the windows itself. Next a silicon rubber ring is placed on top of the window and then the aluminium front plate (tapered side facing up) is then mounted using six M4 x 8mm internal hex screws. The screws should be screwed in and tightened in a way to provide even pressure across the surface of the aluminium front plate. Skived PTFE tape can also be used on the sample ring to help create an internal seal between the PEEK sample ring and the windows. The sample ring opening is larger than that of the opening on the front plate, but smaller than the windows being used, so that a larger sample volume can be accommodated/probed.

The cell can accommodate a range of window diameters (6 - 25 mm) and ma-

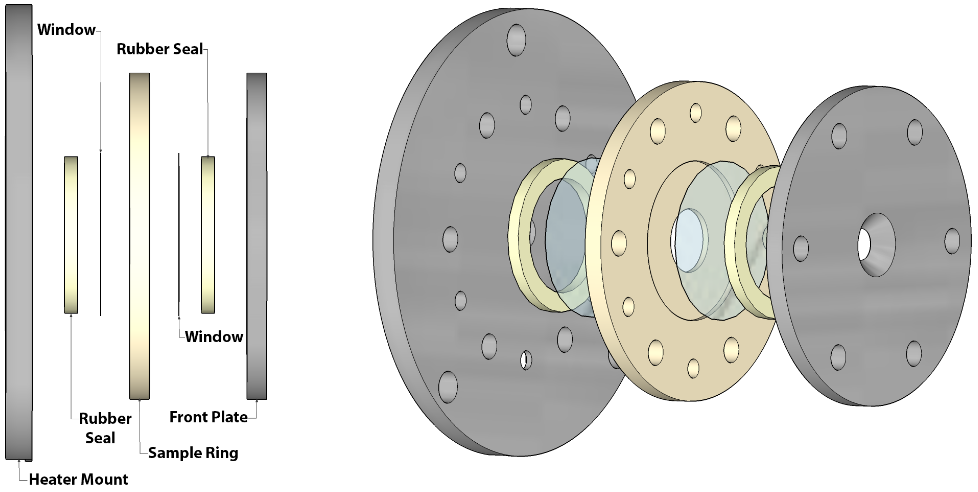

Figure 6.4: Diagram of the *in-situ* rotating hydrothermal cells sample environment enclosure.

terials depending on sample ring used, to make finding suitable windows easier (not restricted to a single specific window diameter), and means that the sample environment can be tailored to that of the experiment. Also, with the use of larger windows more sample can also be accommodated, through widening of the sample chamber within the sample ring. Once sealed, the sample chamber can then be taken from the lab to the beamline, where the heater can be mounted into the grooves found at the rear of the sample chamber (in the heater mount, see figure 6.4), and then the sample chamber can be mounted on to the cell stand using three M6 screws. The heater is a 120 V, 800W Watlow Ultramic 600 advanced ceramic heater with a maximum temperature of 400°C, that uses a k-type thermocouple for temperature monitoring.[114] The eurotherm and power supply used for this heater have been integrated into Diamond's I22 beamline so that it can be run remotely. A piece of Superwool™ (a good thermal insulator, 0.06 W/mk at 200°C) can also be placed between the sample holder and the stand to prevent heat transfer from the heater to the stand, and the bearing that it houses. Full rotation of the cell is possible for room temperature experiments, however when the heater is needed for experiments a maximum rotation of 340°, which can be performed in a back-and-forth motion. Full rotation is not possible due to the wires providing power to the heater and the thermocouple. Due to these wires a hard stop has also been incorporated into the final design of the cell for safety reasons.

The cell stand houses a bearing to assist in the smooth rotation of the cell. The cell utilises standard sized bearings (6305) so that they can be easily obtained and changed depending on needed use. For most use cases that cell can be equipped with a SKF Deep groove ball bearing model 6305-2Z/C3 that has maximum working temperature of 120°C.[113] This will be suitable for all hydrothermal uses of the cell as the temperature of the bearing is much lower than that in the sample chamber of the cell. However, for use at higher temperatures, where the use of PEEK sample rings are not possible the use of a graphite based, self lubricating bearing, such as the SKF Deep groove ball bearing, model 6305-2Z/VA228 can be used up to the maximum temperature of the cell's heater (400°C). The cell stand is also equipped with a stepper motor (Quicksilver motor QCI-A23K3), and a timing belt for the rotation of the cell.[112] The motor has a USB interface so that it can be controlled remotely from a PC.

The stand is made up of four main parts. The vertical stand, which houses the bearing using a push fit and grub screws to hold it in place. Inside the bearings internal opening is the sample mount, which is essentially a hollow cylinder of aluminium. It is hollow to allow the beam to pass through the centre of rotation of the cell. At one end of this cylinder there is a mount for the sample chamber to be attached to. At the bottom of the cell there is a mounting for the motor. The motor is connected to the sample mount hollow cylinder using a timing belt, which can be tensioned depending upon the mounting position of the motor. The motor mounting plate is also equipped with mounting holes so that the cell can be mounted securely on a beamline. The holes are spaced to fit a standard M6 breadboard. Orthographic representation of the final design can be seen in figure 6.5.

6.4.6 Thermal Properties

Between the sample and the heater is 1 mm of aluminium. This thin piece of aluminium is strong enough to withstand the strain it is placed under from sealing the cell and allows for good thermal conductivity from the heater to the sample. The cell is heated using a 800W Watlow Ultramic 600 advanced ceramic heater with

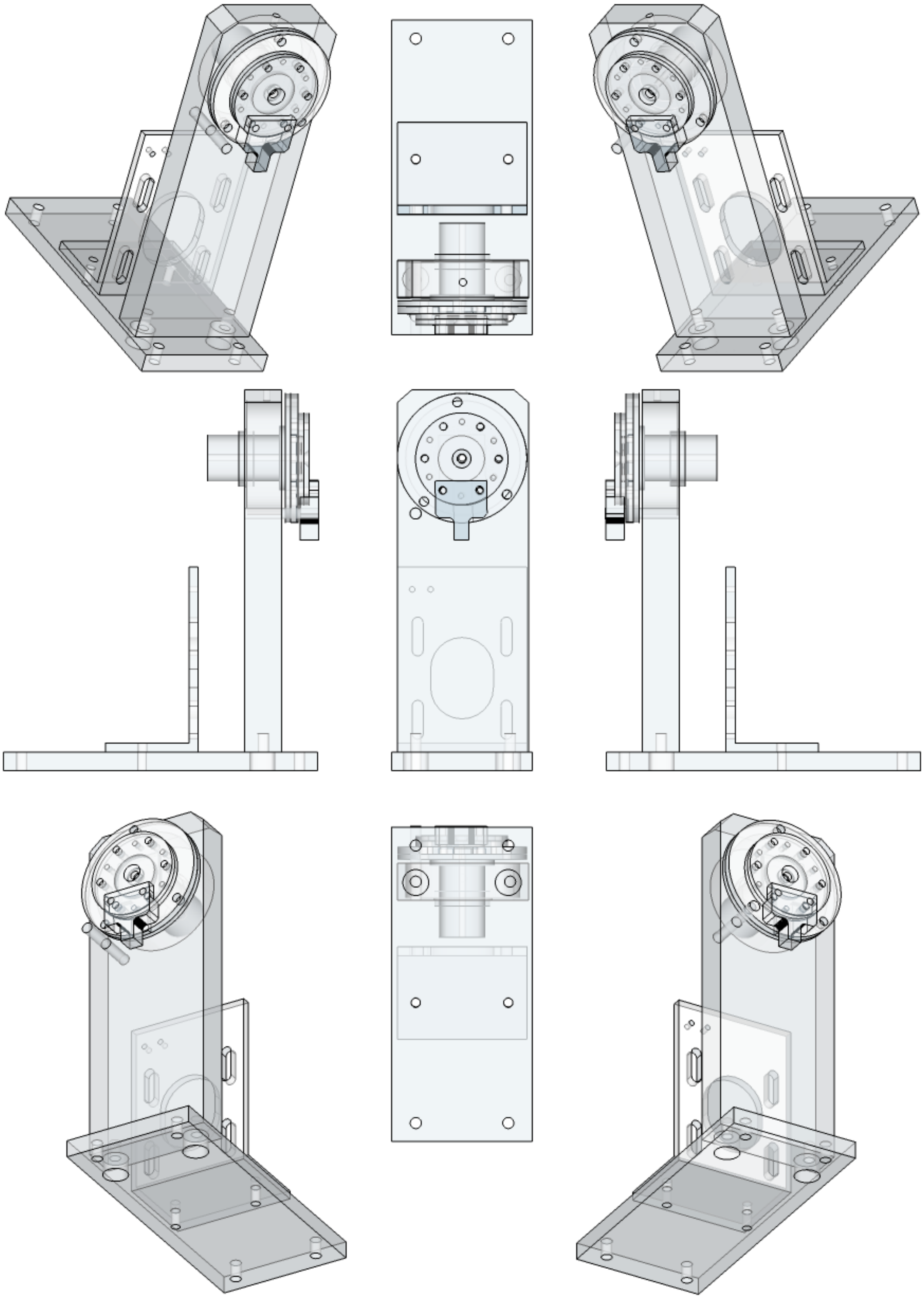

Figure 6.5: Orthographic representations of the *in-situ* rotating hydrothermal cell including all machined parts.

a built in thermocouple. Temperature control is performed by a Eurotherm PID controller that capable of reading the K-type thermocouple built into the ceramic

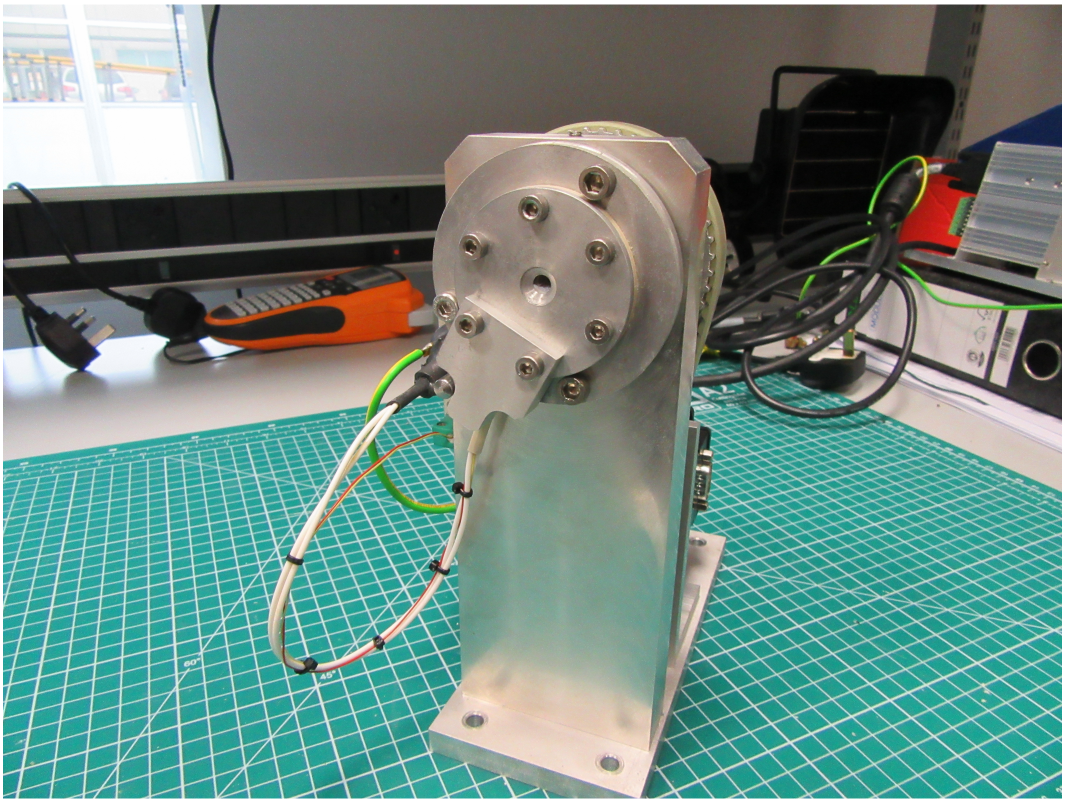

Figure 6.6: The final design for the *in-situ* rotating hydrothermal cell.

heater. When the heater is powered, heat is transferred to the sample, however, as the thermocouple is built into the heater, we do not know accurately the sample temperature and there is a temperature offset between the heater and the sample. The temperature of the sample will be lower as the heat has to transfer through the 1 mm of aluminium of the heater mount and some heat is transfer from the heater to the cell stand. This unwanted heat transfer to the stand can, however, be negated by placing a 2 mm piece of Superwool™, which is a good thermal insulator (thermal conductivity of 0.06 W/mk at 200°C), between the heater mount and cell mount. It is possible to account for the temperature offset by measuring the sample temperature independently of the heater. This was done by drilling a hole into the top of the sample ring for placing a second thermocouple directly into the sample to probe the temperature offset. Temperature offset tests were performed using silicone oil in the sample chamber, which was subjected to a series of heating tests where the stage temperature was set and the sample temperature was left to equilibrate. These tests revealed how the ceramic heater heats up almost instantaneously to the set temperature and that the temperature of the cell reaches equilibrium within a 5 minute period (figure 6.7). From these test, the temperature offset from the set temperature and the sample temperature were calculated and it was found that there is a linear relation between the sample temperature and set point that can be expressed as:

$$T_{cell} = 0.73 T_{stage} + 6.21 \tag{6.4}$$

This expression if for the cell where a 2 mm pathlength is used. This expression also changes when it is equipped with a 2 mm piece of Superwool™ between the heater mount and the stand this relation changes to:

$$T_{cell} = 0.79 T_{stage} + 6.46 \tag{6.5}$$

The relationship is also linear but a steeper gradient is observed, indicating its better performance (up to an 8.23% increase in temperature). This change, between using the Superwool™ and not, represents a 13.5°C temperature increase on average for set point temperatures between 200 - 230°C and 9.5°C average increase for set point temperatures between 100 - 200°C.

6.5 Experimental

SAXS experiments were performed at Diamond Light Source, UK on beamline I22. A sample to camera distance of 9.233m was utilised at an energy of 12.4KeV to give an accessible q-range of 0.0018 - 0.18Å^{-1}. The rotating cell was equipped with a PEEK sample ring with 1 mm pathlength. The cell was loaded with a 70μl aliquot of a 3 M aqueous solution of 250nm amorphous silica spheres was loaded into the *in-situ* cell's sample chamber. The loaded sample chamber was then subsequently fixed to the cell stand and placed on the beamline. Rotation of the cell was controlled through the QuickControl software provided by QuickSilver Controls, Inc. Through the use of this software the amount of rotation could be controlled

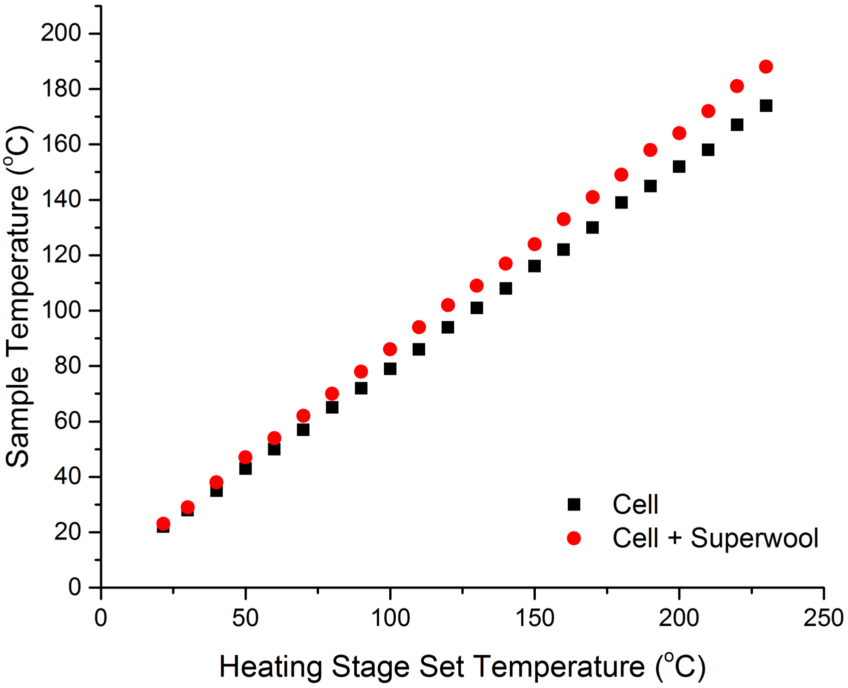

Figure 6.7: Equilibriun sample temperature as a function of the set temperature of the heating stage.

alongside the speed of rotation. Prior to each individual experiment the sample was vigorously agitated. The collected SAXS data was then background processed using DAWN.

6.6 Results and Discussions

6.6.1 No Rotation

Figure 6.8 shows the processed SAXS data obtained from a 3 M solution of 250 nm SiO_2 spheres in water. The sample was not subjected to any mechanical agitations during data collection and it can been seen that in the space of the first 10 seconds that the scattering data changes quite radically. The change can be seem most prominently in the first maxima observed between 0.003 - 0.004Å^{-1}. Figure 6.9 shows how this effect continues over the first 5 minutes of data collection. These changes in intensity of the data and the shape of the maxima can be mistaken

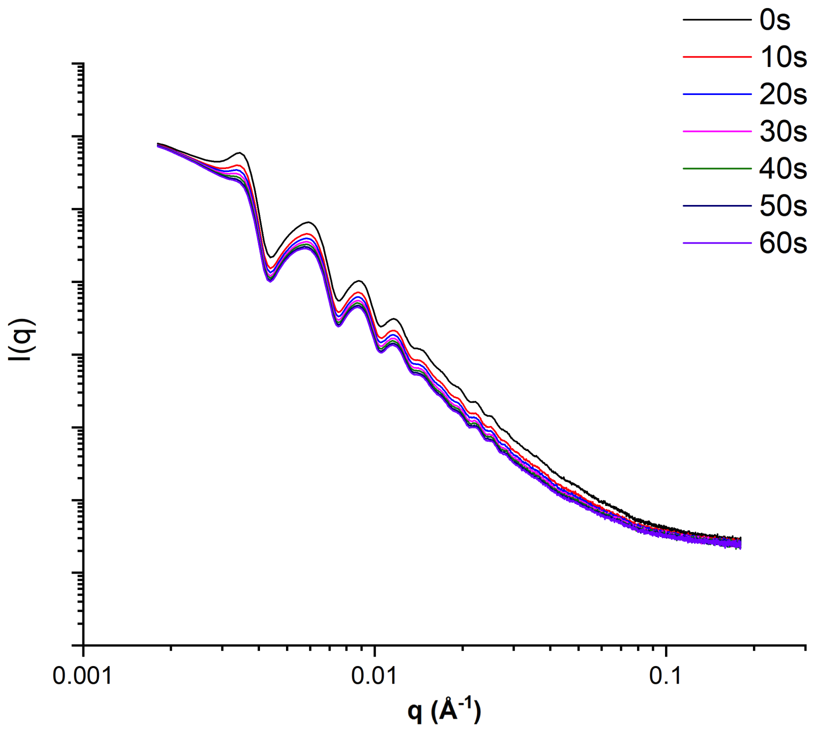

Figure 6.8: SAXS data collected on a solution of 250 nm SiO_2 spheres dispersed in water, showing how the data is effected by sedimentation of particles over the course of 1 minute.

for mechanistic changes occurring during *in-situ* experiments, though the drop in intensity is actually caused by the presence of less sample (SiO_2 in this case) in the beam. This also causes the change in shape of the maxima in the data, as with a higher concentration of particles present within the beam, more secondary scattering incidents occur leading to a larger presence of structure factor being present within the data.

As SAXS is an averaging technique, and the data collected is said to be representative of the sample as a whole, however, for many experiments this may not be true, especially for heterogeneous systems where the sedimentation of particles is a problem. This is because the whole sample volume is not being probed and only an averaged scattering pattern of the particles in the beam is actually obtained. This can lead to problems with reproducibility, as the data collected may not be representative of the whole sample. The early effects of sedimentation on the data are the most drastic, however these can be most easily missed. The sample in this experiment was vigorously mixed prior to data collection, however with set up times between experiments on beamlines, times for safety searches to be completed and additional time for data collection to actually begin the initial changes in the sample could be missed completely, again bringing up reliability problems for many experiments.

This is a problem that effects the data more and more over time, meaning the final stages of a reaction are the easiest to miss, and experiments maybe thought of as failures due to changes in sample concentrations resulting in loss of signal, meaning that sample is no longer being a problem. This also raises many other questions, such as, when collecting data on the growth of particles over time, are the larger particles being probed or is the growth of these particles being missed completely due to sedimentation?

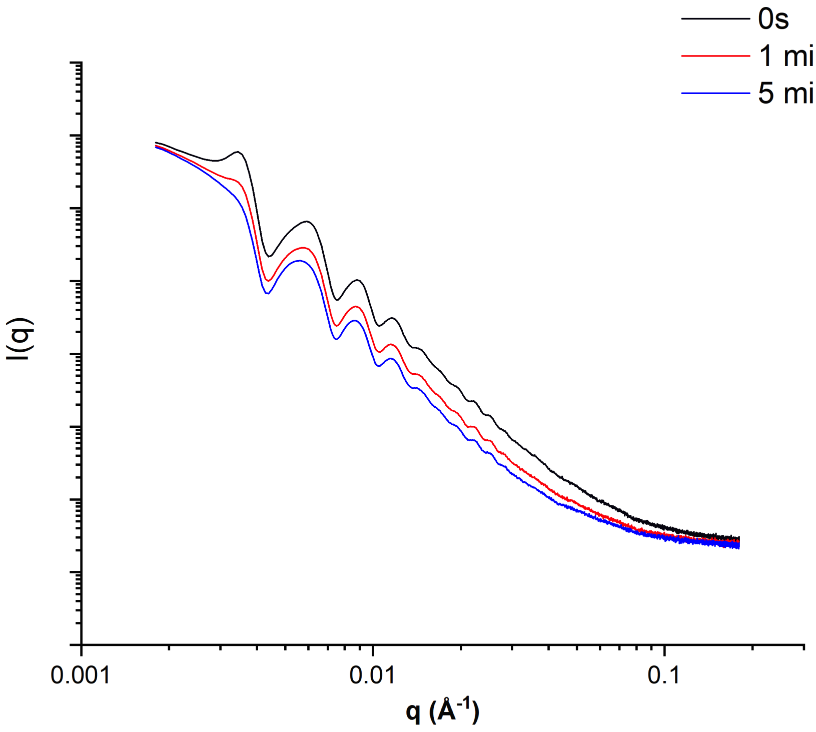

Figure 6.9: SAXS data collected on a solution of 250 nm SiO_2 spheres dispersed in water, showing how the data is effected by sedimentation of particles over the course of 5 minute.

This changes in data showing in figure 6.9 occur due to the sedimentation of the SiO_2 particles in water. To visualise the sedimentation we can use the transmission data from the experiment, alongside the Beer-Lambert equation to work out how much SiO_2 is in the beam at any set time throughout the experiment. The Beer-Lambert equation can be written as:

$$T = e^{-2\mu R} \tag{6.6}$$

Where T is the transmittance of the sample, μ is the sample's X-ray absorption, and R is the sample radius. As we are essentially interested in finding the sample thickness we can rearrange the equation to obtain the sample diameter which will give a rough idea of the actual sample thickness:

$$\frac{ln(T)}{-2\mu} = R \tag{6.7}$$

$$\frac{ln(T)}{-\mu} = D \tag{6.8}$$

Utilising the above equation we can have a good idea of how much SiO_2 is in the beam at any point during the experiments. Figure 6.10 shows the transmission values collected over a 5 minute period of time, on a 3 M solution of 250 nm SiO_2 sphers in water at room temperature. The sample was held within the rotating cell, however, for this experiment the sample was not rotated so that it was possible to see the effects of sedimentation has upon the sample. Figure 6.10 also shows the amount of SiO_2 in the beam, calculated using the Beer-Lamber equation.

From this data we can see that the transmission increase over time, meaning that the amount of sample in the beam is decreasing. It is possible to see that at the start of the experiment there is 348 μm in the beam, and this initially drops quite

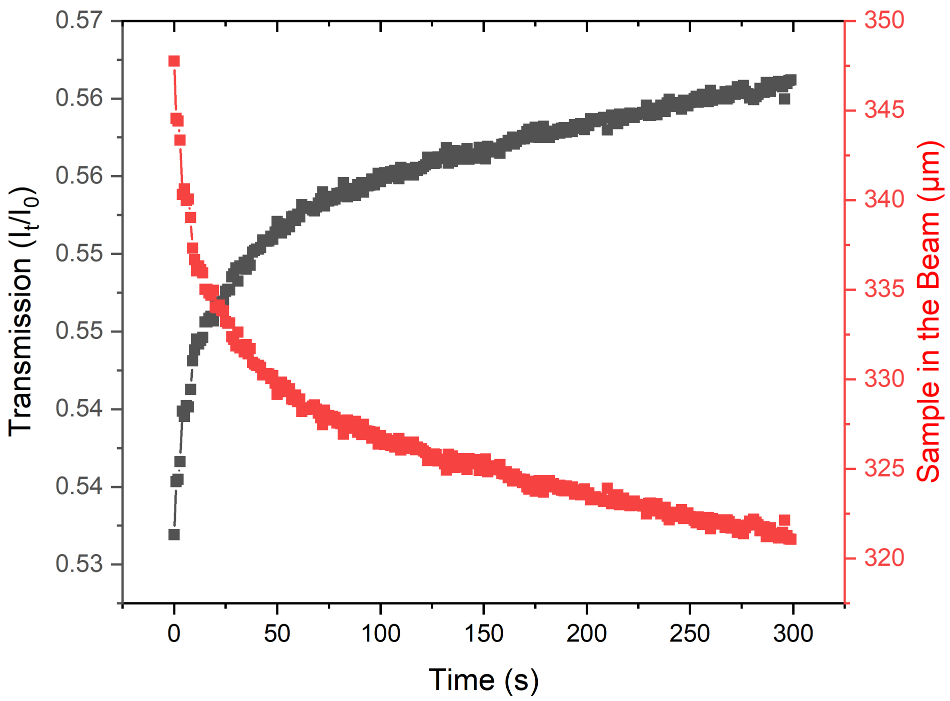

Figure 6.10: Orthographic representations of the *in-situ* rotating hydrothermal cell including all machined parts.

rapidly over the first 60 seconds before slowing. After five minutes there is only 321 μm in the beam, equivalent to almost an 8% loss of SiO_2 in the beam over a 5 minute period. As mentioned in section 6.1, at elevated temperatures the problem of sedimentation increases greatly. For example, at 80°C sedimentation rates are over x2.8 faster, meaning for *in-situ* experiments where heating is involved, the problems associated with sample sedimentation will be increased greatly.

6.6.2 Sample Rotation

Figure 6.11 shows how rotation speed effects the rate of sedimentation over the course of a 30 minute experiment, when the cell is rotated 180° in a back and forth motion. It can be seen that when the rotation speed is relatively fast (total rotation time = 150 ms), the fraction of sample in the beam is much lower than observed when there is no rotation. This low fraction of silica in the beam can be explained as not being due to sedimentation, but due to centrifugal forces acting upon the

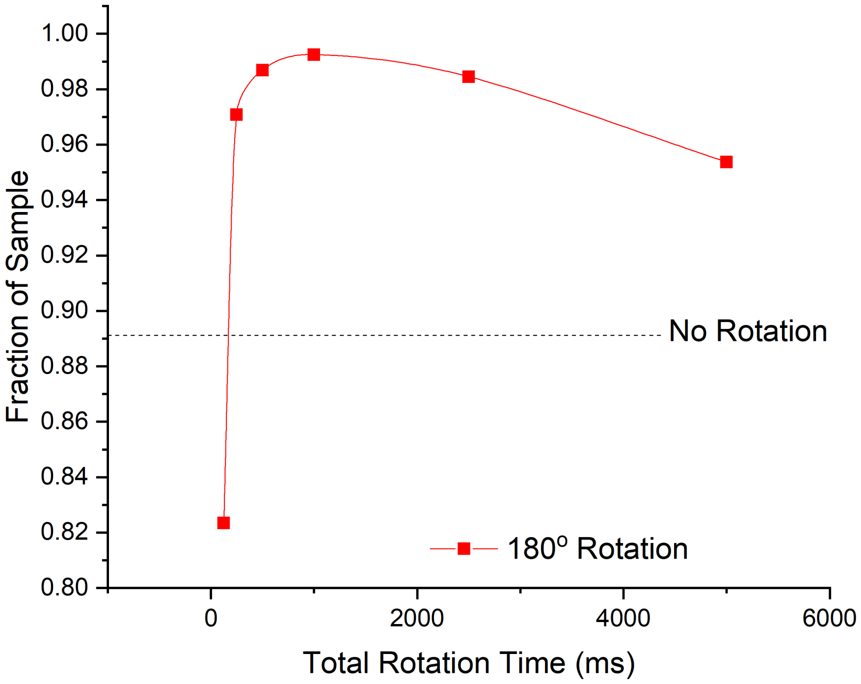

Figure 6.11: The sedimentation of SiO_2 when rotated in a back-and-forth motion over 180° rotation, performed at six different rotation speeds (low total rotation time = greater rotation speed). Each point corresponds to the fraction of SiO_2 left in the beam after 30 minutes of rotation, and the fraction of SiO_2 left in the beam when the sample is subjected to no rotation is marked by a dashed black line.

sample effectively pushing the SiO_2 to the edges of cell and out of the beam. This high speed rotation results in nearly a 20% loss of sample in the beam can after 30 minutes of rotation.

However, as the speed of rotation is decreased from 100 to 250 ms it can be seen that nearly 15% more sample is observed in the beam (from 82.4% at 100 ms to 97.1% at 250 ms), this is also an 8% increase in SiO_2 observed than with no rotation. The trend of slowing rotation speed and observing increasing amounts of sample in the beam stays true up to a rotation speed to 1000 ms where $>$ 99% of the sample remains in the beam over a 30 minute period. However, upon decreasing the speed further it can be seen that less sample remains in the beam over this period of time. This indicates that the speed of rotation is insufficient, at rotations speeds slower then 1000 ms, for adequately agitation of the sample, meaning that there is some sedimentation observed, however, the slow speeds can be still be more effective than allowing the sample to be stagnant.

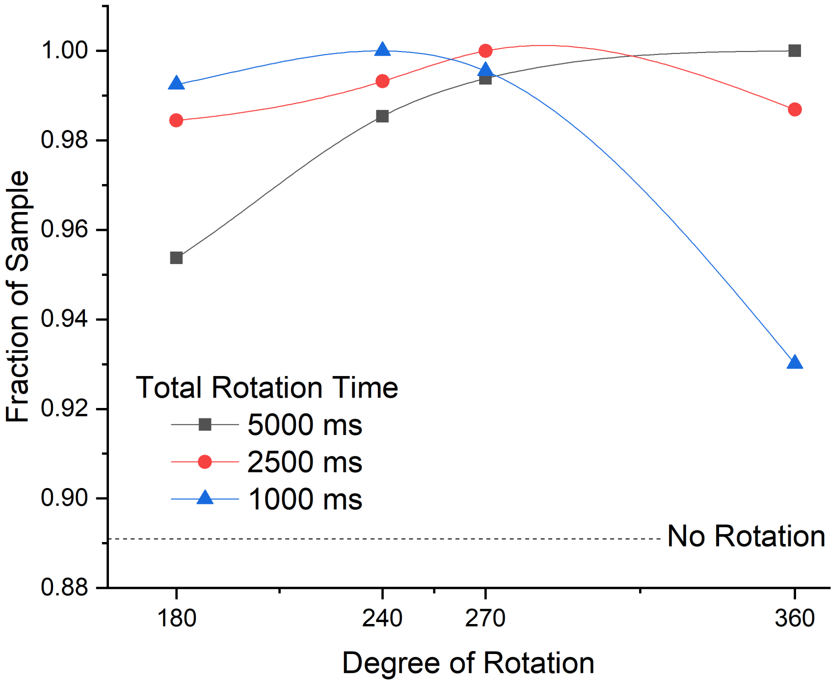

Figure 6.12: Comparison of the rotation speed and the degree of rotation and its effectiveness at preventing sedimentation on a 3 M solution of SiO_2 in water at 25°C.

The effects on the degree of rotation was also probed using the rotating cell. Figure 6.12 shows how different degrees of rotation, with the same rotation speeds, effects particle sedimentation after 30 minutes. As we saw in figure 6.11 we can see with 180° back-and-forth rotation having a rotation of c.a. 1000 ms per rotation is best. Though, when comparing the speeds used for 360° of rotation, slower rotation speed are more effective.

A trend can bee seen where effective speeds for preventing sedimentation, i.e. speeds where centrifugal forces are not prominent, and speeds that are not too slow to be effective. As the rotation speed is increased, a less degree of rotation is required to prevent sedimentation effectively, and similarly with lower rotation speeds, a larger degree of rotation is required. Figure 6.12 also shows how with all four tested degrees of rotation, it was possible to keep $> 99\%$ of the sample in the beam. Optimum rotation parameters for preventing the sedimentation 250 nm SiO_2 spheres in water, is to rotate the sample by 360° at 5000 ms rotation^{1}, or 270° at 2500 ms rotation^{1} or 240° at 1000 ms rotation^{1}.

6.7 Summary

By rotating samples during data collection the sedimentation of particles can be successfully avoided. By carefully choosing the parameters for rotation the sedimentation of particles can be negated during *in-situ* SAXS experiments. The new cell's simplistic design for ease of fabrication and use of off the shelf parts means replacement parts are either inexpensive to manufacture and or widely available. It is also good to note that due to the cells versatile design it can also be utilised on many beamlines using a multitude of different synchrotron or neutron techniques to obtain data on heterogeneous systems without having to deal with issues arising from the sedimentation or particles over time. For example, for use in XAS experiments, where the sedimentation of the sample in the beam can cause drastic changes in data quality. The cell would also be useful for use with the collection of lab based scattering measurements due to the techniques slow data collection. Even though measurement times at a synchrotron can be very short this does not take into account the time taken to lock-up the hutch, perform safety searches, and to align samples, which are all time consuming tasks that come part in parcel with collecting data at a synchrotron. These few minutes are long enough for sedimentation to have an effect on the sample and in-turn effect the data collected. A further advantage of rotating samples for scattering experiments comes from the fact that the measured scattering is averaged over the texture of the sample, an effect that is utilised a great deal in powder diffraction.

Bibliography

[1] G W Morey and P Niggli. The hydrothermal formation of silicates, A review. *Journal of the American Chemical Society*, 35(9):1086–1130, 1913.

[2] A N Lobachev. *Crystallization Processes under Hydrothermal Conditions*. Consultants Bureau, New York, 1973.

[3] A Rabenau. The Role of Hydrothermal Synthesis in Preparative Chemistry. *Angewandte Chemie International Edition in English*, 24(12):1026–1040, 1985.

[4] R Roy. Accelerating the Kinetics of Low-Temperature Inorganic Syntheses, 1994.

[5] M Yoshimura and H Suda. Hydrothermal processing of hydroxyapatite: past, present, and future. In *Hydroxyapatite and related materials*, pages 45–72. CRC Press, Boca Raton, 1994.

[6] K Byrappa and Y Masahiro. Hydrothermal Technology Principles and Applications. In *Handbook of Hydrothermal Technology*, pages 1 – 52. 2013.

[7] M Yoshimura and K Byrappa. Hydrothermal processing of materials: Past, present and future. *Journal of Materials Science*, 43(7):2085–2103, 2008.

[8] J W Mullin. Nucleation. In *Crystallization*, pages 181–215. 2001.

[9] R Bunsen. -. *Poggmdorf's Ann.*, 46:97, 1839.

[10] K Byrappa and Y Masahiro. History of Hydrothermal Technology. *Handbook of Hydrothermal Technology*, pages 51–73, 2013.

[11] K F E V Schafhäutl. *The latest geological hypotheses and their relation to science in general (Die neuesten geologischen Hypothesen und ihr Verhältniß zur Naturwissenschaft überhaupt)*. The Royal Bavarian Academy of Sciences, 1845.

[12] F Wohler. Grundriss der Organischen Chemie (1840), cited by R. Bunsen. *Ann. Chim. Phys.*, 65:80, 1848.

[13] H D Senarmont. Resume du cours de physique. *Annales de Chimie et de Physique*, 32(142):145, 1851.

[14] H D Senarmont. Expérience Sur La Formation Des minéraux Parvoie Humide Dans Les gîtes métallifères concrétionnés Sénarmont. *Annual Review of Physical Chemistry*, pages 129–175, 1851.

[15] H D Senarmont. Recherches sur les Propriétés optiques biréfringentes des corps isomorphes. *Annales de Chimie et de Physique*, (32):132, 1851.

[16] M. Daubree. Observations Sur Le Metamorphisme, Et Recherches Experimentales Sur Quelques-Uns Des Agents Qui Ont Pu Le Produire. *ANNALES DES MINES*, 12:326, 1858.

[17] E T Allen, J L Crenshaw, and J Johnston. The mineral sulphides of iron. *American Journal of Science*, 33(195):236, 1912.

[18] H Sainte-Claire Deville. -. *Comptes rendus des s{é}ances de l'Acad{é}mie des sciences*, 54:324, 1862.

[19] K V Chroustshoff. Studies in Hydrothermal Alteration. *Annales de Chimie et de Physique*, 3:286, 1873.

[20] J B Hannay. The Artificial Formation of the Diamond. *Nature*, 49(1275):530–530, apr 1894.

[21] C Friedel and E Sarasin. -. *Comptes Rendus Chimie*, 92:1378, 1881.

[22] A D Schulten. On the Reproduction of analcime (Sur la Reproduction de l'analcime). *Bull. Soc. Fr. Mineral. Cristallogr.*, 5:9, 1882.

[23] W Ramsay. Report on the Conditions under which Sedimentary Material is convertible into Metamorphic Rock. *Report of the British Association for the Advancement of Science*, page 240, 1882.

[24] K V Chroustshoff. Studies in Hydrothermal Alteration. *Bulletin De La Societe Chimique De France*, 10:36, 1887.

[25] W Bruhns. Apparatus, a steel bomb lined with platinum. *Neues Jahrbuch für Mineralogie*, 2:65, 1889.

[26] C Doetler. Recrystallization of apophyllite. *Neues Jahrbuch für Mineralogie*, page 139, 1890.

[27] K V Chroustshoff. Studies in Hydrothermal Alteration. *Comptes Rendus Chimie*, 122:679, 1890.

[28] R W Goranson. Solubility of water in granite magmas. *Transactions, American Geophysical Union*, 12(1):183, 1931.

[29] G W Morey. Hydrothermal Synthesis. *Journal of the American Ceramic Society*, 36(9):279–285, sep 1953.

[30] G Spezia. On the growth of Quartz (Sull'accrescimento del Quarzo). *Atti della Accademia di scienze*, 35:107, 1900.

[31] G Spezia. La pressione e' chimicamente inattive nella solubilite e riecostituzione del quarzo. *Atti della Reale Accademia delle scienze di Torino*, 40:262, 1904.

[32] H E Boeke. Die Schmelzerscheinungen und die umkehrbare unwandlung des calcium-carbonats. *Neues Jahrbuch für Mineralogie, Geognosie, Geologie und Petrefaktenkunde*, 1:212, 1912.

[33] G Tammann and R Mehl. *The states of aggregation: the changes in the state of matter in their dependence upon pressure and temperature*. Van Nostrand, Basel, 1925.

[34] G Demazeau, A Marbeuf, M Pouchard, and P Hagenmuller. Sur une série de composés oxygènes du nickel trivalent derivés de la perovskite. *Journal of Solid State Chemistry*, 3(4):582–589, nov 1971.

[35] G W Morey. Neue kristallisierte Silikate von Kalium und Natrium. Darstellung und allgemeine Eigenschaften. *Zeitschrift fur anorganische Chemie*, 86(1):305–324, feb 1914.

[36] G W Morey. The ternary system H2O-K2SiO3-SiO2. *Journal of the American Chemical Society*, 39(6):1173–1229, 1917.

[37] N L Bowen. The Behavior of Inclusions in Igneous Magmas. *The Journal of Geology*, 30(6):570, 1922.

[38] H Smyth and L H Adams. The system, calcium oxide-carbon dioxide. *Journal of the American Chemical Society*, 45(5):1167–1184, 1923.

[39] R S Feigelson. *Crystal Growth through the Ages: A Historical Perspective*, volume 1. Elsevier B.V., second edi edition, 2014.

[40] R Nacken. Artificial Quartz Crystals. *U.S. Office of Technical Services Report*, PB-18,748, 1946.

[41] R Nacken. Hydrothermal synthese als grundlage fur zuchtung von quarzkristallen. *Chem. Z.*, 74:749, 1950.

[42] R Nacken. Report on Research Contract for Synthesis of Oscillator Crystals. *Captured German Report RDRDC*, 13(18), 1946.

[43] R M Barrer and D W Riley. Sorptive and molecular-sieve properties of a new zeolitic mineral. *Journal of the Chemical Society (Resumed)*, page 133, 1948.

[44] R M Barrer. Synthesis of a zeolitic mineral with chabazite-like sorptive properties. *Journal of the Chemical Society (Resumed)*, page 127, 1948.

[45] R M Barrer. -. *Journal of the Society of Chemical Industry*, 44:130, 1945.

[46] R M Barrer. Syntheses and reactions of mordenite. *Journal of the Chemical Society*, 0:2158–2163, 1948.

[47] R M Barrer. Separations using zeolitic materials. *Discussions of the Faraday Society*, 7:135, 1949.

[48] O F Tuttle. A New Hydrothermal Quenching Apparatus, 1948.

[49] G C Kennedy. A portion of the system silica-water. *Economic Geology*, 45(7):629–653, 1950.

[50] G W Morey and J M Hesselgesser. The solubility of some minerals in superheated steam at high pressure. *Strain*, 73:865–875, 1951.

[51] D M Roy and R Roy. Synthesis and Stability of Minerals in the System MgO-Al2O3-SiO2-H2O. *American Mineralogist*, 40:178, 1954.

[52] O F Tuttle and J L England. Preliminary Report on the System SiO2-H20. *Bulletin of the Geological Society of America*, 66:149–152, 1955.

[53] A C Walker and E Buehler. Growing Large Quartz Crystals. *Industrial & Engineering Chemistry*, 42(7):1369–1375, 1950.

[54] R A Laudise. Kinetics of Hydrothermal Quartz Crystallization. *Journal of the American Chemical Society*, 81(3):562–566, 1959.

[55] R A Laudise and R A Sullivan. Pilot plant production of synthetic quartz. *Chemical Engineering Progress*, 55(5):55, 1959.

[56] E U Franck. Experimental Investigations of Fluids at High Pressures and Elevated Temperatures. *NATO Advanced Study Institutes Series*, 41:221–257, 1978.

[57] E U Franck. Survey of selected non-thermodynamic properties and chemical phenomena of fluids and fluid mixtures. *Physics and Chemistry of the Earth*, 13-14(C):65–88, 1981.

[58] H C Helgeson. Prediction of the thermodynamic properties of electrolytes at high pressures and temperatures. *Physics and Chemistry of the Earth*, 13-14(C):133–177, 1981.

[59] T M Seward. Metal complex formation in aqueous solutions at elevated temperatures and pressures. *Physics and Chemistry of the Earth*, 13-14(C):113–132, 1981.

[60] S Somiya. Proceedings of the first International Symposium on Hydrothermal Reactions. *Gakujutsu Bunken Fukyu-Kai, Japan*, page 965, 1982.

[61] A Filice and R Speed. Quartz glass pressure vessels for hydrothermal studies. *Glass and Ceramics*, 49:1114–1119, 1964.

[62] G W Morey and F E Ingerson. The pneumatolytic and hydrothermal alteration and synthesis of silicates. *Economic Geology*, 32(5_Suppl):607–761, aug 1937.

[63] A J Caporaso, E D Kolb, and R A Laudise. Hydrothermal growth of zinc oxide crystals, 1963.

[64] O F Tuttle. 2 Pressure Vessels for Silicate-Water Studies. *Geological Society of America bulletin*, 60(10):1727–1729, 1949.

[65] J W Kolis. Acentric lithium borate crystals, method for making, and applications thereof, 2003.

[66] R Roy and E F Osborn. Some simple aids in the hydrothermal investigation of mineral systems. *Economic Geology*, 47(7):717–721, nov 1952.

[67] W C Luth and O F Tuttle. Externally heated cold-seal pressure vessels for use to 10,000 bars and 750C. *The American Mineralogist*, 48:1401–1403, 1963.

[68] J S Huebner. Buffering Techniques for Hydrostatic Systems at Elevated Pressures. In *Research Techniques for High Pressure and High Temperature*, pages 123–177. Springer, Berlin, 1971.

[69] A D Edgar. *Experimental Petrology: Basic Principles and Techniques*. Clarendon Press, Oxford, 1973.

[70] A C Walker. Hydrothermal Synthesis of Quartz Crystals. *Journal of the American Ceramic Society*, 36(8):250–256, 1953.

[71] K Byrappa and Y Masahiro. Apparatus. *Handbook of Hydrothermal Technology*, pages 75–137, 2013.

[72] H L Barnes. Investigations in Hydrothermal Sulfide Systems. In *Research Techniques for High Pressure and High Temperature*, pages 317–355. Springer-Verlag, New York, 1971.

[73] R A Laudise. *The Growth of Single Crystals*. Prentice-Hall, Englewood Cliffs, 1970.

[74] S Taki. Improvement of growth process and characterization of quartz crystals. *Progress in Crystal Growth and Characterization of Materials*, 23:313–339, 1991.

[75] E Polak, J Munn, P Barnes, S E Tarling, and C Ritter. Time-resolved neutron diffraction analyses of hydrothermal syntheses using a novel autoclave cell. *Journal of Applied Crystallography*, 23(4):258–262, aug 1990.

[76] P Barnes, S M Clark, D Häusermann, E Henderson, C H Fentiman, M N Muhamad, and S Rashid. Time-resolved studies of the early hydration of cements using synchrontron energy-dispersive diffraction. *Phase Transitions*, 39(1-4):117–128, sep 1992.

[77] J Munn, P Barnes, D Häusermann, S A Axon, and J Klinowski. In-situ studies of the hydrothermal synthesis of zeolites using synchrotron energy-dispersive X-ray diffraction. *Phase Transitions*, 39(1-4):129–134, sep 1992.

[78] R I Walton and D O'Hare. Watching solids crystallise using in situ powder diffraction. *Chemical Communications*, (23):2283–2291, 2000.

[79] Y Zhou, E Antonova, W Bensch, and G R Patzke. In situ X-ray diffraction study of the hydrothermal crystallization of hierarchical Bi2WO6 nanostructures. *Nanoscale*, 2(11):2412, 2010.

[80] N Pienack and W Bensch. In-situ monitoring of the formation of crystalline solids. *Angewandte Chemie - International Edition*, 50(9):2014–2034, 2011.

[81] R J Francis, S O'Brien, A M Fogg, P S Halasyamani, D O'Hare, T Loiseau, and G Férey. Time-resolved in-situ energy and angular dispersive X-ray diffraction studies of the formation of the microporous gallophosphate ULM-5 under hydrothermal conditions. *Journal of the American Chemical Society*, 121(5):1002–1015, 1999.

[82] R I Walton, F Millange, D O'Hare, A T Davies, G Sankar, and C R Catlow. In situ energy-dispersive X-ray diffraction study of the hydrothermal crystallization of zeolite A. 1. Influence of reaction conditions and transformation into sodalite. *Journal of Physical Chemistry B*, 105(1):83–90, 2001.

[83] R J Francis and D O'Hare. The kinetics and mechanisms of the crystallisation of microporous materials. *Journal of the Chemical Society, Dalton Transactions*, (19):3133–3148, 1998.

[84] A J Norquist and D O'Hare. Kinetic and mechanistic investigations of hydrothermal transformations in zinc phosphates. *Journal of the American Chemical Society*, 126(21):6673–6679, 2004.

[85] W Fan, M Ogura, G Sankar, and T Okubo. In situ Small-Angle and Wide-Angle X-ray Scattering Investigation on Nucleation and Crystal Growth of Nanosized Zeolite A. *Journal of Physical Chemistry B*, 103(10):1639–1650, 1999.

[86] W Fan, M O'Brien, M Ogura, M Sanchez-Sanchez, C Martin, F Meneau, K I Kurumada, G Sankar, and T Okubo. In situ observation of homogeneous nucleation of nanosized zeolite A. *Physical chemistry chemical physics : PCCP*, 8(11):1335–1339, 2006.

[87] A M Beale, L M Reilly, and G Sankar. Watching the crystallisation of complex oxides by in situ X-ray techniques. *Applied Catalysis A: General*, 325(2):290–295, 2007.

[88] A M Beale and G Sankar. In situ study of the formation of crystalline bismuth molybdate materials under hydrothermal conditions. *Chemistry of Materials*, 15(1):146–153, 2003.

[89] D R Modeshia, R J Darton, S E Ashbrook, and R I Walton. Control of polymorphism in NaNbO3 by hydrothermal synthesis. *Chem. Commun.*, 3430(1):68–70, 2009.

[90] F Millange, M I Medina, N Guillou, G Férey, K M Golden, and R I Walton. Time-resolved in situ diffraction study of the solvothermal crystallization of some prototypical metal-organic frameworks. *Angewandte Chemie - International Edition*, 49(4):763–766, 2010.

[91] S J Moorhouse, N Vranje, A Jupe, M Drakopoulos, and D O'Hare. The oxford-diamond in situ cell for studying chemical reactions using time-resolved x-ray diffraction. *Review of Scientific Instruments*, 83(8), 2012.

[92] G R Williams and D O'Hare. Towards understanding, control and application of layered double hydroxide chemistry. *Journal of Materials Chemistry*, 16(30):3065, 2006.

[93] G Muncaster, A T Davies, G Sankar, R Catlow, J Meurig Thomas, S L. Colston, P Barnes, R I Walton, and D O'Hare. On the advantages of the use of the three-element detector system for measuring EDXRD patterns to follow the crystallisation of open-framework structures. *Physical Chemistry Chemical Physics*, 2(15):3523–3527, 2000.

[94] R J Francis, S J Price, J S O Evans, S O'Brien, D O'Hare, and S M Clark. Hydrothermal synthesis of microporous tin sulfides studied by real-time in situ energy-dispersive x-ray diffraction. *Chemistry of Materials*, 8(8):2102–2108, 1996.

[95] F Rey, G Sankar, J M Thomas, P A Barrett, D W Lewis, C Richard, A Catlow, S M Clark, and G N Greaves. Synchrotron-Based Method for the Study of

Crystallization: Templated Formation of CoALPO-5 Catalyst. *Chemistry of Materials*, 7(8):1435–1436, 1995.

[96] A T Davies, G Sankar, C R Catlow, and S M Clark. Following the Crystallization of Microporous Solids Using EDXRD Techniques. *J. Phys. Chem. B*, 101(48):10115–10120, 1997.

[97] P Norby, A Nørlund Christensen, and J C Hanson. In situ studies of zeolite syntheses using powder diffraction methods. Crystallization of instant zeolite A powder and synthesis of CoAPO-5. In *Studies in Surface Science and Catalysis*, pages 179–186. Elsevier B. V., 1994.

[98] P Norby. Hydrothermal conversion of zeolites: An in situ synchrotron X-ray powder diffraction study. *Journal of the American Chemical Society*, 119(22):5215–5221, 1997.

[99] P Norby. In-situ XRD as a tool to understanding zeolite crystallization. *Current Opinion in Colloid and Interface Science*, 11(2-3):118–125, 2006.

[100] B R Pauw, J S Pedersen, S Tardif, M Takata, and B B Iversen. Improvements and considerations for size distribution retrieval from small-angle scattering data by Monte Carlo methods. *Journal of Applied Crystallography*, 46:365–371, 2013.

[101] A K Cheetham and C F Mellot. In Situ Studies of the Sol-Gel Synthesis of Materials. *Chemistry of Materials*, 9(11):2269–2279, 1997.

[102] P Norby, C Cahill, C Koleda, and J B Parise. A reaction cell for in situ studies of hydrothermal titration. *Journal of Applied Crystallography*, 31(3):481–483, 1998.

[103] B Vistad, D E Akporiaye, and K P Lillerud. Identification of a key precursor phase for synthesis of SAPO-34 and kinetics of formation investigated by in situ X-ray diffraction. *Journal of Physical Chemistry B*, 105(50):12437–12447, 2001.

[104] J Chen, J Bai, H Chen, and J Graetz. In situ hydrothermal synthesis of LiFePO4 studied by synchrotron X-ray diffraction. *Journal of Physical Chemistry Letters*, 2(15):1874–1878, 2011.

[105] C Kongmark, R Coulter, S Cristol, A Rubbens, C Pirovano, A Löfberg, G Sankar, W Van Beek, E Bordes-Richard, and R N Vannier. A comprehensive scenario of the crystal growth of γ-Bi 2MoO6 catalyst during hydrothermal synthesis. *Crystal Growth and Design*, 12(12):5994–6003, 2012.

[106] D D Liyanage, R J K A Thamali, A A K Kumbalatara, J A Weliwita, and S Witharana. An Analysis of Nanoparticle Settling Times in Liquids. *Journal of Nanomaterials*, 2016, 2016.

[107] K J Laidler and J H Meiser. *Physical Chemistry*. Benjamin-Cummings Pub Co, Menlo Parkm California, 1982.

[108] H Lamb. *Hydrodynamics*. Cambridge University Press, 6th editio edition, 1994.

[109] R F Weiner, R Matthews, J J Peirce, and P A Vesilind. *Environmental Engineering*. Butterworth Heinemann, Oxford, 4th editio edition, 2003.

[110] Y S Touloukian, R W Powell, C Y Ho, and P G Klemens. Thermophysical Properties of Matter: Thermal Conductivity of Metallic Elements and Alloys. *Journal of Materials Engineering and Performance*, 50(1):862–871, 2011.

[111] D Parker, J Bussink, H T van de Grampel, G W Wheatley, E U Dorf, E Ostlinning, K Reinking, F Schubert, O Jünger, and R Wagener. Polymers, High-Temperature. In *Ullmann's Encyclopedia of Industrial Chemistry*. Wiley-VCH Verlag GmbH & Co. KGaA, Weinheim, Germany, oct 2012.

[112] QuickSilver Controls, Inc, Motion Control Products, www.quicksilvercontrols.com, 2018.

[113] SKF Group, Bearings, units and housings, www.skf.com, 2018.

[114] Watlow, Ultramic Advanced Ceramic Heaters, www.watlow.com, 2018.

Chapter 7

General Conclusions and Future Work

In this thesis advance X-ray scattering techniques have been utilised to explore the formation of zeolites and MOFs. The formation of conventional Silicalite-1 was probed using three different silica precursors under the same conditions to reveal the presence to two distinctive mechanism for the growth of crystalline Silicalite-1. To expand this study in the future synthesis parameters should be varied, in an attempt to promote growth of Silicalite-1 through a single formation mechanism. This could be attempted initially through preforming syntheses with different precursor ratios or under different synthesis conditions.

The formation of Silicalite-1 was also probed using a novel silica precursor to synthesize hierarchical structures. Through this study the formation mechanism for the incorporation of macropores was explored and the novel material was characterised using a multitude of different techniques. It was found that multiple formation mechanism are present within the system and again future work should focus on tailoring synthesis condition to favour the formation of hierarchical structures. Work should also be put into tailoring pore size through careful selection of precursors, and into expanding this method of creating macropores into catalytically active zeolite structures (see appendix B.1.3).

The formation of ZIF-8 was also explored using X-ray scattering techniques. It was observed that these MOFs form *via* prenucleation clusters, something that does not follow the classical nucleation theory that has been proposed for the formation of some MOF systems. This would could be expanded upon through further exploration of temperature conditions, with smaller jumps in temperature measured. The study could also be expanded to investigating synthesis ratios, the use of different solvents and modulators, and could be expanded to more MOFs starting with other cubic systems such as HKUST-1 and ZIF-67.

Finally, the design and commissioning of a new *in-situ* hydrothermal cell was presented. This new cell has the ability to prevent the sedimentation of particles suspended within a solution through rotation. The cell is designed primarily for the collection of X-ray scattering data, however the design is adaptable and with the incorporation of a large sample chamber and larger windows it can be utilised at numerous beamlines with a variety of characterisation techniques. The cell is capable of producing hydrothermal conditions and is equipped with appropriate safety features to allow for its safe use.

Appendix A

Nucleation and Growth of Zeolites

A.1 Formation of Silicalite-1 from TEOS

A.1.1 *In-situ* SAXS Data (high-q)

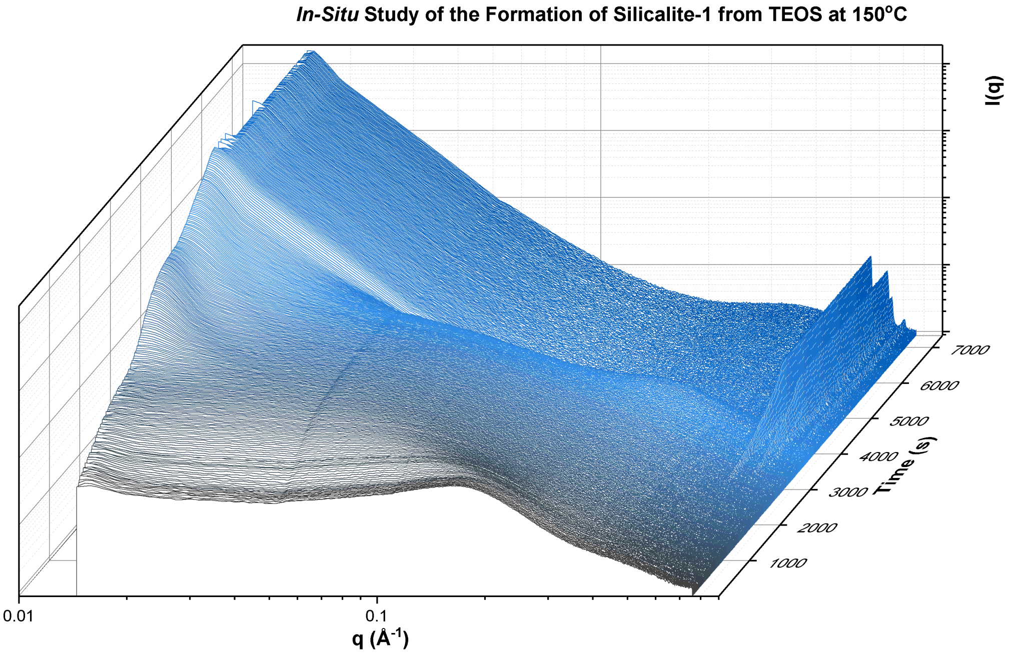

Figure A.1: *In-situ* SAXS data of the formation of Silicalite-1 from TEOS at 150°C.

A.1.2 SAXS Fits

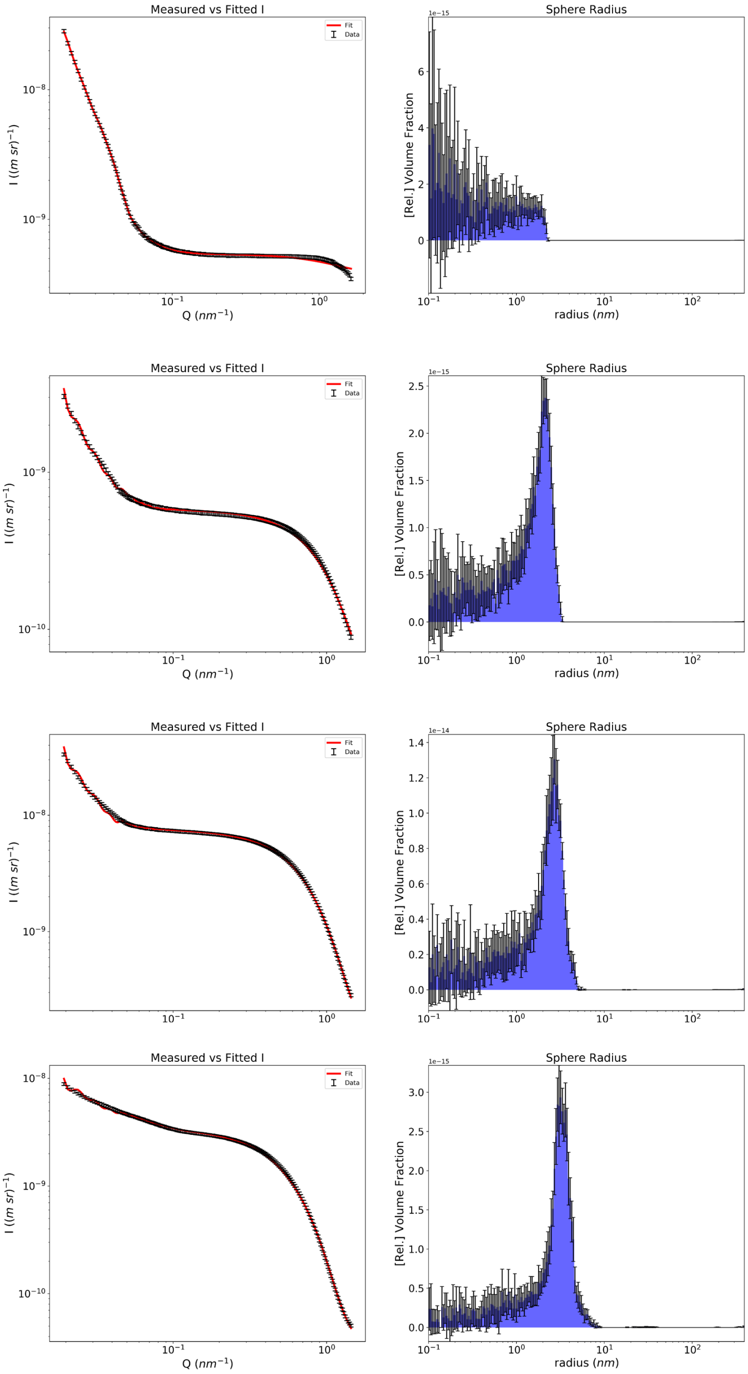

Figure A.2: Fits of the *in-situ* SAXS data collected on the formation of Silicalite-1 from TEOS at 150°C. Scans taken after 480, 720, 960 and 1200 seconds, top to bottom respectively

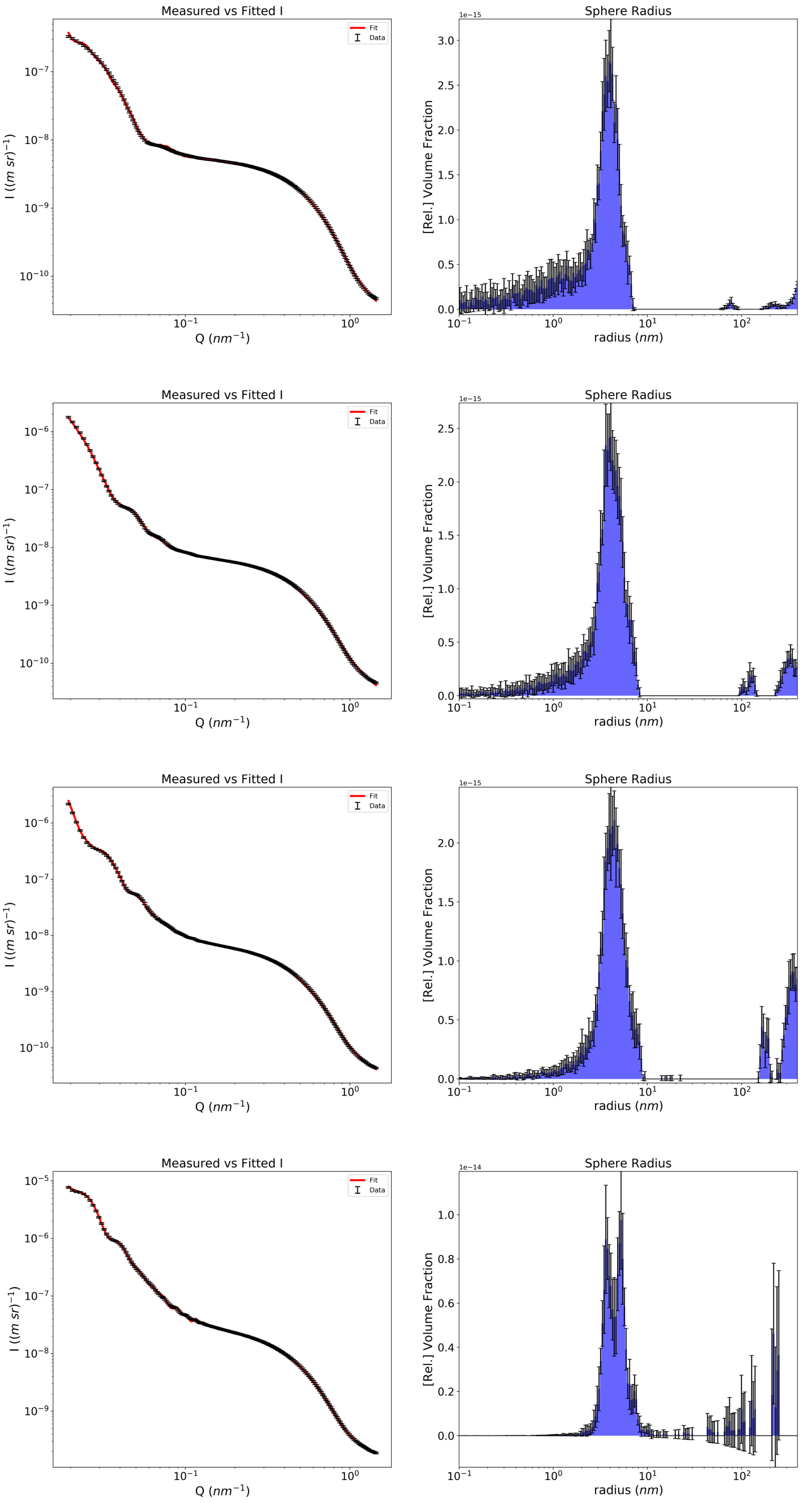

Figure A.3: Fits of the *in-situ* SAXS data collected on the formation of Silicalite-1 from TEOS at 150°C. Scans taken after 1440, 1680, 1920 and 2160 seconds, top to bottom respectively

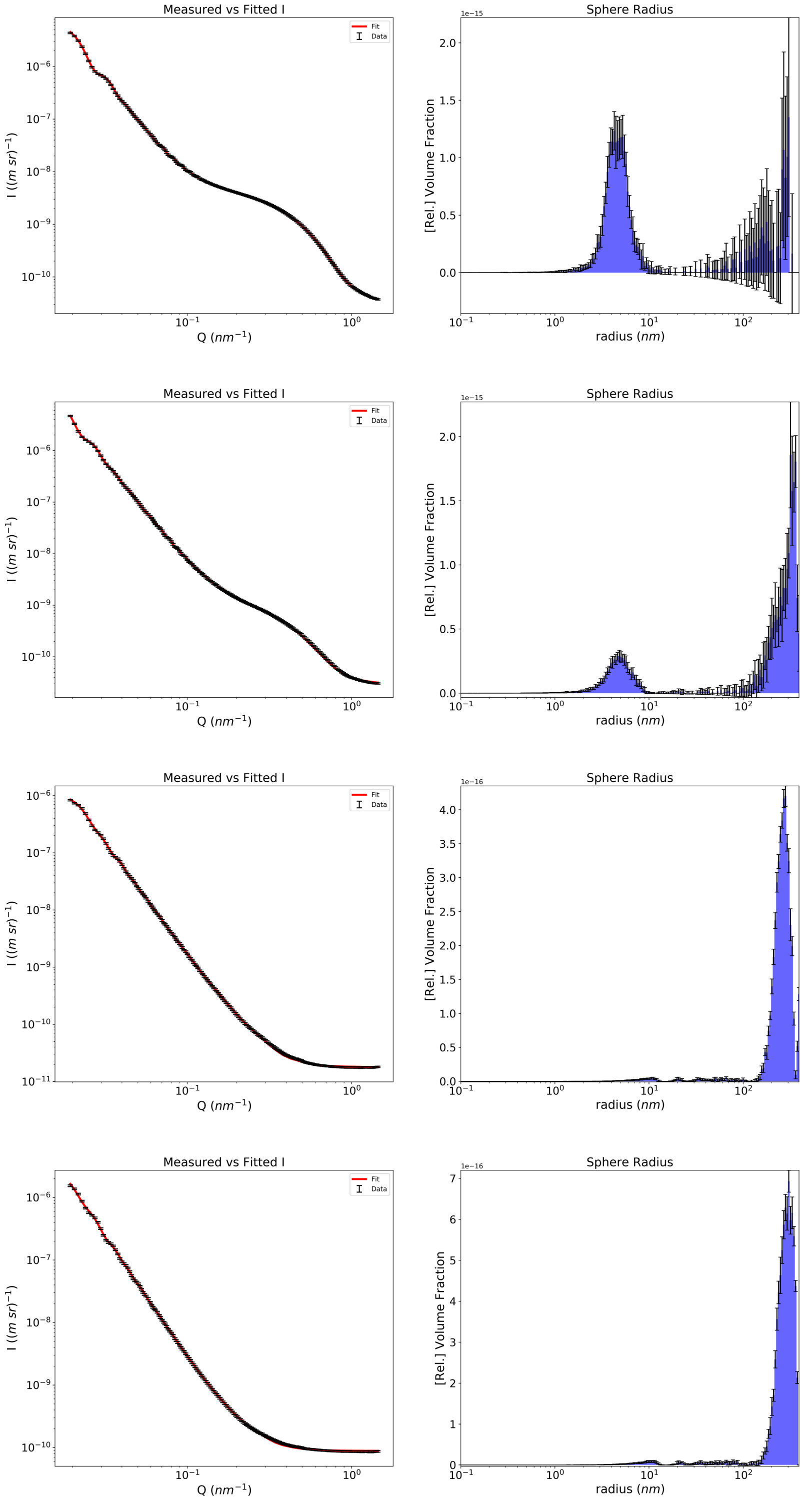

Figure A.4: Fits of the *in-situ* SAXS data collected on the formation of Silicalite-1 from TEOS at 150°C. Scans taken after 2400, 2640, 2880 and 3120 seconds, top to bottom respectively

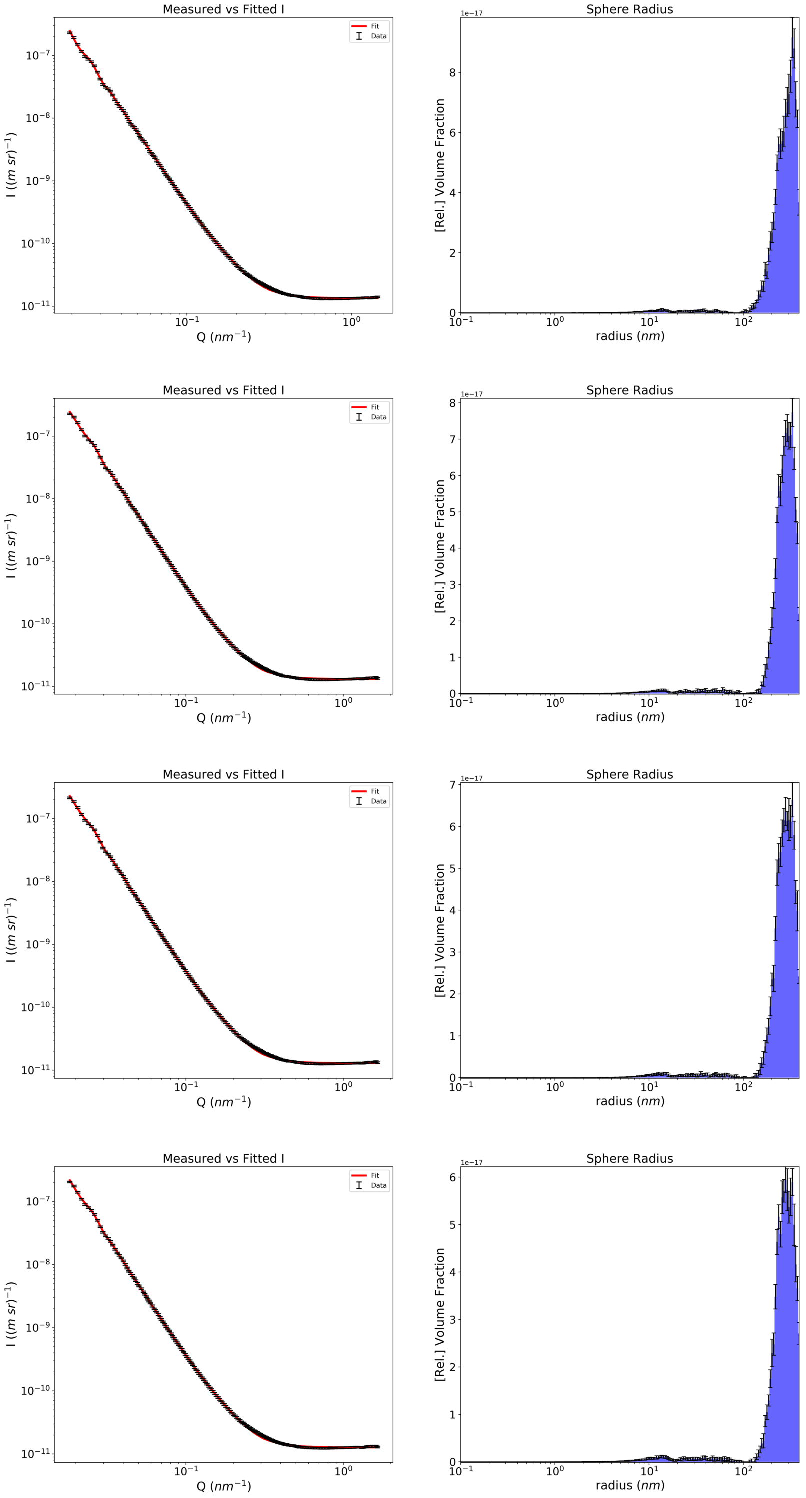

Figure A.5: Fits of the *in-situ* SAXS data collected on the formation of Silicalite-1 from TEOS at 150°C. Scans taken after 3360, 3600, 3840 and 4080 seconds, top to bottom respectively

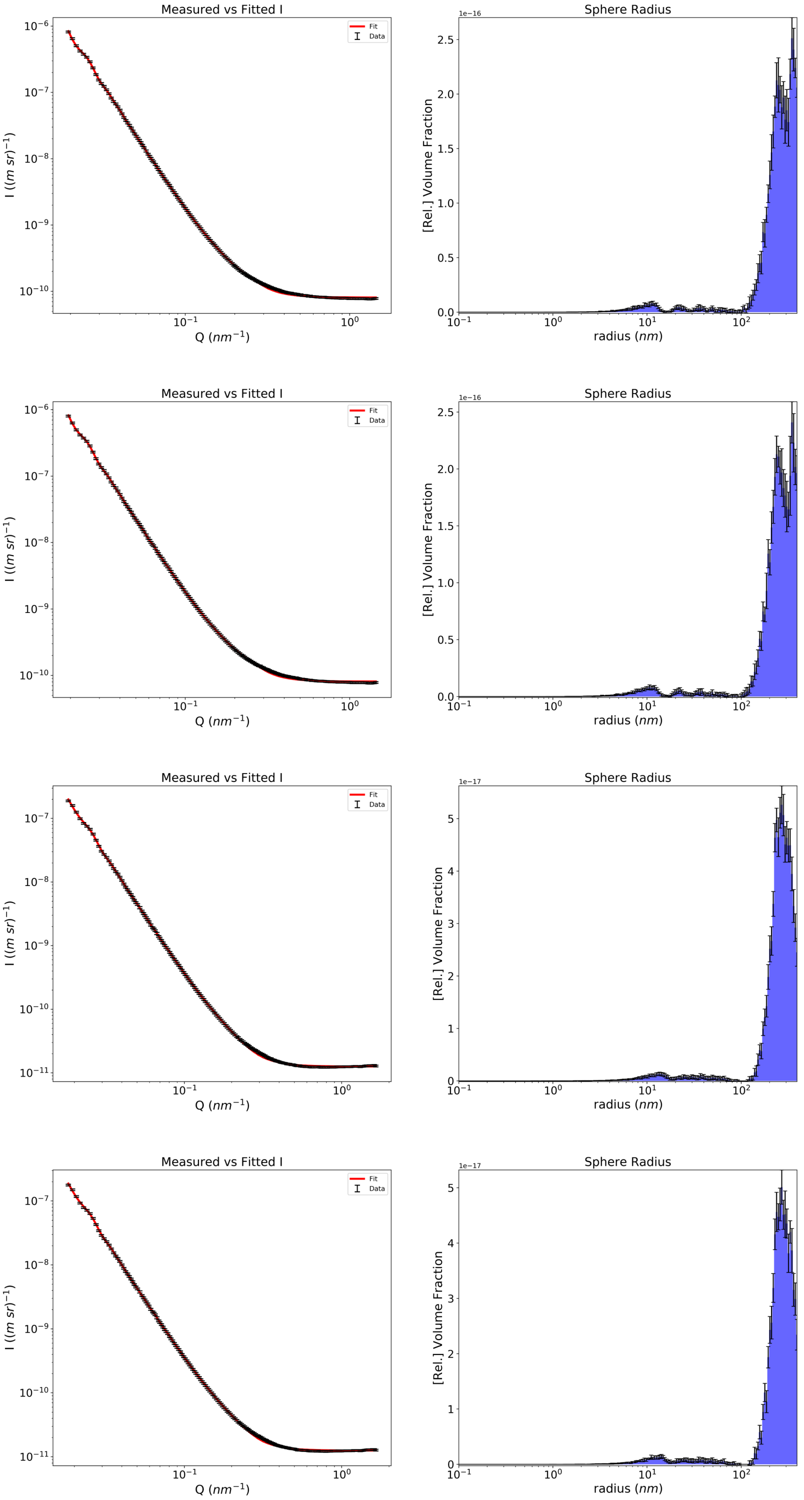

Figure A.6: Fits of the *in-situ* SAXS data collected on the formation of Silicalite-1 from TEOS at 150°C. Scans taken after 4320, 4560, 4800 and 5040 seconds, top to bottom respectively

A.2 Formation of Silicalite-1 from Ludox AS-40

A.2.1 *In-situ* SAXS Data (high-q)

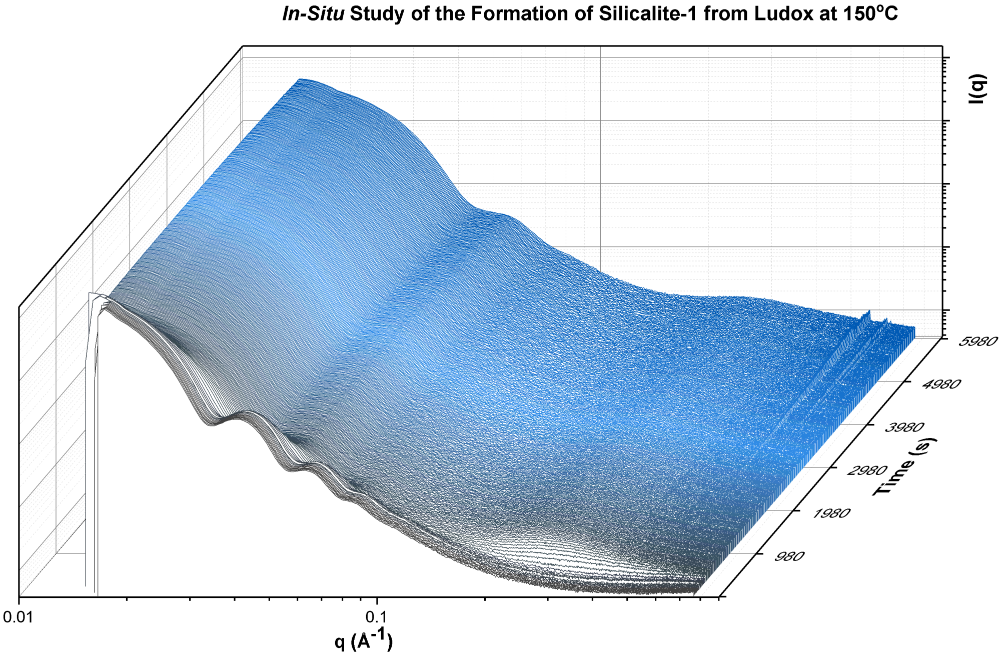

Figure A.7: *In-situ* SAXS data of the formation of Silicalite-1 from TEOS at 150°C.

A.2.2 SAXS Fits

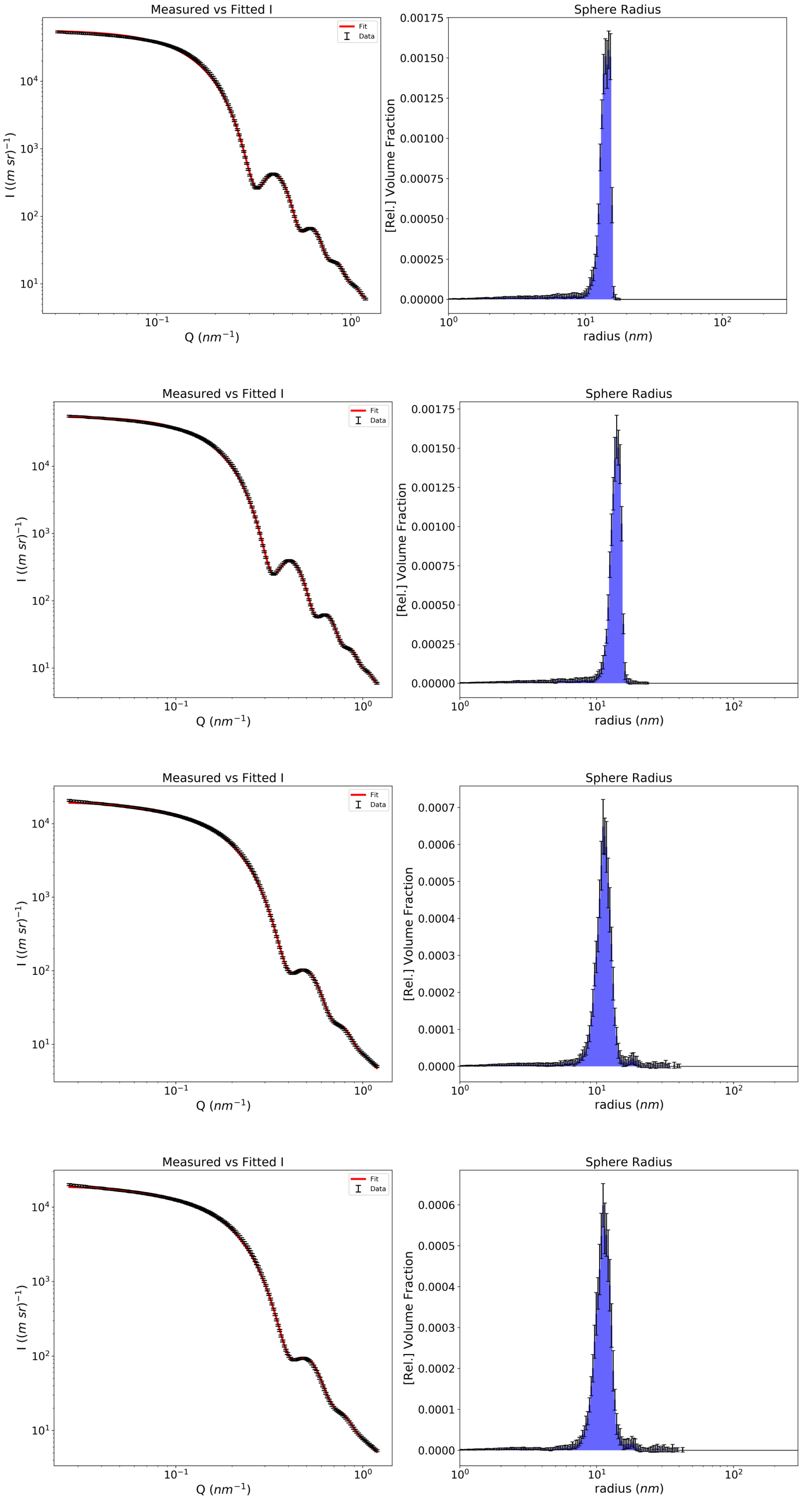

Figure A.8: Fits of the *in-situ* SAXS data collected on the formation of Silicalite-1 from Ludox at 150°C. Scans taken after 1, 400, 800 and 1200 seconds, top to bottom respectively

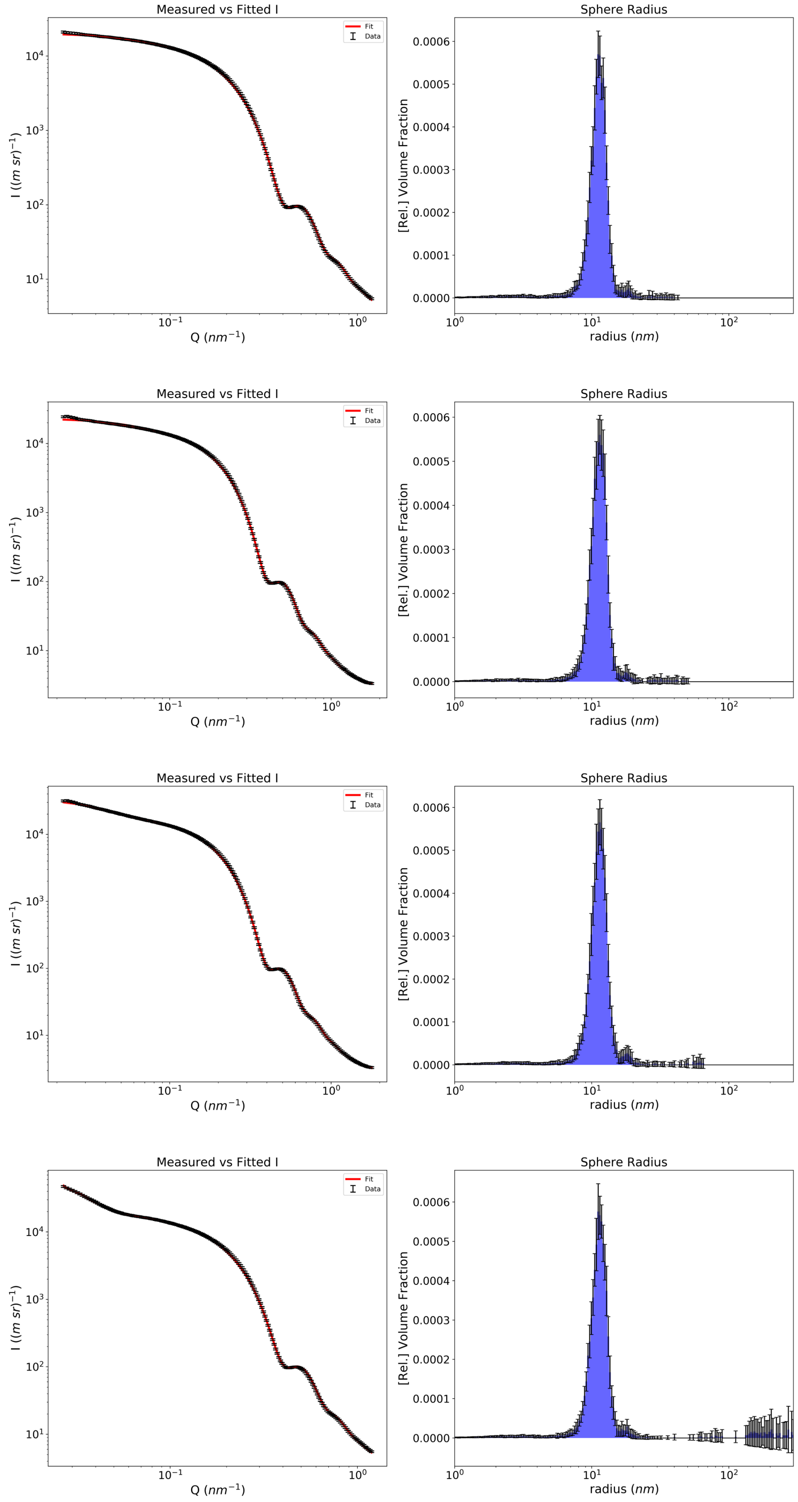

Figure A.9: Fits of the *in-situ* SAXS data collected on the formation of Silicalite-1 from Ludox at 150°C. Scans taken after 1600, 2000, 2400, and 2800 seconds, top to bottom respectively

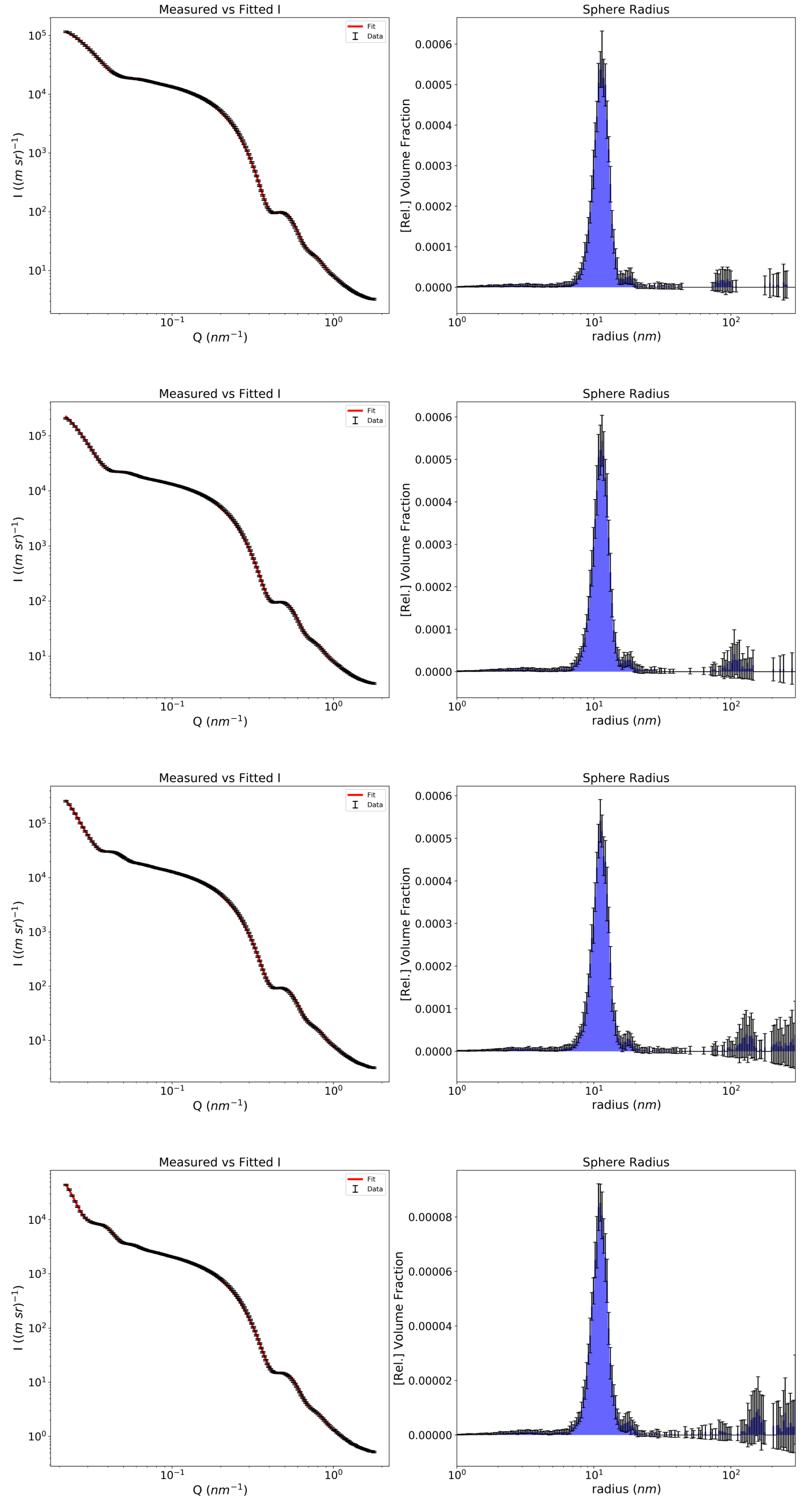

Figure A.10: Fits of the *in-situ* SAXS data collected on the formation of Silicalite-1 from Ludox at 150°C. Scans taken after 3200, 3600, 4000, and 4400 seconds, top to bottom respectively

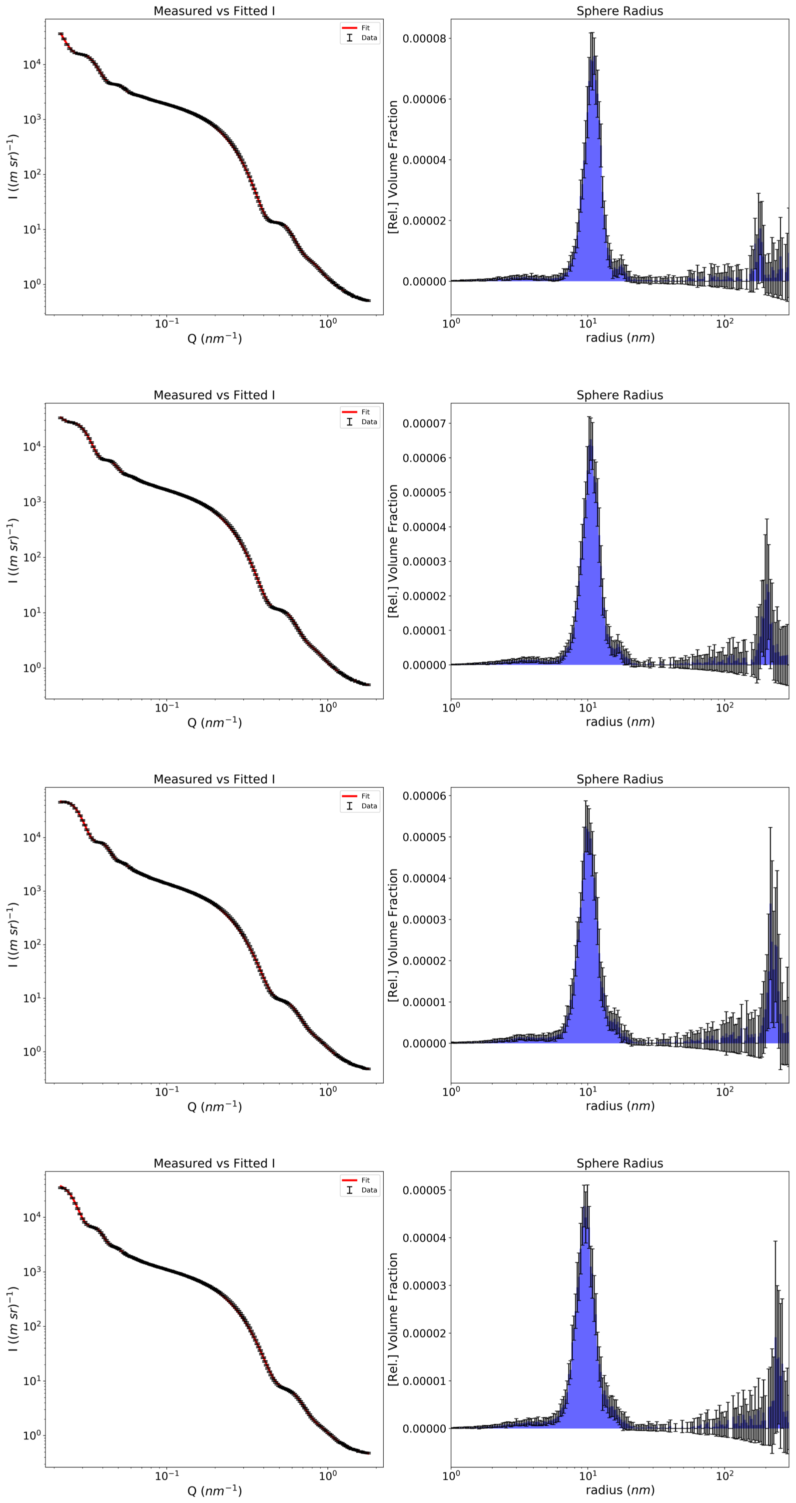

Figure A.11: Fits of the *in-situ* SAXS data collected on the formation of Silicalite-1 from Ludox at 150°C. Scans taken after 4800, 5200, 5600, and 6000 seconds, top to bottom respectively

A.3 Formation of Silicalite-1 from Fumed Silica

A.3.1 SAXS Fits

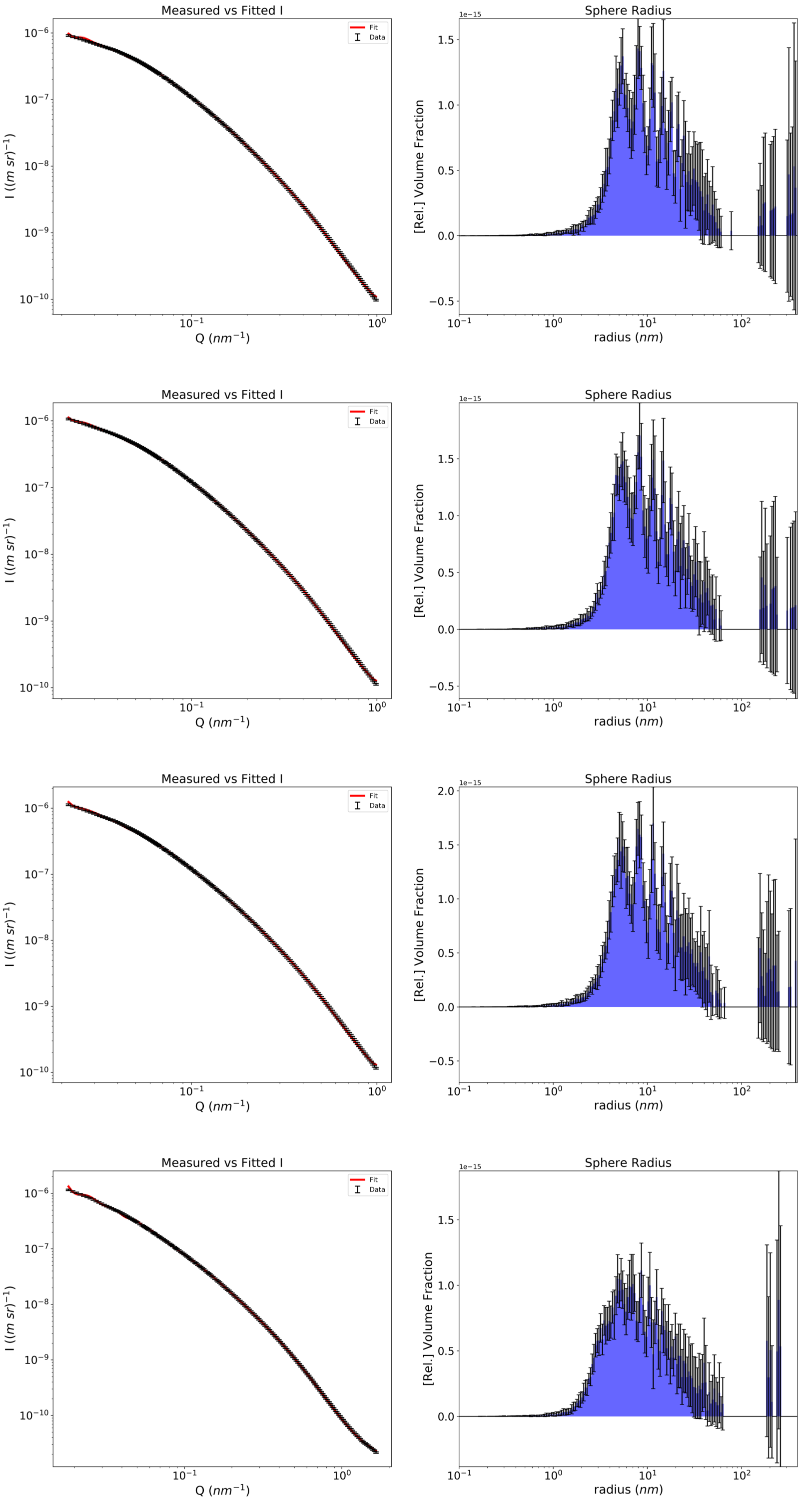

Figure A.12: Fits of the *in-situ* SAXS data collected on the formation of Silicalite-1 from fumed silica at 150°C. Scans taken after 1, 240, 480 and 720 seconds, top to bottom respectively

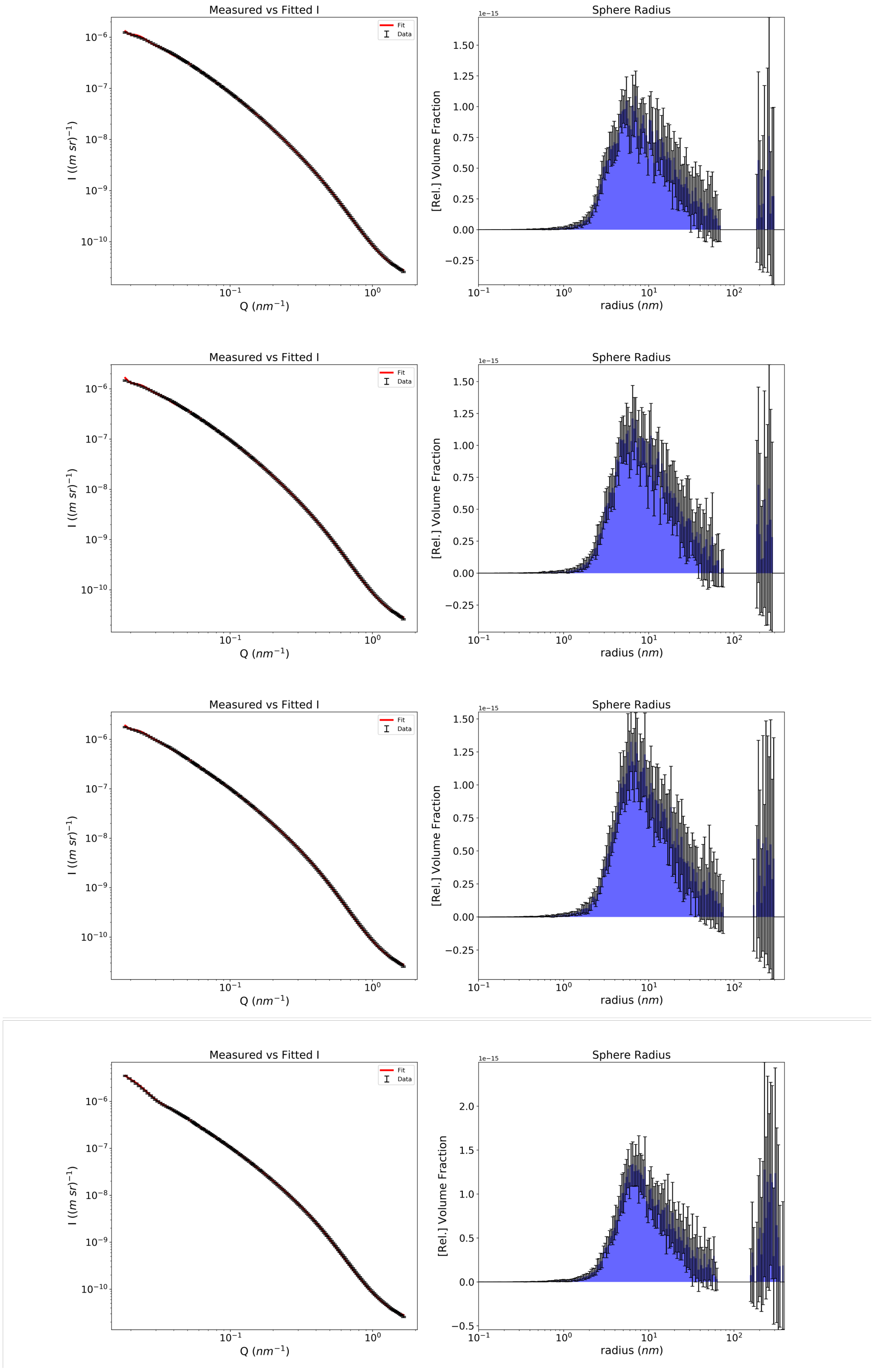

Figure A.13: Fits of the *in-situ* SAXS data collected on the formation of Silicalite-1 from fumed silica at 150°C. Scans taken after 960, 1200, 1440 and 1680 seconds, top to bottom respectively

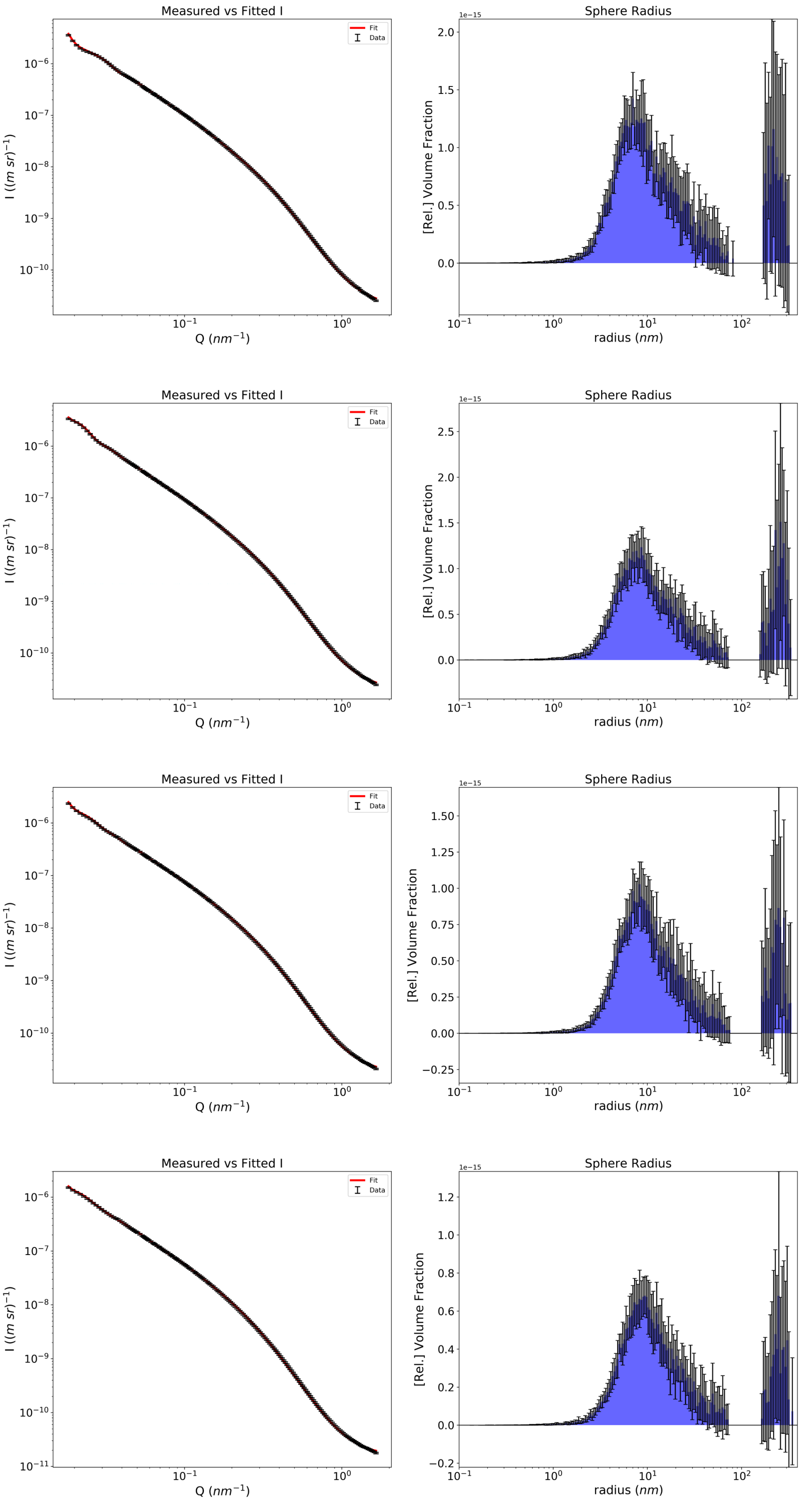

Figure A.14: Fits of the *in-situ* SAXS data collected on the formation of Silicalite-1 from fumed silica at 150°C. Scans taken after 1920, 2160, 2400 and 2640 seconds, top to bottom respectively

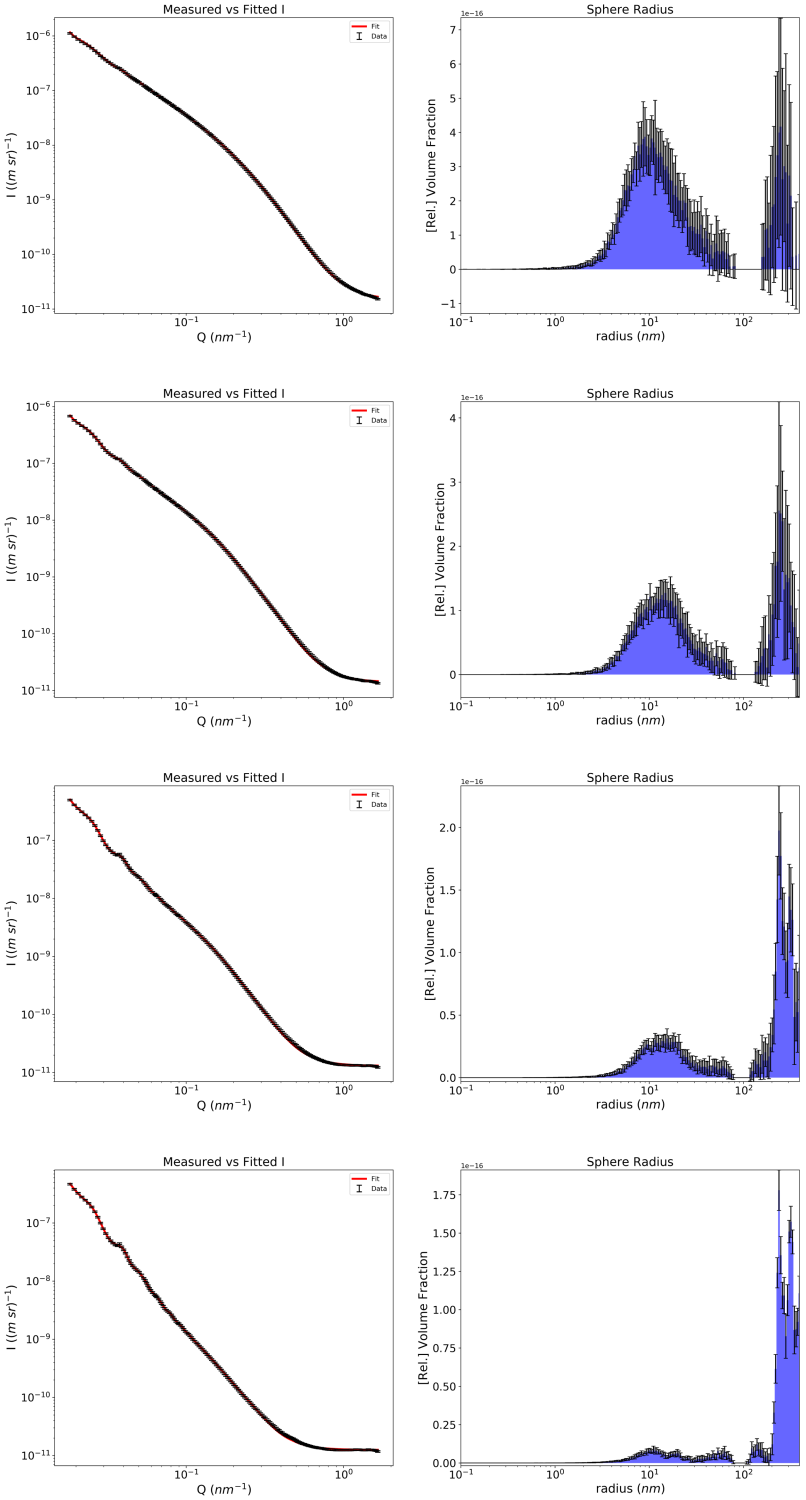

Figure A.15: Fits of the *in-situ* SAXS data collected on the formation of Silicalite-1 from fumed silica at 150°C. Scans taken after 2880, 3120, 3300 and 3360 seconds, top to bottom respectively

Appendix B

Synthesis of Hierarchical Zeolites

B.1 Formation of Macroporous Silicalite-1

B.1.1 *In-situ* SAXS Data (high-q) Fits

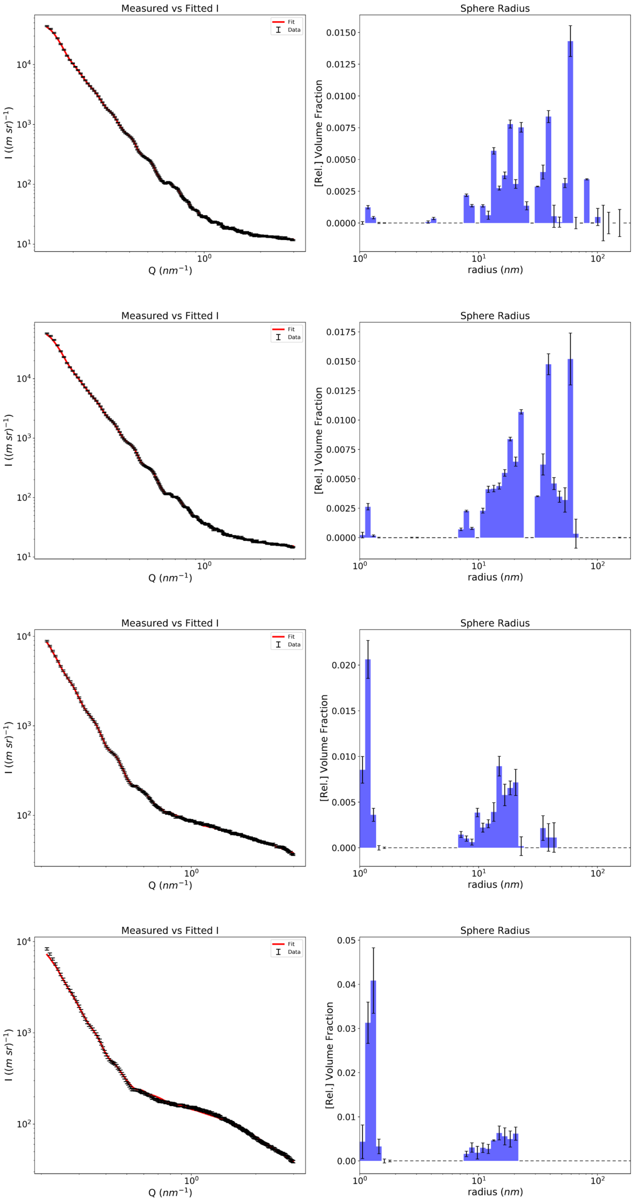

Figure B.1: Fits of the *in-situ* SAXS data collected on the formation of macroporous Silicalite-1 from 500 nm silica nanospheres at 160°C. Scans taken after 0, 800, 1200 and 2000 seconds, top to bottom respectively

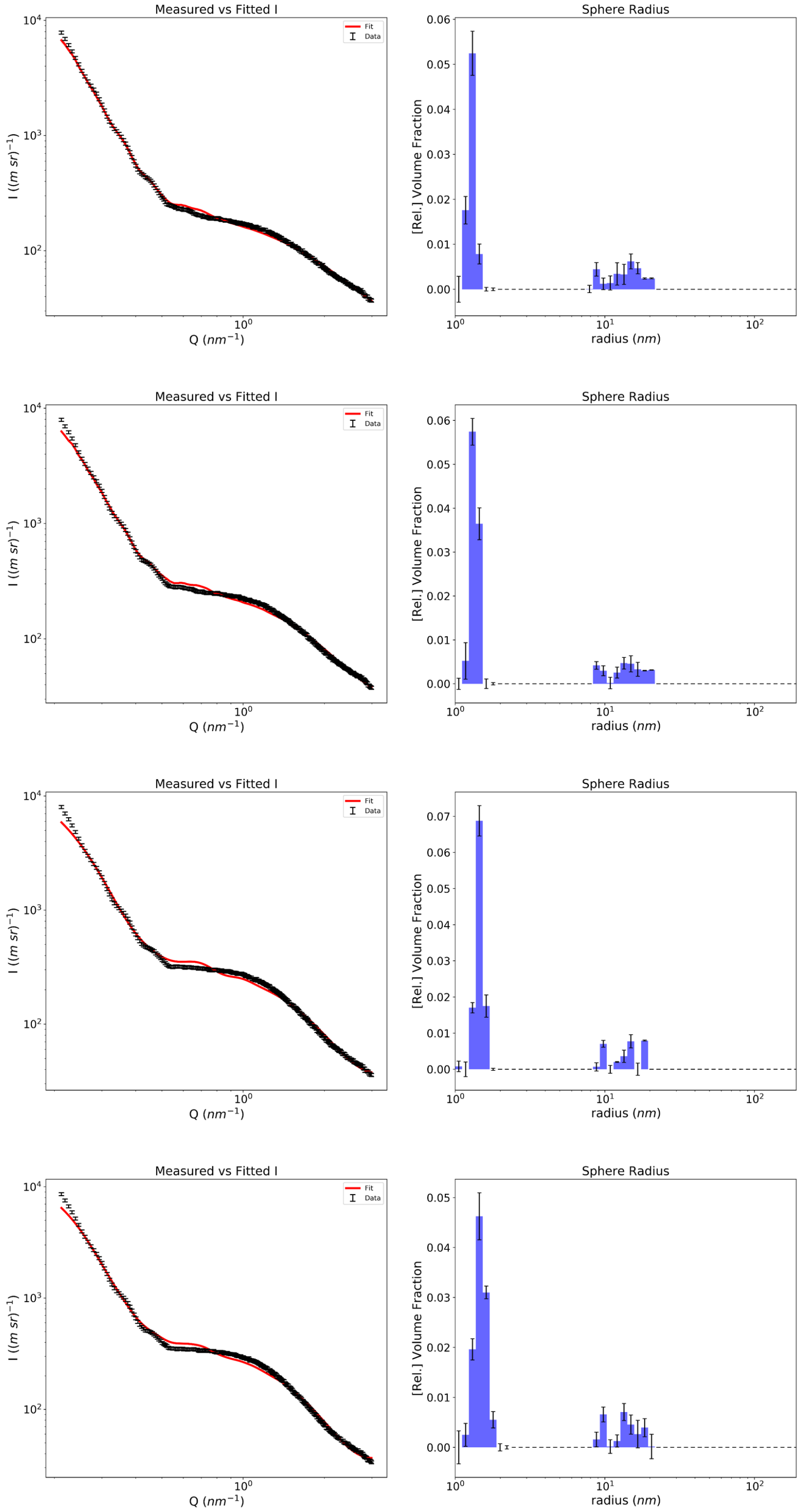

Figure B.2: Fits of the *in-situ* SAXS data collected on the formation of macroporous Silicalite-1 from 500 nm silica nanospheres at 160°C. Scans taken after 2400, 3200, 4400 and 5200 seconds, top to bottom respectively

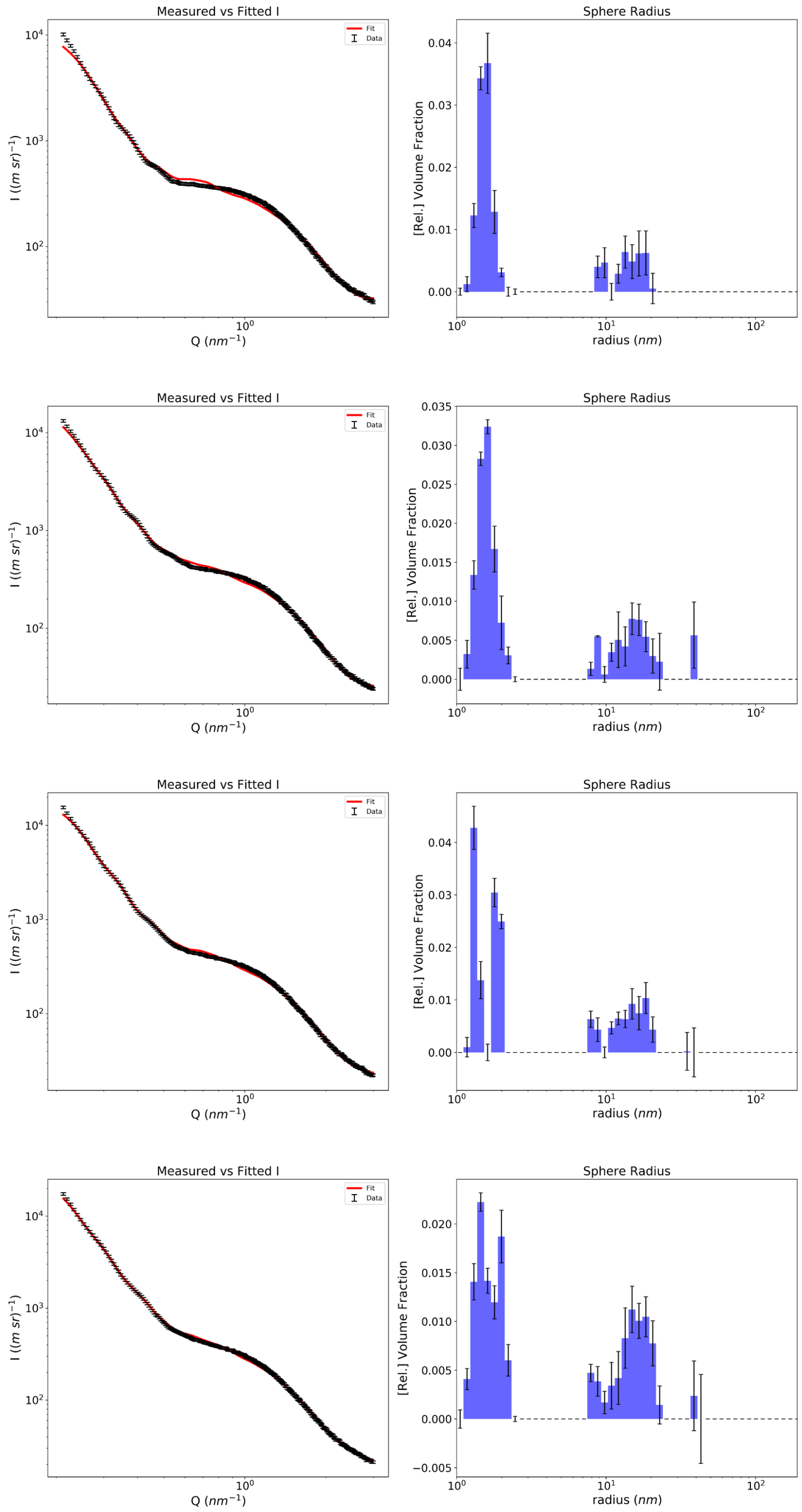

Figure B.3: Fits of the *in-situ* SAXS data collected on the formation of macroporous Silicalite-1 from 500 nm silica nanospheres at 160°C. Scans taken after 6000, 6800, 7600 and 8400 seconds, top to bottom respectively

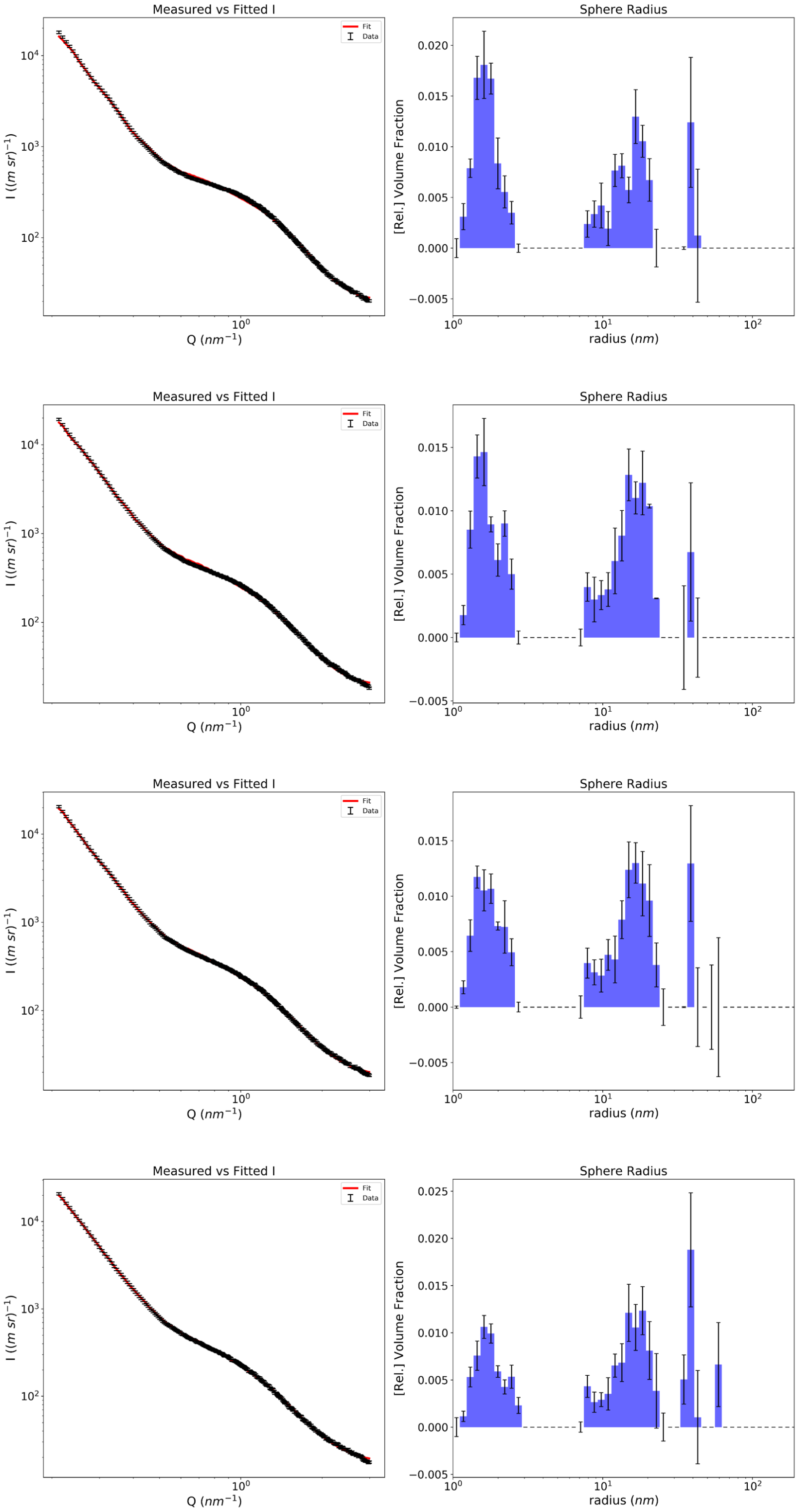

Figure B.4: Fits of the *in-situ* SAXS data collected on the formation of macroporous Silicalite-1 from 500 nm silica nanospheres at 160°C. Scans taken after 8800, 9600, 10000 and 10400 seconds, top to bottom respectively

B.1.2 *In-situ* SAXS Data (low-q) Fits

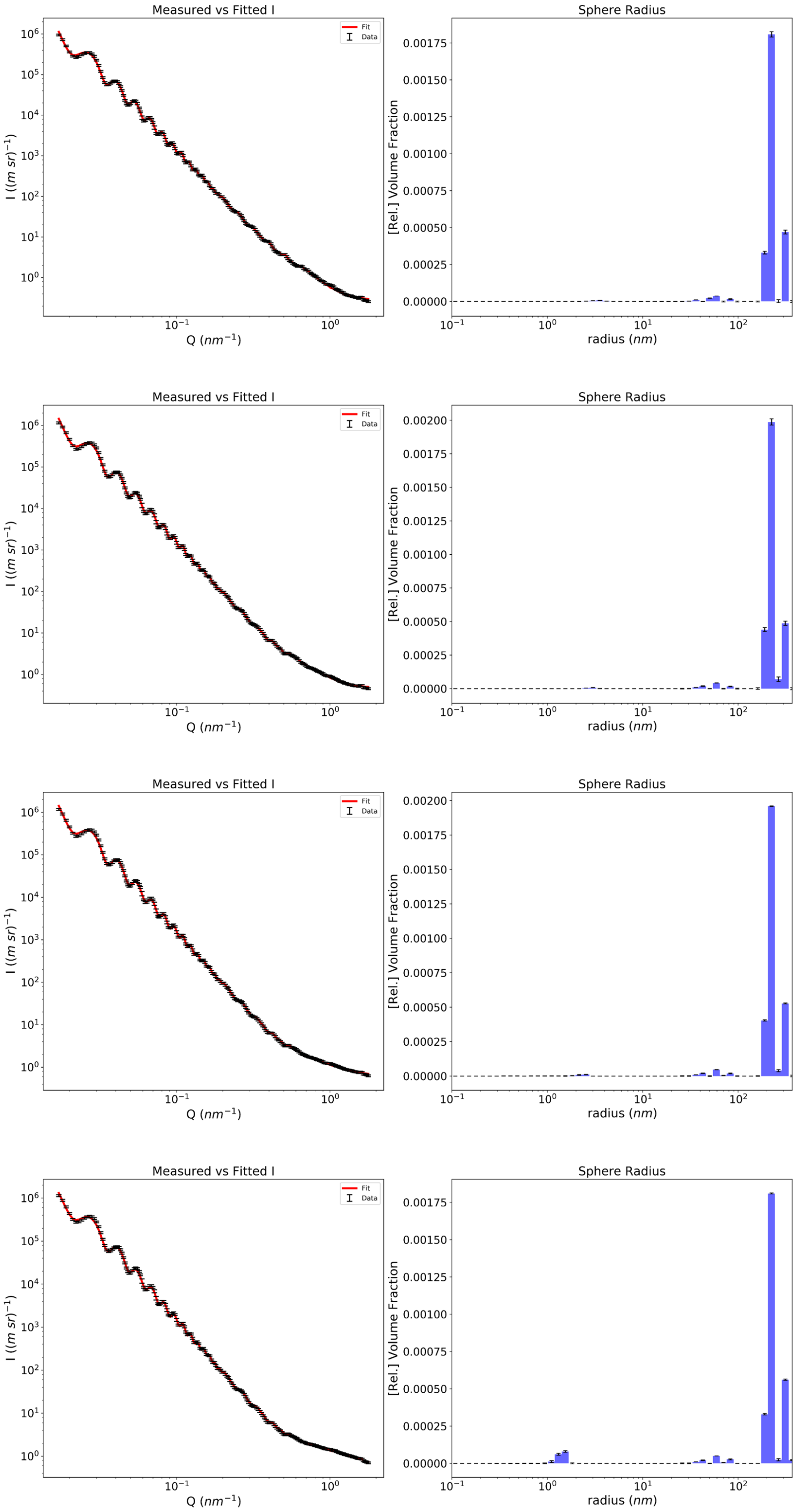

Figure B.5: Fits of the *in-situ* SAXS data collected on the formation of macroporous Silicalite-1 from 500 nm silica nanospheres at 160°C. Scans taken after 0, 1000, 3200 and 4000 seconds, top to bottom respectively

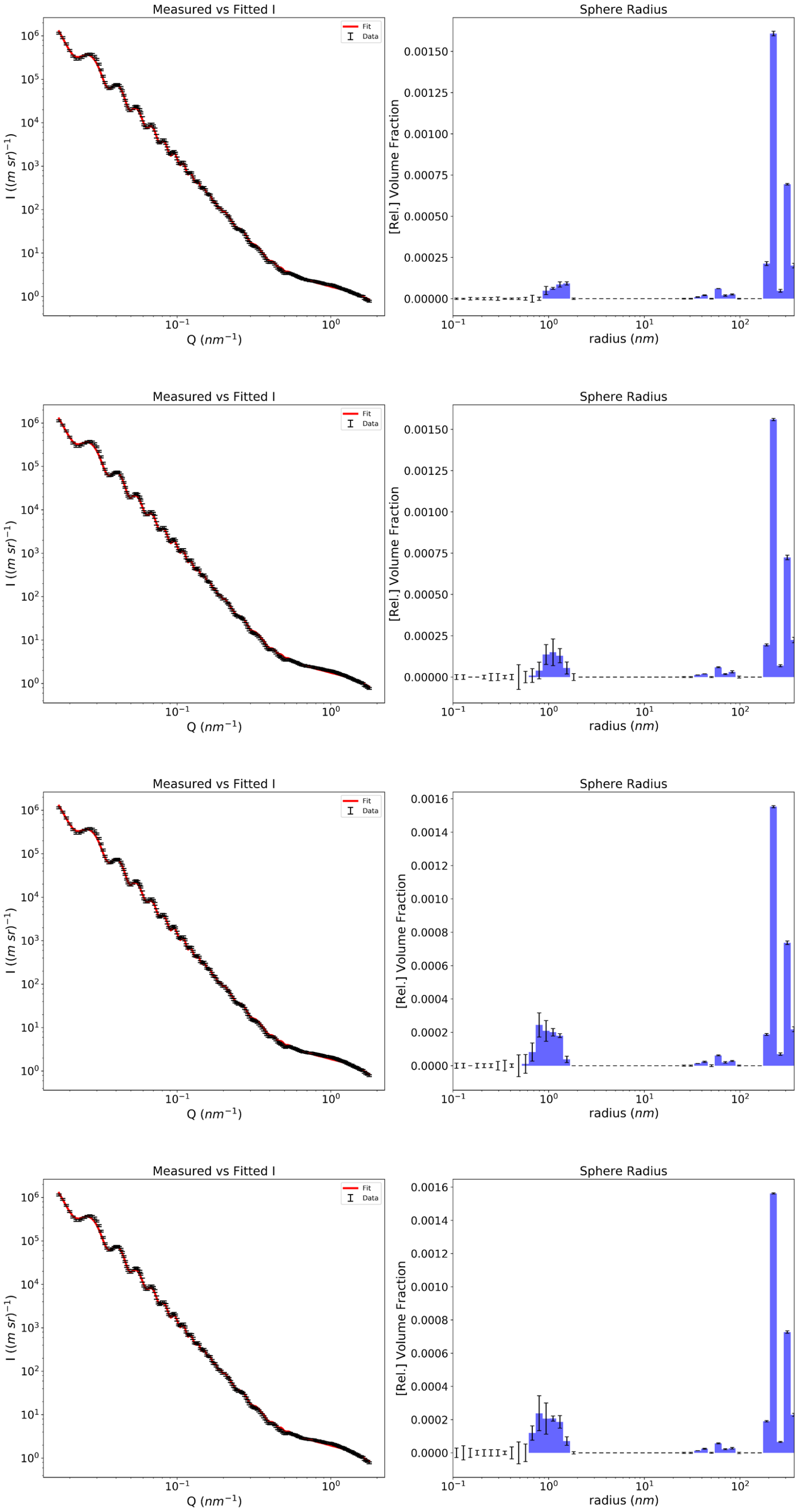

Figure B.6: Fits of the *in-situ* SAXS data collected on the formation of macroporous Silicalite-1 from 500 nm silica nanospheres at 160°C. Scans taken after 4800, 5600, 6400 and 7200 seconds, top to bottom respectively

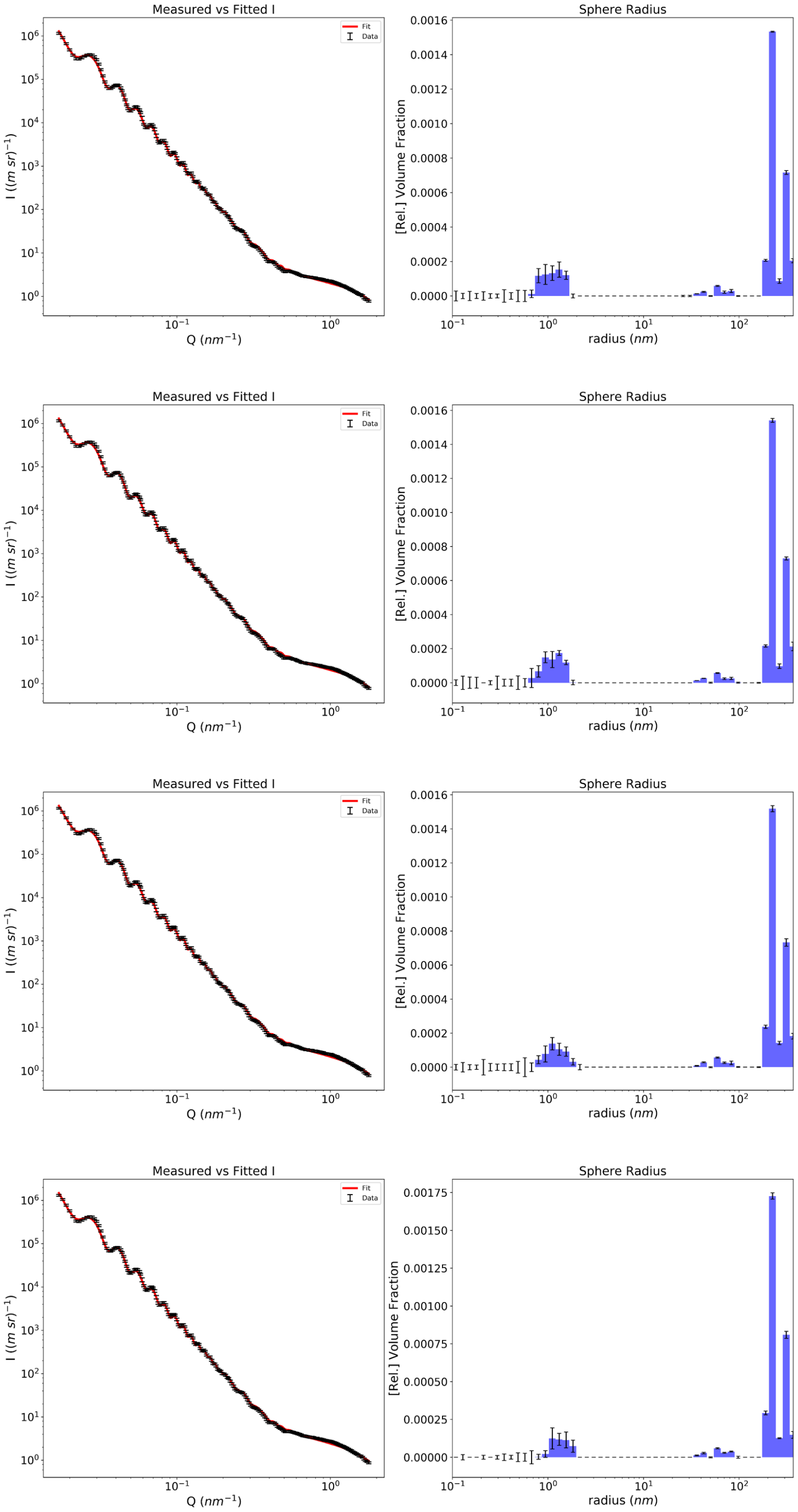

Figure B.7: Fits of the *in-situ* SAXS data collected on the formation of macroporous Silicalite-1 from 500 nm silica nanospheres at 160°C. Scans taken after 8000, 8400, 8800 and 9600 seconds, top to bottom respectively

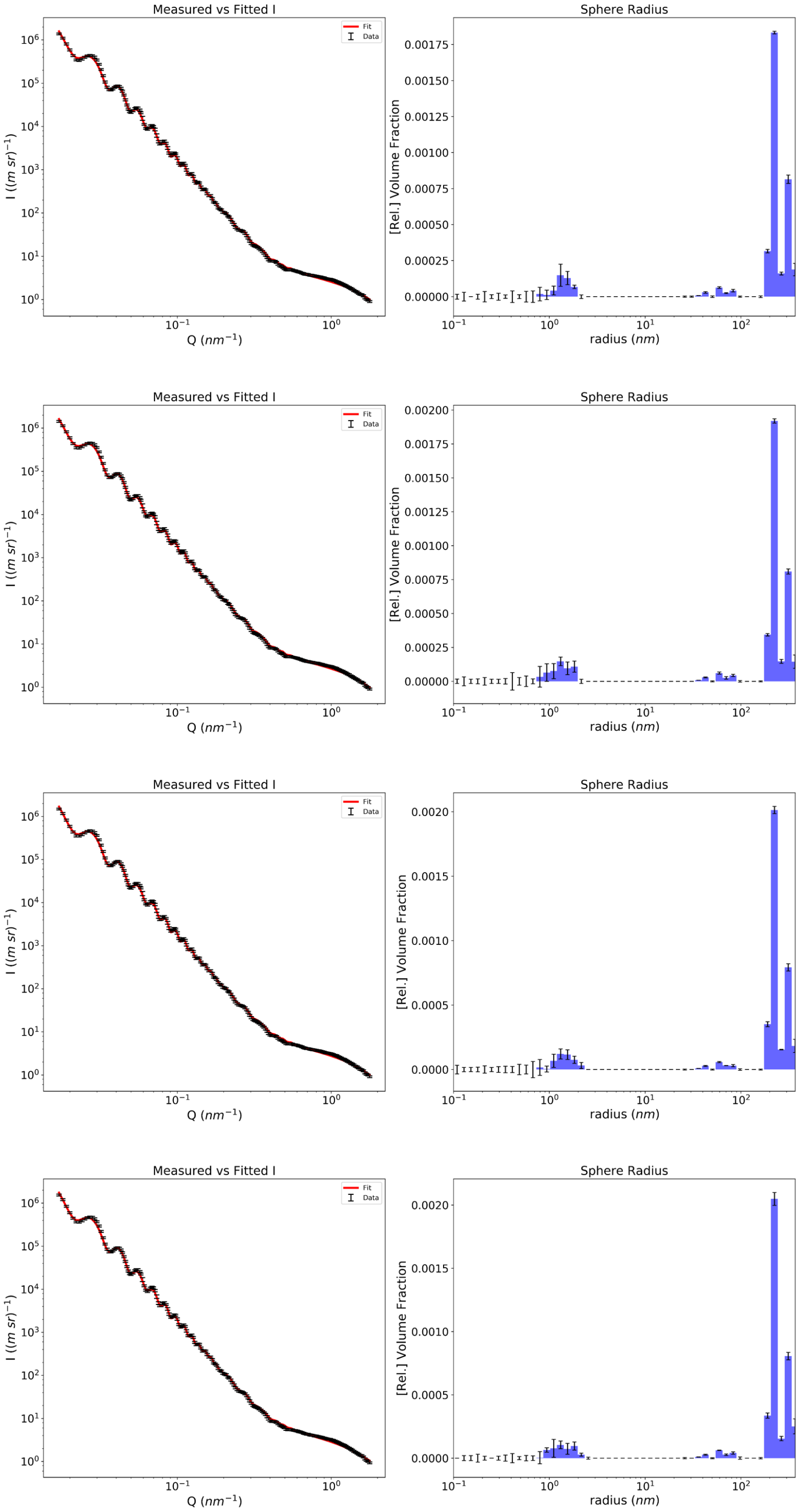

Figure B.8: Fits of the *in-situ* SAXS data collected on the formation of macroporous Silicalite-1 from 500 nm silica nanospheres at 160°C. Scans taken after 10000, 10400, 10800 and 11200 seconds, top to bottom respectively

B.1.3 Aluminium Incorporation into Hierarchical Zeolites

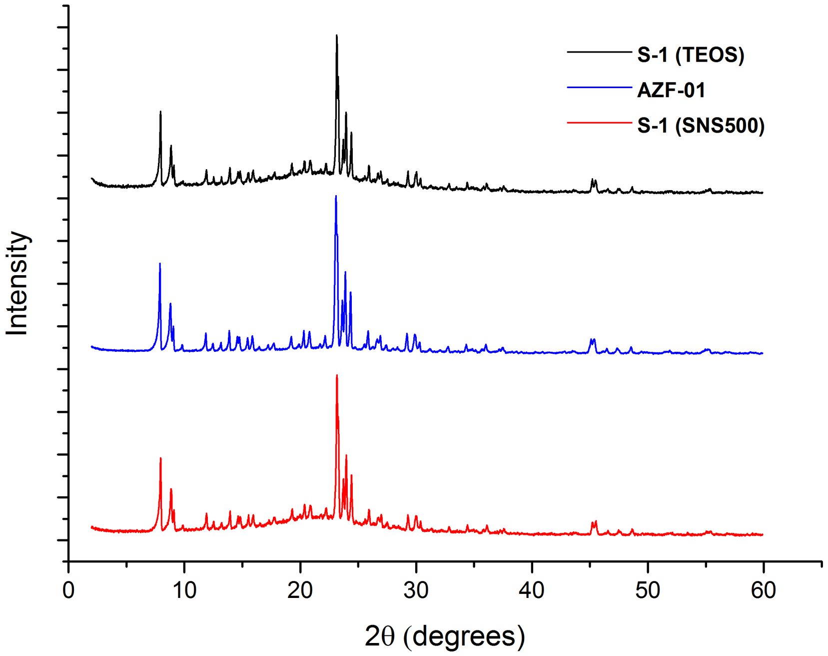

Figure B.9: PXRD patterns of hierarchical ZSM-5 (AZF-01) and hierarchical Silicalite-1 samples formed from 500 nm silica nanospheres, and conventional Silicalite-1 at 160°C.

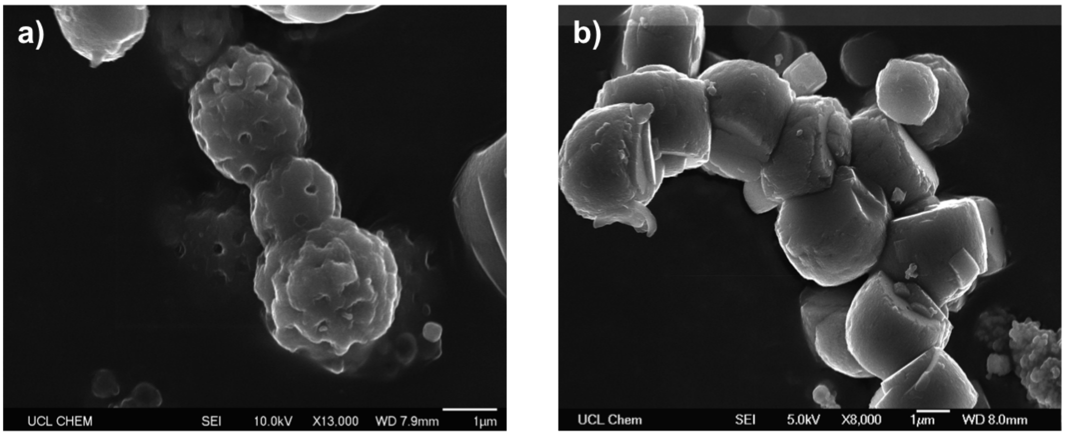

Figure B.10: SEM images of ZSM-5 samples formed from 500 nm silica nanospheres.

Figure B.11: SEM images of ZSM-5 samples formed from 500 nm silica nanospheres.

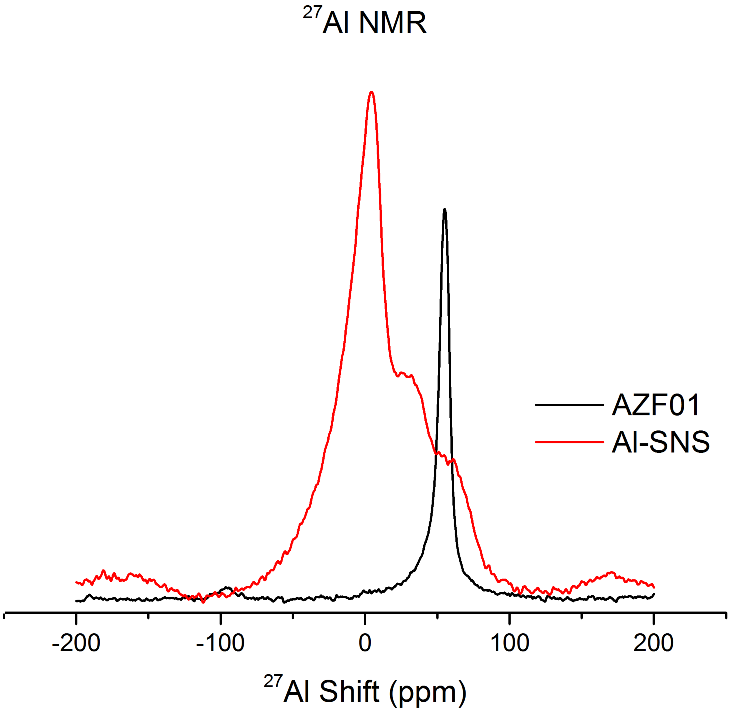

Figure B.12: ^{27}Al MAS-NMR spectrum of impregnated 500 nm silica spheres (Al-SNS), and hierarchical ZSM-5 (AZF01). Peak observed at 55.1 ppm for AZF01 sample is associated with tetrahedrally coordinated aluminum species within the zeolites frameworks, whilst signals observed at c.a. 30 and c.a. 0 ppm are associated with 5- and 6-coordinate aluminium species respectively.

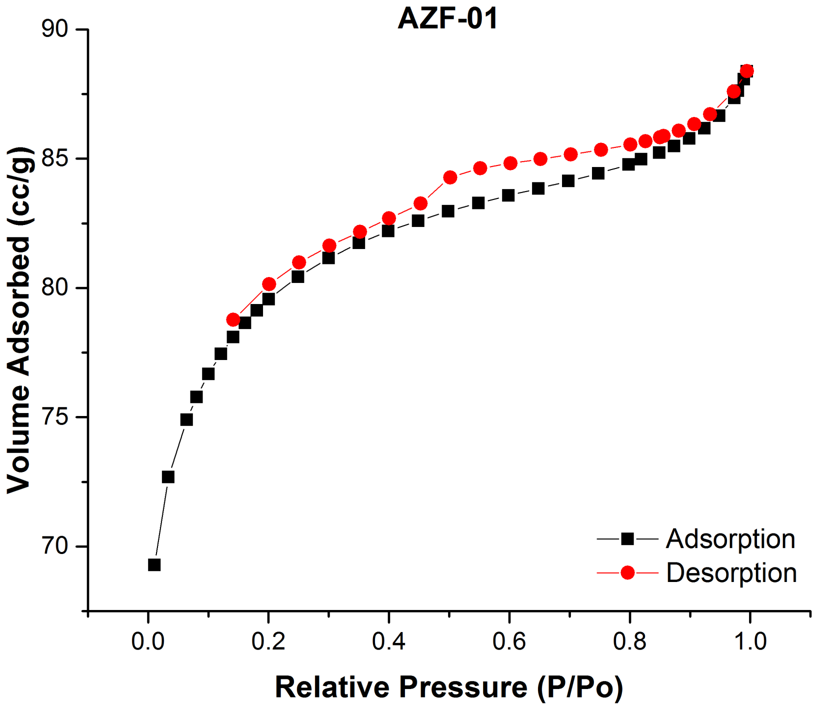

Figure B.13: N_2 adsorption-desorption isotherms of hierarchical ZSM-5 sample (AZF-01). Sample was found to have a surface area 282.043 m^2/g, and isotherm observed is similar to that seen for macroporous silicalite-1 samples.

Appendix C

Nucleation and Growth of Metal

Organic Frameworks

C.1 Formation of ZIF-8

C.1.1 Formation of ZIF-8 at 14°C

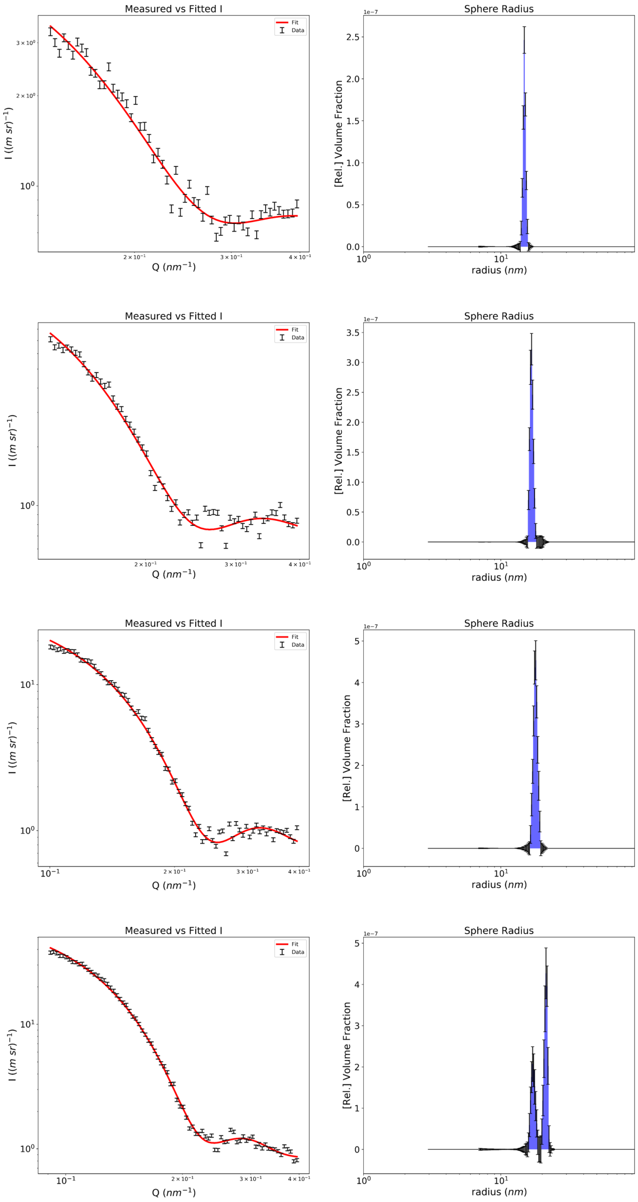

Figure C.1: Fits of the *in-situ* SAXS data collected on the formation of ZIF-8 at 14°C. Scans taken after 120, 132, 144 and 156 seconds, top to bottom respectively

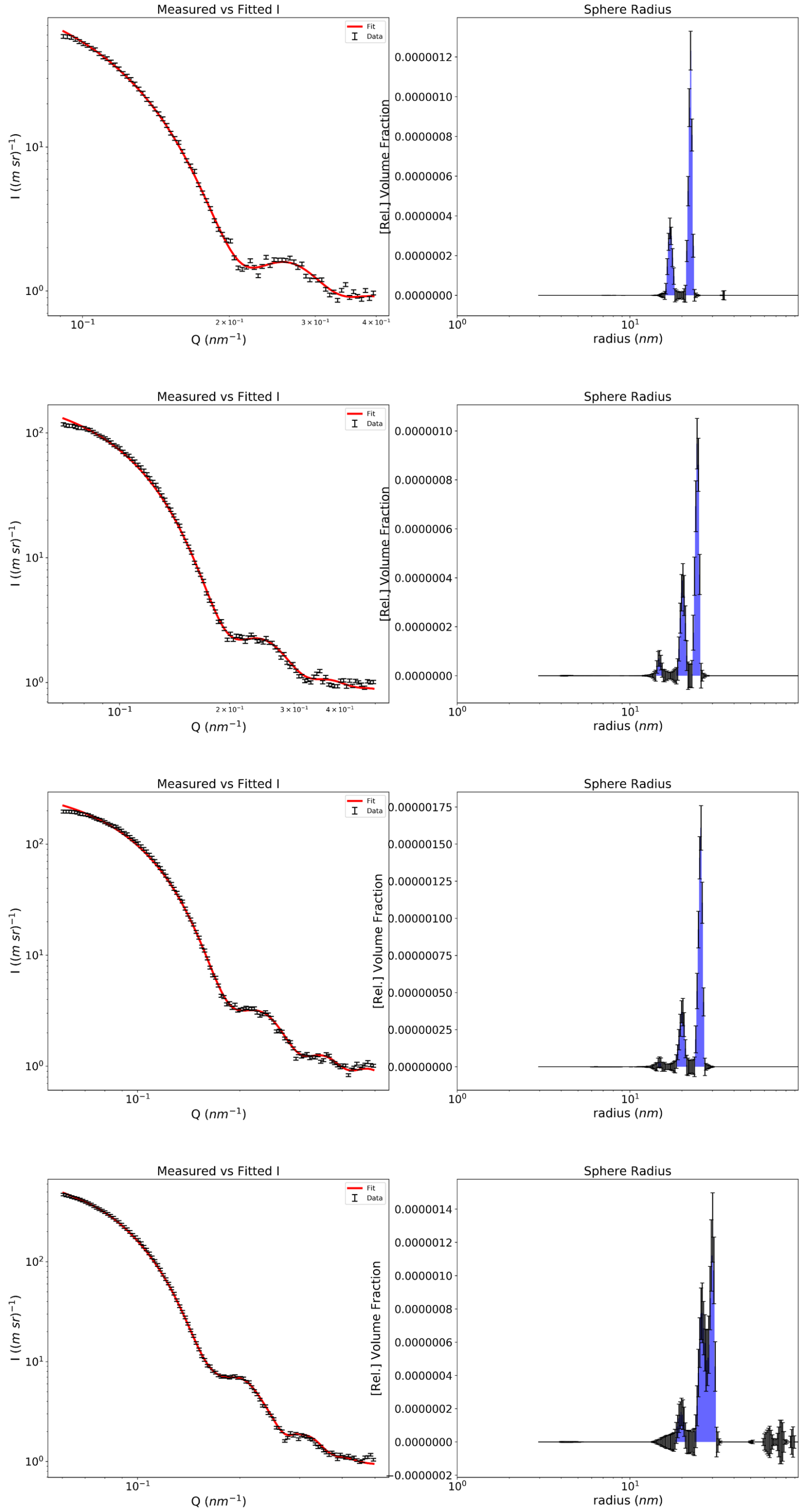

Figure C.2: Fits of the *in-situ* SAXS data collected on the formation of ZIF-8 at 14°C. Scans taken after 168, 180, 192 and 220 seconds, top to bottom respectively

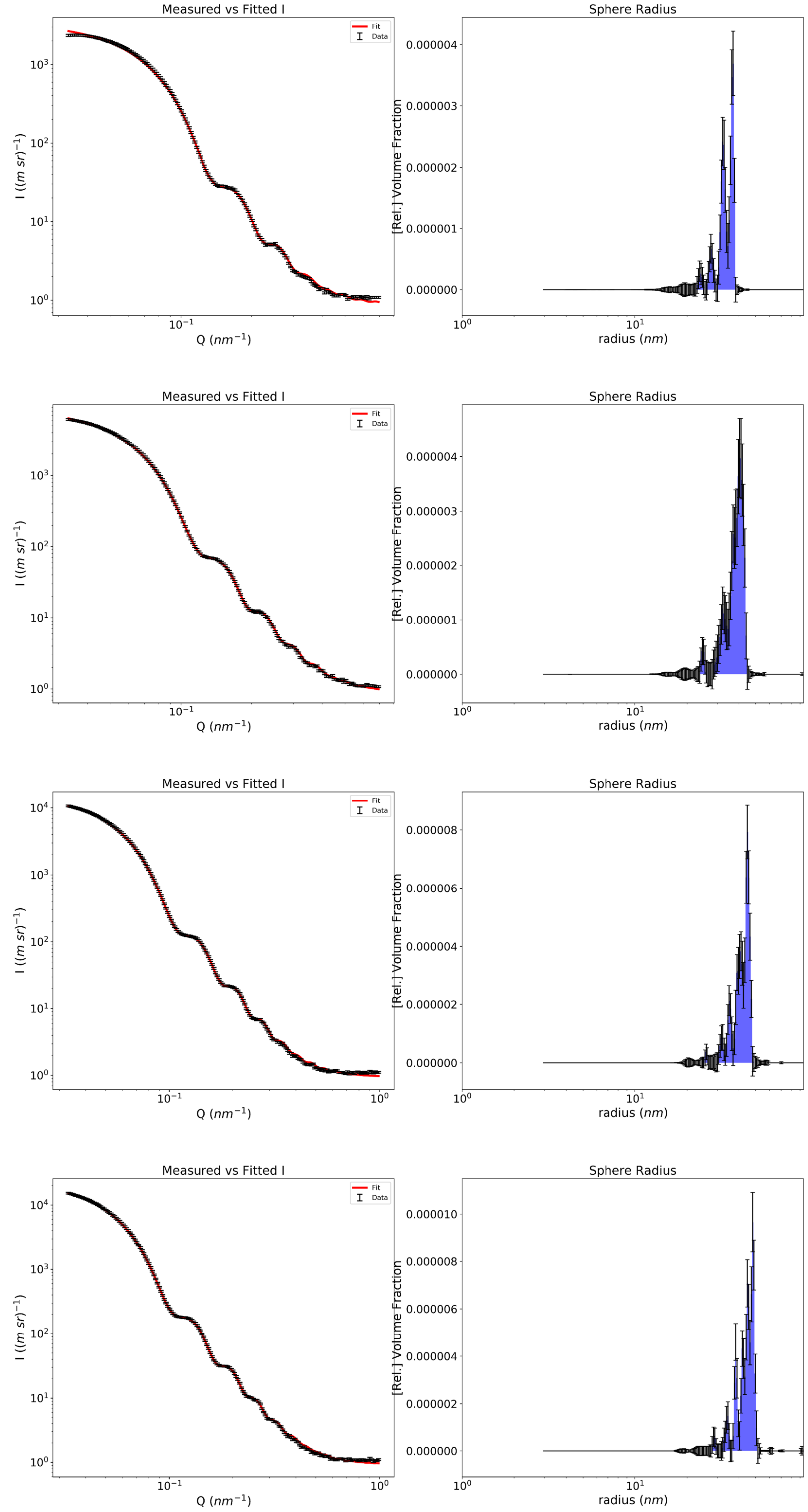

Figure C.3: Fits of the *in-situ* SAXS data collected on the formation of ZIF-8 at 14°C. Scans taken after 280, 340, 400 and 466 seconds, top to bottom respectively

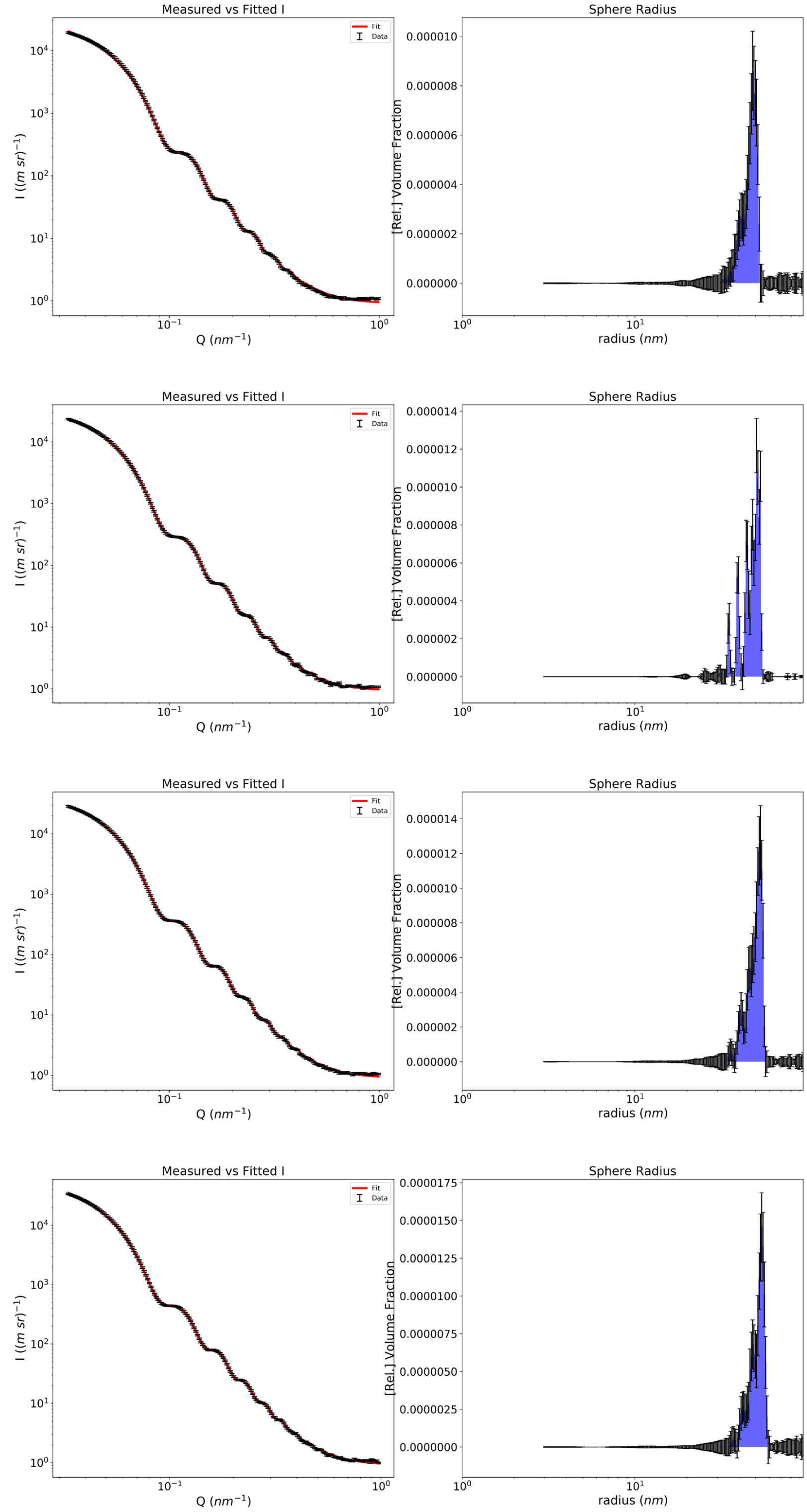

Figure C.4: Fits of the *in-situ* SAXS data collected on the formation of ZIF-8 at 14°C. Scans taken after 520, 580, 680 and 800 seconds, top to bottom respectively

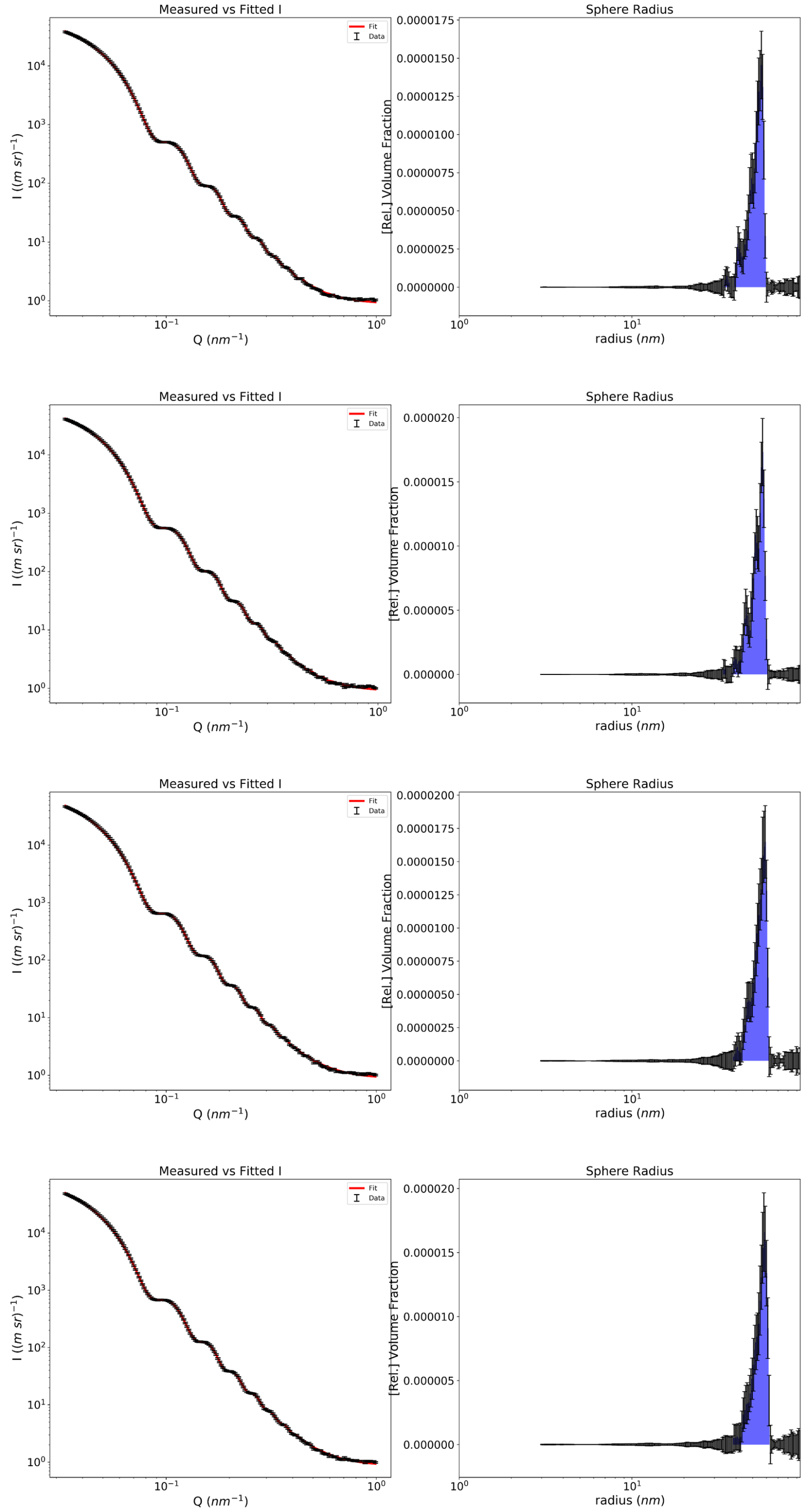

Figure C.5: Fits of the *in-situ* SAXS data collected on the formation of ZIF-8 at 14°C. Scans taken after 920, 1040, 1320 and 1440 seconds, top to bottom respectively

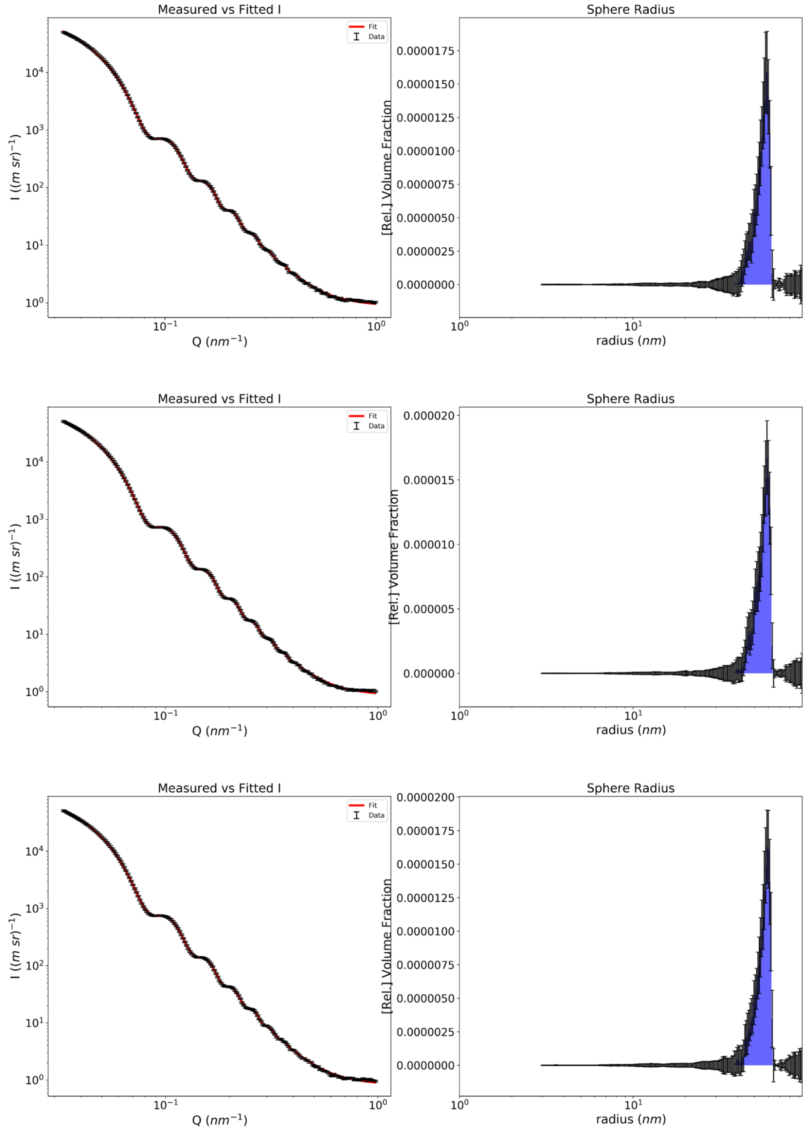

Figure C.6: Fits of the *in-situ* SAXS data collected on the formation of ZIF-8 at 14°C. Scans taken after 1560, 1680 and 1800 seconds, top to bottom respectively

C.1.2 Formation of ZIF-8 at 22°C

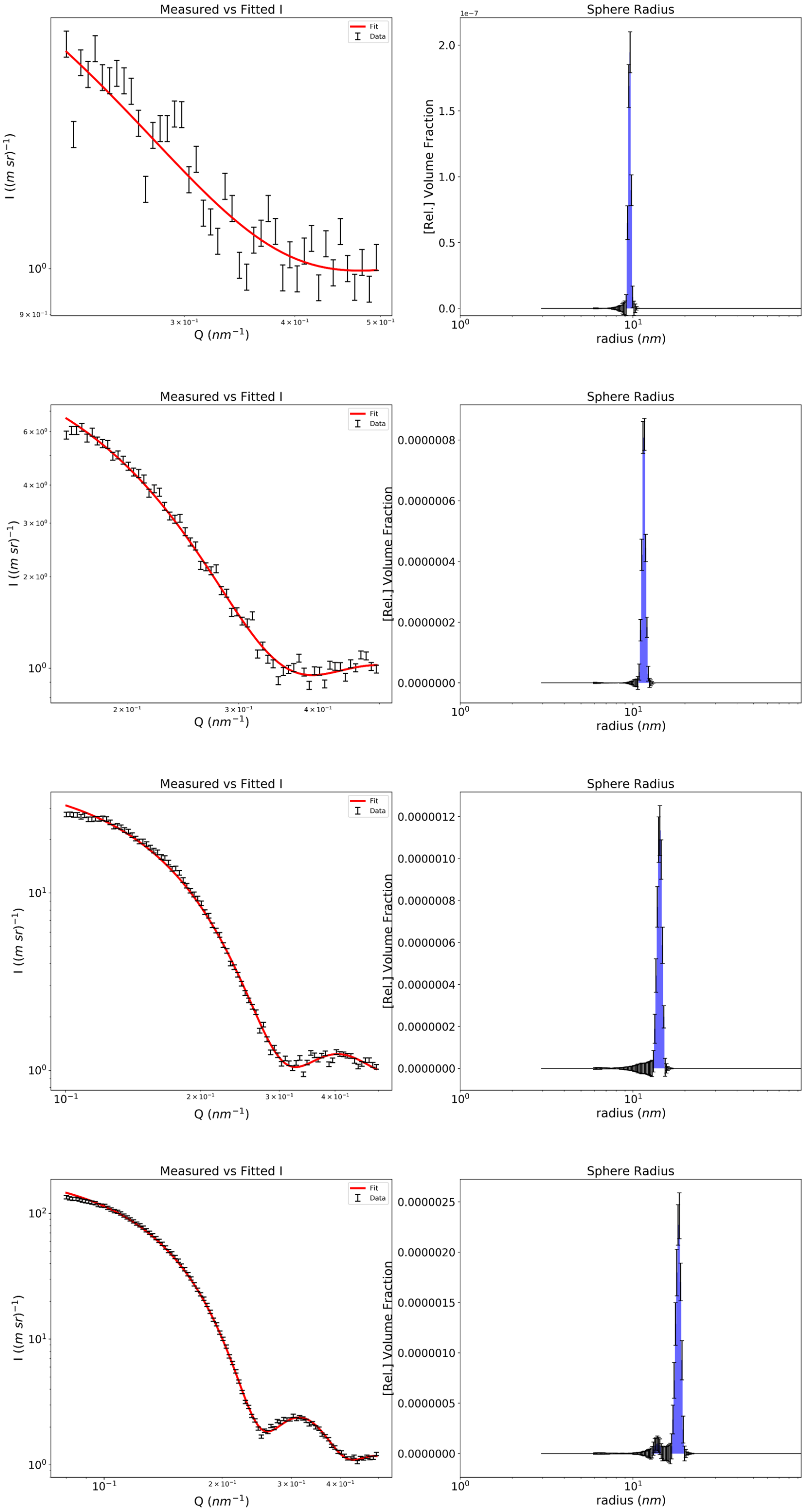

Figure C.7: Fits of the *in-situ* SAXS data collected on the formation of ZIF-8 at 22°C. Scans taken after 32, 40, 48 and 60 seconds, top to bottom respectively

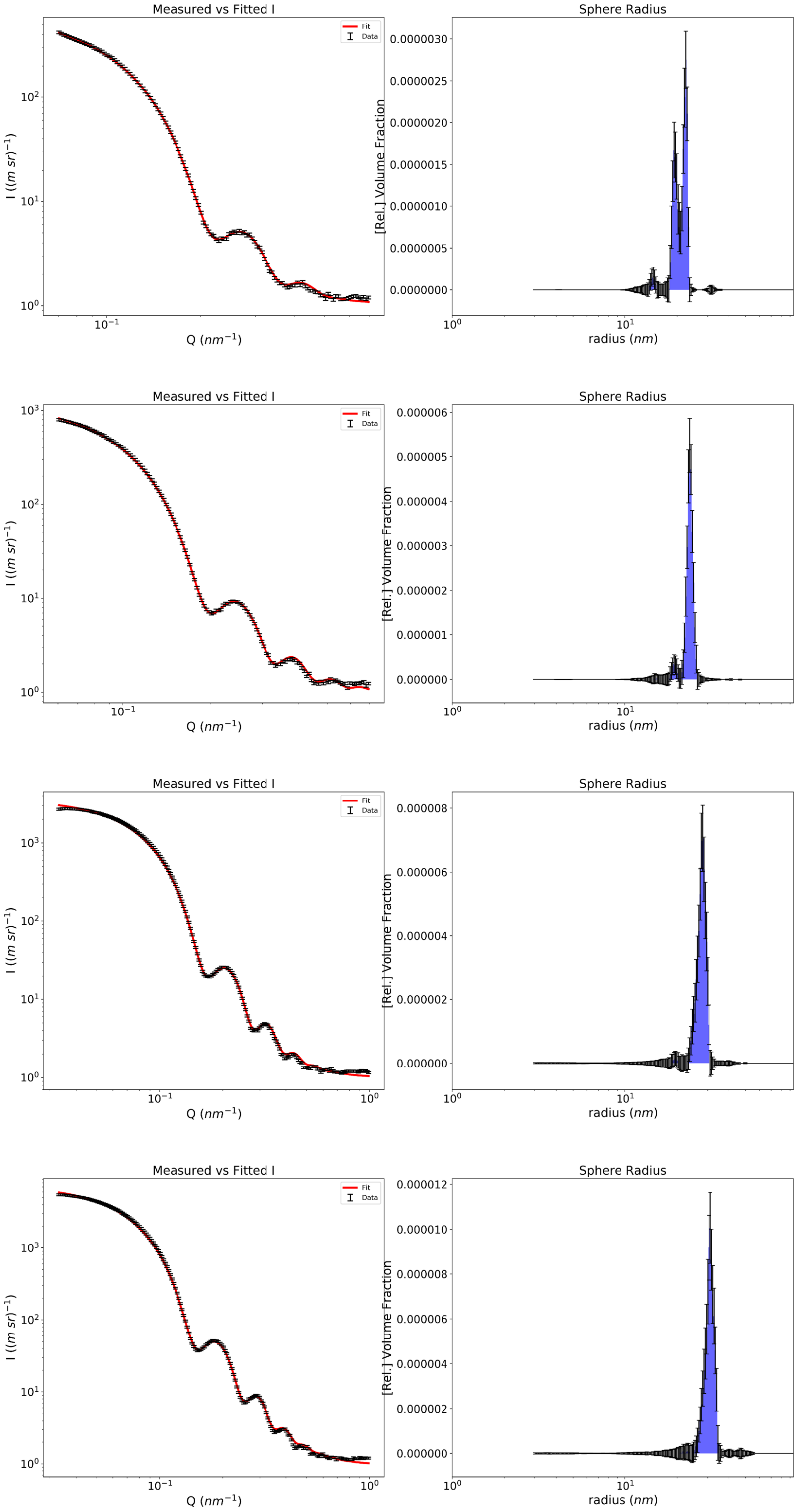

Figure C.8: Fits of the *in-situ* SAXS data collected on the formation of ZIF-8 at 22°C. Scans taken after 70, 80, 100 and 120 seconds, top to bottom respectively

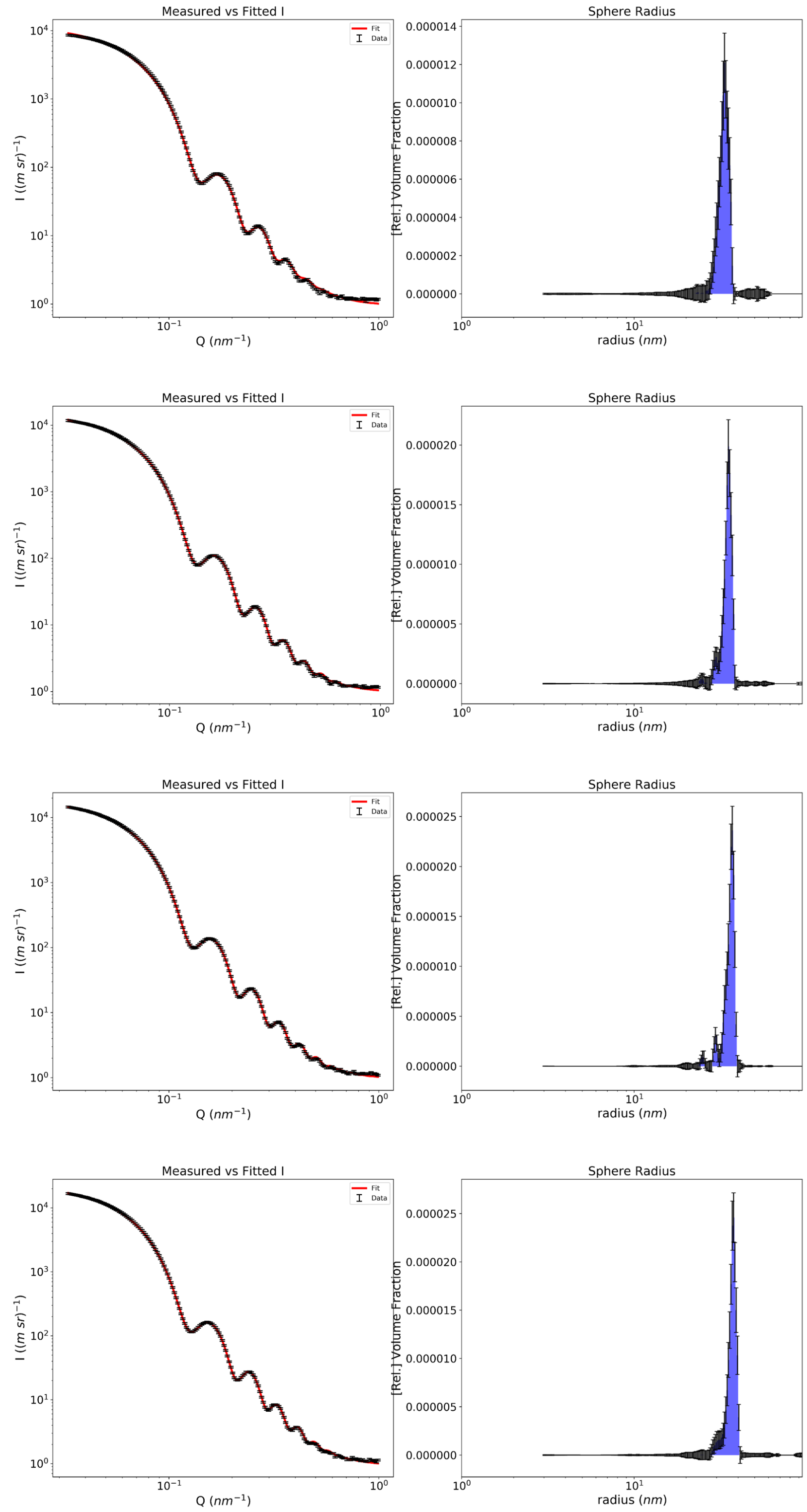

Figure C.9: Fits of the *in-situ* SAXS data collected on the formation of ZIF-8 at 22°C. Scans taken after 140, 160, 180 and 200 seconds, top to bottom respectively

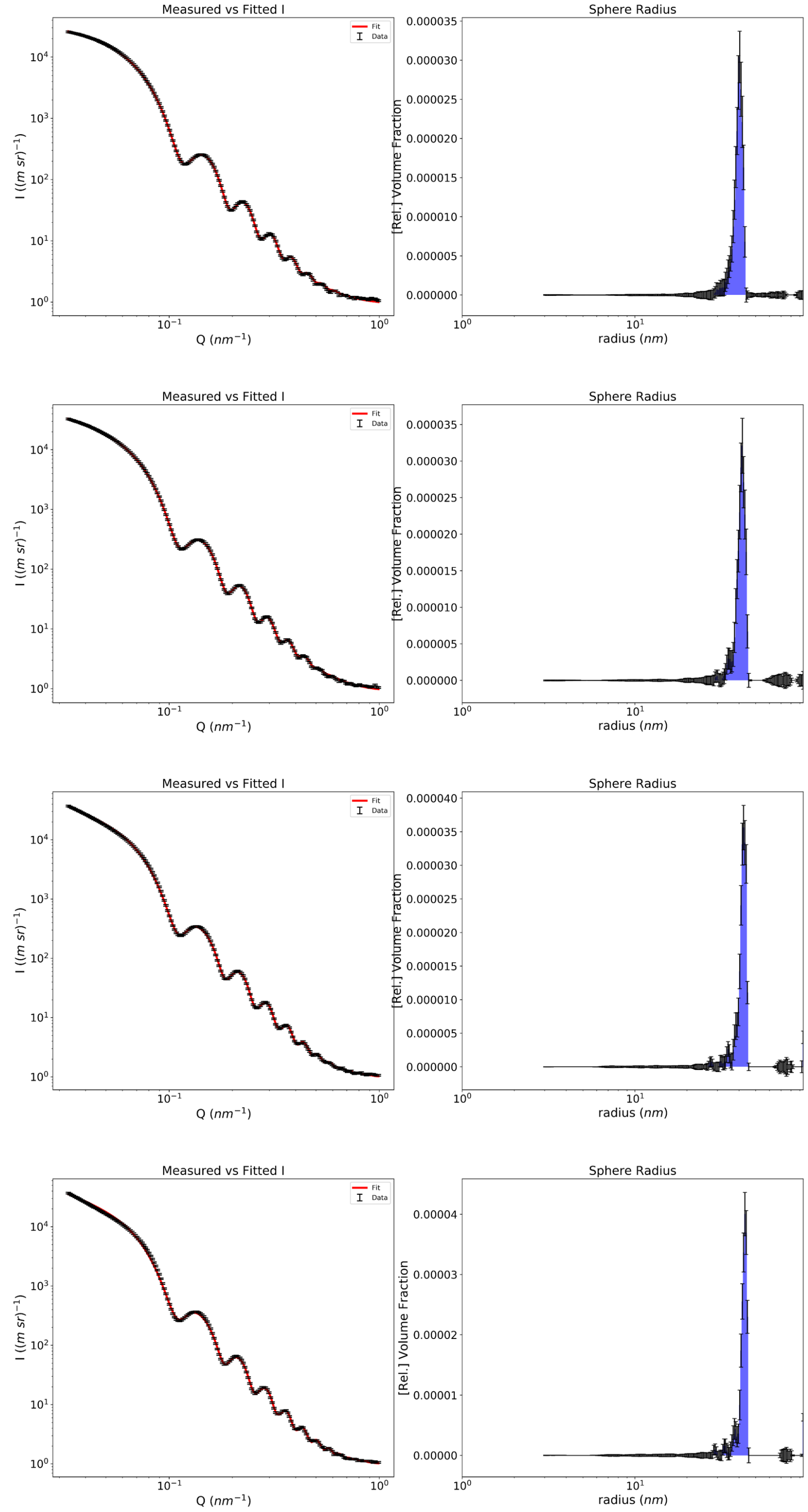

Figure C.10: Fits of the *in-situ* SAXS data collected on the formation of ZIF-8 at 22°C. Scans taken after 300, 400, 500 and 600 seconds, top to bottom respectively

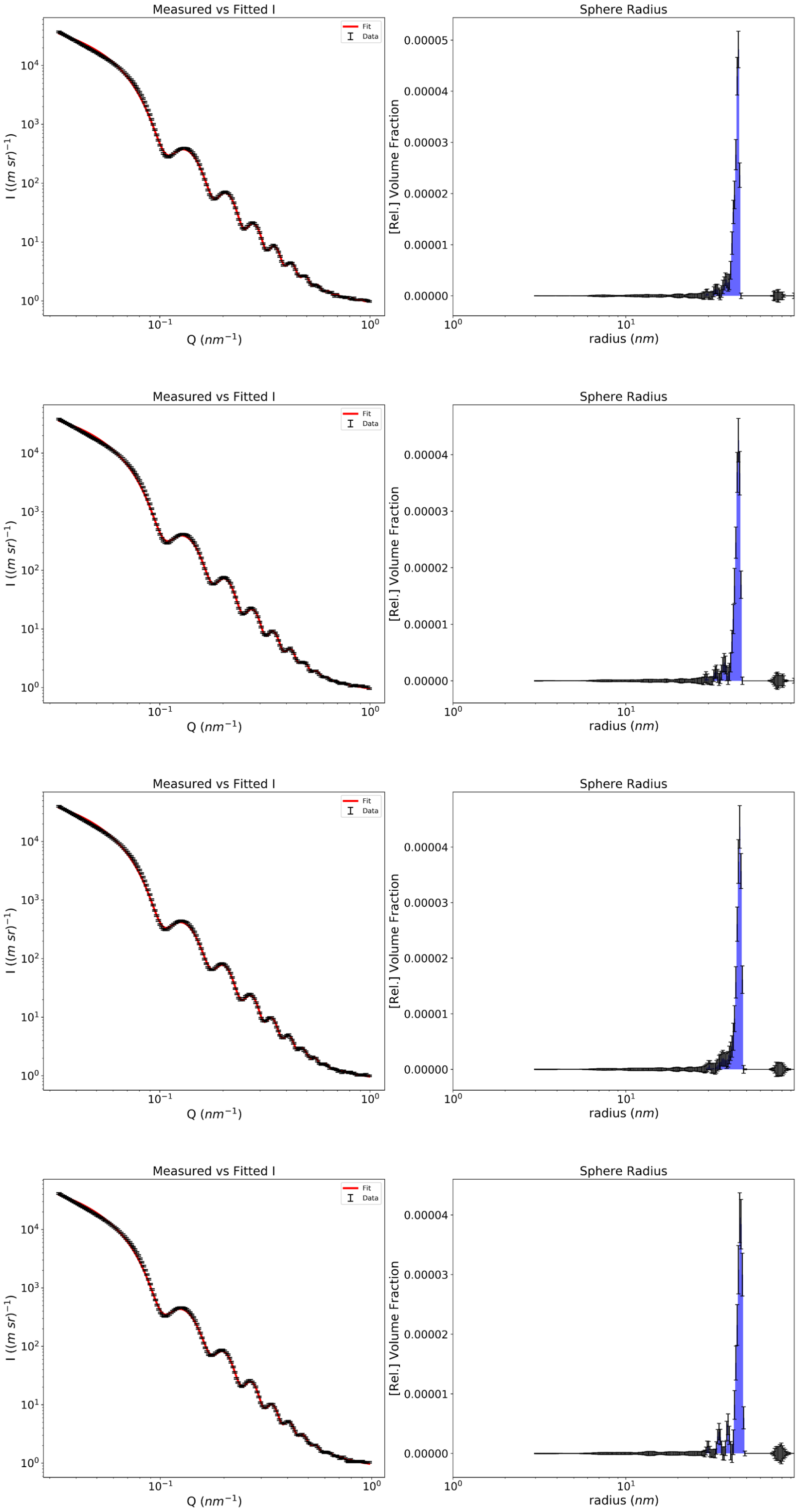

Figure C.11: Fits of the *in-situ* SAXS data collected on the formation of ZIF-8 at 22°C. Scans taken after 800, 1000, 1400 and 1800 seconds, top to bottom respectively

C.1.3 Formation of ZIF-8 at 44°C

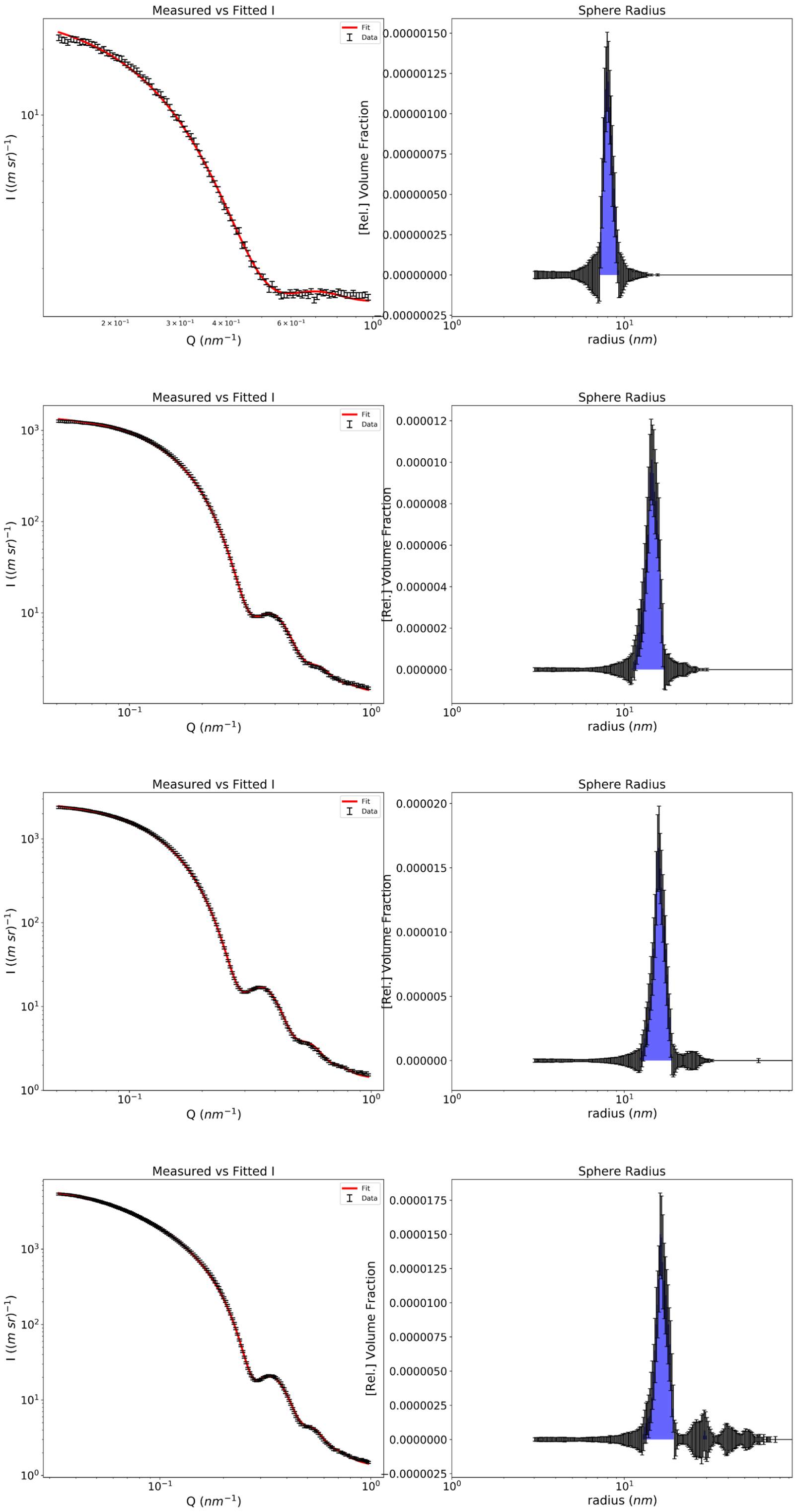

Figure C.12: Fits of the *in-situ* SAXS data collected on the formation of ZIF-8 at 44°C. Scans taken after 8, 20, 30 and 40 seconds, top to bottom respectively

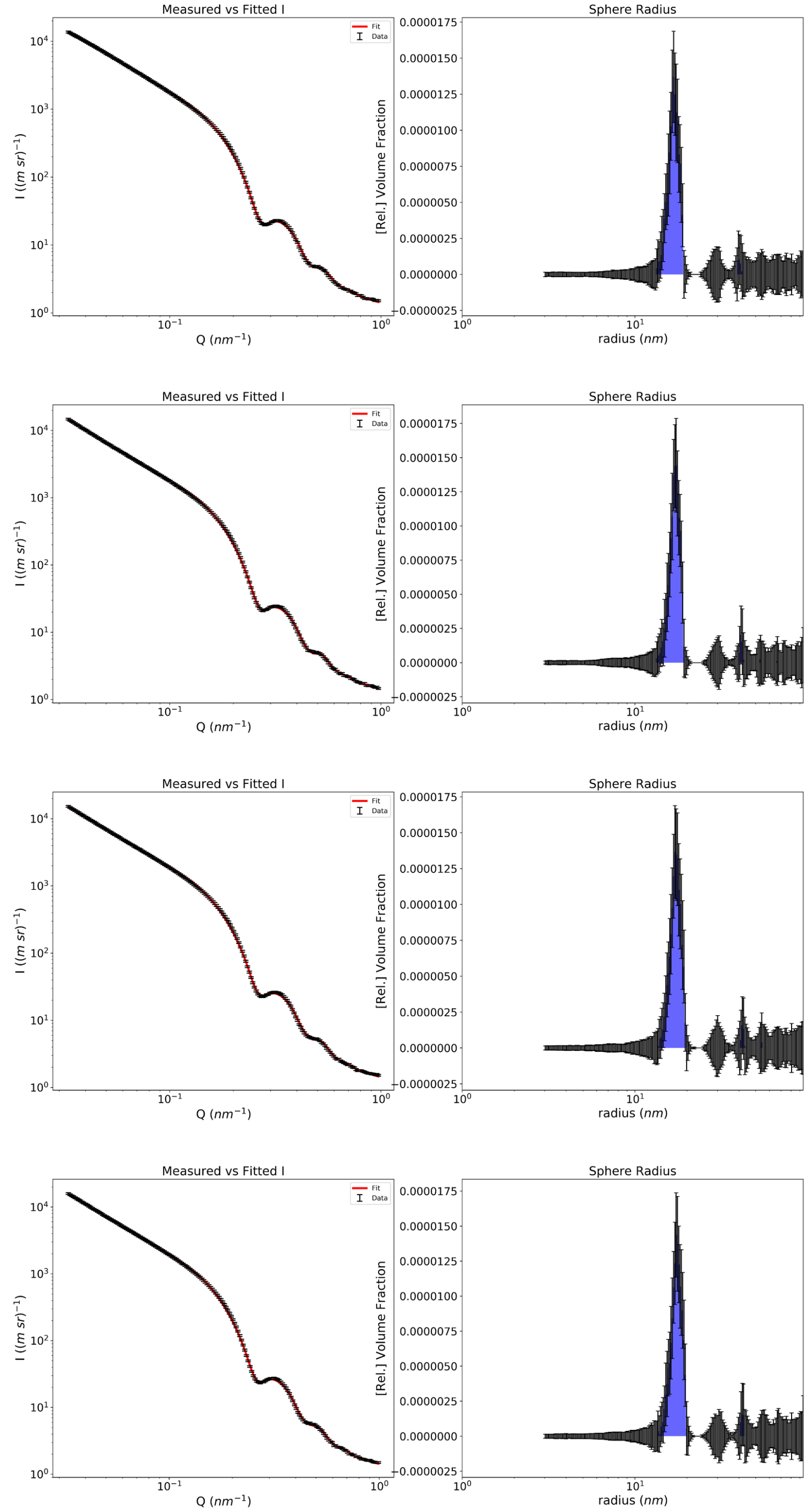

Figure C.13: Fits of the *in-situ* SAXS data collected on the formation of ZIF-8 at 44°C. Scans taken after 50, 60, 70 and 80 seconds, top to bottom respectively

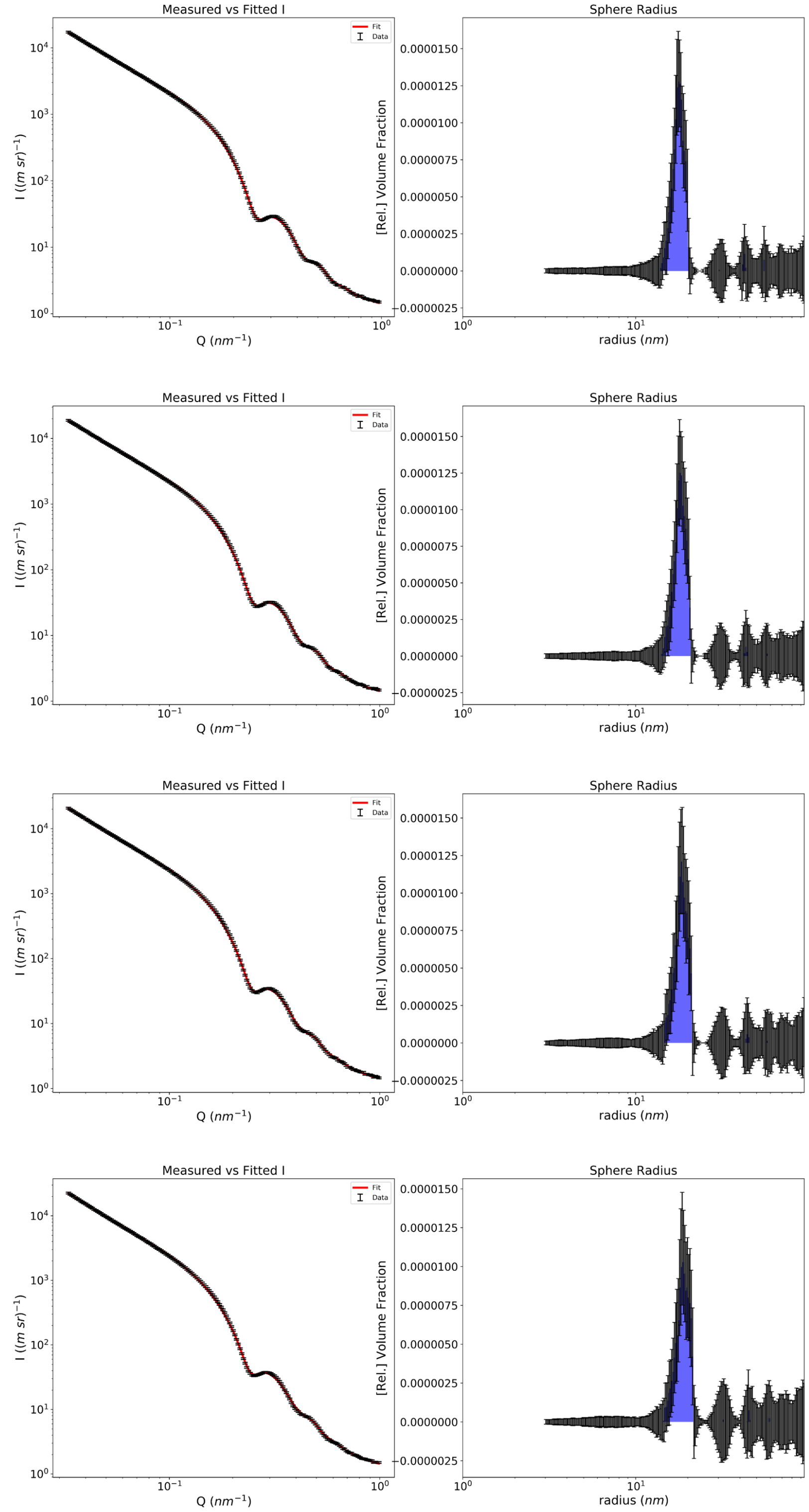

Figure C.14: Fits of the *in-situ* SAXS data collected on the formation of ZIF-8 at 44°C. Scans taken after 100, 140, 200 and 300 seconds, top to bottom respectively

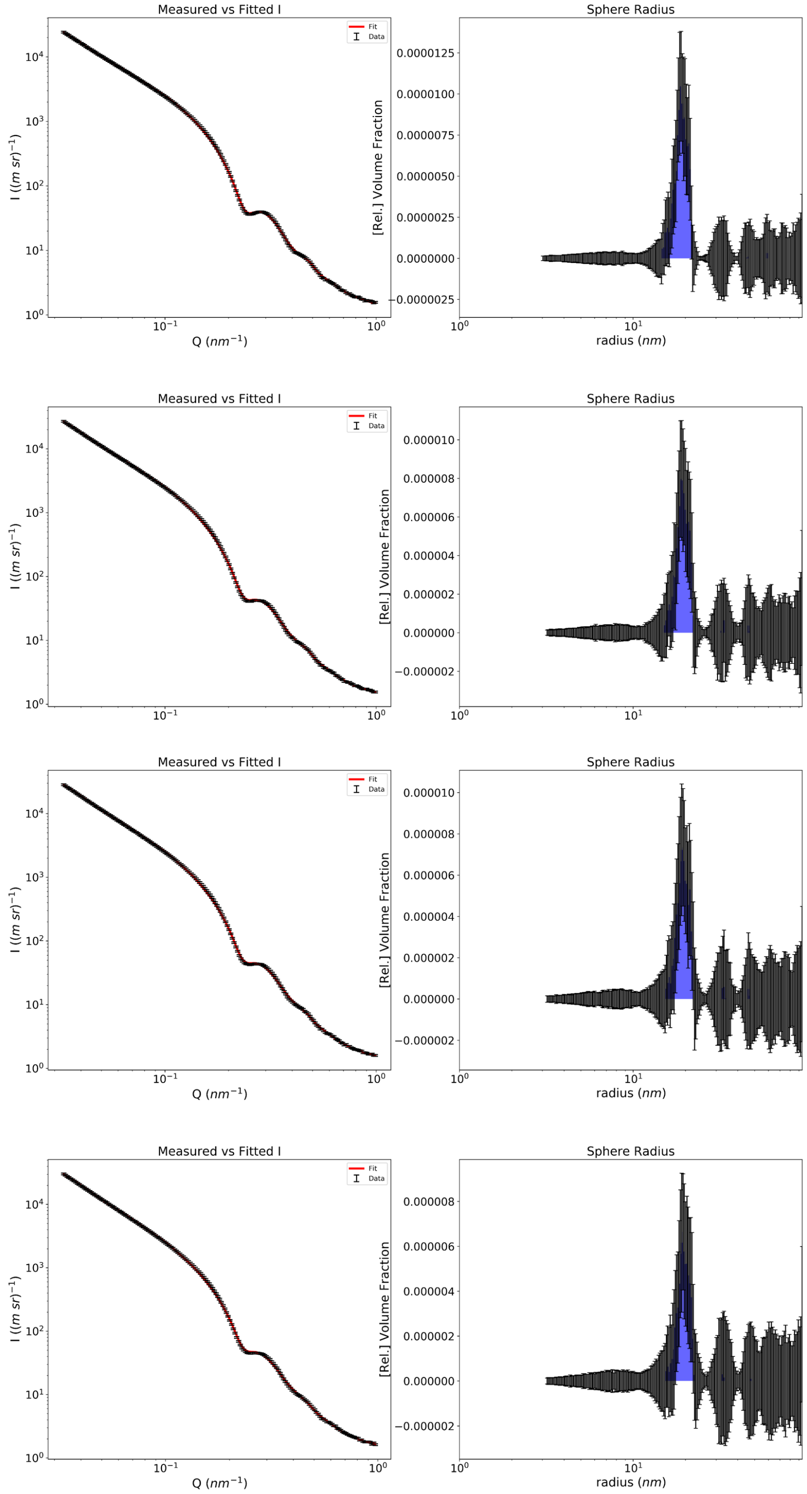

Figure C.15: Fits of the *in-situ* SAXS data collected on the formation of ZIF-8 at 44°C. Scans taken after 400, 800, 1200 and 1800 seconds, top to bottom respectively

C.1.4 Formation of ZIF-8 at 55°C

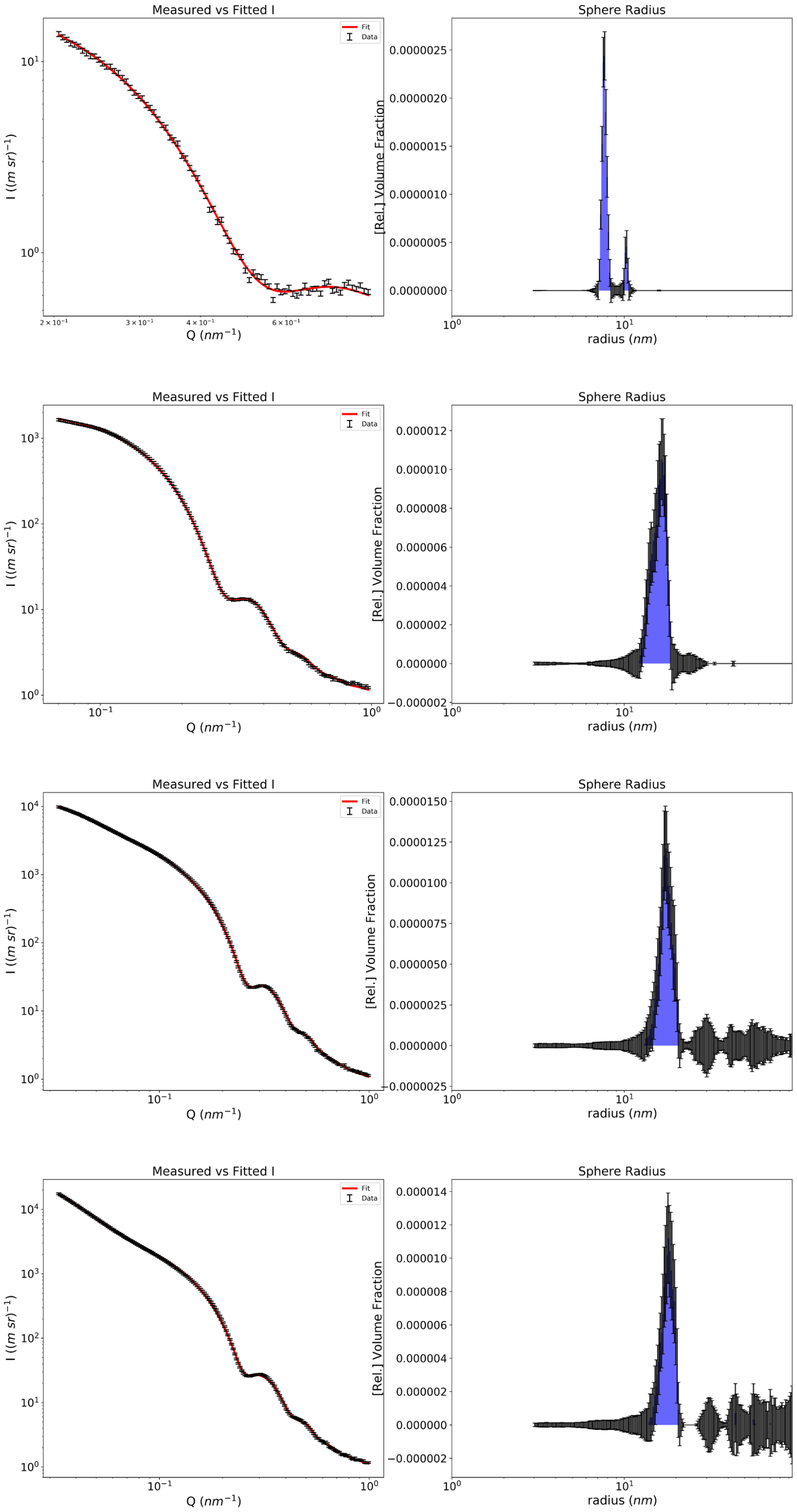

Figure C.16: Fits of the *in-situ* SAXS data collected on the formation of ZIF-8 at 55°C. Scans taken after 6, 18, 32 and 46 seconds, top to bottom respectively

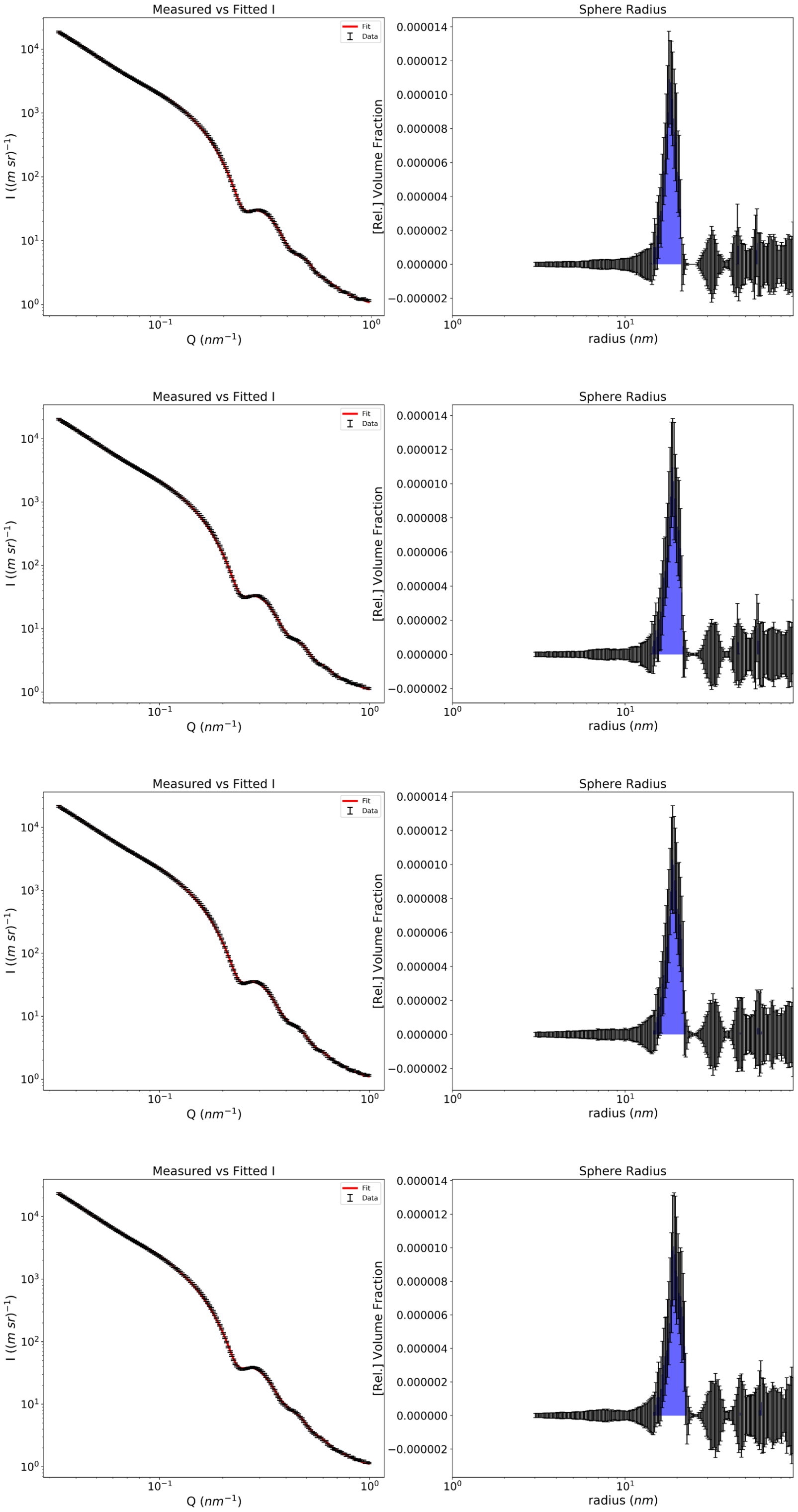

Figure C.17: Fits of the *in-situ* SAXS data collected on the formation of ZIF-8 at 55°C. Scans taken after 60, 80, 100 and 140 seconds, top to bottom respectively

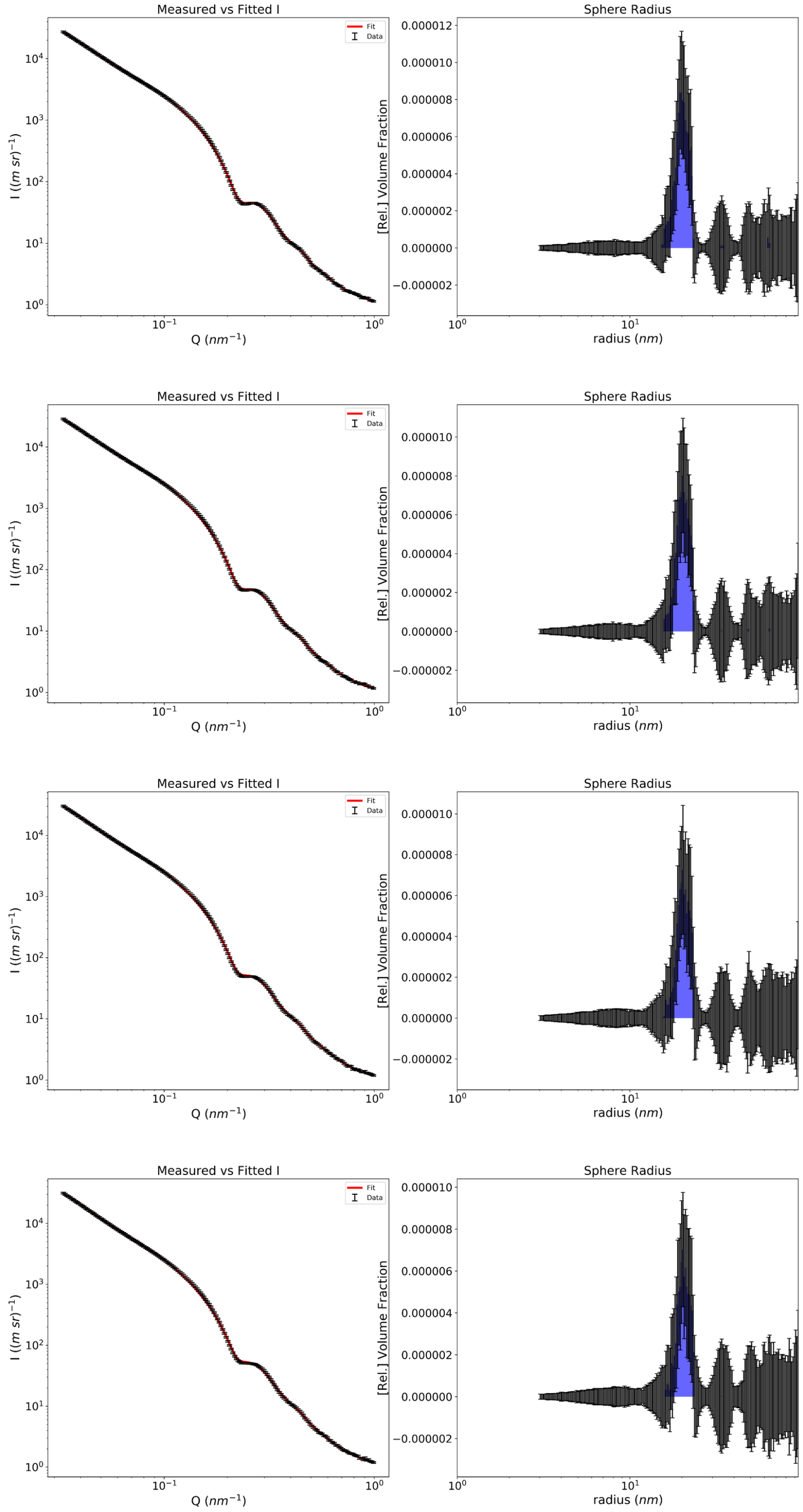

Figure C.18: Fits of the *in-situ* SAXS data collected on the formation of ZIF-8 at 55°C. Scans taken after 300, 400, 600 and 800 seconds, top to bottom respectively

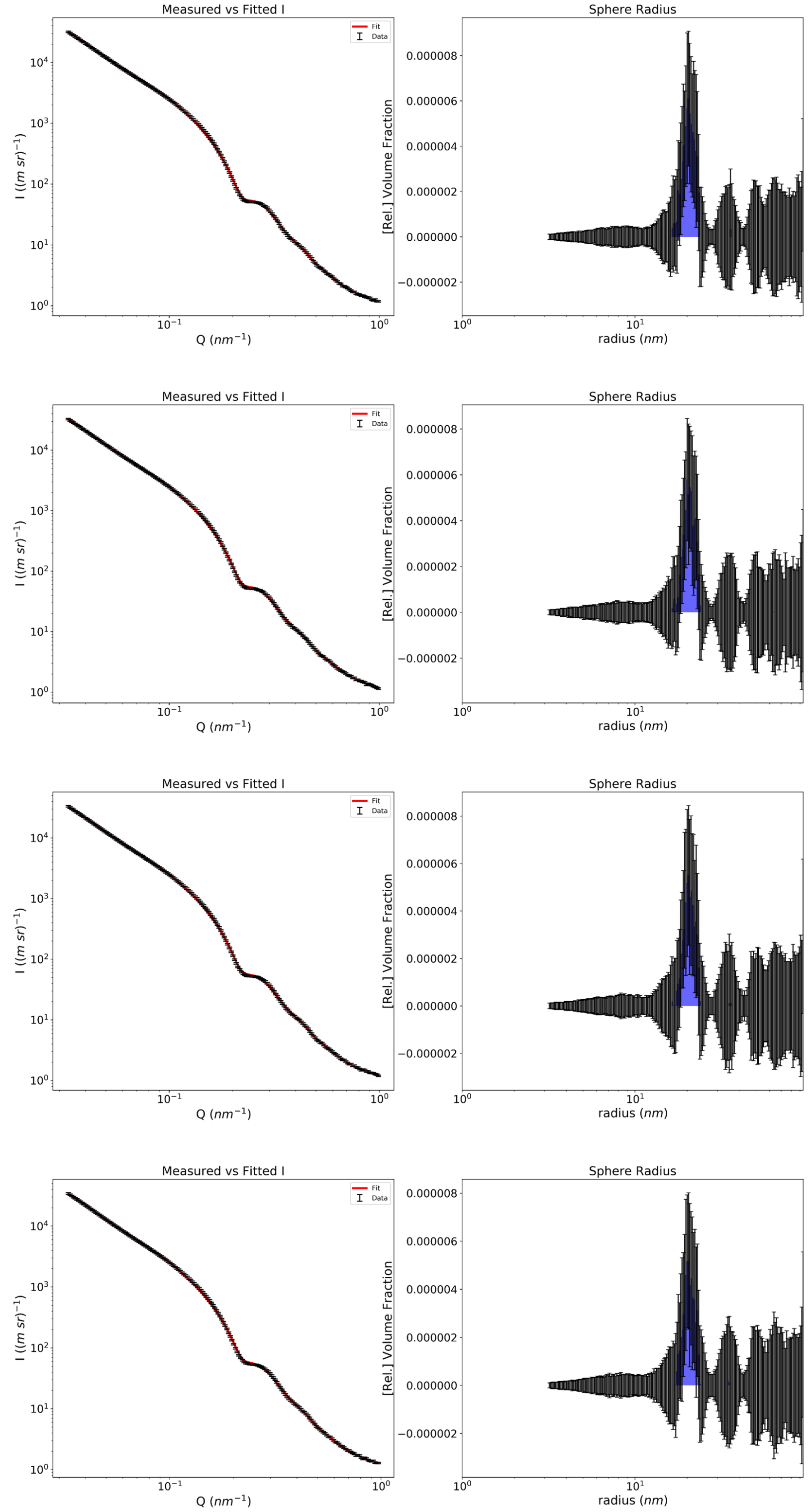

Figure C.19: Fits of the *in-situ* SAXS data collected on the formation of ZIF-8 at 55°C. Scans taken after 1000, 1300, 1500 and 1800 seconds, top to bottom respectively